



SPACOMM 2011

The Third International Conference on Advances in Satellite
and Space Communications

April 17-22, 2011

Budapest, Hungary

SPACOMM 2011 Editors

Massimiliano Laddomada, Texas A&M University - Texarkana, USA

Timothy Pham, Jet Propulsion Laboratory / California Institute of Technology, USA

SPACOMM 2011

Foreword

The Third International Conference on Advances in Satellite and Space Communications [SPACOMM 2011], held between April 17 and 22 in Budapest, Hungary, constituted an attempt to evaluate the state of the art on academia and industry on the satellite, radar, and antennas based communications bringing together scientists and practitioners with challenging issues, achievements, and lessons learnt.

Significant efforts have been allotted to design and deploy global navigation satellite communications systems. Satellite navigation technologies, applications, and services still experience challenges related to signal processing, security, performance, and accuracy. Theories and practices on system-in-package RF design techniques, filters, passive circuits, microwaves, frequency handling, radars, antennas, and radio communications and radio waves propagation have been implemented. Services based on their use are now available, especially those for global positioning and navigation. For example, it is critical to identify the location of targets or the direction of arrival of any signal for civilians or on-purpose applications; smart antennas and advanced active filters are playing a crucial role. Also progress has been made for transmission strategies; multiantenna systems can be used to increase the transmission speed without need for more bandwidth or power. Special techniques and strategies have been developed and implemented in electronic warfare target location systems.

We take here the opportunity to warmly thank all the members of the SPACOMM 2011 Technical Program Committee, as well as the numerous reviewers. The creation of such a broad and high quality conference program would not have been possible without their involvement. We also kindly thank all the authors who dedicated much of their time and efforts to contribute to SPACOMM 2011. We truly believe that, thanks to all these efforts, the final conference program consisted of top quality contributions.

Also, this event could not have been a reality without the support of many individuals, organizations, and sponsors. We are grateful to the members of the SPACOMM 2011 organizing committee for their help in handling the logistics and for their work to make this professional meeting a success.

We hope that SPACOMM 2011 was a successful international forum for the exchange of ideas and results between academia and industry and for the promotion of progress in the areas of satellite and space communications.

We are convinced that the participants found the event useful and communications very open. We also hope the attendees enjoyed the historic charm of Budapest, Hungary.

SPACOMM 2011 Chairs:

Loredana Arienzo, Joint Research Centre, European Commission - Varese, Italy

Igor Bisio, University of Genoa – Italy

Piero Cornice, ProVision Communication Technologies Ltd. - Bristol, UK

Alejandro Canovas Solbes, Polytechnic University of Valencia, Spain

Heung-Gyoon Ryu, Chungbuk National University, Republic of Korea
Massimiliano Laddomada, Texas A&M University - Texarkana, USA
Haibin Liu, Aerospace Engineering Consultation Center-Beijing, China
Daniel Massicotte, Université du Québec à Trois-Rivières, Canada
Stelios Papaharalabos, ISARS/National Observatory of Athens, Greece
Ling Pei, Finnish Geodetic Institute, Finland
Timothy Pham, Jet Propulsion Laboratory / California Institute of Technology, USA
Stephan Sand, German Aerospace Center (DLR)- Wessling, Germany
Michael Sauer, Corning Cable Systems, USA
Ian Troxel, SEAKR Engineering, Inc., USA
Piotr Tyczka, Poznan University of Technology, Poland

SPACOMM 2011

Committee

SPACOMM Advisory Chairs

Igor Bisio, University of Genoa - Italy
Heung-Gyoon Ryu, Chungbuk National University, Republic of Korea
Massimiliano Laddomada, Texas A&M University - Texarkana, USA
Stelios Papaharalabos, ISARS/National Observatory of Athens, Greece
Piotr Tyczka, Poznan University of Technology, Poland
Daniel Massicotte, Université du Québec à Trois-Rivières, Canada

SPACOMM Space Agency Liaison Chairs

Haibin Liu, Aerospace Engineering Consultation Center-Beijing, China
Stephan Sand, German Aerospace Center (DLR)- Wessling, Germany

SPACOMM Industry/Research Chairs

Michael Sauer, Corning Cable Systems, USA
Piero Cornice, ProVision Communication Technologies Ltd. - Bristol, UK
Ian Troxel, SEAKR Engineering, Inc., USA
Loredana Arienzo, Joint Research Centre, European Commission - Varese, Italy
Ling Pei, Finnish Geodetic Institute, Finland
Timothy Pham, Jet Propulsion Laboratory / California Institute of Technology, USA

SPACOMM Publicity Chair

Alejandro Canovas Solbes, Polytechnic University of Valencia, Spain

SPACOMM 2011 Technical Program Committee

Taufik Abrao, Universidade Estadual de Londrina, Brazil
Markos P. Anastasopoulos, National Technical University of Athens, Greece
Loredana Arienzo, Joint Research Centre, European Commission - Varese, Italy
Iva Bačić, University of Zagreb, Croatia
Marco Baldi, Università Politecnica delle Marche - Ancona, Italy
Javier Barria, Imperial College London, UK
Mark Bentum, University of Twente & ASTRON, The Netherlands
Igor Bisio, University of Genoa - Italy, Italy
Abdur Rahim Biswas, CREATE-NET - Trento, Italy
Roksana Boreli, NICTA / University of NSW - Alexandria, Australia
Daniele Borio, University of Calgary, Canada
Enzo Alberto Candreva, University of Bologna, Italy
Shkelzen Cakaj, Telecom of Kosovo / Prishtina University, Kosovo
Yifan Chen, University of Greenwich, UK
Piero Cornice, ProVision Communication Technologies Ltd. - Bristol, UK
Leonardo Dagui de Oliveira, Escola Politécnica da Universidade de Sao Paulo, Brazil
Vittorio Dainelli, Rheinmetall Italia S.p.A. - Rome, Italy
Francescantonio Della Rosa, Tampere University of Technology, Finland

Scott Enserink, University of California - Los Angeles, USA
Thierry Gayraud, LAAS-CNRS, Université de Toulouse, France
Mathieu Gineste, Thales Alenia Space, France
Heikki Hurskainen, Tampere University of Technology, Finland
Christian Ibars, Centre Tecnologic de Telecomunicacions de Catalunya - CTTC - Castelldefels, Spain
Peter Jung, Universität Duisburg-Essen, Germany
Joséphine Kohlenberg, IT/ Telecom et Management SudParis - Evry, France
Markku Kojo, University of Helsinki, Finland
Massimiliano Laddomada, Texas A&M University - Texarkana, USA
Haibin Liu, Aerospace Engineering Consultation Center-Beijing, China
Simona Lohan, Tampere University of Technology, Finland
Krešimir Malarić, University of Zagreb, Croatia
Herwig Mannaert, University of Antwerp, Belgium
Daniel Massicotte, Université du Québec à Trois-Rivières, Canada
Emmanouel T. Michailidis, University of Piraeus, Greece
Marina Mondin, Politecnico di Torino, Italy
Sergio Montenegro, German Aerospace Center - Bremen, Germany
Lim Nguyen, University of Nebraska-Lincoln, USA
Brian Niehöfer, Technische Universität Dortmund, Germany
Pasquale Pace, DEIS - University of Calabria, Italy
Stelios Papaharalabos, ISARS/National Observatory of Athens, Greece
Gerard Parr, University of Ulster-Coleraine, UK
Ling Pei, Finnish Geodetic Institute, Finland
Cathryn Peoples, University of Ulster - Coleraine, UK
Dionysia K. Petraki, National Technical University of Athens, Greece
Timothy Pham, Jet Propulsion Laboratory / California Institute of Technology, USA
Prashant Pillai, University of Bradford, UK
Luigi Portinale, Università del Piemonte Orientale "A. Avogadro" - Alessandria, Italy
Freddy Pranajaya, UTIAS/Space Flight Laboratory, USA
Ronals Raulefs, German Aerospace Center, Germany
Gianluca Reali, University of Perugia, Italy
Vincent Roca, INRIA Rhone-Alpes, France
Heung-Gyoon Ryu, Chungbuk National University, Republic of Korea
Michael Sauer, Corning Cable Systems, USA
Stephan Sand, German Aerospace Center (DLR)- Wessling, Germany
Gonzalo Seco Granados, Universitat Autònoma de Barcelona, Spain
Ana Maria Sierra Diaz, Telefónica I+D - Madrid, Spain
Danai Skournetou, Tampere University of Technology, Tampere, Finland
Heidi Steendam, Ghent University, Belgium
Ian Troxel, SEAKR Engineering, Inc., USA
Piotr Tyczka, Poznan University of Technology, Poland
In-Bok Yom, ETRI (Electronic & Telecommunication Research Institute) - Daejeon City, South Korea
Zhiwen Zhu, Communications Research Centre Canada, Canada

Copyright Information

For your reference, this is the text governing the copyright release for material published by IARIA.

The copyright release is a transfer of publication rights, which allows IARIA and its partners to drive the dissemination of the published material. This allows IARIA to give articles increased visibility via distribution, inclusion in libraries, and arrangements for submission to indexes.

I, the undersigned, declare that the article is original, and that I represent the authors of this article in the copyright release matters. If this work has been done as work-for-hire, I have obtained all necessary clearances to execute a copyright release. I hereby irrevocably transfer exclusive copyright for this material to IARIA. I give IARIA permission to reproduce the work in any media format such as, but not limited to, print, digital, or electronic. I give IARIA permission to distribute the materials without restriction to any institutions or individuals. I give IARIA permission to submit the work for inclusion in article repositories as IARIA sees fit.

I, the undersigned, declare that to the best of my knowledge, the article does not contain libelous or otherwise unlawful contents or invading the right of privacy or infringing on a proprietary right.

Following the copyright release, any circulated version of the article must bear the copyright notice and any header and footer information that IARIA applies to the published article.

IARIA grants royalty-free permission to the authors to disseminate the work, under the above provisions, for any academic, commercial, or industrial use. IARIA grants royalty-free permission to any individuals or institutions to make the article available electronically, online, or in print.

IARIA acknowledges that rights to any algorithm, process, procedure, apparatus, or articles of manufacture remain with the authors and their employers.

I, the undersigned, understand that IARIA will not be liable, in contract, tort (including, without limitation, negligence), pre-contract or other representations (other than fraudulent misrepresentations) or otherwise in connection with the publication of my work.

Exception to the above is made for work-for-hire performed while employed by the government. In that case, copyright to the material remains with the said government. The rightful owners (authors and government entity) grant unlimited and unrestricted permission to IARIA, IARIA's contractors, and IARIA's partners to further distribute the work.

Table of Contents

Antenna Noise Temperature for Low Earth Orbiting Satellite Ground Stations at L and S Band <i>Shkelzen Cakaj, Bexhet Kamo, Indrit Enesi, and Olimpjon Shurdi</i>	1
Adapting DVB-SH system parameters to mobile environments <i>Sokchenda Sreng, Benoit Escrig, and Marie-Laure Boucheret</i>	7
Concepts and Technologies for a Terabit/s Satellite <i>Paul Thompson, Barry Evans, Laurent Castenet, Michel Bousquet, and Takis Mathiopoulos</i>	12
Multi-port Power Amplifier Calibration Estimation Technique Based on ICA Algorithm <i>Zhiwen Zhu and Xinping Huang</i>	20
On Design of Optimized Low-Density Parity-Check Codes Starting From Random Constructions <i>Fred Daneshgaran, Massimiliano Laddomada, and Marina Mondin</i>	24
End-To-End Communication Model based on DVB-S2's Low-Density Parity-Check Coding <i>Iva Bacic, Josko Kressic, and Kresimir Malaric</i>	30
Identification of Abnormal System Noise Temperature Patterns in Deep Space Network Antennas Using Neural Network Trained Fuzzy Logic <i>Thomas Lu, Timothy Pham, and Jason Liao</i>	35
Overview of Experimental Module CANDARMA <i>Sinan Gokgoz, Orhan Sengul, Burak Yalciner, Sancay Kirik, Fethi Turk, and Ali Bircan</i>	41
Researching a Robust Communication Link for Cubesats: OPTOS, a new Approach <i>Victor Miguel Aragon, Alvaro Garcia, Ricardo Amaro, Cesar Martinez, and Fany Sarmiento</i>	45
Manufacturing and Testing of Ka-band Communication Payload of COMS <i>Jin Ho Jo, Moon Hee You, Seong Pal Lee, and Jae Hoon Kim</i>	51
The On Board Software of the Herschel HIFI Instrument <i>Lorenzo Piazzo, Anna Maria Di Giorgio, Francesco Nuzzolo, Pasquale Cerulli-Irelli, Luc Dubbeldam, David Ikhenade, Scige Liu, Sergio Molinari, and Stefano Pezzuto</i>	57
Public Protection and Disaster Relief by Satellite-based Communications Network <i>Yong-Min Lee</i>	63
The OFDM Joint Radar-Communication System: An Overview <i>Yoke Leen Sit, Christian Sturm, Lars Reichardt, Thomas Zwick, and Werner Wiesbeck</i>	69

Study on CFDP and DTN Architectures for ESA Space Missions <i>Felix Flentge</i>	75
Setting up a Student Satellite Receiving System in the United Arab Emirates <i>Youssef El Haj, Mustafa Harbaji, Lutfi Albasha, and Nidhal Guessoum</i>	81
Characterizing Network Architecture for Inter-satellite Communication and Relative Navigation in Precise Formation Flying <i>Rui Sun, Jian Guo, Eberhard K. A. Gill, and Daan C. Maessen</i>	85
Hybrid Acquisition of CBOC Galileo Signals under Multiple Correct-window Hypothesis <i>Elena Simona Lohan, Alexandru Rusu-Casandra, and Ion Marghescu</i>	91
UWB Localization System with TDOA Algorithm Using Experimental Measurements <i>Abdelmadjid Maali, Genevieve Baudoin, Hassane Mimoun, and Abdelaziz Ouldali</i>	97

Antenna Noise Temperature for Low Earth Orbiting Satellite Ground Stations at L and S Band

Shkelzen Cakaj

Post and Telecommunication of Kosovo,
Faculty of Electrical and Computing Engineering,
Prishtina University, Kosovo
shkelzen.cakaj@ptkonline.com
shkelzen.cakaj@fulbrightmail.org

Bexhet Kamo, Indrit Enesi, Olimpjon Shurdi

Faculty of Information Technology
Polytechnic University of Tirana, Albania
bkamo@fti.edu.al; ienesi @fti.edu.al;
oshurdi@fti.edu.al

Abstract - Low Earth Orbit (LEO) satellites are used for public communications and for scientific purposes. Most of the scientific satellites communicate with ground stations at S - band. Environmental satellites usually contain also equipment for search and rescue services communicating with ground terminals at L - band. The antenna noise temperature impacts satellite ground station performance. Antenna noise temperature is a measure of the effective noise integrated over the entire antenna pattern. On these bands the ionosphere effects are negligible. Heavy rain attenuation is considered as the most important atmospheric factor on determining antenna temperature on L and S bands. In this paper, the calculation and comparison of antenna noise temperature, caused under the worst propagation case, of the hypothetical satellite ground station implemented in different cities of Europe is given.

Keywords - LEO; Satellite; Antenna; Noise; Temperature

I. INTRODUCTION

Low Earth Orbit (LEO) satellites provide opportunities for investigations for which alternative techniques are either difficult or impossible to apply. Thus, it may be expected that such missions will be further developed in the near future especially in fields where similar experiments by purely Earth-based means are impracticable. Ground stations have to be established in order to communicate with such satellites, and the quality of communication depends on the performance of the satellite ground station, in addition to that of the satellite [1]. The downlink performance is commonly defined through a receiving system *Figure of Merit*. Figure of Merit depends on system noise temperature, consequently on antenna noise temperature [2]-[4]. The concern of this paper is the variation of antenna noise temperature at L and S band in Europe [5], [6].

At Section II, the concept of downlink budget expressed by range equation, the downlink margin and Figure of Merit are given. A general overview of system temperature, considering the best and the worst propagation case is presented at Section III. The paper aims to compare heavy rain attenuation impact on antenna noise temperature at different cities in Europe, as covered by Section IV.

II. DOWNLINK BUDGET

In downlink budget calculations, of the greatest interest is receiving system signal to noise ratio $[(S/N)$ or $(S/N_0)]$ expressed by *range equation* [7], as:

$$\frac{S}{N_0} = \frac{EIRP(G/T_s)}{kL_sL_0} \quad (1)$$

where *EIRP* is Effectively Isotropic Radiated Power from the transmitter. Considering that $N=N_0B$, $N_0=kT$ where, N_0 is spectral noise density, B receiver bandwidth, $k=1.38 \cdot 10^{-23}$ W/HzK is Boltzmann's constant, and expressing Eqn. 1 in decibels yields:

$$\frac{S}{N_0} (dB) = EIRP - L_s - L_0 + G/T_s + 228.6 \quad (2)$$

L_s is free space loss and L_0 denotes other losses (polarization loss, misspointing etc). The downlink margin (*DM*) is defined as:

$$DM = (S/N)_r - (S/N)_{rdq} \quad (3)$$

where the r indicates expected signal to noise ratio to be received at receiver, and rdq means required signal to noise ratio by customer, based on defined performance. So, a positive value of *DM* is an indication of a good system performance. In efforts to maintain a positive link margin, we might trade among parameters of range equation. If all parameters of the link are rigorously treated (the worst case), high link margin is not needed to be designed. In satellite industry expressions "link can be closed" and "link can not be closed" are often used, meaning respectively that error performance satisfies or not satisfies [7].

The reception quality of the satellite receiving system is commonly defined through a *Receiving System Figure of Merit* as G/T_s [7]:

$$T_s = T_A + T_{comp} \quad (4)$$

where G is receiving antenna gain, T_s is receiving system noise temperature, T_A is antenna noise temperature and T_{comp} is composite noise temperature of the receiving system, including lines and equipment. The Figure of Merit G/T_s expresses the impact of external and internal noise factors.

III. SYSTEM TEMPERATURE

Schematically the satellite ground station receiving system and environment concept is presented in Figure 1.

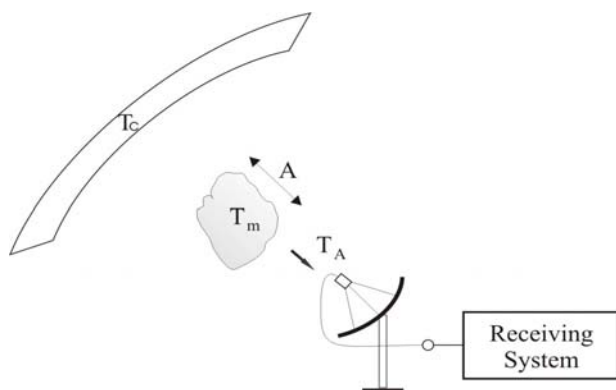


Figure 1. Satellite ground station and environment.

In Figure 1, T_C represents the sky noise temperature, T_m is medium temperature and A is medium attenuation. It is clear that unwanted noise, is in part, *injected via antenna* ($kT_A B$) and a part is *generated internally* ($kT_{comp} B$) by line loss and equipment [7], [8].

A. Antenna temperature

In front of receiving antenna different noise sources (natural, man-made or interferences) are present. The antenna temperature depends on where the antenna is looking at. From this surrounding environment (external sources) antenna will pick up a part of this noise power as:

$$N_A = kT_A B \quad (5)$$

where B is receiver's bandwidth.

Under assumptions, that solid angle subtended by the noise source is much larger than antenna solid angle, antenna sees the sky without medium attenuation and antenna itself is considered lossless, then antenna noise temperature T_A is equal to the sky noise temperature T_C .

$$T_A = T_C \quad (6)$$

Referring to [6] at L and S band the sky noise temperature is $T_C = (3-10)$ K. This is *the best propagation* case, where $T_A = T_C$.

Due to an atmospheric process the absorption increases the antenna noise temperature. If it is considered the total cosmic temperature as T_C , the absorptive medium temperature as T_m and the attenuation due the absorptive process as A , then antenna noise temperature T_A is [8]:

$$T_A = T_m (1 - 10^{-A/10}) + T_C 10^{-A/10} \quad (7)$$

T_C is 3K to 10K and T_m from 275K to 290K for rain. [6]. LEO satellites move too fast over the ground station. Ground station's antenna has to track the satellite's movement. Thus, the antenna's elevation angle varies, also. Considering sky noise temperature as $T_C = 10$ K, antenna noise temperature as function of elevation angle is presented in Figure 2 [3].

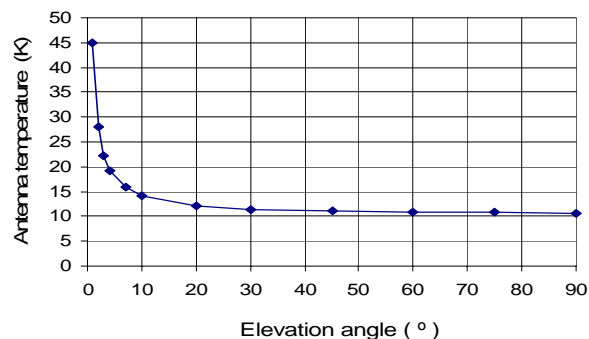


Figure 2. Antenna noise temperature

Figure 2, shows that under a perpendicular elevation angle it is the lowest antenna temperature.

B. Rain attenuation

Atmospheric attenuation depends mainly on the liquid water content along the propagation path. For the link budget calculation, including all types of hydrometeors, it is sufficient as the worst propagation case in Europe to be considered a heavy rain.

The attenuation of a wave due to rain depends on the following: number of raindrops along the path, the size of drops and the length of the path through the rain. If $P_r(0)$ is the signal power before the rain region, $P_r(r)$ is the signal power after the rain region, and r is the path length through the rain region, then the propagation loss L (in decibels) because of rain attenuation is given by [8]:

$$L = 10 \log \frac{P_r(0)}{P_r(r)} \quad (8)$$

In practice, the propagation loss due to rain attenuation is usually expressed via the *specific attenuation* γ in [dB/km] so, the propagation loss L is:

$$L = \gamma \cdot l_r \quad (9)$$

where γ is the specific rain attenuation expressed in [dB/km] and l_r is rain path length in [km]. Specific attenuation depends on rain structure (including drops' radius r_d , drop size distribution $n(r)$, rain refractive index m) and frequency f as:

$$\gamma = F[r_d, n(r), m, f] \quad (10)$$

But, based on the specific attenuation model of ITU-R [8] it is found that γ (*specific rain attenuation*) depends only on the rainfall rate R , measured on the ground in millimeters per hour. From this empirical model, the usual form of expressing γ is:

$$\gamma = a \cdot R^b \text{ [dB/km]} \quad (11)$$

where a and b are constants which depend on frequency, polarization and average rain temperature [8]. Table I, shows values of a and b at various frequencies at 20 °C for both polarizations [ITU 838, ITU-R P838-1].

TABLE I. PARAMETERS OF EMPIRICAL RAIN ATTENUATION MODEL

Frequency (GHz)	a_h	b_h	a_v	b_v
1.0	0.0000259	0.9691	0.0000308	0.8592
1.5	0.0000443	1.0185	0.0000574	0.8957
2.0	0.0000847	1.0664	0.0000998	0.9490
2.5	0.0001321	1.1209	0.0001464	1.0085
3.0	0.0001390	1.2322	0.0001942	1.0688
3.5	0.0001155	1.4189	0.0002346	1.1387
4.0	0.0001071	1.6009	0.0002461	1.2476

The specific rain attenuation depends on the geographical location of the ground station, respectively on rainfall rate at that location. A normal rain fall rate in Central Europe is 5 [mm/h]. For most of Europe a rainfall rate of 30 [mm/h] is suitable, except for some of Mediterranean regions where rainfall rates up to 50 [mm/h] have to be used [5], [6], [8]. Considering Eqn. 11 and Table I, it is calculated specific rain attenuation for different rainfall rates at different frequencies (L and S band) for horizontal and vertical polarization, presented in Table II and Table III.

TABLE II. SPECIFIC RAIN ATTENUATION FOR HORIZONTAL POLARIZATION AT 20 °C.

Rainfall rate (mm/h)	$R=30$	$R=40$	$R=50$
Frequency (GHz)			
1.0	0.000699	0.000924	0.001147
1.5	0.001415	0.001897	0.002381
2.0	0.003184	0.004328	0.005491
2.5	0.005978	0.008253	0.010599
3.0	0.009185	0.013094	0.017237
3.5	0.014403	0.021664	0.029733
4.0	0.024803	0.039312	0.056191

TABLE III. SPECIFIC RAIN ATTENUATION FOR VERTICAL POLARIZATION AT 20 °C.

Rainfall rate (mm/h)	$R=30$	$R=40$	$R=50$
Frequency (GHz)			
1.0	0.000572	0.000732	0.000887
1.5	0.001207	0.001562	0.001908
2.0	0.002517	0.003307	0.004087
2.5	0.004520	0.006042	0.007567
3.0	0.007362	0.010012	0.012708
3.5	0.011280	0.015652	0.020181
4.0	0.017138	0.024456	0.032415

Table II and Table III confirm that the specific rain attenuation increases with rainfall rate and frequency. For the same frequency and the same rainfall rate it is lower rain attenuation for vertical polarization, thus, vertical polarization is more convenient for communication under rain conditions. Passing through a rain medium, except the attenuation the polarization state of a wave can change also; such a vertical polarized wave can occur as a horizontal polarized wave. This is called *rain depolarization*. Depolarization depends on rain attenuation. Lower rain attenuation means less depolarization loss and vice versa. Problem of depolarization is avoided applying circular polarization, what is the most applicable polarization for satellite communication. Since, horizontal polarization is more sensitive on rain, representing the worst propagation case from the polarization point of view, further analyses relate on horizontal polarization. Specific rain attenuation for different frequencies and different rainfall rates for horizontal polarization as the worst case is presented in Figure 3.

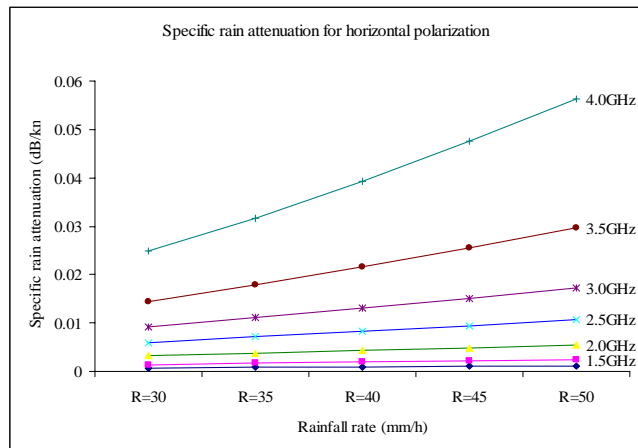


Figure 3. Specific rain attenuation for horizontal polarization.

Rain attenuation A [dB] depends on the specific rain attenuation γ and the rain path length l_r . The rain attenuation path length geometry is presented in Figure 4 [8].

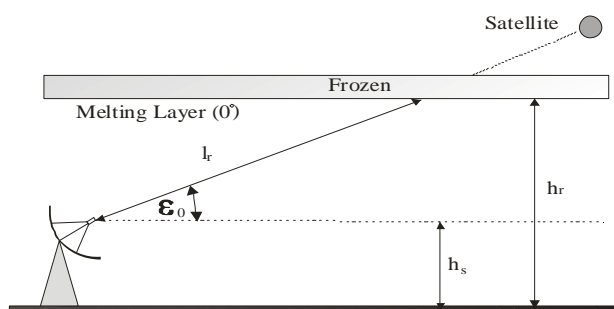


Figure 4. Rain attenuation path geometry.

All heights in Figure 4 are considered above mean sea level and ϵ_0 stands for the elevation angle. The effective rain height h_r in Figure 4, is the same as the height of the melting layer, where the temperature is usually around 0°C . The representative values for effective rain height vary according to the latitude ϕ of the ground station. Since Europe belongs to the Northern Hemisphere, these values expressed in [km], are given by [8]:

$$\begin{aligned} h_r &= 5 - 0.075(\phi - 23) \text{ for } \phi > 23 \\ h_r &= 5 \text{ for } 0 \leq \phi \leq 23 \end{aligned} \quad (12)$$

The rain path length from the Figure 4 can be expressed as:

$$l_r = \frac{h_r - h_s}{\sin \epsilon_0} \quad (13)$$

where the h_s is altitude of the ground station. Thus, the rain attenuation A (dB) for rain path length l_r is:

$$A = \gamma l_r = aR^b l_r = aR^b \frac{\Delta h}{\sin \epsilon_0} \quad (14)$$

where is $\Delta h = h_r - h_s$. For rain paths under too low elevation angle (ex. $\epsilon_0 < 5^\circ$), it is necessary to take into the account the variation of rain in the horizontal direction [8].

LEO satellites move too fast over the Earth. Obviously, the satellite's path length over the ground station for different passes is not the same [1]; consequently the rain path length between the satellite and the ground station is not constant and varies for each orbit path. Considering the whole horizon in the azimuth range of $0^\circ - 360^\circ$, in any direction of the horizon plane the natural barriers will differ [9]. The practical acquisition and loss elevation values ranges from $1^\circ - 4^\circ$. In order to avoid the problem of natural barriers, designers predetermine the lowest elevation of the horizon plane which is applied during link budget calculations. The horizon plane with a predetermined minimal elevation is considered the *designed horizon plane*. Usually, for meteorological and search and rescue satellites operating on S and L band respectively, the ground station horizon plane is defined above 5° elevation [10] [11]. By this reason all further analyses as the worst case consider the communication under 5° elevations. For rain attenuation calculations, some cities of Europe are chosen where hypothetically is supposed to be implemented a satellite ground station dedicated for scientific or search and rescue services. The horizon plane of ground stations is supposed above 5° elevation. From the <http://earth.google.com/> are provided latitude and altitude of these cities and presented in Table V. Rain path length is calculated based on Eqn. 13.

TABLE V. ALTITUDE, LATITUDE AND RIAN PATH LENGTH.

Location	Altitude (h_s) [m]	Latitude [$^\circ$]	h_r [km]	$l_r = \frac{h_r - h_s}{\sin 5^\circ}$ [km]
Madrid	588	40.4	3.695	35.7
Tirana	104	41.3	3.625	40.4
Rome	14	41.9	3.582	41.0
Prishtina	65	42.6	3.525	33.0
Zagreb	130	45.8	3.290	36.3
Vienna	190	48.2	3.110	33.5
Paris	34	48.8	3.060	34.8
Brussels	76	50.8	2.915	32.6
London	14	51.5	2.862	32.7
Berlin	34	52.5	2.786	31.6

Applying Eqn. 14 it is calculated rain attenuation in (dB) for heavy rain storm in Europe ($R=50\text{mm/h}$) under 5° elevation and horizontal polarization as the worst propagation case for the link budget and presented in Table VI.

TABLE VI. RAIN ATTENUATION (dB) IN EUROPE AT 5° EL.

Location	1GHz	2GHz	3GHz	4GHz
Madrid	0.041	0.196	0.615	2.000
Tirana	0.046	0.221	0.696	2.270
Rome	0.047	0.225	0.706	2.303
Prishtina	0.037	0.181	0.568	1.854
Zagreb	0.041	0.199	0.625	2.039
Vienna	0.038	0.184	0.577	1.882
Paris	0.039	0.191	0.599	1.955
Brussels	0.037	0.179	0.561	1.831
London	0.037	0.179	0.563	1.837
Berlin	0.036	0.173	0.544	1.775

Results from Table VI are graphically given in Figure 5. The variation in rain attenuation for the highest rainfall rate in Europe is presented in Figure 6.

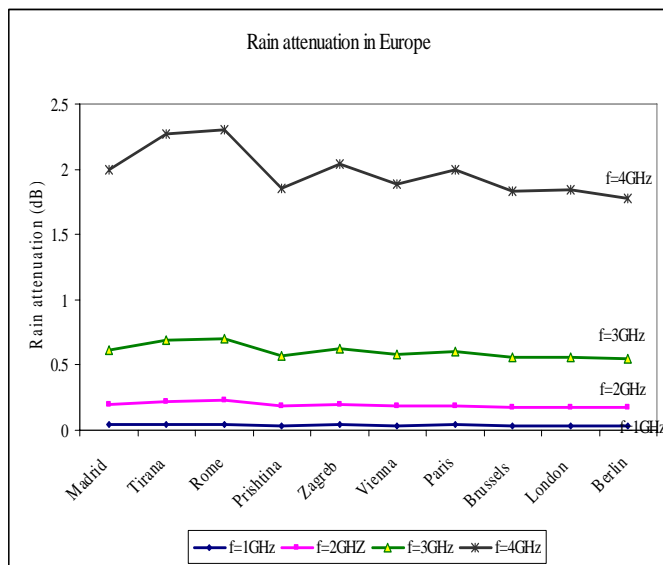


Figure 5. Rain attenuation in Europe.

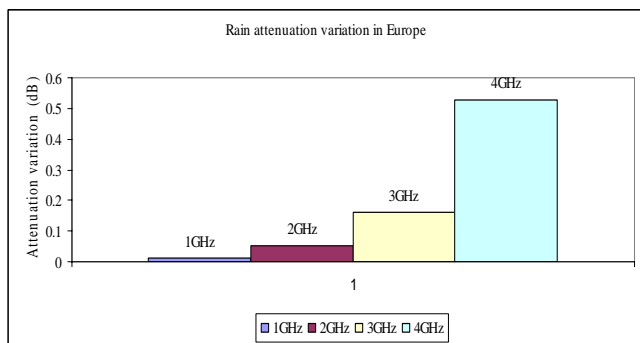


Figure 6. Rain attenuation variation in Europe.

Rain attenuation variation at 2GHz is less than 0.16dB and at 4GHz is less than 0.6dB. This is the first indication that the satellite ground station will perform approximately equally in different cities.

IV. ANTENNA TEMPERATURE COMPARISON

Considering Eqn 7 about antenna temperature calculation and data from Table VI related to heavy rain attenuation in Europe ($R=50\text{mm/h}$) under 5° elevation as the worst propagation case, it is calculated antenna noise temperature and presented in Table VII. For these calculations it is considered $T_c = 10\text{K}$ and $T_m = 290\text{K}$.

TABLE VII. ANTENNA TEMPERATURE (K) IN EUROPE AT 5° EL.

Location	1GHz	2GHz	3GHz	4GHz
Madrid	12.6	22.3	46.9	113.3
Tirana	12.9	23.8	51.4	123.9
Rome	13.0	24.1	52.0	125.2
Prishtina	12.3	21.7	44.3	107.0
Zagreb	12.6	22.4	47.4	114.8
Vienna	12.4	21.6	44.8	108.5
Paris	12.5	22.4	46.0	111.5
Brussels	12.3	21.3	43.8	106.3
London	12.3	21.3	43.8	106.3
Berlin	12.3	20.9	42.9	103.9

Data from Table VII in Figure 6 and Figure 7 are given.

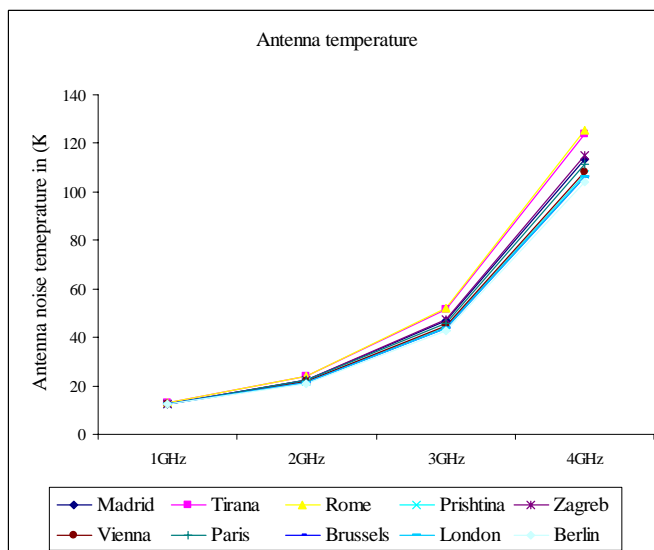


Figure 7. Antenna temperature in Europe.

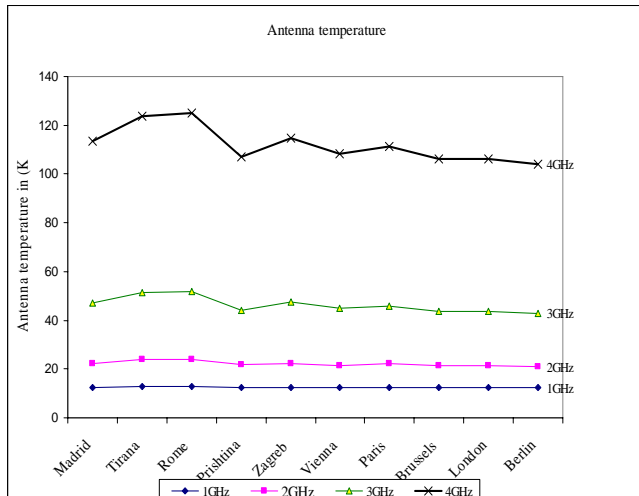


Figure 8. Antenna temperature in Europe.

Figure 6, confirms the fact that antenna noise temperature increases approximately exponentially with the raise on frequency. Figure 7 and Figure 8, show that the variation in antenna noise temperature among European cities increases with raise of frequency, also. The difference of the highest and the lowest antenna noise temperature for European cities is presented in Table VIII.

TABLE VIII. ANTENNA NOISE TEMPERATURE (K) DIFFERENCE

Frequency	1GHz	2GHz	3GHz	4GHz
Ant. temp. ΔT_A (K)	0.7	3.2	9.1	21.3

Obviously with raise on frequency this difference increases, and for 1GHz and 2GHz it is negligible. This means that communication between satellites and ground stations at L band, dedicated for search and rescues services, will have very similar performance in Europe. At S band, the upper edge at 4GHz is considered. For the case of communication on 4 GHz, it is considered a hypothetical ground station with composite temperature (including lines and equipment) of $T_{comp} = 70$ K [12] and receiving antenna with gain of $G = 35$ dBi. For the ground station implemented in Rome, where the antenna noise temperature is the highest, yields the Figure of Merit as:

$$\left(\frac{G}{T_s}\right)_{ROME} = 12.1dB \tag{15}$$

Further, considering the same equipment implemented in Berlin, where the antenna noise temperature is the lowest, yields the Figure of Merit as:

$$\left(\frac{G}{T_s}\right)_{BERLIN} = 12.6dB \tag{16}$$

The difference in Figure of Merit, between Rome and Berlin as cities with the highest and the lowest antenna temperature caused because of heavy rain under very low elevation angle of 5° , it is 0.5 dB. Considering that the most of communication among satellites and ground stations is above 5° , ground station will perform almost similarly at most of Europe in L and S band.

V. CONCLUSION

The antenna noise temperature has an effect to the link performance expressed by range equation. Only rain attenuation on antenna temperature is considered. Other local influences are not subject of this paper. Considering horizontal polarization transmission, and heavy rain under too low elevations as the worst propagation case, it is confirmed that the reception quality of a ground station within central Europe at L and S bands does not highly depend on location. The difference in Figure of Merit, between Rome and Berlin as cities with the highest and the lowest antenna temperature under the worst propagation case, it is always less than 0.5 dB at L and S band. This low difference in Figure of Merit, become negligible at circular polarization applications.

REFERENCES

- [1] S. Cakaj and K. Malaric, "Rigorous analysis on performance of LEO satellite ground station in urban environment," International Journal of Satellite Communications and Networking, Vol. 25, No. 6, pp. 619-643, UK, November/December 2007.
- [2] D. Roddy, "Satellite communications", McGraw Hill, New York 2006.
- [3] M. Richharia, "Satellite communication systems", McGraw Hill, New York 1999.
- [4] G. Maral and M. Bousquet, "Satellite communication systems", John Willey & Sons, Ltd, Chichester, England, 2002.
- [5] S.Cakaj and K. Malaric, "Rain attenuation at Low Earth Orbiting satellite ground stations", 48th International Symposium ELMAR 2006 focused on Multimedia Systems and Applications 7-09, IEEE June 2006, Zadar, Croatia, pp. 247-250.
- [6] S. Cakaj and K. Malaric, "Rain Attenuation Modelling for Low Earth Orbiting Satellite Ground Station at S- band in Europe", 18th IASTED International Conference on Modelling and Simulation, MS 2007, May 30 -June 1 2007, IASTED, Montreal, Canada, pp. 17-20.
- [7] B. Sklar, "Digital Communication", Prentice Hall PTR, New Jersey 2005.
- [8] S.R. Saunders, "Antennas and propagation for wireless communication system", John Willey & sons, Inc, 1993.
- [9] S. Cakaj, "Practical Horizon Plane and Communication Duration for Low Earth Orbiting (LEO) Satellite Ground Stations", WSEAS Journal: Transactions on Communications, Issue 4, Volume 8, April 2009, pp. 373-383.
- [10] I. W. Taylor and M. O. Vigneault, "A neural network application to search and rescue satellite aided tracking (SARSAT), In Proceedings of the Symposium/ Workshop on Applications of Experts Systems in DND, pp. 189 -201, Royal Military Coll. of Canada, 1992.
- [11] C. Bulloch, "Search and Rescue by satellite - Slow steps toward an operational system", Interavia (ISSN 0020 -5168), vol.42, pp. 275 - 277, 1987.
- [12] S. Cakaj and K. Malaric "Composite Noise Temperature at Low Earth Orbiting Satellite Ground Station", International Conference on Software, Telecommunications and Computer Networks, SoftCOM 2006, IEEE Sep. 29 -Oct.1 2006, Split, Croatia, pp.214-217.

Adapting DVB-SH system parameters to mobile environments

Sokchenda Sreng
Université de Toulouse
 INP-ENSEEIH/IRIT
 Toulouse, France
 sokchenda.sreng@enseeiht.fr

Benoît Escrig
Université de Toulouse
 INP-ENSEEIH/IRIT
 Toulouse, France
 benoit.escrig@enseeiht.fr

Marie-Laure Boucheret
Université de Toulouse
 INP-ENSEEIH/IRIT
 Toulouse, France
 marie-laure.boucheret@enseeiht.fr

Abstract—A performance analysis of the digital video broadcasting - satellite to handheld (DVB-SH) system in presence of ground mobile terminals (GMTs) is presented. The paper focuses on the Doppler spread issue. Indeed, the mobility of GMTs induces a Doppler spread in the orthogonal frequency division multiplexing (OFDM) signal that destroys the orthogonality of subcarriers. The loss of orthogonality produces inter-carrier interference (ICI) and hence a degradation of the system performance in terms of symbol error probability. The paper presents the conditions in which this degradation can be compensated for by an increase in the signal to noise ratio (SNR) at the receiver side. The result depends on both the modulation scheme and the speed of GMTs. Inversely, having a maximum allowable margin on the received SNR allows us to determine an upper bound on the mobile station velocity.

Keywords-DVB-SH; Doppler spreading; degradation.

I. INTRODUCTION

DVB-SH is a broadcast standard for the delivery of video and data stream to GMTs. In a DVB-SH system, GMTs receive signals from two network segments: the Satellite Component (SC) and the Complementary Ground Component (CGC). The SC ensures geographical global coverage while the CGC provides cellular-type coverage. On the CGC, the OFDM modulation scheme has been chosen as it is the basis of both Digital Video Broadcasting - Terrestrial (DVB-T) and Digital Video Broadcasting - Handheld (DVB-H) systems. On the SC, two transmission schemes are available: Time Division Multiplexing (TDM) or OFDM leading to two reference architectures termed SH-A and SH-B. SH-A uses OFDM both on the satellite and the terrestrial link while SH-B uses TDM on the satellite link and OFDM for the terrestrial link.

The signals received by GMTs suffer from several impairments according to the corresponding segment: delay, Doppler shift and Doppler spreading. Delay and Doppler shift issues have been addressed in the DVB-SH standard [1] [2] by the implementation of a SH frame Information Packet (SHIP). This synchronization scheme is similar to the Megafame Initialization Packet (MIP) in DVB-T and the pre-compensation of the time delay variation at the gateway location. The principles of synchronization can be summarized as follows.

- SHIP inserter performs the insertion of a GPS-based time stamp ($\pm 0.1 \mu s$ accuracy) in the SH-Frame indicating the transmission time of the beginning of the next SH Frame.
- Single Frequency Network (SFN) adapters in the transmitters (repeaters) perform buffering of incoming MPEG-TS packets and transmission of SH Frame aligned with GPS relative time stamp.

On the other hand, the Doppler spreading on DVB-SH signals has not been addressed to the same extent. This issue needs to be investigated more precisely because the Doppler spreading has a great impact on the physical layer performance. Indeed, the Doppler spread destroys the orthogonality of subcarriers in the OFDM signal and generate power leakage among subcarriers, known as ICI. The loss of orthogonality has been characterized in [3] [4] [5] [6]. In [6], the ICI and the degradation due to Doppler spreading have been evaluated. The purpose of this paper does not consist in proposing the receiving technique in order to reduce the Doppler spread instead system parameters will be adjusted in order to cope with the constraints. More precisely, the effect of the Doppler spread can be reduced by limiting the mobile velocity. Another approach consists in adding an additional margin on the received SNR per symbol. To avoid Doppler spread impairments, the speed of GMTs should not exceeds a maximum allowable value. This maximum allowable velocity should not induce a Doppler spread higher than 13.28% of the subcarrier spacing [7]. For example, when the carrier spacing in a 2k mode is 2.79 kHz, it has been shown that the system still achieves the target performance provided that the Doppler spread does not exceed a value of 0.37 kHz. This induces a maximum velocity for the GMT of 183.9 km/h.

In this paper, we propose another method to mitigate the Doppler spreading by compensating for the degradation of the SNR per symbol at the input of the decoder. The required margin can be estimated. We compute the difference in terms of SNR per symbol using the symbol error probability curve which is affected by a Doppler spread and another one without Doppler spreading. This method can be applied only to any OFDM modulation scheme of the CGC (e.g., SH-A

and SH-B).

The rest of this paper is organized as follows. In Section II, we describe the Doppler spreading induced by the two segments of the DVB-SH system. In Section III, we evaluate the relation of the ICI and the degradation of SNR per symbol. In Section IV, methods of dimensioning are provided. Finally, the conclusions are given in Section V.

II. DOPPLER SPREADING IN DVB-SH SYSTEMS

A. Doppler spread induced on the SC segment

The satellite motion and the ground terminal mobility induce a Doppler shift and a Doppler spread [8].

- The Doppler shift ν_0 is given by, $\nu_0 = \frac{V_{sr}}{\lambda}$, where V_{sr} represents the radial velocity of the satellite and λ is the signal wavelength.
- The Doppler spread σ_ν is defined such that σ_ν^2 is a sum of three terms.

$$\begin{aligned}\sigma_\nu^2 &= \sigma_{\nu,g}^2 + \sigma_{\nu,s}^2 + \sigma_{\nu,ch}^2 \\ &= \left(\frac{V_g}{\Lambda_c}\right)^2 + \left(\frac{\Omega_s}{\alpha_c}\right)^2 + \left(\frac{1}{T_{ch}}\right)^2\end{aligned}\quad (1)$$

The first term $\sigma_{\nu,g}^2 = \left(\frac{V_g}{\Lambda_c}\right)^2$ is due to the ground terminal motion, where V_g represents the ground terminal velocity and Λ_c is the coherence length, usually of the order of the signal wavelength.

The second term $\sigma_{\nu,s}^2 = \left(\frac{\Omega_s}{\alpha_c}\right)^2$ is the Doppler spread originated by the motion of satellite. Ω_s is the angular velocity of the satellite and α_c is the coherence angle. The angular velocity of the geostationary earth orbit (GEO) satellite should theoretically be zero. In practical cases, this parameter is non zero but it is some four orders less than the same parameter for a low earth orbit (LEO) satellite.

The third term $\sigma_{\nu,ch}^2 = \left(\frac{1}{T_{ch}}\right)^2$ is the channel self Doppler spread, where T_{ch} is the characteristic time constant which describes the effects of moving and changing objects in the vicinity of the ground station.

B. Doppler spread induced on the CGC segment

On the CGC segment, the Doppler spread is mainly produced by the mobility of GMTs for fixed relay stations. For mobile relay stations, the total Doppler spread is the sum of the Doppler spreads induced by both GMTs and relay stations [9]. The average Doppler shift is zero. Let V_g be the velocity of the GMT and V_r , the velocity of the relay station, then the total Doppler spread can be expressed as:

$$F_d = \frac{V_g}{c} \times f_c + \frac{V_r}{c} \times f_c \quad (2)$$

where f_c is the carrier frequency and $c = 3.10^8 m/s$ is the speed of light.

III. ICI AND DEGRADATION

In this section, we evaluate the ICI and the degradation of the SNR per symbol due to Doppler spreading. We assume that each subcarrier is transmitted in a frequency flat Rayleigh fading channel which corresponds to the channel between relay stations and GMTs. The OFDM system uses N subcarriers. For typical modulation schemes such as phase-shift keying (PSK) and quadrature-amplitude modulation (QAM), the carrier to interference ratio (C/I) on subcarrier i is given in [6] as:

$$\frac{C}{I} = \frac{1}{\frac{(NTF_d)^2}{2} \sum_{k=1, k \neq i}^N \frac{1}{(k-i)^2}} \quad (3)$$

where F_d is the maximum Doppler spread. As in typical C/I computations, we assume that the interference produced by other subchannels is an additive noise. Without interference and Doppler spreading, the signal to noise ratio per symbol is E_s/N_0 , where E_s denotes the mean energy received per symbol and $2N_0$ denotes the variance of the AWGN noise in an equivalent low pass channel model. With interference and Doppler spreading, the signal to interference plus noise ratio is $E_s/(N_0 + N_I)$, where $E_s = C/R_s$, $N_I = I/R_s$ and $R_s = 1/T$ is the input symbol rate. Then we obtain:

$$\frac{E_s}{N_0 + N_I} = \frac{\frac{E_s}{N_0}}{1 + \frac{E_s}{N_0} \left(\frac{C}{I}\right)^{-1}} \quad (4)$$

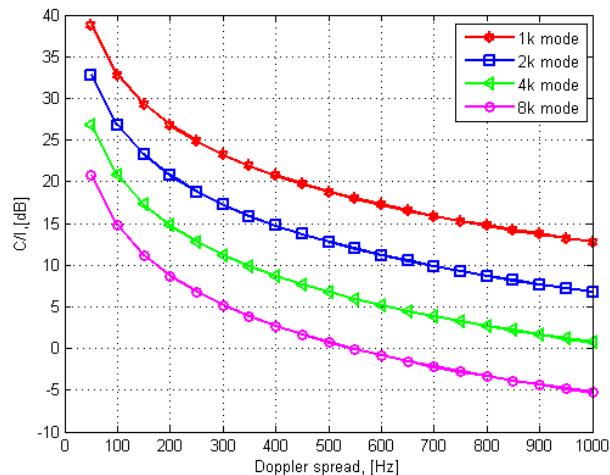
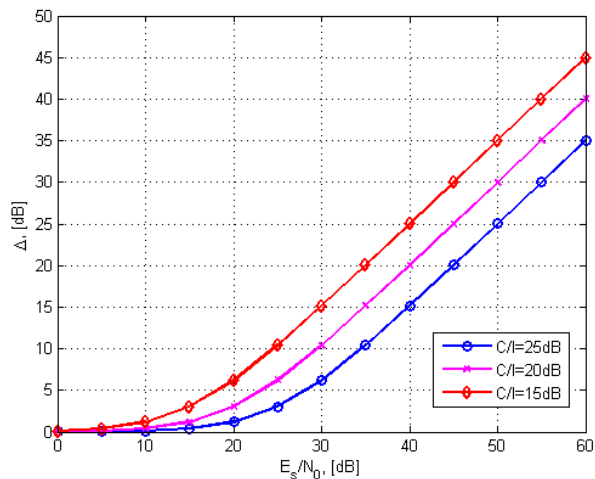
So, in decibel,

$$\begin{aligned}\Delta_{dB} &= \left[\frac{E_s}{N_0 + N_I}\right]_{dB} - \left[\frac{E_s}{N_0}\right]_{dB} \\ &= -10 \log\left[1 + \frac{E_s}{N_0} \left(\frac{C}{I}\right)^{-1}\right]\end{aligned}\quad (5)$$

Equation (5) gives the degradation Δ_{dB} of the signal to noise ratio at the receiver when there are interferences between subcarriers.

The C/I curves of the middle subcarrier index $k = N/2$ are plotted versus the Doppler spread F_d in Figure 1 for several DVB-SH transmission modes at a carrier frequency of 2.175 GHz and a bandwidth of 5 MHz. The 8k mode is experiencing more interference than the other modes because its subcarrier spacing is smaller than the one of other modes.

For a given C/I of 15 dB, the 1k mode can support a Doppler spread of 800 Hz and Doppler spread of 400 Hz for the 2k mode. For the same value of C/I , the 4k mode allows a maximum Doppler spread of 200 Hz while the 8k mode can support only 100 Hz. According to these Doppler spread values, we can calculate the maximum allowable velocity for the GMT. The numerical values of the maximum allowable velocity for the GMT for a 5 MHz DVB-SH bandwidth channel at 2.175 GHz and C/I of 15 dB are shown in Table I. We see that the 1k mode allows the GMT moves at a maximum speed of 397.22 km/h while the 2k mode can support up to 198.61 km/h. On the other hand, the 4k


 Figure 1. C/I curves as a function of Doppler spread.

 Figure 2. Degradation Δ_{dB} as a function of E_s/N_0 .

mode provides a maximum allowable velocity for the GMT of 99.30 km/h. Finally, the 8k mode can only support at the maximum speed of 49.65 km/h.

Figure 2 illustrates the degradation due to Doppler spreading with respect to the E_s/N_0 ratio for several values of C/I . We observe that the degradation not only depends on the C/I ratio but also on the E_s/N_0 ratio. For small values of E_s/N_0 , the degradation has less influence on the system performance. In particular, when E_s/N_0 is smaller than 10 dB the degradation is less than 2 dB.

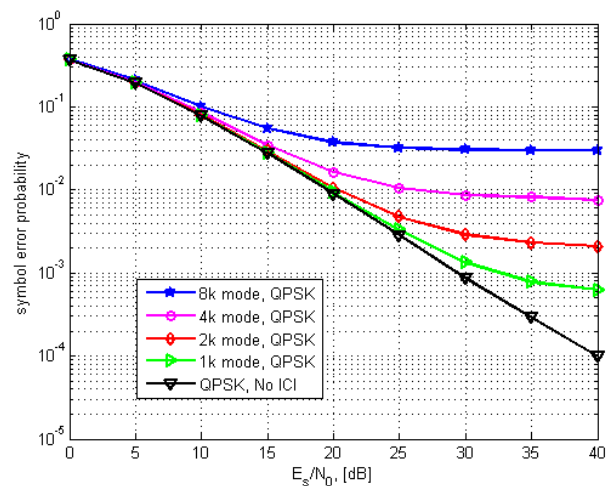
IV. DIMENSIONING OF THE DVB-SH SYSTEM ACCORDING TO THE DOPPLER SPREADING

In this section, we express the degradation of SNR per symbol, E_s/N_0 , which corresponds to the velocity of GMTs. This degradation is estimated by computing the difference

Table I
MAXIMUM ALLOWABLE VELOCITY FOR THE GMT FOR A 5 MHz DVB-SH BANDWIDTH CHANNEL AT 2.175 GHz AND A C/I OF 15 dB

Mode	FFT size	Subcarrier spacing [kHz]	Doppler spread [Hz]	Maximum velocity [km/h]
1k	1024	5.580	800	397.22
2k	2048	2.790	400	198.61
4k	4096	1.395	200	99.30
8k	8192	0.698	100	49.65

in E_s/N_0 between the symbol error probability curve which is affected by the Doppler spreading and the one without Doppler spreading with respect to the same target value of symbol error probability. Figure 3 through 6 are plotted by using the expression of symbol error probability of Rayleigh OFDM QPSK and 16-QAM and replacing the expression of E_s/N_0 by $E_s/(N_0 + N_I)$ derived in (4).


 Figure 3. Performance of uncoded QPSK OFDM system in Rayleigh channel with carrier frequency $f_c=2.175$ GHz, and mobile speed of 50 km/h.

Figures 3 and 4 illustrate the symbol error probability of uncoded QPSK OFDM and uncoded 16-QAM OFDM for several modes of DVB-SH over a frequency-selective Rayleigh channel under the Doppler spread, F_d , of 100 Hz, corresponding to a mobile speed of 50 km/h. The carrier frequency is 2.175 GHz. When the E_s/N_0 is large, the ICI is the limiting factor in performance at any mobile speed. For example, when the target symbol error probability is in the order of 10^{-2} , the degradation of uncoded QPSK modulation are 0.5 dB for 1k mode, 1 dB for 2k modes, and around 6 dB for 4k mode while the degradation can not be computed (NC) for 8k mode. In case of uncoded 16-QAM, the degradation are 2 dB for 1k mode and NC for

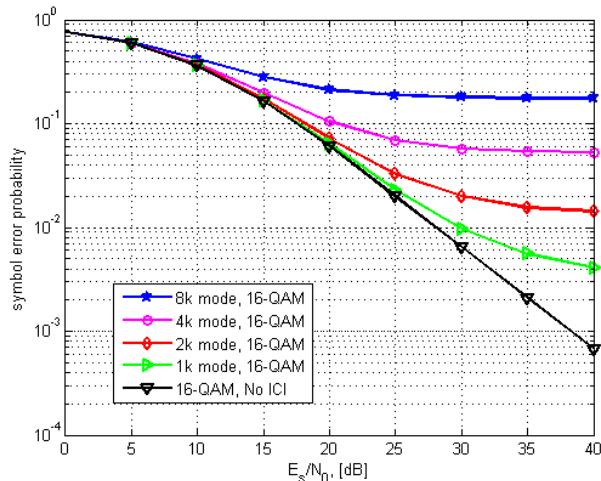


Figure 4. Performance of uncoded 16-QAM OFDM system in Rayleigh channel with carrier frequency $f_c=2.175$ GHz, and mobile speed of 50 km/h.

Table II

THE REQUIRED MARGIN FOR A 5 MHz DVB-SH BANDWIDTH CHANNEL AT 2.175 GHz AND MOBILE SPEED OF 50 km/h WITH TARGET SYMBOL ERROR PROBABILITY OF 10^{-2}

Mode	1k	2k	4k	8k
uncoded QPSK	0.5 dB	1 dB	6 dB	NC
uncoded 16-QAM	2 dB	NC	NC	NC

other modes. Hence, we can not compensate the degradation for uncoded QPSK 8k mode and the same for uncoded 16-QAM 2k, 4k and 8k mode.

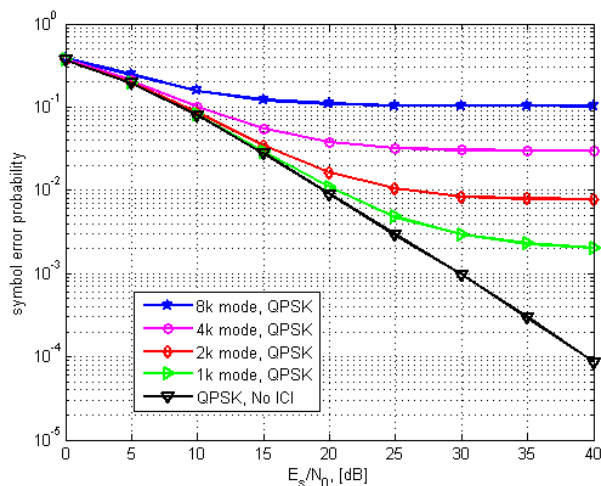


Figure 5. Performance of uncoded QPSK OFDM system in Rayleigh channel with carrier frequency $f_c=2.175$ GHz, and mobile speed of 100 km/h.

The other performance curves for uncoded QPSK OFDM

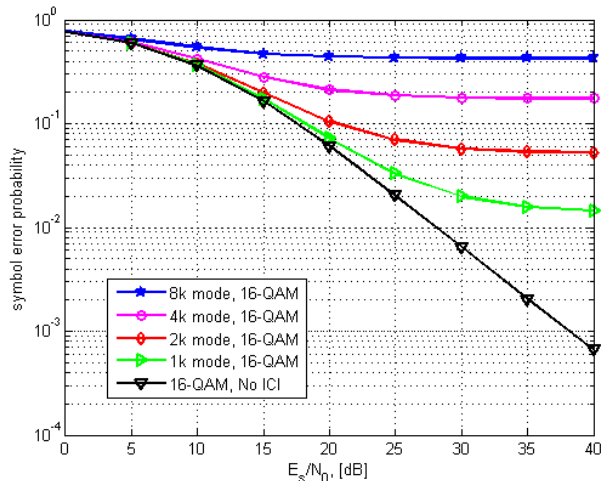


Figure 6. Performance of uncoded 16-QAM OFDM system in Rayleigh channel with carrier frequency $f_c=2.175$ GHz, and mobile speed of 100 km/h.

Table III

THE REQUIRED MARGIN FOR A 5 MHz DVB-SH BANDWIDTH CHANNEL AT 2.175 GHz AND MOBILE SPEED OF 100 km/h WITH TARGET SYMBOL ERROR PROBABILITY OF 10^{-2}

Mode	1k	2k	4k	8k
uncoded QPSK	1 dB	6 dB	NC	NC
uncoded 16-QAM	NC	NC	NC	NC

and uncoded 16-QAM OFDM Rayleigh channel are plotted in Figures 5 and 6 with carrier frequency $f_c=2.175$ GHz under Doppler spread, F_d , of 200 Hz, corresponding to the mobile speed of 100 km/h. If the target symbol error probability is in the order of 10^{-2} , we see that only two modes of the uncoded QPSK modulation can be compensated for the degradation, 1 dB for 1k mode and 6 dB for 2k mode. The other modes are totally degraded and can not be compensated for because their minimum symbol error probabilities are higher then the target value.

V. CONCLUSIONS AND FUTURE WORKS

In this paper, the maximum mobile speed of GMTs with respect to the required minimum C/I value was determined. Then the degradation was evaluated with respect to the target system performance. This degradation could be compensated for by the margin before decoding. It was also shown that the degradation does not only depend on the mobile velocity but also depend on the modulation scheme. For high Doppler spread, for example when the velocity of the GMT is 100 km/h, the DVB-SH system using 16-QAM OFDM modulation is totally degraded and the compensation is not possible. So, one way to solve this problem is to limit the velocity of the GMT to an appropriate level, which is one of the interesting subjects for future research.

REFERENCES

- [1] ETSI. Digital Video Broadcasting (DVB), "DVB-SH Implementation Guidelines," *Doc. Ref. ETSI TS 102 584*, v1.1.1(2008-12).
- [2] P. Kelley, "Overview of the DVB-SH specifications," *Int. J. Satell. Commun. Syst. Network.*, May. 2009, pp. 198-214.
- [3] P. Robertson and S. Kaiser, "The effects of Doppler spreads in OFDM (A) mobile radio systems," in *Proc. IEEE Veh. Technol. Conf.*, vol. 1, Sep. 1999, pp. 329-333.
- [4] P. Robertson and S. Kaiser, "Analysis of the loss of orthogonality through Doppler spread in OFDM system," in *Proc. IEEE Globecom*, Dec. 1999, pp. 701-706.
- [5] D.T. Harvatin and R.E. Ziemer, "Orthogonal frequency division multiplexing performance in delay and Doppler spread channels," in *Proc. IEEE Veh. Technol. Conf.*, vol. 3, 1997, pp. 1644-1647.
- [6] T. Wang, J. G. Proakis, E. Masry, and J. R. Zeidler, "Performance degradation of OFDM systems due to Doppler spreading," *IEEE Trans. Wireless Commun.*, vol. 5, No. 6, June 2006, pp. 1422-1432.
- [7] A. E. Rubio, "Practical guide to designing a DVB-SH network for RF Engineers," *Bell Labs Tech. J.* 13(4), 2009, pp. 207-226.
- [8] I. Frigyes, B. G. Molnár, R. Vallet, Z. Herczku, and Z. Bodnár, "Doppler spread characteristics of satellite personal communication channels," *Int. J. Satell. Commun. Syst. Network.*, 2001, pp. 251-262.
- [9] A. S. Akki and F. Haberk, "A Statistical Model of Mobile-to-Mobile Land Communication Channel," *IEEE Trans. Veh. Technol.*, vol. 35, Feb. 1986, pp. 2-7.

Concepts and Technologies for a Terabit/s Satellite

Supporting future broadband services via satellite

Paul Thompson, Barry Evans
CCSR, University of Surrey
Surrey, England
e-mail: p.thompson@surrey.ac.uk

Michel Bousquet
TeSA
Toulouse, France
e-mail: Michel.bousquet@isae.fr

Laurent Castenet
ONERA
Toulouse, France
e-mail: Laurent.castenet@onera.fr

Takis Mathiopoulos
ISARS
Athens, Greece
e-mail: mathio@space.noa.gr

Abstract— In this paper we investigate the next but one generation of fixed satellite systems and the technological challenges that face this generation which we define as operational by 2020. Various technologies and architectural concepts are presented with a view to identifying the most promising to pursue. The dimensioning of the system has demonstrated that several new technologies are appropriate for development before such a satellite system is feasible. Work is continuing to investigate these in more detail but we feel there to be no technology show stopper for a Terabit/s satellite by 2020.

Keywords—satellite communications; broadband, advance systems Internet over satellite.

I. INTRODUCTION

In this paper we investigate the next but one generation of fixed satellite systems and the technological challenges that face this generation which we define as operational by 2020. The current generation of large geostationary satellites are characterized by a capacity of up to 10Gb/s and are about 6 Tonnes in weight. They have historically predominately operated in C and Ku bands but with Ka band now coming into use and in general are multi beam with less than 100 beams per satellite. Just on the horizon is the next generation which will take the capacity up to 100Gb/s but with similar sized satellites making use of a larger number of beams and more complex payloads. These will take us through to 2015 or beyond; but what comes next? Here we look at this following generation of satellites and set ourselves the challenge of a further order of magnitude increase in capacity to a Terabit/s satellite [1]. The paper will concentrate on a single geostationary satellite but we recognise that there could be other solutions; for example constellations or multiple smaller co-located (clusters) satellites. We see the drive for higher capacities in three areas; Data Relay, Broadcasting and Broadband Access. Each has its own and different specialised requirements for

the satellite. Herein we will concentrate on the third of these; the Broadband Access satellite for the 2020's.

Broadband access to the internet is a growing service area and satellite is ideally placed to deliver such services to areas that are uneconomic for terrestrial systems. Recently Cisco have predicted internet demands of 104 Peta bytes per second for Europe by 2012 which is 10 times the internet traffic in 2007 with such growth to continue for the rest of the decade. By 2013 an average European household bandwidth will be 500GB/month. On average this would require in excess of 30Mb/s for domestic users wherever they are. This represents a considerable increase on the Digital Plans adopted for European countries currently which aim at 2Mb/s for all. Terrestrial systems will not be able to economically cover the whole population base at these rates, even with LTE-A becoming the endemic mobile standard by this timescale, and thus broadband by satellite on a Europe wide basis will be a key provider of the future internet architecture in order to avoid the so called Digital Divide. It is also forecast that following the migration of speech services from fixed to mobile, Broadband is likely to follow suite in the latter part of the decade increasing the importance of satellite delivery to ensure full coverage.

Until recently, Fixed Satellite Service (FSS) satellites have so far been developed such that they can flexibly meet a wide range of service roles thereby covering diverse market places. Such systems are not optimum for broadband services and tended to be power limited but are increasingly also becoming bandwidth limited. Their ability to provide services at comparable cost/bit to terrestrial systems has been technology limited due to this lack of optimisation. However they have the advantage of wide coverage and this will persist for broadcast and multicast services but can also be used to good affect for low density user services for example in rural areas. The cost/bit comparator still exists and whilst rural users might expect to pay a small premium it cannot be too far out of line with terrestrial costs. In the

short term the challenge is to reduce the cost/bit by an order of magnitude and in the longer term (2020) by two orders of magnitude. This paper concerns the technology advances needed to bring this about and leads us to a Terabit/s satellite by 2020 by adopting a bespoke broadband optimised design.

There are some issues which are immediately apparent. As the demand for satellite capacity has steadily increased the limits of traditional Ku band satellites due to congestion of orbital slots is evident as well as the limitations in the spectrum available to cope with predicted demands. In addition these satellites are built to cover wide geographical areas and hence have limitations to support flexible distribution of bandwidth that will be needed for a European Broadband satellite application. These limitations force us to look at higher frequency bands of Ka and above where it becomes easier to realise a larger number of spot beams on board the satellite and hence via frequency reuse achieve the capacity requirements.

Broadband demand is being met terrestrially by local loop systems such as ADSL 2 but as the requirements exceed 10Mb/s only around 40% of households in the UK will be able to be serviced. Fibre to the Home (FFTH) across Europe is patchy and unlikely to be the answer for 20 to 30 years if ever in some areas. Wireless terrestrial is also at the mercy of spectrum allocation which is non uniform and LTE-A systems to deliver in excess of 30 Mb/s across cells is still a long way off and may never reach the rural areas. Thus the market in Europe indicates that there is demand for satellite services of this type. A study by IDATE in 2009 [2] considered the households that were not covered by broadband considered as the unserved market as follows;

- Western Europe 5.2 million
- Baltic countries 0.6 million
- Eastern Europe 6.6 million
- North Africa 18.0 million

In addition, there have been three studies of market demand conducted recently (2009);

- 1) Northern Sky research [3]
A ten year forecast which indicates that by 2018 satellite broadband will reach 1.2 million subscribers in Europe.
- 2) SES ASTRA study [4]
A detailed country by country study which includes the increased take up of terrestrial broadband and indicates addressable satellite markets not being served by terrestrial in low/median and high by 2020 as 0.44/0.85/1.25 million.
- 3) Eutelsat study [5]
Indicates that the addressable market for satellite broadband will reach 3.5 million by 2018.

The above studies all indicate a significant market for European satellite broadband in terms of households that

will not be served by terrestrial means even given the increase in terrestrial provision. If we include North Africa in the coverage the market becomes very large.

The remainder of this paper is structured as follows,

- Spectrum availability – assessment & implications;
- System architecture and satellite beams;
- Gateway/UT & beam parameters;
- Power and bandwidth requirements;
- Satellite Power Assumptions;
- Adoption of the Smart Gateway Concept;
- Achievable Performance;
- Other studies;
- Making the Terabit/s satellite a reality;
- Conclusions.

II. SPECTRUM AVAILABILITY

As we have already mentioned it can be demonstrated that Ku band does not possess sufficient spectrum for a Terabit/s satellite and so we will concentrate on both the Ka and the Q/V bands which have FSS allocations.

a) Ka Band

Exclusive bands for satellite are –19.7-20.2 and 29.5-30 GHz that is 2x 500 MHz across the European Union (EU) and this is proposed for use by both HYLAS and Eutelsat Ka-SAT. Under European Electronic Communications Committee (ECC) decisions [6], [7] these bands are exempt from individual licensing for low eirp terminals (<50dBW (recently updated in the UK to 55dBW) and in some countries 60dBW). All other parts of Ka band have shared primary frequency allocations and thus would be subject to coordination at particular earth station sites. The band 20.2 to 21.2 GHz is a dual military use band with the possibility of reuse but this would be difficult to coordinate across Europe and hasn't been considered herein.

Up Link

27.5-29.5 GHz shared with Fixed Services (FS); some portions auctioned in UK requiring coordination.

24.75 -25.25 GHz in ITU Regions 2/3 but not Region 1.

Hence 2.5 GHz is available but with restrictions.

Down Link

17.3-19.7 GHz shared with Broadcasting Satellite Service (BSS) feeder links and also FS with many terrestrial links operating across EU needing coordination and maybe restricted to rural areas.

21.4-22 GHz in ITU Regions 1/3 shared FS/Mobile/BSS. Hence 3 GHz is available but with restrictions.

The current EU interest regarding the use of Ka-Band are currently under review and a draft report indicates the various interests in the European Conference of Postal and Telecommunications Administrations (CEPT) [8].

b) Q/V Band

There are no exclusive bands for satellite (FSS) here and thus all this spectrum is subject to coordination with other users, even the User Terminals (UT's). This is not a show stopper but complicates the business model.

Up Link (V)

42.5-43.5 GHz is shared with FS/Mobile/RA. Portions auctioned in UK (3 operators paired with above);
47.2-50.2 GHz is shared with FS/Mobile but with military and Outside Broadcast restrictions;
50.4-51.4 GHz is shared with FS/Mobile but military restrictions in some countries.

Down Link(Q)

37.5-39.5 GHz is shared with FS/Mobile/Space research. This band is extensively used by FS.
40.5-42.5 GHz is shared with FS/Broadcasting/BSS/Mobile. Portions of this band have been auctioned in UK (3 operators) and in some other countries, requiring coordination.

Hence 5 GHz available for the uplink and 4 GHz for the downlink but with restrictions and coordination is needed. CEPT ERC/DEC has provisions in some parts of the spectrum and in some countries priority is given to military use.

c) Spectrum Summary

The spectrum for an EU wide satellite system is very complex with country to country variations and only 2 x 500MHz exclusive in Ka band. It may be that satellite operators have failed to lobby adequately for these bands and now some action is needed especially in Q/V bands with both the regulators and in WRC to restore sufficient spectrum for future systems.

III. SYSTEM ARCHITECTURE AND SATELLITE BEAMS

In order to achieve the Terabit/s satellite capacity we will need to use advanced air interfaces and frequency reuse beams from the satellite. We will assume basing the air interface on the current DVB-S2 standard and suggest later any modifications that might be required.

The DVB-S2 Standard [9] and its associated Guidelines document [10] give parameters for the air interface.

We have chosen to adopt a filter roll-off factor of 0.2 to represent modern equipment performance.

For system architecture analysis purposes the parameters given in Table 1 have been selected as a starting point recognising that Adaptive Coding and Modulation (ACM) and Fade Mitigation Techniques (FMT) using other mod codes may be useful in combating rain fades.

TABLE 1 WAVEFORM PARAMETERS CONSIDERED

Modulation	Eb/No (dB)	C/N in BW	spectral efficiency (b/s-Hz in BW)	FEC
16 APSK	6.4	10.8	2.75	5/6
32 APSK	8.1	13.5	3.43	5/6

Frequency reuse in the multi-spotbeam satellite antenna is commonly taken as either 3 or 4 colour with higher values (beyond 4) having diminishing returns. Current generation satellites at Ka band produce of the order of 80-100 beams to cover Europe.

In order to obtain an initial and preliminary estimate of the numbers of beams we have assumed either 16 or 32 APSK being in common use by 2020, with 3 and 4 colour reuse in the user beams occupying approximately 3 GHz of bandwidth at Ka band and take advantage of the fact that the gateway beams are significantly geographically separated permitting the use of the entire 4 GHz of bandwidth at Q/V band in each beam.

a) Limitations of beam number analysis

It is important to note that such an initial estimate is based upon bandwidth, spectral efficiency, frequency reuse and polarization reuse only and factors such as spacecraft payload, EIRP, C/N and C/I have been neglected in this initial assessment, as it is aimed at scoping the number of beams rather than determining a definitive solution. Thus, we have performed an initial set of calculations using a range of frequency reuse colours and polarizations with the stated spectral efficiency in order to assess various architectures. Furthermore the initial analysis considers uniform traffic loading in each beam and a practical system may require a higher number of beams than those suggested to account for non-uniform traffic whilst achieving a Terabit/s throughput.

IV. GATEWAY/UT & BEAM PARAMETERS

For an internet access service a star configuration into a gateway is to be preferred and so we now look at system architectures which have separate beams to User Terminals (UTs) and to Gateway Earth Station. We consider that the Gateway Earth Station will cover several UT beams and thus there will be fewer of them but they will carry greater capacity and hence need to be allocated more bandwidth.

a) Mixed Ka and Q/V solution

We have found that an initial architecture that employs the use of Q/V bands on the feeder links and Ka band for the UT links [11] appears to offer the best throughput. It should be noted that at Ka-band under existing regulation only 500 MHz would be in the exclusive satellite band and thus some of the UT's would need to coordinate. This is not seen as a major hurdle but regulators would need to adopt an on-line fast-track scheme.

b) UT beams

The bandwidth available is 2.5 GHz on the uplink (all bandwidth allocated to the user link as the feeder link is at Q/V band) and potentially 3 GHz on the down. For 2.5 GHz, three frequency reuse colours and 32 APSK the initial numbers of beams is found to be around **175** (or 88 with dual polarization) recognizing the limitations of our analysis as given in III a) above.

c) Gateway beams

The bandwidth available is 4 GHz on the up link and 5 GHz on the down link. For 4 GHz and the conditions above and using one frequency colour (possible because of large geographical gateway beam separation) the number of beams is 38 (or 19 with dual polarization) recognizing the limitations of our analysis as given in III a) above.

As already mentioned there are shared services in this spectrum and thus the siting of the Gateway Earth Stations would need to be considered on a country by country basis.

Use of 16APSK would increase the number of beams substantially. Figure 1 to Figure 3 depict initial beams configured for European coverage recognizing the limitations of our analysis as given in III a) above.

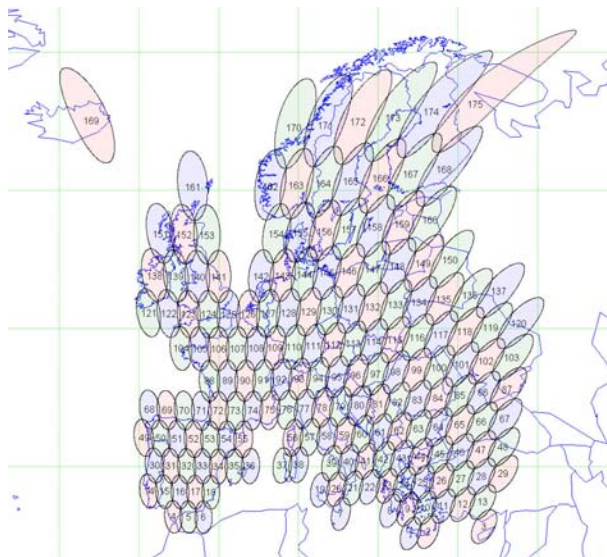


Figure 1. Representative 175 single polarised user beams over Europe

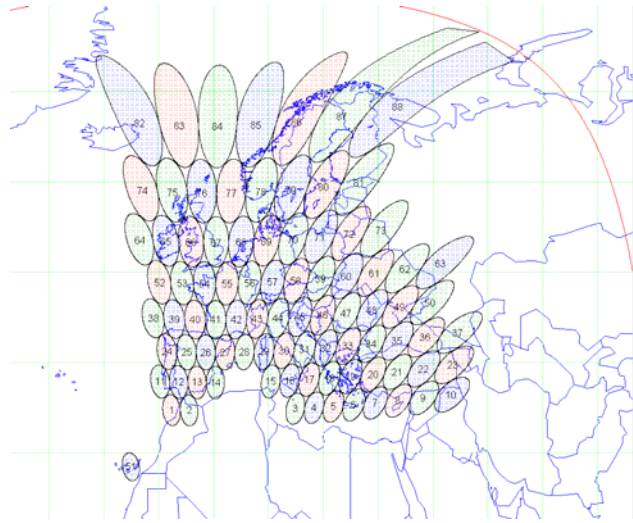


Figure 2. Representative 88 dual polarised user beams over Europe

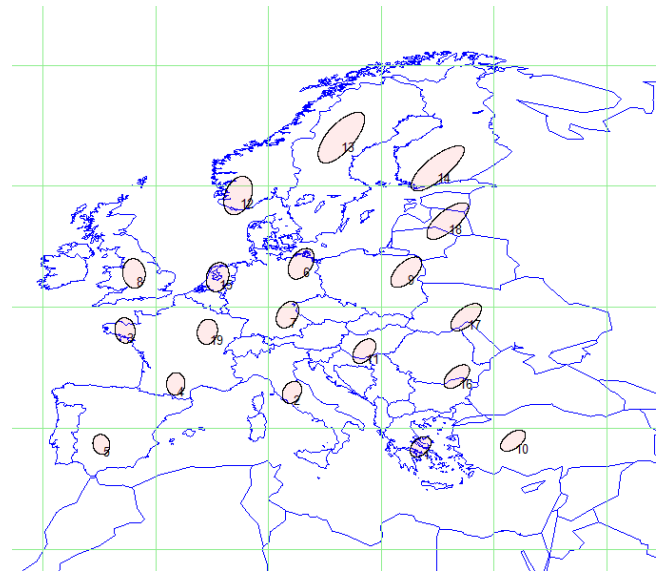


Figure 3. Representative dual polarised 19 beam Gateway configuration over Europe

V. POWER AND BANDWIDTH REQUIREMENTS

Here we look at power/bandwidth requirements for the Q/V-Ka band architecture in order to get some initial assessment of its feasibility. We will make some initial assumptions.

Pending further study of the relationship between beams and antenna size we assume that we have a 5m foldable reflector antenna for the UT side and a 2.5m reflector antenna on the Gateway Earth Station side of the satellite.

Assuming 65% efficiency on both we have;

Gateway Earth Station Band:

Gain Sat Rx (50 GHz) =60.5 dBi

Gain Sat Tx (40 GHz) =58.5 dBi

For a payload temp of 400K the G/T=34.4 dB/K

For a 15 W transponder output power the downlink eirp =70.3 dBW or 67.3 dBW at Edge of Coverage (eoc).

UT Band:

- Gain Sat Rx (30GHz) =62 dBi
- Gain Sat Tx (20GHz) =58.5 dBi

For a payload temp of 400K the G/T=36 dB/K
 For a 50W HPA output power the transponder downlink eirp =75.5 dBW or 72.5 dBW at eoc.

For the forward link we assume a bandwidth of one GHz and in the reverse link we assume that 40Mb/s users with 32 APSK would need a bandwidth of 10 MHz.

Ka band UT:

Baseline UT is taken as a 0.75m dish with a noise temperature of 150 K and G/T of 20.3 dB/K.
 The transmit EIRP will be taken as 55 dBW representing the current allowable non coordinated value agreed in many EU countries. Thus the SSPA would be 8.8 W.

Q/V GATEWAY EARTH STATION:

The baseline Gateway Earth Station is taken as a 5m dish which has a transmit gain of 66.5 dBi at 50 GHz and a receive gain of 64.5 dBi at 40 GHz. On the transmit side with a 2 dB feeder loss and 16W transmit power the eirp is 76.5dBW.

It should be noted that moving to a larger diameter Gateway Earth Station antenna would increase the Gateway Earth Station costs significantly (50 GHz operation) and the extra performance is not necessarily needed as the system is self-interference limited and not thermal noise limited.

We assume a G/T of 38 dB/K which represents an overall earth station noise temp of 450 K which seems reasonable in this band.

Total rain fading across Europe has been evaluated using the ITU-R model assuming an availability of 99.9% for the Gateway Earth Station and 99.7% for the UT's thus for single site worst case conditions the potential margins required are given in Table 2 along with typical Free Space Loss figures.

TABLE 2 POTENTIAL FADING ACROSS EUROPE

Frequency (GHz)	99.7 % (dB)	99.9 % (dB)	FSL (dB)
20	3	6	210
30	11	15	214
40	15	20	216
50	23	27	218

Of course not all Gateway Earth Stations and UT's will be faded at the same time and to get a better idea of the overall degradations we include the spatial variations of the rain and to determine the average system reductions in capacity.

For the purposes of this feasibility analysis we have chosen to examine the system capabilities under clear sky conditions and have assumed that rain faded conditions can then be addressed by appropriate application of FMT such as ACM. This initial working assumption will be studied further to assess its validity.

VI. SATELLITE POWER ASSUMPTIONS

The trend is to larger satellites with upwards of 10 tonnes being possible in 2020. However the longer term power limits of the payload are constrained by the volume available under the launcher fairing. With current series of launchers this is estimated to constrain the payload power to circa 20KW EOL [12]. Thus it is important to ensure that the number of beams dimensioned in the previous section can be suitably fed by HPA power within the satellite payload power limits for the forward and return downlinks.

VII. ADOPTION OF THE SMART GATEWAY CONCEPT

The Smart Gateway architecture employs a number of Gateway Earth Stations which are inter-connected with terrestrial feeds to form an agile routing of feeder link data that can be used in a diversity manner to combat fades on the gateway to satellite links [13]. The approach is depicted in Figure 4.

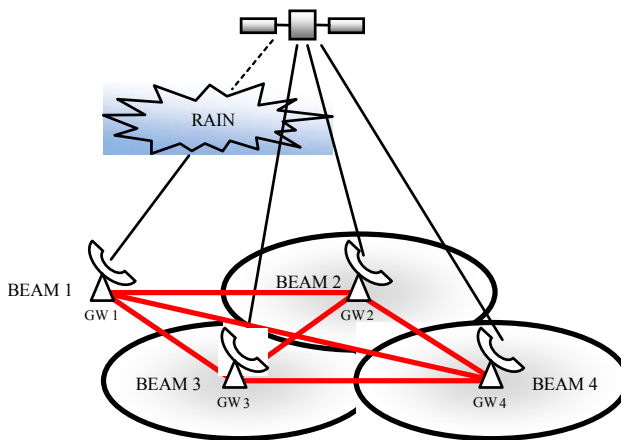


Figure 4. Smart Gateway Concept

According to this concept:

- Existing gateways are inter-connected to form a terrestrial network.
- Each user is serviced by a number of gateway feeder links.
- In the event of a gateway experiencing outage or reduced capacity, some or all user traffic can be re-directed terrestrially to any one of the remaining gateways, in any spot beam.

Advantages:

- Reduced cost → no additional gateways/antennas.
- Diversity gain → many more gateways, greater inter-site distance.
- Efficient gateway usage → all gateways simultaneously operational.
- Efficient resource usage → can utilise capacity wherever it exists.
- Implicit fault tolerance, opportunity to load balance and improve throughput.

Disadvantages:

- The allocation of gateway feeder link capacity to users is a critical function.
- Control/Switching algorithms required to detect capacity fluctuations and make traffic allocation decisions to achieve aims.
- A high degree of synchronisation in the gateway network is required.
- Some level of 'intelligence' is required in the Network and terminals.

Smart Gateways can potentially be used to avoid interference and to minimize the propagation effects for each gateway. Initial studies have shown this concept can be useful and simulations performed using traffic / weather statistics assumptions have demonstrated the advantages of the concept. The concept is attractive but as yet still immature and needs further consideration, especially at the payload level. This initial work will be followed up with improved assumptions to investigate load balancing as well as switching issues.

VIII. ACHIEVABLE PERFORMANCE

Based upon the parameters detailed above the performance was assessed under clear sky link conditions for the forward and return links.

The combined $C/(N+I)$ for the forward link was 14.6 dB for a co-channel C/I of 20 dB. This represented a margin of 1.1 dB over the required value of 13.5 dB.

A key limiting factor here is the C/I of the satellite antenna beams. This needs to be investigated in more detail.

In the forward link it may be appropriate to adopt beam hopping as this has the potential to improve the downlink C/I (adjacent channel) to around 25dB but again this requires further studies.

The combined $C/(N+I)$ for the return link was 15.0 dB for a co-channel C/I of 20 dB. This represented a margin of 1.5 dB over the required value of 13.5 dB.

The EoC eirp has been estimated assuming 100 x 10 MHz simultaneous carriers and sharing the power between them.

As for the forward link the C/I of the satellite antenna dominates the performance. Use of beam hopping on the return link would be more complicated as the UT's would need to synchronise with the on board system. Hence it would be more useful to study in detail the aggregate effect of the sporadic transmissions on the return link to see if the C/I is in fact improved. This requires figures on beam loading and activity ratios. On the Gateway Earth Station side the situation is improved due to beams at the same frequency being spaced further apart.

Here again we see a need for further consideration on how to improve the co-channel C/I on the satellite antenna.

IX. OTHER STUDIES

Other studies have been undertaken and include:-

- o Forward Link: to assess the ACM operation in Ka-band and investigate the potential for new MODCODs for rainy regions, using simulated precipitation field models (see figure 5);
- o Return Link: to investigate ACM on the return link (DVB-RCS NG like) at Ka-band;
- o Evaluation of the beam displacement due to satellite movements & resulting C/I degradation with the potential to exploit terrestrial mobile hand over concepts to combat the effect of beam movement;
- o Evaluation of C/I in the return link with appropriate traffic patterns and utilisation figures;
- o The potential of higher order modulation and coding;
- o Further evaluation of the feasibility of the Smart Gateway approach and its impact on the payload and system architectures;
- o Accurate assessment of the system availability using a space time-channel model which facilitates
 - Test of routing strategies for smart gateways
 - Evaluation of the effectiveness of ACM on the users links
 - Possible minimization of the required payload flexibility.

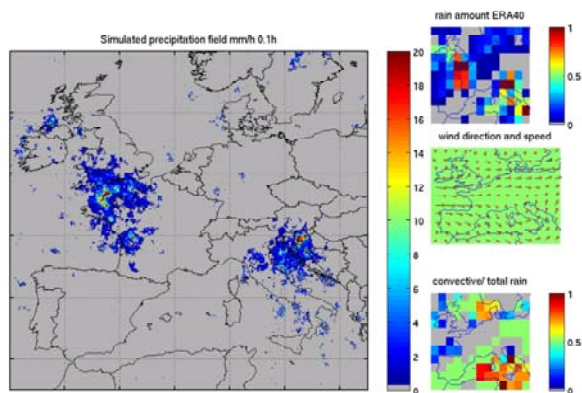


Figure 5. Typical simulated precipitation field

X. MAKING THE TERABIT/S SATELLITE A REALITY

As indicated above the straight application of current technology will not allow the proposed Terabit/s satellite to provide adequate QoS and thus we need to look towards innovations to solve this problem. Some possible areas are discussed below.

a) Improved C/I antenna performance

In order to achieve the capacity a large number of beams with a large overall frequency reuse factor is required. The downside of this is the increased interference components which sum up to contribute to the overall C/I. Current simulations of systems with a high number of spot beams demonstrate that the C/I is a significant challenge as the system is could be interference limited. Thus, in both the forward and return directions the satellite antenna C/I performance is an important factor in minimizing the number of beams required.

Some consideration has been given to the use of beam hopping on the forward link that may help to achieve flexibility with an acceptable number of RF chains and also to provide dual polarization in very hot spots with acceptable payload complexity but may not provide any improved C/I performance. For the reverse direction with many more beams and UT's the adoption of beam hopping is much more difficult as in each beam the UT's would have to be synchronized to the on board hopping which would complicate the terminals. However the return link is composed of bursts and there will be an activity factor associated with the transmissions across the beams and thus the aggregated interference considered so far is not a true reflection of reality. A more detailed investigation of the interference performance in general is thus needed.

b) Power requirements on the satellite

As already indicated payload power is likely to be a major constraint in achieving the Terabit/s. The HPAs already consume most of the payload power budget considered feasible (20 kW) and any special routing features (such as may be appropriate to match the Smart Gateway concept) will increase these demands.

c) Operation of ACM at Ka band and above

Conventional modulation and coding advances in the air interface have taken us close to the Shannon bound and therefore straight advances in this area will produce diminishing returns. Other means of increasing diversity that are applied in terrestrial systems suffer from the constraints of the satellite link apart from adaptive coding and modulation (ACM). ACM is being used effectively in DVB-S2 and partially in DVB-RCS at Ku band to combat rain fades by selecting one of twenty eight MOD/COD pairs available within DVB-S2. Such systems are constrained by the return link delay between the Gateway Earth Station and the UT compared with the time variation of the channel itself. As rain fading is a relatively slow mechanism it is possible to compensate fades across the MOD/COD range of 18dB, although in practice it will be slightly less than this. It is believed that at Ka band the current ACM could cope with the fading range for 99.7% availability on the UT links (but not higher) but for the Gateway Earth Station and Q/V bands the fades may exceed the current range. We have assumed that fades would not occur on both links simultaneously.

If we were to operate the UT's on Q/V bands we would need to examine a wider fading range and to extend the MOD/COD combinations. At the bottom end the system works down to an $E_s/N_0 = -2.4\text{dB}$ and extending further is possible but will incur difficulties SNR estimation and synchronization. At the top end the issue is more power from the satellite but this could be preferable as schemes higher than 32 APSK, such as 64 APSK or 64 QAM, should be possible by 2020. However, the co-channel C/I may constrain any benefits from such an approach.

d) Achieving the availability on the Gateways

As indicated above in the system dimensioning rain on the Gateway Earth Station uplinks is a major problem at Q/V bands. We could employ up path power control but the range of fading is so large that this would bring with it other major problems. Site diversity could be used but finding an uncorrelated rain site with acceptable ground connections is expensive and may be impossible. Thus, as indicated earlier, we consider smart site diversity systems in which the Gateway Earth Station's are interconnected to a Network Control Centre (NCC) which connects UT beams to one of the Gateway Earth Station's from the pool. Thus when a Gateway Earth Station is indicated to go into a deep fade the NCC performs a handover to another unfaded Gateway

Earth Station and switches all the UT forward and return links to that Gateway Earth Station. Since the Gateway Earth Station's are widely spaced a much better decorrelation of fading is available than for short distance diversity and the availability is increased. Including even a small number of Gateway Earth Stations in this configuration provides much improved availabilities at reduced fade margins. The handover process is crucial if no traffic is to be lost and at the same time we minimize signaling load in the system. Having established such a system it is also possible to include load balancing between the Gateway Earth Station's so as to ensure that outage switching doesn't cause an unexpected overload and to more balance the overall system.

As a more distant and challenging gateway architecture some studies are being initiated into the possibility of employing a network of gateways employing optical communications to the satellite. These studies will consider the maturity of the technology and the number of such gateways in the network.

XI. CONCLUSIONS

This paper has addressed concepts and issues relating to a Terabit/s satellite for 2020 that will be capable of reducing the cost/bit for broadband delivery and thus allowing satellite services to reach rural areas not feasible for terrestrial systems. The dimensioning of the system has demonstrated that several new technologies are appropriate for development before such a satellite system is feasible. Key amongst these are improved C/I techniques for the satellite antennas, smart Gateway Earth Station networks and improved ACM. Work is continuing to investigate all these in more detail but we feel there to be no technology show stopper for a Terabit/s satellite by 2020.

ACKNOWLEDGMENT

The authors wish to acknowledge the contribution of ESA towards this work and for their part funding the

SatNEx-III Network of Excellence under which the work was conducted. Acknowledgement is also given to DLR, Germany who manage SatNEx-III on behalf of its partners.

REFERENCES

- [1] Jean-Didier Gayraud, 'Terabit Satellite: Myth or Reality?', SPACOMM 2009, The First International Conference on Advances in Satellite and Space Communications. July 20-25, 2009. Colmar, France
- [2] IDATE consulting and research report 'Broadband satellite in Europe and North Africa, residential market outlook' March 2009
- [3] Northern Sky Research-Broadband satellite market study 2009
- [4] SES ASTRA compilation of external sources 2009.
- [5] Eutelsat internal study; Broadband satellite addressable markets 2009
- [6] ECC/DEC/(06)02:Exemption from Individual Licensing of LEST operating within 10.70–12.75 GHz or 19.70–20.20 GHz space-to-Earth and 14.00–14.25 GHz or 29.50–30.00 GHz
- [7] ECC/DEC/(06)03: Exemption from Individual Licensing of HEST with e.i.r.p. above 34 dBW
- [8] Draft Report on the 'Use of the frequency bands 27.5-30.0 GHz and 17.3-20.2 GHz by satellite networks', CEPT working group FM, May 2010, adopted for public consultation.
- [9] ETSI EN 302 307: Digital Video Broadcasting (DVB); Second generation framing structure, channel coding and modulation systems for Broadcasting, Interactive Services, News Gathering and other broadband satellite applications (DVB-S2)
- [10] ETSI TR 102 376: Digital Video Broadcasting (DVB) User guidelines for the second generation system for Broadcasting, Interactive Services, News Gathering and other broadband satellite applications (DVB-S2)
- [11] B G Evans and P T Thompson, "Key issues and technologies for a Terabit/s satellite", 28th AIAA International Communications Satellite Systems Conference (ICSSC-2010), Anaheim USA, paper number AIAA-2010-8713
- [12] T Hollingsworth, W. Gelon, A. Szeto, A. Applewhite and E. Yee, '25-kW Bus Platform for Communications Satellites' 28th AIAA International Communications Satellite Systems Conference (ICSSC-2010), Anaheim USA, paper number AIAA-2010-8687
- [13] H. Skinnemoen, 'Gateway diversity in Ka-band systems', Fourth Ka Band Utilization Conference, Venice, Italy, 2–4 Nov1998.

Multi-port Power Amplifier Calibration Estimation Technique Based on ICA Algorithm

Zhiwen Zhu and Xinping Huang
 Communications Research Centre Canada
 Ottawa, Ontario, K2S 8H2 Canada
 Emails: {zhiwen.zhu, xinping.huang}@crc.gc.ca

Abstract—A multi-port power amplifier (MPA) is a multi-input and multi-output system that is capable of amplifying several input signals simultaneously by a set of shared amplifiers without mutual interference. In a practical MPA, the component imperfections reduce the port isolation, which introduces leakage or cross-port interference among the output ports. In this paper, an independent component analysis (ICA) based technique is developed to estimate a calibration matrix that minimizes the effects of the imperfections. The MPA output signals are used in the estimation of the calibration matrix. Simulation studies show that the proposed calibration matrix estimation technique can lead to a significant improvement in the MPA output port isolation.

Keywords-Multi-port power amplifier; Calibration; Independent component analysis; JADE;

I. INTRODUCTION

Multi-beam satellite communication systems can achieve a high antenna gain and thus improve their effective isotropically radiated power and gain/noise temperature. In such a system, users may move from one geographic area to another serviced by different beams. As a result, traffic may not be distributed uniformly among the beams and it fluctuates over time. A multi-port power amplifier (MPA) based architecture [1]-[3] is an effective approach to enable flexible power allocation in multiple beam systems to address capacity variations among the beams during the lifespan of the satellite.

An MPA is a multi-input and multi-output system that is capable of amplifying multiple input signals simultaneously using shared amplifiers. Ideally, the MPA amplifies the multiple input signals and outputs them separately via different output ports without any mutual interference. In practice, component imperfections in the MPA reduce the port isolation, which introduces leakage or cross-port interference among the output ports.

The component imperfections can be reasonably well controlled over temperature and time at low frequencies [4], but it is difficult and costly at microwave frequencies and above. Some methods have been presented to linearize the nonlinearity of the PAs in the MPA [5], [6]. Assuming that the PAs are linear, a type-based calibration technique, which exploits the uniqueness of the statistics for a given

communication signal, has been presented [7] to compensate for the imperfections in other MPA components. In this paper, we develop a technique based on the independent component analysis (ICA) algorithm [8], [9] to estimate a calibration matrix to compensate for MPA imperfections. This technique does not require any prior information about the MPA input signals except that they are independent. The ICA is a statistical and computational approach with many applications, including source separation and biomedical signal processing. Here, the proposed technique uses a conventional ICA algorithm, i.e., the joint approximate diagonalization of eigenmatrices (JADE) [8], to estimate the input-output transfer function of the MPA from its output signals. A calibration matrix, i.e. the inverse of the MPA transfer function, is applied to the input signals before feeding them to the MPA to compensate for the impairments in the MPA. Computer simulations are used to demonstrate the performance of the proposed technique.

The paper is organized as follows: Section II describes the MPA model. Section III presents the ICA based calibration matrix estimation technique. Simulation results are given in Section IV. Section V concludes the paper.

II. MULTI-PORT POWER AMPLIFIER MODEL

An N -port MPA system has N input ports and N output ports. It is composed of an input hybrid matrix (IHM), a set of N shared power amplifiers (PA), and an output hybrid matrix (OHM). The IHM is made up of 3dB, 90° hybrid couplers, and has N input ports and N output ports. The PAs operate in their linear region, and each of the PA inputs is connected to one output port of the IHM. The PA outputs are connected to the inputs of the OHM that is identical in structure to the IHM. Fig. 1 shows a functional block diagram of a 4-port MPA.

Ideally, the MPA's input signals are summed together by the IHM with different phase relations to generate N summed signals. Each summed signal is amplified by one PA, and then fed to one input port of the OHM. The OHM combines its input signals coherently to generate the amplified original input signals. If there are no component mismatches/imperfections, the transfer function of the MPA,

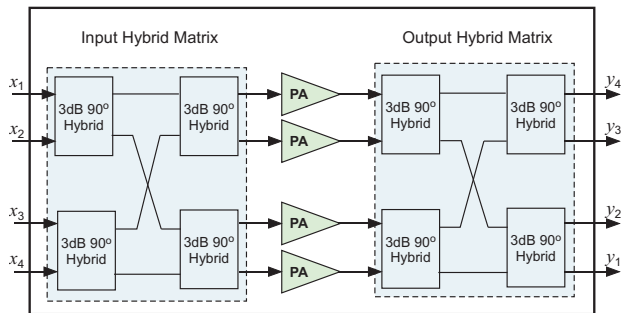


Figure 1. Functional block diagram of a 4-port MPA.

denoted by an $N \times N$ square matrix \mathbf{A} , is an anti-diagonal matrix. In this paper we reverse the output port order such that \mathbf{A} is represented by a diagonal matrix $G\mathbf{I}$, where G represents a complex gain of the MPA, and \mathbf{I} is an $N \times N$ identity matrix. Without loss of generality, we assume $G = 1$.

The input and output relationship of the MPA can be expressed by

$$\mathbf{y} = \mathbf{A}\mathbf{x} \quad (1)$$

where $\mathbf{x} = [x_1, x_2, \dots, x_N]^T$ denotes the input signal vector, $\mathbf{y} = [y_1, y_2, \dots, y_N]^T$ denotes the output signal vector, and the superscript "T" denotes the vector transpose. It should be noted that \mathbf{y} and \mathbf{x} are functions of time with the time index t being implied for ease of presentation.

In the ideal MPA, each input signal is co-amplified by the shared PAs and then combined coherently for output via individual output ports without mutual interference due to the diagonal transfer function. However, in reality, the component mismatches/imperfections destroy the diagonal property of the MPA transfer function, yielding a transfer function represented by a full square matrix with non-zero complex-valued elements

$$\mathbf{A} = \begin{bmatrix} a_{1,1} & a_{1,2} & \dots & a_{1,N} \\ a_{2,1} & a_{2,2} & \dots & a_{2,N} \\ \vdots & & \ddots & \vdots \\ a_{N,1} & a_{N,2} & \dots & a_{N,N} \end{bmatrix}$$

$a_{k,l}$ ($k, l = 1, 2, \dots, N$), which represents the transfer characteristics from the l th input port to the k th output port. Normally, $|a_{k,k}| \approx 1$ for $k = 1, 2, \dots, N$, while $|a_{k,l}| \ll 1$ for $k \neq l$, where $|\cdot|$ denotes the complex norm operator. Therefore, the inverse of \mathbf{A} always exists.

III. ICA BASED ESTIMATION TECHNIQUE OF THE CALIBRATION MATRIX

The objective of the MPA calibration is to eliminate the leakage among different ports by restoring the diagonal property of its transfer function. Figure 2 illustrates a simplified functional block diagram of an N -port MPA with the

calibration function. The MPA output signals are sampled in parallel, and used in the digital signal processor (DSP) to estimate the calibration matrix.

The output of the MPA with calibration can be expressed by

$$\mathbf{y} = \mathbf{A}\mathbf{C}\mathbf{x} \quad (2)$$

where \mathbf{C} denotes the calibration matrix. If $\mathbf{A}\mathbf{C} = \mathbf{I}$, the MPA is perfectly calibrated, which occurs when $\mathbf{C} = \mathbf{A}^{-1}$.

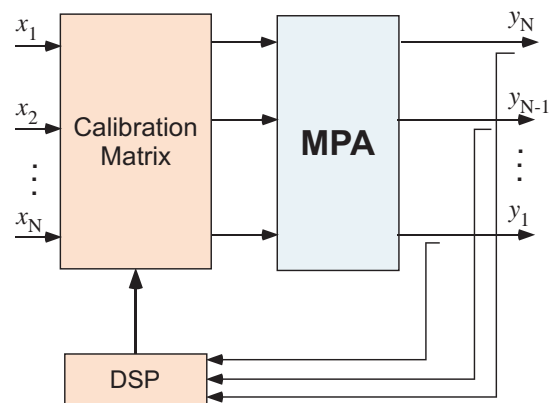


Figure 2. Simplified functional block diagram of the MPA with calibration function.

To determine \mathbf{C} , let's assume that x_n s are independent non-Gaussian signals with zero mean and unit variance. That is, $E[\mathbf{x}\mathbf{x}^H] = \mathbf{I}$, where $E[\cdot]$ is the mathematical expectation operator and the superscript "H" denotes Hermite transpose. At the MPA output, y_n 's become correlated due to the signal leakage.

The ICA-based estimation technique consists of three steps. In the first step, we pre-whiten y_n 's by multiplying a full ranked matrix \mathbf{M} , yielding a new vector $\mathbf{z} = \mathbf{M}\mathbf{y}$, where $\mathbf{z} = [z_1, z_2, \dots, z_N]^T$, such that z_n 's are mutually uncorrelated and all have unit variance, i.e., \mathbf{z} becomes $E[\mathbf{z}\mathbf{z}^H] = \mathbf{I}$. This transformation is always possible and can be accomplished by classic principal component analysis or singular value decomposition. \mathbf{M} is constructed from the eigenvalues and eigenvectors of the covariance matrix of \mathbf{y} [9]. After transformation, we have

$$\mathbf{z} = \mathbf{M}\mathbf{y} = \mathbf{M}\mathbf{A}\mathbf{x} = \mathbf{B}\mathbf{x} \quad (3)$$

where $\mathbf{B} = \mathbf{M}\mathbf{A}$ is an orthogonal matrix due to the assumptions on \mathbf{x} : it holds $E[\mathbf{z}\mathbf{z}^H] = \mathbf{B}E[\mathbf{x}\mathbf{x}^H]\mathbf{B}^H = \mathbf{I}$. According to Eq. (3), $\mathbf{e} = \mathbf{B}^{-1}\mathbf{z} = \mathbf{B}^H\mathbf{z}$ will be the estimate of \mathbf{x} , where $\mathbf{e} = [e_1, e_2, \dots, e_N]^T$.

In the second step, the orthogonal matrix \mathbf{B} is determined by the JADE algorithm as a unitary maximizer of the cost function

$$\zeta(\mathbf{B}) = \sum_{i,k,l=1}^N |\text{cum}(e_i, e_i^*, e_k, e_l^*)|^2$$

where $cum(e_i, e_i^*, e_k, e_k^*)$ denotes the 4th-order cumulants of \mathbf{e} [8]. Thus \mathbf{B} can be obtained as

$$\mathbf{B} = \arg \max_{\mathbf{B}} \zeta(\mathbf{B}) \quad (4)$$

Eq. (4) is equivalent to minimize the sum of all the squared cross-cumulants, i.e. distinct indices in the first and second terms as $cum(e_i, e_j^*, e_k, e_l^*)$.

For the complex N -dimensional random vector \mathbf{e} , its 4th-order cumulants are associated with a quadricovariance denoted by \mathbf{Q} , defined as a linear matrix-to-matrix mapping $\mathbf{R} \rightarrow \mathbf{S} = \mathbf{Q}(\mathbf{R})$ by

$$s_{ij} = \sum_{k,l=1}^N cum(e_i, e_j^*, e_k, e_l^*) r_{kl} \quad (5)$$

where \mathbf{R} and \mathbf{S} are $N \times N$ matrices with entries r_{ij} and s_{ij} , respectively. There exist N^2 real numbers λ_n and N^2 orthogonal matrices \mathbf{R}_n , satisfying $\mathbf{Q}(\mathbf{R}_n) = \lambda_n \mathbf{R}_n$, $n = 1, 2, \dots, N^2$. Note that \mathbf{Q} is actually a 4th-order tensor and \mathbf{R}_n 's are the eigenmatrices of \mathbf{Q} associated to its eigenvalues λ_n . It has been proved [8] that the quadricovariance \mathbf{Q} has exactly rank N so that only N out of all λ_n s are non-zero. The cost function in Eq. (4) becomes

$$\zeta(\mathbf{B}) = \sum_{n=1}^N \lambda_n \|\text{diag}(\mathbf{B}\mathbf{R}_n\mathbf{B}^H)\|^2 \quad (6)$$

where $\|\text{diag}(\cdot)\|$ is the norm of the vector built from the diagonal elements of the matrix argument. According to Eq. (6), the unitary matrix \mathbf{B} can be obtained by a joint diagonalization of the N eigenmatrices \mathbf{R}_n .

However, it is well known that the JADE algorithm has two inherent ambiguities: permutation ambiguity and scaling ambiguity. That is, \mathbf{A} can be estimated as

$$\mathbf{A} = \mathbf{M}^{-1}\mathbf{B}\mathbf{D}\mathbf{P} \quad (7)$$

where \mathbf{D} is an $N \times N$ nonsingular diagonal matrix that stands for the scaling ambiguity, and \mathbf{P} is an $N \times N$ permutation matrix that is simply obtained from an identity matrix with its rows and columns being re-ordered.

In the third step, we will solve the ambiguity issue. From the assumption that \mathbf{A} has much larger diagonal elements than off-diagonal elements, we can obtain \mathbf{P} that re-orders $\mathbf{M}^{-1}\mathbf{B}$ so that the larger elements are on its diagonal position. The scaling factor in \mathbf{D} can be estimated from the eigenvalues of the first step as the diagonal elements in an ideal \mathbf{A} are 1. Having determined the estimate of \mathbf{A} of Eq. (7), the calibration matrix can be derived as $\mathbf{C} = \mathbf{A}^{-1}$.

To achieve a better estimation performance and to track variations of the MPA characteristics, the above 3-step procedure can be repeated as follows:

(i) Set $k = 0$ and $\mathbf{C}_k = \mathbf{I}$;

(ii) Estimate a new \mathbf{C} from the MPA output signals using the above 3-step procedure;

(iii) Update the calibration circuit according to $\mathbf{C}_{k+1} = \mathbf{C}_k\mathbf{C}$;

(iv) Increment $k = k + 1$ and go to (ii).

IV. COMPUTER SIMULATIONS

To validate the ICA based MPA calibration technique, computer simulations using Matlab have been performed for a 4-port MPA. It is assumed that the hybrids in the IHM and the OHM have a gain error within ± 1 dB and a phase error within $\pm 10^\circ$, and the PAs have a gain variation within ± 1 dB and a phase variation within $\pm 10^\circ$. The actual errors are generated from a uniform random number generator. The amplitude and phase in the resulting MPA transfer function used in our simulations is listed below, respectively:

$$\begin{bmatrix} 1.04 & 0.13 & 0.13 & 0.18 \\ 0.07 & 0.96 & 0.16 & 0.09 \\ 0.18 & 0.11 & 1.11 & 0.06 \\ 0.12 & 0.16 & 0.05 & 1 \end{bmatrix}$$

and

$$\begin{bmatrix} 1.3^\circ & -122.4^\circ & -9.1^\circ & -149.8^\circ \\ -112.6^\circ & -13.6^\circ & 25.0^\circ & -16.1^\circ \\ 173.2^\circ & -62.5^\circ & 11.3^\circ & -174.2^\circ \\ 95.7^\circ & 167.1^\circ & -87.3^\circ & 0^\circ \end{bmatrix}$$

Without loss of generality, one element is normalized to 1 in order to have a unique solution. The four input signals are QPSK, 16QAM, 8PSK, and 16QAM modulated with variances of 1, 2.25, 1, and 2.25, respectively. These signals are square root raised cosine pulse-shaping filtered with rolloff factors of 0.25, 0.35, 0.35, and 0.25. The simulation uses 8 samples per symbol. 10^5 samples, i.e. 12,500 symbols, are used in the simulation to calculate the cumulants. The 3-step procedure is repeated 10 times.

The error vector magnitude (EVM) is used to measure the quality of the MPA output signals. It is defined as

$$\text{EVM} = \sqrt{\frac{\sum_{l=1}^L |D_{ideal,l} - D_{meas,l}|^2}{\sum_{l=1}^L |D_{ideal,l}|^2}} \times 100\% \quad (8)$$

where $D_{meas,l}$ is the value of the l th received symbol, $D_{ideal,l}$ is the ideal value of the l th symbol, and L is the total number of symbols used in the calculation. The EVM is essentially a measure of the interference to signal ratio.

Figure 3 illustrates the constellation of the MPA output signals without calibration. It clearly shows that the signal constellation scatters widely due to the cross port interference caused by the MPA imperfections. Figure 4 shows the constellations of the MPA output signals after calibration. We observe that the proposed ICA-based technique significantly reduces the cross-port interference and restores

the signal constellations. The EVM values before and after calibration are summarized in Table I, which shows that they are reduced from 24% to 0.6% for QPSK, from 28% to 0.7% for 8PSK, and from 26% to 2% for 16QAM, respectively.

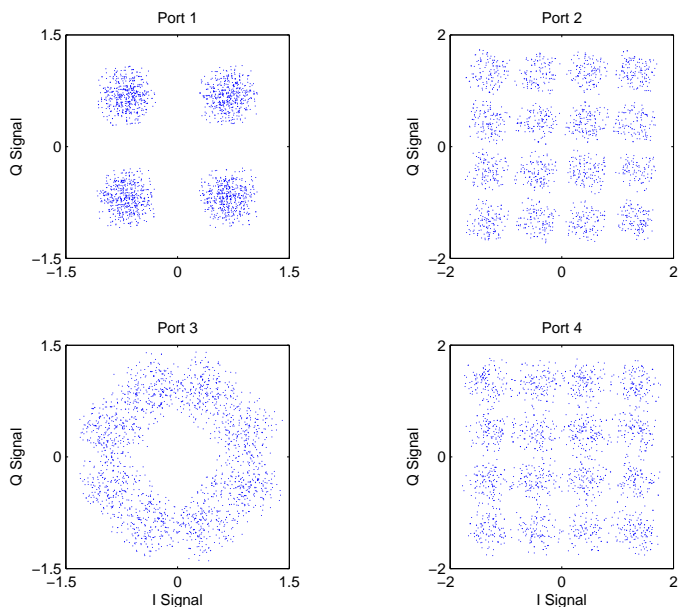


Figure 3. Signal constellations before calibration.

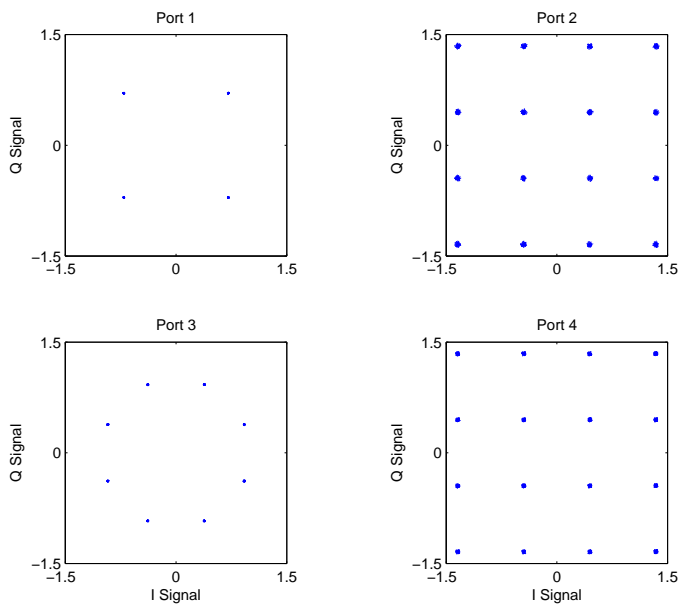


Figure 4. Constellations after calibration.

V. CONCLUSIONS

An MPA calibration technique based on the independent component analysis algorithm has been proposed in this paper. It applies a calibration matrix to the MPA input signals

TABLE I
EVM VALUES BEFORE AND AFTER CALIBRATION.

Port#	Before (%)	After (%)
1 (QPSK)	24.10	0.63
2 (16QAM)	25.65	2.12
3 (8PSK)	28.26	0.74
4 (16QAM)	27.11	1.94

before feeding them to the MPA in order to precompensate for the impairments in the MPA. The calibration matrix is estimated using the JADE algorithm. Simulation results show that the proposed technique can significantly reduce the cross-port interference in the MPA output ports, which in turn greatly improves the system performance.

REFERENCES

- [1] S. Egami and M. Kawai, "An adaptive multiple beam system concept", *IEEE JSA in Communications*, vol. 5, no. 4, pp. 630-636, May 1987.
- [2] M. Kanaka and S. Egami, "Reconfigurable multiport amplifiers for in-orbit use", *IEEE Trans. on Aerosp. Electron. Syst.*, vol. 42, no. 1, pp. 228-236, Jan. 2006.
- [3] A. Mallet, A. Anakabe, J. Sombrin, and R. Rodriguez, "Multiport-amplifier-based architecture versus classical architecture for space telecommunication payloads", *IEEE Trans. on Microwave Theory Tech.*, vol. 54, no. 12, pp. 4353-4361, Dec. 2006.
- [4] L. Dayaratna, L. Walshak, and T. Mahdawi, "TACeS Communication Payload System Overview," *18th AIAA Int. Satellite Commun. Sys. Conf. and Exhibit*, pp.246-250, 2000.
- [5] T. Kaho, Y. Yamaguchi, T. Nakagawa, K. Araki, and K. Araki, "A novel adaptive linearization technique for a balanced-amplifier array," *IEICE Trans. on Electronics*, vol. E89-C, no. 10, pp. 1448-1453, Oct. 2006.
- [6] X. Huang and M. Caron, "Benefit of linearizing power amplifiers in multi-port amplifier subsystems," *IEEE Int. Symp. on Circuits and Systems*, pp. 1260-1263, May 2008.
- [7] Z. Zhu, X. Huang, and M. Caron, "Ka-band Multi-port Power Amplifier Calibration Experiment and Results." *The 2nd Int. Conf. on Advances in Satellite and Space Communications*, pp.11-14, 2010.
- [8] J. F. Cardoso and A. Souloumiac, "An efficient technique for the blind separation of complex sources," *IEEE Signal Processing Workshop on Higher-Order Statistics*, pp. 275-279, 1993.
- [9] P. Comon, "Independent component analysis - a new concept?" *Signal Processing*, vol. 36, no. 3, pp. 287-314, Apr. 1994.

On Design of Optimized Low-Density Parity-Check Codes Starting From Random Constructions

Fred Daneshgaran
ECE Department
California State University
Los Angeles, USA
e-mail: fdanesh@calstatela.edu

Massimiliano Laddomada
EE Department
Texas A&M University-Texarkana
Texarkana, USA
e-mail: mladdomada@tamut.edu

Marina Mondin
DELEN
Politecnico di Torino
Turin, ITALY
e-mail: mondin@polito.it

Abstract—In this paper we present a novel two step design technique for Low Density Parity Check (LDPC) codes, which, among the others, have been exploited for performance enhancement of the second generation of Digital Video Broadcasting-Satellite (DVB-S2). In the first step we develop an efficient algorithm for construction of quasi-random LDPC codes via minimization of a cost function related to the distribution of the length of cycles in the Tanner graph of the code. The cost function aims at constructing high girth bipartite graphs with reduced number of cycles of low length. In the second optimization step we aim at improving the asymptotic performance of the code via edge perturbation. The design philosophy is to avoid asymptotically weak LDPCs that have low minimum distance values and could potentially perform badly under iterative soft decoding at moderate to high Signal to Noise Ratio (SNR) values. Subsequently, we present sample results of our LDPC design strategy, present their simulated performance over an AWGN channel and make comparisons to some of the construction methods presented in the literature.

Keywords-Block codes; iterative decoding; LDPC; low density parity check codes; minimum distance; near-codeword.

I. INTRODUCTION

Low-density parity-check codes were discovered by Gallager [1] in 1962 but did not receive much attention at the time essentially for complexity reasons. In [2], Tanner resurrected LDPCs generalizing them through the introduction of the so-called Tanner graph. Only recently in 1999, Mackay [3] demonstrated that LDPCs when optimally decoded are capable of achieving information rates up to the Shannon limit.

To date, there are three main classes of LDPC constructions that can be summarized as follows:

- **Density evolution optimized LDPCs:** these LDPCs are designed by exploiting some analytic properties of the probability density functions of the log-likelihood ratios (LLRs) associated with both the bit and check nodes in the Tanner graph during iterative decoding [4].
- **Combinatorial and Algebraically designed LDPCs ([5]-[12]):** the approach is aimed at designing well structured LDPC codes based on cyclic difference families, affine configurations, Margulis-Ramanujan algebraic designs and pseudorandom constructions.
- **Graph-theoretically designed LDPCs ([13]-[15]):** this class of codes make use of graph-theoretical properties to design good LDPCs.

- **Randomly designed LDPCs ([16]-[20]):** this class of codes exploits random techniques to design parity-check matrices of good LDPCs.

In this paper we present an effective algorithm for design of "optimized" LDPCs. The design is accomplished in two steps. Given a specific set of values (k, n) for the LDPC code, in the first step the goal is to design a related Tanner graph having a pre-specified distribution of both bit and check node degrees. In connection with this latter point, we note that we have not taken into account *optimal* degree distributions, even though we are conscious of the fact that optimal degree sequences have been proposed aimed at designing capacity-achieving degree sequences for the Binary Erasure Channel (BEC). We invite the interested reader to review [21] for a systematic study of capacity-achieving sequences of LDPCs for the BEC. The objective function for the first step in our design process is related to the cycle-distribution of the LDPC. In the second step, we consider the problems related to trapping sets/near-codewords/stopping sets by an indirect method. In particular, given the very high complexity of explicitly enumerating and determining these sets which are problematic for iterative decoding for any practically sized LDPC, we shall use a specific instance of a recursive algorithm proposed in [22] to optimize the LDPCs.

II. THE LDPC DESIGN ALGORITHM

In this section we present the basic rationales behind the proposed quasi-random algorithm for LDPC design. It is known that the belief-propagation decoder used for decoding LDPCs provides optimum decoding over cycle-free Tanner graphs $T(H)$. Hence, an obvious design goal is to try to minimize the influence of the cycles on the iterative decoder. This in turn suggests that a good way of designing LDPCs may be to try to maximize the smallest length cycle over all the cycles in $T(H)$ (i.e., to try to maximize the girth), while simultaneously attempting to minimize the multiplicities of the shortest length cycles in any bit node $v_{1,i} \in V_1, \forall i = 1, \dots, n$, or equivalently, the multiplicities of the cycles in any check nodes $v_{2,j} \in V_2, \forall j = 1, \dots, m$ for increasing length of the cycles above the minimum value. Another design issue that should be considered for the LDPC is the minimum distance of the code. In [22], based on experimental results we have

found that the error-floor performance of a *randomly-designed* LDPC code is often constrained by its minimum distance. Note that it is known that structured codes present error-floor performance that are constrained by near-codewords/stopping sets, or more generally trapping sets [23], [24]. Unfortunately, it is not a simple task to design a LDPC code by considering both trapping sets and the minimum distance of the code. This is essentially due to the combinatorial complexity of the problem for any practically sized LDPC. In the approach proposed in this paper, we attack the problem of achieving both goals in two successive steps. In the first step, we design random LDPCs of a given size (k, n) and given bit node distribution $d_{v,i}$, $\forall i = 1, \dots, n$, whereby $d_{v,i}$ is the degree of the i -th bit node in $T(H)$, by inserting one edge in $T(H)$ at a time on a best effort basis via iterative minimization of a suitable cost function strictly related to the cycle multiplicities for any given bit node. The design is accomplished with a constraint of guaranteeing regular check node degrees. This is because experimental evidence in the literature suggests that certain check node distributions lead to LDPCs with relatively good performance in Additive White Gaussian Noise (AWGN) channels. However, the algorithm proposed here is general in that any suitable check node degree distribution can be imposed during the design.

In a second step, we optimize the edge positions using an instance of the algorithm proposed in [22], whose aim is to maximize the minimum distance of a specific LDPC code. Efficient minimum distance estimation is needed in this process and is conducted through a variant of the error-impulse method proposed by Berrou [25].

We consider the parity-check matrix H of a generic LDPC as a probabilistic space $\Omega = G(n_V, M)$ whereby n_V is the number $n = |V_1|$ of bit nodes of the code plus the number $m = |V_2|$ of the check nodes (i.e., in the case of a Tanner graph $T(H)$ associated to a LDPC code¹ $n_V = n + m$), and M is the overall number of edges in $T(H)$. For simplicity, in what follows we consider regular LDPC codes in which the number of ones in any column of H (i.e., the number of bit node edges) is equal to d_v .

Consider an algorithm to insert one edge at a time in order to create a matrix H corresponding to a regular Tanner graph $T(H)$ containing d_v edges for every bit node. Enumerate the edges with i , where $i = 1, \dots, M = n \cdot d_v = m \cdot d_c$. Denote by X_l the variable representing the number of cycles of length l in $T(H)$, so that X_l is a random variable over the space Ω .

Let $X_{l,i}$ be the random variable representing the number of length- l cycles resulting from the addition of the i -th edge in $T(H)$. A suitable algorithm for the design of random instance of LDPC codes should try to at least minimize the number of length-4 cycle (i.e., the random variable $X_{4,i}$) for any edge $i = 1, \dots, M$. A specific instance of this algorithm is proposed in the following.

¹Note that we consider matrix H with m rows and n columns. This simply means that the actual rate of the code is $R \geq m/n$. In the case in which the m rows are linearly independent then $m = n - k$ and the LDPC has full rate k/n .

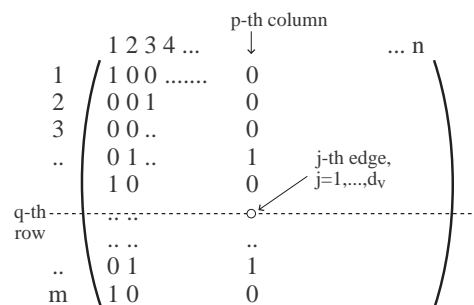


Fig. 1. Edge-by-edge growth of a sample LDPC parity-check matrix.

- 1) Set the bit node degree distribution $d_v(j)$, $j = 1, \dots, n$.
- 2) Set the number i of inserted edges to zero.
- 3) For any j from 1 to n perform the following tasks:
 - For any p from 1 to $d_v(j)$:
 - a) generate a random set P of N_m uniformly distributed candidate positions whereby $P = \{p_k, k = 1, \dots, N_m : p_k \in [1, \dots, m]\}$,
 - b) choose the position p_m where to insert the i -th edge by minimizing the cost function,

$$p_m = \min_{p_k \in P} X_{4,i}(p_k) \quad (1)$$
 whereby, $X_{4,i}(p_k)$ is the number of length-4 cycles over all the partial graphs $T(H)$, when the i -th edge is inserted at the j -th bit node in the p_k -th row of the parity check matrix.
 - c) Increase the inserted edge counter $i \leftarrow i + 1$.
 - End (for p).
- 4) End (for j).

This algorithm is clearly suboptimal. An optimum algorithm would require the minimization of $X_{4,j}(p_k)$ for any inserted edge j by re-positioning all the previous inserted edges for $i = 1, \dots, j - 1$. Clearly, this approach is impractical due to very high complexity. Our proposed algorithm on the other hand evaluates the position in which to insert the i -th edge without consideration about the positions of the previous inserted edges. The next theorem assures the necessary condition to decouple the effects of the selection of the i -th edge from that of the $(i + 1)$ -th edge, on the random variable $X_{4,i+1}$. This in turn suggests that on the average and for the block length tending to infinity, we can add one edge at a time without consideration about the past (i.e., a greedy edge insertion paradigm).

Theorem I: Consider the random construction of a Tanner graph $T(H)$ with vertex sets V_1, V_2 , with $|V_1| = n$, $|V_2| = m = \frac{n \cdot d_v}{d_c}$, as proposed based on the greedy algorithm above, with d_v the average bit node degree and d_c the average check node degree. Then, for any $i = 1, \dots, M - 1$, we have:

$$\lim_{n \rightarrow \infty} E[X_{4,i+1} | X_{4,i}] = E[X_{4,i}]$$

Proof: Consider step $(i + 1)$ (i.e., we have already inserted i edges and we wish to add the $(i + 1)$ -th edge). We conjecture that the $(i + 1)$ -th edge does not introduce, on the average and for $n \rightarrow \infty$, any additional length-4 cycles in comparison to the average number of length-4 cycles present at the end of the previous step.

Suppose we add the $(i + 1)$ -th edge in $T_i(H)^2$ corresponding to the j -th edge in the p -th column, with $j = 1, \dots, d_v$ (in Fig. 1 we have $d_v = 3$). With this setup, the p -th column is identified by $p = \lceil \frac{i+1}{d_v} \rceil$.

Consider the evaluation of the number of length-4 cycles in $T_{i+1}(H)$ after the insertion of the $(i + 1)$ -th edge conditioned on the number of length-4 cycles present at the end of the i -th iteration (i.e., the conditioning $X_{4,i+1}|X_{4,i}$ on the probabilistic space $\Omega = G(n_v, M)$). By observing that the insertion of a new edge can only increase the number of length-4 cycles by at most a constant amount, the following relation holds $X_{4,i+1}|X_{4,i} = X_{4,i} + c, \forall i = 1, \dots, M - 1$. Hence, we have the inequality:

$$X_{4,i} \leq X_{4,i+1}|X_{4,i} \leq X_{4,i} + c, \forall i = 1, \dots, M - 1 \quad (2)$$

Of interest is the probability $P(X_{4,i+1} - X_{4,i} = 0|X_{4,i} = \chi)$ (i.e., the probability that the generic $(i + 1)$ -th edge does not add any length-4 cycles conditioned on the fact that the number of length-4 cycles in the previous stage was χ).

To find this probability, consider the scheme of Fig. 1 in which a pivot point identifies at most $(d_c - 1)(d_v - 1)$ intersection points, each point corresponding to the intersection of a row and column whereby there exists a '1' in the q -th row and p -th column. Note that the number of ones in any row is less than or equal to d_c , while the number of ones in any column is less than or equal to d_v .

The probability that no cycle of length-4 is generated by insertion of a new edge at position (q, p) in H can be lower-bounded by the probability that all the $(d_c - 1)(d_v - 1)$ intersection points identified above, will have zeros. Using counting arguments, the probability of having a zero at any given intersection is:

$$a = \min\left(\frac{n - d_c}{n}, \frac{m - d_v}{m}\right),$$

from which we obtain the lower-bound:

$$P(X_{4,i+1} - X_{4,i} = 0|X_{4,i} = \chi) \geq a^{(d_c-1)(d_v-1)}.$$

Above is the probability that during the insertion of the j -th edge in the p -th column, we do not have d_c ones per row and d_v ones per column. From this lower-bound we get the upper-bounded:

$$P(X_{4,i+1} - X_{4,i} \geq 1|X_{4,i} = \chi) \leq 1 - a^{(d_c-1)(d_v-1)}$$

From these results we can write:

$$E[X_{4,i+1}|X_{4,i}] \leq (j - 1) \cdot \min(d_c - 1, p - 1) \cdot \left[1 - a^{(d_c-1)(d_v-1)}\right] + \chi \quad (3)$$

²The subscript i in $T_i(H)$ is used to signify the fact that the Tanner graph contains the first i edges.

where $(j - 1) \cdot \min(d_c - 1, p - 1)$ is the maximum number of length-4 cycles that can be introduced. Suppose $\frac{n-d_c}{n} < \frac{m-d_v}{m} \implies a = \frac{n-d_c}{n} = 1 - \frac{d_c}{n}$, from which one obtains $a^{(d_c-1)(d_v-1)} \approx 1 - (d_c - 1)(d_v - 1) \frac{d_c}{n}$, and in turn, $1 - a^{(d_c-1)(d_v-1)} \approx (d_c - 1)(d_v - 1) \frac{d_c}{n}$. Hence, (3) can be written as follows:

$$E[X_{4,i+1}|X_{4,i}] \leq \chi + (d_v - 1)^2 (d_c - 1) \frac{d_c}{n} \approx \chi + \frac{d_c^2 d_v^2}{n} \quad (4)$$

In the limit, for block size tending to infinity, one obtains the result:

$$\lim_{n \rightarrow \infty} E[X_{4,i+1}|X_{4,i}] = \chi = E[X_{4,i}] \quad (5)$$

□

The length-4 cycles are not the only one problematic factor limiting the LDPC performance. In our LDPC design, we have used a more general cost function taking into account longer length cycles as well. The cost function adopted for LDPC design takes on the general form:

$$f(T_i(H)) = \sum_{l=4}^{l_{max}} X_{l,i} \cdot L^{-l} \quad (6)$$

where i is the index of the edge to be inserted, and l_{max} is the greatest cycle length taken into account during the LDPC design. In the previous equation, $T_i(H)$ is used to signify the fact that the cost function is evaluated on the partially constructed Tanner graph after insertion of the i -th edge. A good tradeoff between code performance and complexity burden can be obtained by considering $l_{max} = 8$. The constant L is a weighting factor useful for making the smallest length cycles more undesirable than longer length cycles. Extensive tests suggests that the value $L = 10$ may be a good compromise value for LDPC design.

It is clear that the proposed algorithm aims at minimizing the cycle distribution at each bit node in $T(H)$. However, as noted in the introduction, with this design philosophy, while the randomly designed LDPC may have good performance especially for low E_b/N_o ratios, the random approach does not assure either a good minimum distance, or a good cycle clustering. For tackling this issue, we used a second optimization step aiming at code optimization in the error-floor.

III. OPTIMIZATION OF THE RANDOMLY DESIGNED LDPCs

As noted above, the second step in our LDPC design algorithm is an optimization step whereby we aim at improving the performance of the code in the error-floor region. Implicit in such a strategy is a need for an efficient algorithm to estimate the minimum distance of a given LDPC. The performance of LDPC codes may be limited by pseudo-codewords. There are however cases when the LDPC decoder behaves as a Maximum-Likelihood (ML) decoder. This is specially so for randomly constructed LDPC codes operating at medium to high SNR values. In such cases, estimation of the minimum distance d_m can be useful to assess asymptotic performance. In short, apart from theoretical interest in designing LDPCs with large d_m , the technique is useful in eliminating LDPC

codes that are poor by virtue of having a low d_m . However, we emphasize that if a code has a high d_m , simulations would still be needed to assess real performance.

An effective algorithm for estimating the minimum distance of turbo codes, called the Error Impulse (EI) was proposed in [25]. Although the rationale behind the method hypothesized a ML decoder, the algorithm has shown reasonably good performance with the sub-optimal iterative decoding algorithms used for turbo-codes. In order to keep the presentation concise, we refer the interested reader to [25] for details on the theoretical rationale beyond the algorithm. Suffice it to say that the algorithm exploits the capabilities of a ML soft decoder to prevent EI input patterns. With a reasoning based on the Euclidean space geometry, in [25] it was shown that under the hypothesis that the all-zero codeword is transmitted, the minimum distance of a linear code is equal to the minimum error impulse strength A_i over all the codeword bits $i = 1, \dots, n$ which is able to make the iterative decoder diverge from the detected all-zero vector. A drawback of this algorithm for LDPCs is that it could converge toward a wrong minimum distance because of the sub-optimality of the iterative decoder and presence of decoding cycles.

In what follows, we shall briefly review the algorithm proposed in [22] with the modifications suited to what is needed in this paper. Unlike the EI technique whereby one can only obtain information about the minimum distance of the code, the proposed algorithm evaluates the minimum distance by enumerating the codewords, along with their multiplicities of the input error events to which the sum-product decoder for LDPCs converge when perturbed by an error pattern constituted by at most two EIs located in two different codeword positions. The idea is to perturb the all-zero transmitted codeword with a noise pattern able to make the iterative decoder diverge from the all-zero decoded word toward a codeword \hat{c} that with high probability, would be the minimum distance codeword (i.e., the codeword with the smallest Hamming distance from the all-zero codeword). Then, knowing the strength and position i (with $i = 1, \dots, n$) where the impulse is applied in the span of the codeword that makes the decoder diverge from the all-zero codeword, in the proposed algorithm we apply a second impulse spanning all the codeword bit positions j ($\forall i \neq j$ and $j = 1, \dots, n$) in order to list all the detected codewords close to \hat{c} and different from the all-zero codeword.

We consider transmission of an i.i.d. source bit sequence of length k , encoded with a LDPC of size (k, n) , rate $R_o = k/n$, and with BPSK-modulation transmitted over an AWGN channel. In this way, the i -th received sample y_i at the output of the matched filter at the receiver is $y_i = (2c_i - 1) + n_i$, whereby c_i is the i -th transmitted codeword bit, and n_i is Gaussian noise with variance $\sigma_n^2 = \frac{1}{2R_o E_b / N_o}$.

The algorithm proposed here for estimation of the minimum distance of a generic LDPC code specified by its parity-check matrix H is as follows:

- 1) Assume that the minimum distance of the LDPC is in the range $[d_l, d_u]$, where d_l and d_u are two positive integers.

- 2) Set $A_m = d_u + \frac{1}{2}$, the maximum strength of one EI.
- 3) Consider the i -th bit node on which an EI has to be applied:

- a) set $A = d_l - \frac{1}{2}$;
- b) set flag=true;
- c) while ((flag is true) and $(A \leq A_m - 1)$)
 - $A = A + 1$ (grow the impulse strength one unit at a time until the LDPC decoder fails to decode the all-zero vector);
 - set y_j to -1 , $\forall j = 1, \dots, n$ (all-zero transmitted codeword);
 - set an impulse of strength A at the i -th bit node, i.e., $y_i = y_i + A$;
 - each bit node v_i is assigned an a-posteriori Log-Likelihood Ratio (LLR) evaluated as $L_{v,i} = \frac{2}{\sigma_n^2} y_i$;
 - for any iteration of the LDPC decoder from 1 to a maximum number of iterations N_{it} perform the following tasks:
If the Hamming weight $d_m^i = w_H(\hat{c}^i)$ of the codeword \hat{c}^i obtained by the decoder is different from zero and \hat{c}^i has not been yet encountered during the search, then store d_m^i and update the multiplicities of the codewords with Hamming weights d_m^i ;
 - if the decoded codeword \hat{c} is different from the all-zero vector then set the flag to false;
- d) end of while;
- e) For $j = 1$ to n , and $j \neq i$ (apply a second EI at position j)
 - set y_t to -1 , $\forall t = 1, \dots, n$ (all-zero transmitted codeword);
 - set an impulse of strength A at the i -th bit node, i.e., $y_i = y_i + A$;
 - set an impulse of strength A_m at the j -th bit node, i.e., $y_j = y_j + A_m$;
 - for any iteration of the LDPC decoder from 1 to a maximum number of iterations N_{it} perform the following tasks:
If the Hamming weight $d_m^{i,j} = w_H(\hat{c}^{i,j})$ of the codeword $\hat{c}^{i,j}$ obtained by the decoder is different from zero and $\hat{c}^{i,j}$ has not yet been encountered during the search, then store $d_m^{i,j}$, update the multiplicities of the codewords with Hamming weights $d_m^{i,j}$;
- f) End of For $j = 1$ to n

Some considerations are in order. The algorithm above is used on a randomly designed LDPC one bit node at the time. It allows one to obtain a set of codeword weights along with the respective multiplicities due to EIs located in the positions i and j (if any) in the span of the codeword length.

In the LDPC optimization we have conducted, the algorithm outputs a cost function resembling the Frame Error Rate (FER)

TABLE I
PARAMETERS OF THE LDPCs USED FOR SIMULATION.

(k, n)	(252, 504) L_1	(504, 1008) L_2	(252, 504) L_3	(504, 1008) L_4
d_v	3	3	3	3
d_c	6	6	6	6
C_4	0	0	0	0
C_6	1	0	0	0
C_8	1250	509	474	10
N_{it}	80	80	80	80

upper-bound:

$$F = \sum_{d=d_{min}}^{d_{max}} \mu_d e^{-R_c \frac{E_b}{N_0} d} \quad (7)$$

whereby μ_d is the multiplicity of all the codewords with Hamming weight d provided by the algorithm during the i -th iteration. In case no low-weight codeword distances are found, the algorithm generates $d = \infty$. The latter is used to signify the fact that the LDPC decoder, when perturbed by an EI in the generic bit node position i , corrects this error pattern providing the all-zeros codeword. Another way to look at this algorithm is to consider it as a way of identifying weak bit nodes in the code, i.e., the ones for which the application of an EI makes the decoder converge toward a codeword different from the all-zero codeword. Once the weak bit-nodes are identified, the edges at these weak locations are perturbed randomly while maintaining the node degrees. During perturbation, the associated set of cost functions based on (7) are recomputed and the configuration with least cost is selected.

IV. SIMULATION RESULTS

In this section, we report on some of these results and comparisons to other constructions reported in the literature.

Using the notation:

$$\lambda(x) = \sum_{i=1}^{d_{vmax}} \lambda_i x^{i-1}, \quad \rho(x) = \sum_{i=1}^{d_{cmax}} \rho_i x^{i-1} \quad (8)$$

where, λ_i is the percentage of bit nodes of degree i , and ρ_i is the percentage of check nodes of degree i , the degree distributions for our designed LDPC codes labelled L_1, L_2, L_3, L_4 in Table (I) are as follows:

$$\begin{aligned} L_1: \quad \lambda(x) &= 0.0019 + 0.498x + 0.496x^3 + 0.0039x^4, \\ \rho(x) &= 0.0079x^4 + 0.98x^5 + 0.011x^6; \\ L_2: \quad \lambda(x) &= 0.001 + 0.499x + 0.5x^3, \\ \rho(x) &= 0.0019x^4 + 0.9981x^5; \\ L_3: \quad \lambda(x) &= x^2, \quad \rho(x) = x^5; \\ L_4: \quad \lambda(x) &= x^2, \quad \rho(x) = x^5. \end{aligned}$$

LDPCs labelled L_3 and L_4 are regular LDPCs, while LDPCs labelled L_1, L_2 are considered as systematic (n, k) codes. Each codeword \mathbf{c} is composed of a systematic part \mathbf{u} , and a parity part \mathbf{p}_u forming $\mathbf{c} = [\mathbf{u}, \mathbf{p}_u]$. With this setup and given the matrix $H^{n-k, n}$ of the LDPC code, it is possible to

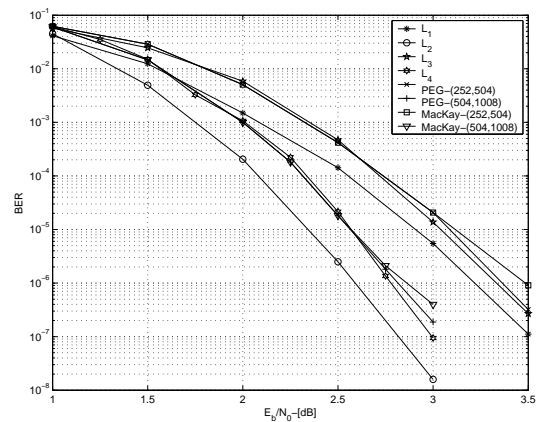


Fig. 2. BER performance of codes L_1, L_2, L_3 whose details are shown in Table (I).

decompose $H^{n-k, n}$ as $H^{n-k, n} = (H^u, H^{p_u})$, where H^u is an $(n-k) \times (k)$ matrix specifying the source bits participating in each check equation, and H^{p_u} is a $(n-k) \times (n-k)$ matrix of the form:

$$H^{p_u} = \begin{pmatrix} 1 & 0 & \dots & 0 & 0 \\ 1 & 1 & 0 & \dots & 0 \\ \dots & \dots & \dots & \dots & \dots \\ 0 & \dots & 0 & 1 & 1 \end{pmatrix}. \quad (9)$$

These LDPC codes have been designed in two steps. In the first step we designed a random bipartite graph with the algorithm proposed in section II whose objective is to insert one edge at the time by choosing the edge positions in such a way as to minimize the cost function in (6) evaluated with $l_{max} = 8$. In the second step we optimized the randomly constructed LDPCs by applying the algorithm proposed in section III. In particular, for any edge at any bit node, we evaluated a new candidate position in the same column in such a way as to minimize the cost function in (7). Between potential edge positions yielding the same value of the cost function in (7), we have chosen the one minimizing our first cost function on the cycle distribution in (6).

For comparison purposes, the LDPCs whose performance are shown in Figs. 3 and 4 are respectively, the Ramanujan LDPC with parameters $q = 13, p = 5, d_v = 3, d_c = 6$ and block length $n = 2184$ [23], and the Margulis code with parameters $p = 11$, girth 8 and block length $n = 2640$. As pointed out in [23], the Ramanujan $q = 13, p = 5$ code is useless as it is evident from the BER/FER performance shown in Fig. 3 since the error-floor is heavily affected by codewords with weight 14 which feature prominently in the BER/FER performance. The Margulis code with block length $n = 2640$ on the contrary, is a good algebraic code for FER values higher than $5 \cdot 10^{-6} \div 10^{-5}$. Below this FER threshold, this code has performance affected by near-codewords instead of low-weight codewords, leading to the observed error-floor.

We optimized both algebraic codes via edge perturbation by repositioning every edge in any bit node of the respective parity check matrices, by choosing a new position in such a

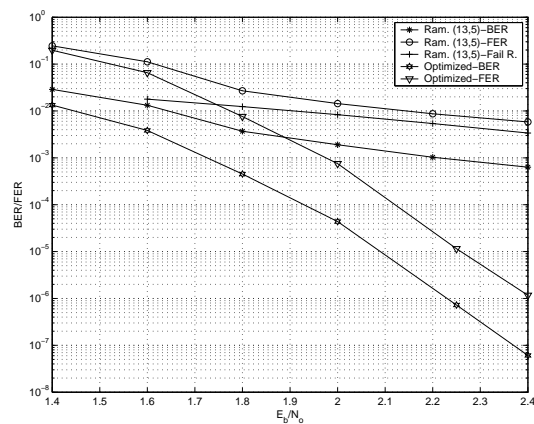
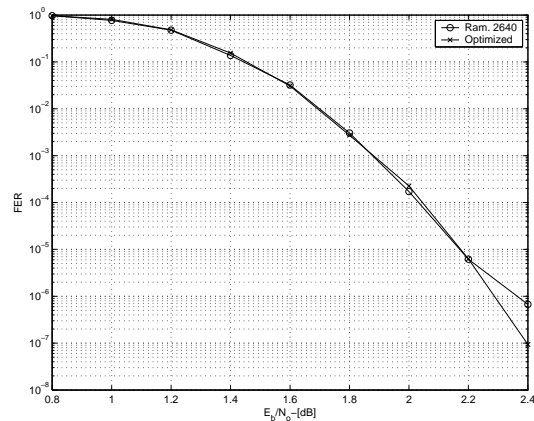


Fig. 3. Performance of the optimized Ramanujan (13,5) LDPC code.


 Fig. 4. Performance of the optimized Margulis 2640, $p = 11$ LDPC code.

way as to minimize the cost function in (7). Between potential edge positions yielding the same value of the cost function in (7), we have chosen the one minimizing our first cost function on the cycle distribution in (6).

V. CONCLUSIONS

In this paper we have presented a two phase design process for LDPC codes with the aim of satisfying several requirements simultaneously: 1) constructing LDPCs with quasi-random structure that have proven to perform well with sub-optimum iterative soft decoding algorithms, 2) constructing tanner graphs for the code with large girth and in general with desirable cycle distribution, and 3) optimizing the designed codes in the error-floor region via edge perturbation coupled by an efficient minimum distance estimation algorithm.

REFERENCES

- [1] R.G. Gallager, "Low-density parity-check codes", *IRE Transactions on Information Theory*, pp. 21 - 28, Jan. 1962.
- [2] R.M. Tanner, "A recursive approach to low complexity codes", *IEEE Transactions on Information Theory*, vol. 27, pp. 533-547, Sept. 1981.
- [3] D.J.C. Mackay, "Good error-correcting codes based on very sparse matrices", *IEEE Transactions on Information Theory*, vol. 45, no. 2, pp. 399 - 431, March 1999.

- [4] T.J. Richardson, M.A. Shokrollahi, and R.L. Urbanke, "Design of capacity-approaching irregular low-density parity-check codes", *IEEE Transactions on Information Theory*, vol. 47, no. 2, pp. 619 - 637, Feb. 2001.
- [5] B. Vasic and O. Milenkovic, "Combinatorial constructions of low-density parity-check codes for iterative decoding," *IEEE Transactions on Information Theory*, vol. 50, no. 6, pp. 1156- 1176, June 2004.
- [6] S.J. Johnson and S.R. Weller, "Construction of low-density parity-check codes from Kirkman triple systems", *IEEE Global Telecommunication Conference*, vol. 2, pp. 970 - 974, Nov. 2001.
- [7] J. Rosenthal and P.O. Vontobel, "Constructions of LDPC codes using Ramanujan graphs and ideas from Margulis", *Proc. of 38th Allerton Conference on Communication, Control and Computing*, pp. 248 - 257, October 2000.
- [8] G. A. Margulis, "Explicit constructions of graphs without short cycles and low-density codes", *Combinatorica*, vol. 2, pp. 71-78, 1982.
- [9] R. Echard and Shih-Chun Chang, "The π -rotation low-density parity check codes", *IEEE Global Telecommunications Conference*, vol. 2, pp.980 - 984, Nov. 2001.
- [10] A. Prabhakar and K. Narayanan, "Pseudorandom construction of low-density parity-check codes using linear congruential sequences", *IEEE Transactions on Communications*, vol. 50, no. 9, pp. 1389-1396, Sep. 2002.
- [11] B. Ammar, B. Honary, Y. Kou, J. Xu, and S. Lin, "Construction of low-density parity-check codes based on balanced incomplete block designs", *IEEE Transactions on Information Theory*, vol. 50, no. 6, pp. 1257 - 1268, June 2004.
- [12] L. Chen, J. Xu, I. Djurdjevic, and S. Lin, "Near-Shannon-limit quasi-cyclic low-density parity-check codes", *IEEE Transactions on Communications*, vol. 52, no. 7, pp. 1038 - 1042, July 2004.
- [13] I. Djurdjevic, S. Lin, and K. Abdel-Ghaffar, "Graph-theoretic construction of low-density parity-check codes", *Communications Letters, IEEE*, vol. 7, no. 4, pp. 171 - 173, April 2003.
- [14] Hu. Xiao-Yu, E. Eleftheriou, and D.M. Arnold, "Progressive edge-growth Tanner graphs", *IEEE Global Telecommunications Conference*, vol. 2, pp. 995 - 1001, Nov. 2001.
- [15] M.G. Luby, M. Mitzenmacher, M.A. Shokrollahi, and D.A. Spielman, "Improved low-density parity-check codes using irregular graphs", *IEEE Transactions on Information Theory*, vol.47, no. 2, pp. 585 - 598, Feb 2001.
- [16] S.A.M. Baghdady, Y.A. Fahmy, and M.M.S. El-Soudani, "An incremental redundancy short length LDPC codes based on random construction techniques"; *IEEE 17th International Conference on Telecommunications (ICT)* pp. 18-22, 2010.
- [17] S. Shebl, N. El-Fishawy, A.A. Elazm, and F.A. El-Samie, "A random construction of LDPC codes using a sub-optimal search algorithm"; *National Radio Science Conference*, pp. 1-10, 2009.
- [18] C. Liang, W. Songyan, Y. Shijun, W. Ziyu, Z. Wenjun, and G. Yunfeng, "Semi-random Construction of Rate-Compatible Low-Density Parity-Check Codes"; *Proceedings of the Third International Conference on Wireless and Mobile Communications*, March 2007.
- [19] Z. Huang, L. Shen, and Z. Ye, "A new random construction for low-density parity-check codes"; *Proceedings of International Conference on Communications, Circuits and Systems*, vol. 1, pp. 139-142, 2005.
- [20] L. Dengsheng, L. Qiang, and L. Shaoqian, "Semi-random construction of quasi-cyclic LDPC codes"; *Proceedings of International Conference on Communications, Circuits and Systems*, vol. 1, pp. 9-13, 2005.
- [21] P. Oswald and A. Shokrollahi, "Capacity-achieving sequences for the erasure channel", *IEEE Transactions on Information Theory*, vol. 48, no. 12, pp. 3017 - 3028, Dec. 2002.
- [22] F. Daneshgaran, M. Laddomada, and M. Mondin, "An algorithm for the computation of the minimum distance of LDPC codes", *ETT-European Transactions on Telecommunications*, vol. 17, no. 1, pp. 57-62, Jan. 2006.
- [23] D.J.C. MacKay and M.S. Postol, "Weakness of Margulis and Ramanujan-Margulis low-density parity-check codes", *Electronic Notes in Theoretical Computer Science*, vol. 74, Pub. by Elsevier Science B. V., 2003.
- [24] T. Richardson, "Error floors of LDPC codes", *In Proc. of 41st Annual Allerton Conf. on Comm., Control, and Comp.*, October 2003.
- [25] C. Berrou, S. Vaton, M. Jézéquel, and C. Douillard, "Computing the minimum distance of linear codes by the error impulse method"; *IEEE Globecom 2002*, pp. 1017-1020, Taipei, Taiwan, 2002.

End-To-End Communication Model based on DVB-S2's Low-Density Parity-Check Coding

Iva Bacic, Josko Kresic, Kresimir Malaric

Department of Wireless Communication

University of Zagreb, Faculty of Electrical Engineering and Computing
Zagreb, Croatia

iva.bacic@fer.hr, josko.kresic@fer.hr, kresimir.malaric@fer.hr

Abstract—The low-density parity-check codes are one of the most promising coding schemes that allow high throughput, high data rate and good error correction like in the DVB-S2 standard that was the first standard in satellite communication using this coding. The paper presents the concept and bases of low-density parity-check codes and the design strategies used. A simulation model of the end-to-end communication based on low-density parity-check coding is described. The model was designed by using the National Instruments' LabVIEW. Simulation results gained with this model show that our model is corresponding to the DVB-S2 standard.

Keywords—DVB-S2, Digital Television, Low-Density Parity-Check Codes, SPA algorithm, Simulation, LabVIEW

I. INTRODUCTION

Low-density parity-check codes (LDPC) are error correction codes and a class of linear block codes that have a very high throughput and very good coding performance [1].

Originally, the low-density parity-check codes were proposed by Robert Gallager in his thesis in 1962 [2], but this work received no attention because of the encoding and decoding complexity at that time. They were "rediscovered" with the appearance of turbo codes in the 90's by MacKay [3]. Recently, LDPC codes are able to compete in performance with turbo codes and they show the advantage of allowing a finer adjustment of trade-off between performance and decoding complexity [4, 5]. They are suitable for any digital environment where high data rate and good error correction is important [6]. Furthermore, they are suitable for implementations that use advantage of parallelism and take effort of the fact that LDPC codes for large block length perform near the Shannon limit of a channel [7, 8, 9]. The DVB-S2 standard is the first standard using low density parity check codes as its forward error correction.

A wide array of other communication application uses LDPC codes such as the 10 Gigabit Ethernet, the broadband wireless access or the deep-space communication [10, 11]. Adoption of LDPC codes is one of the keys to achieve lower transmission power and more reliable communication [11]. In this article, we detail a simulation model of a low-density parity-check channel coding system developed via use of National Instruments' LabVIEW [12].

The low-density parity-check codes and their basic concept are discussed in Section II. Section III describes the LDPC based end-to-end communication model. The performance and results are shown in Section IV. Section V concludes the article.

II. THEORETICAL BACKGROUND

Low-density parity-check codes are binary linear codes where a block of data is encoded into a codeword. They are obtained from sparse bipartite graphs [13], the so called Tanner graph [14] which consists of two types of nodes: of n variable or message nodes and of r check nodes [15]. Out of these graphs can be derived a linear code of block length n and dimension of at least $n-r$. Such a graph representation has an analogue matrix representation. The LDPC codes are specified with their sparse parity-check matrix \mathbf{H} of the size $M \times N$. Two numbers define such a matrix: ω_r is the number of ones in every row and ω_c is the number of ones in every column. If $\omega_c \ll N$ and $\omega_r \ll M$ then such a matrix is called a low-density (sparse) and is usually very large.

When the check node j from the Tanner graph is connected to the variable node i the entry (i, j) of \mathbf{H} is 1 with $j \in \{0, \dots, N-1\}$ and $i \in \{0, \dots, M-1\}$. That means that the corresponding codeword bit takes part in the corresponding parity-check equation [5]. When there is no connection then $\mathbf{H}(i, j) = 0$ [15].

A) Decoding

The decoding algorithm named the sum-product algorithm (SPA) was already proposed by Gallager in 1962 [2, 3]. There are two types of this algorithm: the hard and the soft decision. The hard decision decoding is mainly introduced for educational purpose but since the soft decision decoding provides better decoding results [1] it will be focused on. Soft-decision decoding of LDPC codes is based on concept of belief propagation. It is an iterative process where the information of the received bits is refined iteration by iteration [16]. First, variable node c_j sends its message q_{ij} to the f_j -check node. q_{ij} contains the amount of belief the message bit y_i is a zero and the amount of the belief, P_i that y_i is a one:

$$R = \frac{n}{m}, \tag{9}$$

as well as the number of ones in one column and the maximal number of iterations performed by the encoder and decoder. The program uses this information to calculate the matrix H for the encoding and decoding process. The code rates, according to the standard are [2]: 1/4, 1/3, 2/5, 1/2, 3/5, 2/3, 3/4, 4/5, 5/6, 8/9 and 9/10.

The DVB-S2 standard specifies two word lengths for the LDPC: 16200 or 64800 bits. Since the longer word length is used for sending information through channel, only the word length of 64800 bits will be considered in this paper. It has to be denoted that the coded message, delivered from the encoder is always the same length, but the number of information bits is not constant and depends on the code rate.

For decoding the received messages different algorithms may be used. In our work the Sum-product algorithm decodes the message. It exchanges the soft-information iteratively between variable and check nodes. Updating the nodes can be done with a canonical, two-phased scheduling: In the first phase all variable nodes are updated and in the second phase all check nodes. The processing of individual nodes within one phase is independent and can thus be parallelized. The exchanged messages are assumed to be log likelihood ratios (LLR). Each variable node calculates an update of message according to equations (1)-(5).

Next input parameter for the program is the modulation parameter M for the M-PSK modulation. According to the standard [2], the PSK modulates the message onto the carrier although other modulation types, like the amplitude modulation may be used, too.

For filtering the root-raised cosine filter is used. The default value of the roll-off factor of this filter is set to $\alpha=0.35$ but may be changed to values according to [2].

The user also defines the symbol rate for sending the message.

In our version of the model, there was no use for the BCH (Bose-Chaudhuri-Hocquenghem) encoder. BCH is not very good for error protection and correction itself, but it performs the erasure of error floor after the LDPC encoder encoded the message.

IV. RESULTS

As the result, the BER versus E_b/N_0 curve is plotted in order to show the system performance, analyse the communication quality itself and the parameter influence on communication quality. First, the performance of LDPC coding is shown. The coding gain for the no coded and the LDPC coded message is calculated. The influence of the modulation parameter M is shown and the third simulation result is made in order to show how the code rate affects the communication quality.

In Fig. 2, the BER versus E_b/N_0 graph for the LDPC coded and no coded BPSK is shown. Since communication with higher modulation parameter M gained same conclusion as with the BPSK, this modulation type, being the simplest one was chosen to show system performance. Other relevant system parameters for the simulation are given in Table 1. Simulation result shows that, as expected, coding improves the performance of the communication system. Low-density parity-check coding is an error correction code that ensures not only error protection of the message but also error

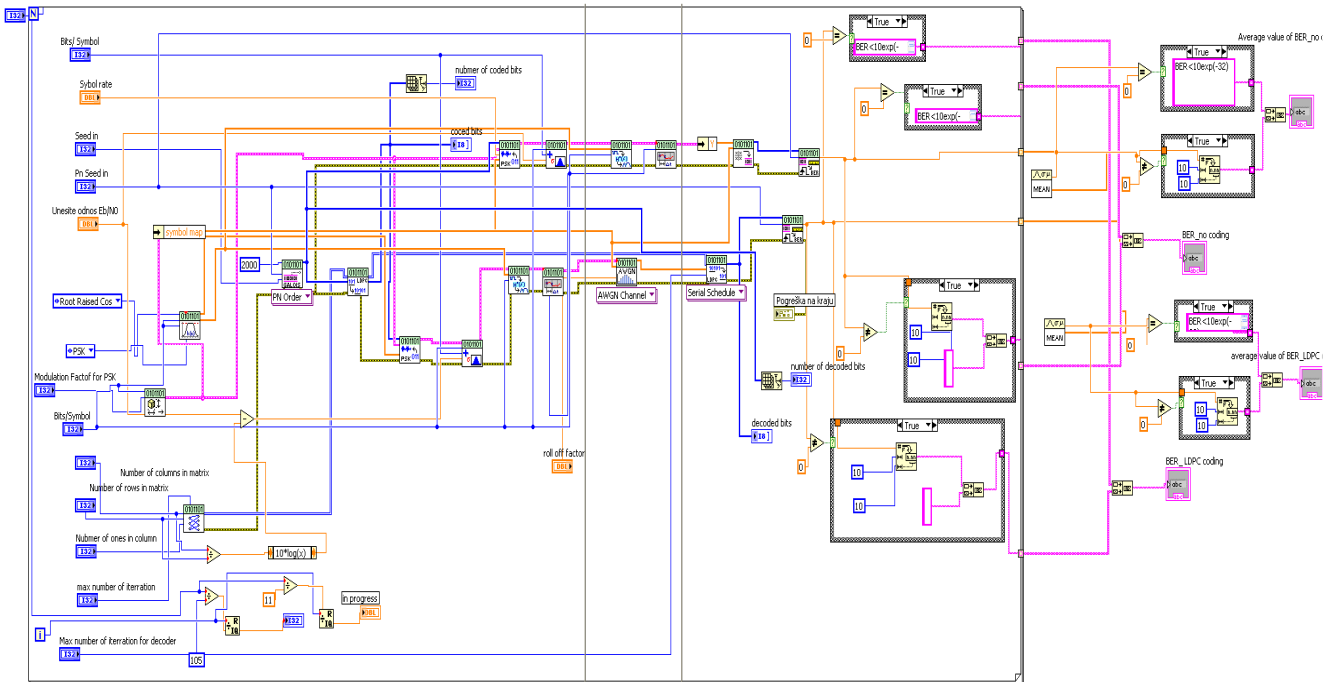


Figure 1. Block diagram of our end-to-end communication model based on DVB-S2's low-density parity-check coding

TABLE I. SYSTEM PARAMETERS FOR SIMULATION 1

System parameters	Modulation type:	BPSK
	Filter's roll-off factor:	$\alpha = 0.35$
	DVB-S2 frame:	64800 bits
	DVB-S2 pilots:	no
	LDPC code rate:	1/2
	Bits per Symbol:	1
	Symbol rate:	30.00000000 Mbaud
Parity-check matrix parameters	Number of iteration:	100
	Number of rows:	200
	Number of coloums:	400
	Number of 1s in row:	5

correction. This is why the coded BER curve is shifted to the left of the BER curve of the no coded message meaning that the transmission is more accurate and better communication quality is ensured. The coding gain for reaching $BER=10^{-6}$ is calculated and amounts coding_gain= 7.4 dB.

The influence of parameter M is tested and communication quality is shown in Fig. 3. Therefore, the QPSK, 8-PSK and 16-PSK modulated, LDPC coded and root raised cosine filtered (with the roll off factor $\alpha=0.35$) message is generated. The code rate $R=3/4$ is achieved with matrix parameters as follows: number of rows in parity-check matrix was 300 and number of columns was 400. There were 5 ones in every column. The maximal number of iteration for the coder and decoder was set to 100. Other system parameters are given in Table 1.

Simulation results show that the BPSK gained the best communication quality. The BER curves for the QPSK and

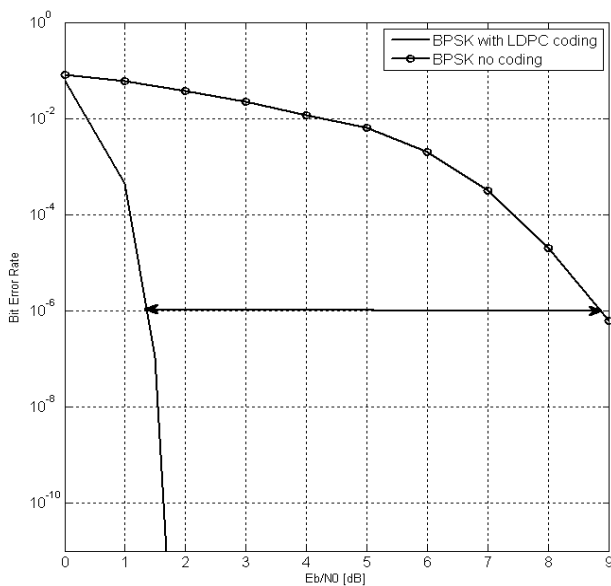


Figure 2. BER versus E_b / N_0 graph for the coded and the no coded message

TABLE II. CODE RATE DEFINED WITH NUMBER OD ROWS AND COLUMNS OF THE PARITY-CHECK MATRIX

Code rate	1/2	2/3	3/4	5/6	7/8
Number of rows	200	200	300	250	350
Number of columns	400	300	400	300	400

the 8-PSK are shifted to the right of QPSK's bit error rate versus E_b / N_0 graph showing that by lowering the modulation factor M , the communication becomes accurate and safer. For the same noise level in system the probability of error during communication is lower.

Figure 4 shows the influence of the code rate on the bit error rate. For modulating the signal onto the carrier the phase shift keying modulation was used with its modulation factor set to $M = 2$. Filtering was done with the root raised cosine filter's roll off factor set to $\alpha=0.35$. The parity-check matrix had 5 ones in every column and its size was changed in order to gain different coding rates according to Table 2. Other parameters were as it is given in Table 1.

Simulation shows that by lowering the code rate, communication becomes much safer. As the code rate reduces, more parity bits are used to protect one single bit. Therefore, a lower code rate ensures better communication quality but provides lower bit rate. With a lower code rate more bits have to be sent for transmitting the same message then with a higher value of the code rate and this takes more time. The lowest bit error rate, with a constant level of noise in system is achieved with code rate set to $R=1/2$. The code rate is defined by the size of the parity-check matrix.

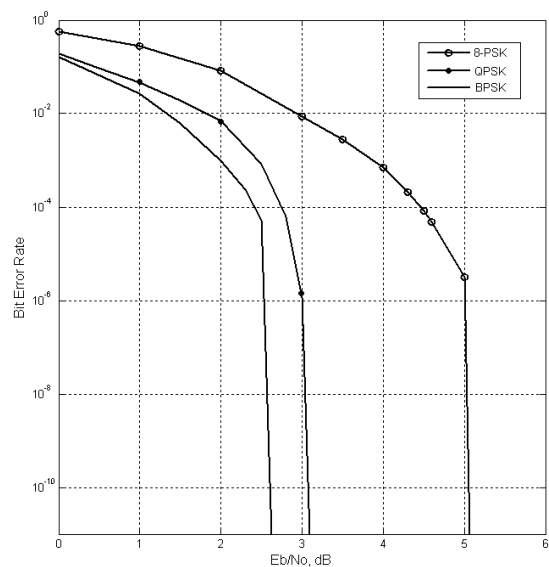


Figure 3. BER versus E_b / N_0 graph for different modulation factors of the phase shift keying modulation message

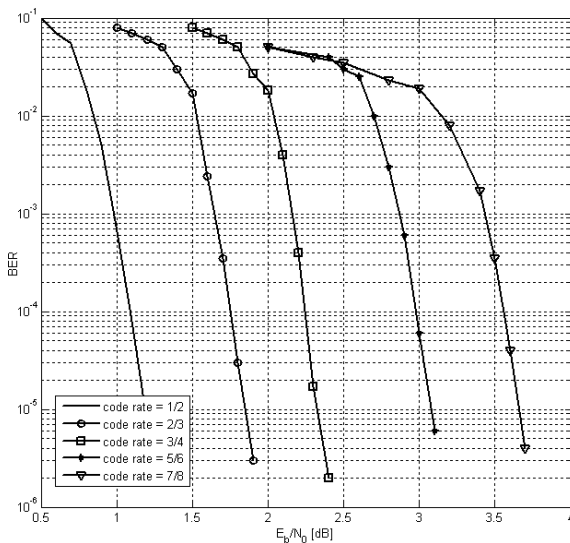


Figure 4. BER versus E_b / N_0 graph for different code rates

The number of rows and columns in the parity-check matrix directly defines the value of bit error rate of the system.

V. CONCLUSION

In this paper, after a basic theoretical background on low-density parity-check codes, our end-to-end simulation model based on DVB-S2's LDPC coding is presented. For modeling the National Instruments' LabVIEW and its Modulation Toolkit were used. Encoding is based on forming the parity-check matrix. At the receiver's side, decoding is done. Decoding of received message is done via the sum-product algorithm and soft decision decoding.

Simulations were made and the influences of different parameters were tested. Results show that low-density parity-check codes improve the communication quality. Lowering the modulation factor M gained a lower bit error rate in system, as well as reducing the code rate. Since, with lower code rate more bits have to be sent for transmitting the same message the transmitting takes a higher bit rate.

In future work, the model will be augmented with an outer BCH encoder in order to improve the existing model and move it closer to the DVB-S2 standard.

REFERENCES

- [1] B. M. J. Leiner, "LDPC Codes – a brief Tutorial", Stud. ID.: 53418L, April 2005.
- [2] R. Gallager, "Low-density parity-check codes", IRE Transaction on Information Theory, vol. 8, Jan. 1962, pp. 21-28.
- [3] D. MacKay, "Good error-correction codes based on very sparse matrices," IEEE Trans. on Information Theory, vol. 45, pp. 399-437, March 1999.
- [4] T. J. Richardson and R. Urbanke, "The capacity of low-density parity-check codes under message passing decoding," IEEE Trans. on Information Theory, vol. 47, pp. 599-618, February 2001.
- [5] T. F. Pegoraro, F. A. L. Gomes, R. R. Lopes, R. Gallo, J. S. G. Panaro, M. C. Paiva, F. A. Oliveira, and F. Lumertz, "Design, Simulation and Hardware Implementation of a Digital Television System: LDPC channel coding," Proc. IEEE Symp. Spread Spectrum Techniques and Applications (ISSSTA 06), Aug. 2006, pp. 203-207, doi: 10.1109/ISSSTA.2006.311763.
- [6] M. Kakooti and J. R. Cavallaro, "Semi-Parallel Reconfigure Architecture for Real-Time LDPC Coding," Proc. International Conference, Information technology: Coding and computing (ITCC 04), vol.1, pp. 579-585, April 2004.
- [7] European telecommunications Standards Institute (ETSI), "Digital Video Broadcasting (DVB) Second generation framing structure for broadband satellite applications, EN 302 307 v1.1.1", www.dvb.org
- [8] A. Morello and V. Mignone, "DVB-S2: the Second Generation Standard for Satellite Broad-Band services," Proc. of the IEEE, Jan. 2006, vol. 94, pp. 210-227, doi: 10.1109/JPROC.2005.861013.
- [9] C. E. Shannon, "A Mathematical Theory of Communication", Reprinted with corrections from The Bell System technical Journal , vol. 27, Oct. 1948, pp. 379-423, 623-656, doi: 10.1.1.161.4366.
- [10] K. S. Andrews, D. Divsalar, D. Dolinar, J. Hamkins, C. R. Jones and F. Pollar, "The development of turbo and LDPC codes for deep-space applications," Proc. of the IEEE, Nov. 2007, vol. 95, pp. 2142-2156, doi: 10.1109/JPROC.2007.905132.
- [11] Z. Zhang, V. Anatharam, M. J. Wainwright and B. Nikolic, "An efficient 10 GBASE-T Ethernet LDPC Decoder Design with Low Error Floors, " IEEE Journal of Solid-State Circuits, vol. 45, April 2010, pp. 843-855, doi: 10.1109/JSSC.2010.2042255.
- [12] G. W. Johnson and R. Jennings, LabVIEW Graphical Programming. The McGraw-Hill Companies, New York, 2006.
- [13] A. Shokrollahi, "LDPC Codes: An Introduction", Digital Foundation, Inc. Ferment, April 2003, doi:10.1.1.110-1008.
- [14] R. Tanner, "A Recursive Approach to Low complexity Codes", IEEE Trans. Informqtion Theory, vol. 27, pp. 533-547, September 1981.
- [15] S. Muller, M. Scherger, M. Kabutz, M. Alles, F. Kienle and N. Wehn, "A novel LDPC Decoder for DVB-S2 IP," IEEE Conference and Exhibition Design, Automation and Tesi in Europe, April 2009, pp. 1308-13013, print ISBN: 978-1-4244-3781-8.
- [16] T. Jokela, "Performance Analysis of Substituting DVB-S2 LDPC Code for DVB-T Error Control Coding System," Proc. IEEE Symp. Braodband Multimedia Systems and Broadcasting (ISBMSB 08), April 2008, pp. 1-5, doi: 10.1109/ISBMSB.2008.4536677.
- [17] S. G. Harihora, M. G. Chandra, B. S. Adiga, D. N. Pramod and P. Balamurilidhar, "A Proposal for the LDPC Decoder Architecture for DVB-S2," Proc. National conference on Communication, India, Jan. 2006, pp. 284-288.
- [18] M. Yang, W. Ryan and Y. Li, "Design of efficiently encodable moderate-length high-rate irregular LDPC codes," IEEE Trans. Communication, vol. 52, pp. 564-571, April 2004, doi: 10.1109/TCOMM.2004.826367.
- [19] M. Eroz, F. W. Sun and L. N. Lee, "DVB-S2 Low Density Parity Check Codes with Near Shannon Limit Performance," International Journal of Satellite Communication and Networking, vol. 22, June 2004, pp. 269-279, doi: 10.1002/sat.787.
- [20] I. Bacic, K. Malaric and Z. Petrunic, "A LDPC Code/Decode Channel Coding Model Based on Sum-Product Algorithm Realization via LabVIEW," Proc. International Conference on Applied Electromagnetics and Communications (ICECom 10), KoREMA, Sept. 2010, ISBN: 987-953-6037-59-9.
- [21] W. J. Gilbert and W. K. Nicholson, Modern Algebra with Applications, 1st ed., New Jersey: John Wiley, 2004.

Identification of Abnormal System Noise Temperature Patterns in Deep Space Network Antennas Using Neural Network Trained Fuzzy Logic

Thomas Lu, Timothy Pham and Jason Liao

Jet Propulsion Laboratory
California Institute of Technology
4800 Oak Grove Dr.
Pasadena, CA 91109, USA

E-mails: Thomas.Lu@jpl.nasa.gov, Timothy.Pham@jpl.nasa.gov, Jason.Liao@jpl.nasa.gov

Abstract – This paper presents the development of a fuzzy logic function trained by an artificial neural network to classify the system noise temperature (SNT) of antennas in the NASA Deep Space Network (DSN). The SNT data were classified into normal, marginal, and abnormal classes. The irregular SNT pattern was further correlated with link margin and weather data. A reasonably good correlation is detected among high SNT, low link margin and the effect of bad weather; however we also saw some unexpected non-correlations which merit further study in the future.

Keywords - Deep Space Network; Neural network training; Fuzzy logic; Pattern identification; System noise temperature; Link margin.

I. INTRODUCTION

The communication between NASA space mission operations teams and their respective spacecrafts in outer space is accomplished via the Deep Space Network (DSN). To ensure proper operations in returning telemetry data to mission operations, sending commands to spacecraft and providing radiometric data for navigation purposes, the DSN equipment generates a large set of self-monitor data. These include key metrics of system performance such as antenna pointing, operating system noise temperature, receiver and decoder lock indications, received telemetry symbol signal-to-noise ratio, telemetry frame quality, etc. These data statistics are generated periodically, in the order of a few seconds, throughout the spacecraft tracking passes. With roughly 1500 tracking passes a month, there is a lot of monitored data to be evaluated.

The DSN recently developed the capability to automatically quantify key metrics through a set of automated performance dashboards, as reported in [1]. These dashboards enable a quick detection of passes with anomalous performance – compared to those that are nominal. One of the tools used to classify the performance of the passes is the fuzzy logic function described in this

paper. This function is trained by an artificial neural network to classify the system noise temperature (SNT).

The SNT reflects the amount of noise that existed in the communications system. Given that the signal comes from a far-away spacecraft at planetary distance, the received power is very weak. The ability to detect the signal is affected by the system noise temperature; the lower the noise, the better chance the system can detect the signal. Thus, there is a strong interest in monitoring and classifying the SNT.

The next section describes key features that are used to distinguish various classes of SNT profiles. Structure of the neural network model employed in the data classification and the recognition training process are presented in Section III. Section IV provides the results of the SNT classification, in terms of the impact to the link conditions (e.g., good, bad, marginal). Further correlation between SNT categories and the link margin of the communications channel with spacecraft is shown in Section V. Section VI further extends the correlation between the SNT and weather – one of the key factors impacting the link margin. The final section summarizes and discusses future direction of this effort.

II. SYSTEM NOISE TEMPERATURE FEATURES

Figure 1 shows a typical sample of SNT measurement for a given pass, in this case with Voyager spacecraft on day-of-year (DOY) 320/2007. Within the figure are plots of predicted SNT (labeled as 810-5, per reference of a JPL-internal document number that reflects such a model), observed SNT, and antenna pointing elevation. The antenna elevation is one of the parameters that affect the SNT. At low elevation, there are more atmospheric layers in the signal path; resulting in a higher noise temperature. The effect of elevation is built into the modeling of the predicted SNT. In this particular pass, the measured SNTs (Blue line) closely follow the predicted curve (Gray line, 810-5).

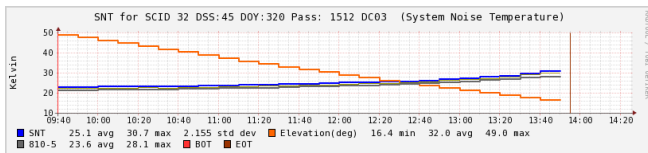
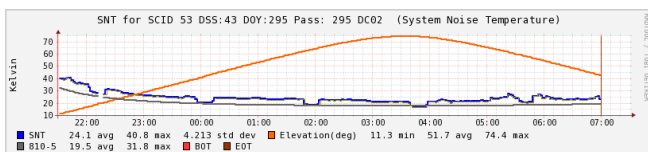
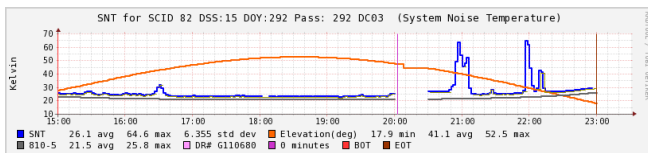


Figure 1: SNT observed and predicted measurement, DOY 320/2007.

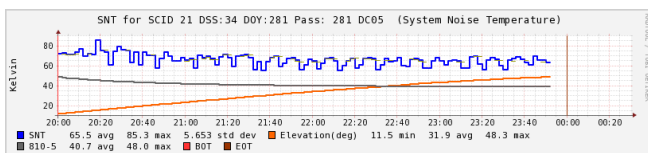
However, sometimes the measured SNT curve would deviate from the predicted performance slightly, as shown in Figure 2(a). At times, there could be very dramatic deviation, as shown in Figures 2(b) and (c). Some of these are known, such as the variation in Figure 2(b) was likely caused by weather conditions. Other variations such as the periodic structure in Figure 2(c) are not fully understood. Our goal is to use the pattern recognition tool described in this paper to find those irregular patterns and then study the causes in details.



(a)



(b)



(c)

Figure 2: Irregular SNT measurement data from various passes.

A simple threshold method may not be able to sufficiently characterize the SNT data since there could be sudden perturbations as shown in the right side of Figure 2(b). The SNT measurement follows the predicted model nicely between 15:00-20:00 GMT, but there are two big peaks around 21:00 and 22:00 GMT, likely caused by bad weather. A simple threshold or mean/standard-deviation method could have missed this event. A more intelligent signal processing method, such as neural network, may be able to detect the abnormal patterns of SNT.

In order to capture various irregular patterns of SNT data, we have designed a set of features of the SNT curves: mean values, standard deviations, peak numbers, peak-to-valley variations, and slope of the peaks. The SNT data for various passes are processed to extract the SNT curve feature vectors; each pass is represented by a feature vector. Each feature vector consists of six elements:

1) Average SNT Difference (from model):

$$\Delta SNT_{ave} = \frac{\sum (SNT_m - SNT_p)}{n} \quad (1)$$

where SNT_m is the measured SNT sequence of pass m with length n. SNT_p is the corresponding predicted values for that m pass.

2) Standard Deviation:

$$STD = \sqrt{\frac{\sum ((SNT_m - SNT_p) - \Delta SNT_{ave})^2}{n}} \quad (2)$$

3) Estimated 1-sigma higher bound of variation:

$$\Delta SNT_h = \Delta SNT_{ave} + STD; \quad (3)$$

4) Estimated 1-sigma lower bound of variation:

$$\Delta SNT_l = \Delta SNT_{ave} - STD; \quad (4)$$

5) SNT Peak Number:

$$K = \text{Number of peak and valley pairs}; \quad (5)$$

where Peak-to-Valley Difference $> STD$;

6) SNT Peak Slope:

$$\text{Slope} = \frac{\text{Max}(Peak_k - Valley_k)}{K}; \quad (6)$$

We need to define the criteria for the SNT irregularities. Since there is no known set rule, we choose the following definition based on observation and experience.

- 1) Averaged SNT is more than 10 K above the performance model, i.e., Averaged SNT Difference, $\Delta SNT_{ave} > 10K$;
- 2) Averaged SNT is more than 10 K below the performance model, i.e., Averaged SNT Difference, $\Delta SNT_{ave} < -10K$;
- 3) Peak to valley variation $> 20 K$;
- 4) Slope $> 5 K/\text{minute}$ or Slope $< -5K/\text{minute}$.

Since the criteria are not simple Boolean operations and that there may be a need for adding non-threshold criteria in later analysis, we were concerned that a simple threshold approach may not be suitable for classifying the SNT patterns. Therefore we decided to design a Fuzzy logic to classify the SNT patterns. A neural network is then used to train the fuzzy logic.

III. NEURAL NETWORK TRAINING

An artificial neural network is an adaptive computational model inspired by the study of biological neural networks [2]. It mimics human biological neural functions that learn by example. The neural net used in this system is a feed-forward back-propagation model, as illustrated in Figure 3. It is composed of separate layers of connected units called neurons. Every neuron of one layer is connected to every neuron of the next layer and each connection has an assigned weight value w . The output of a neuron y in the $(k+1)$ th layer is calculated by a weighted sum of the inputs, x , in the k th layer into that neuron [3]:

$$y_j^{k+1} = f\left(\sum_{i=1}^N w_{ij}^k x_i^k + b_j^k\right) \quad (7)$$

where f is a Sigmoid transfer function which maps the input-output relationship into a range [0, 1].

The feature vector serves as the initial input into the neurons of the first hidden layer. The output of neurons from one layer then feeds into the neurons of the next layer until the output layer returns a confidence value between [0, 1]. This architecture is known as feed-forward neural net.

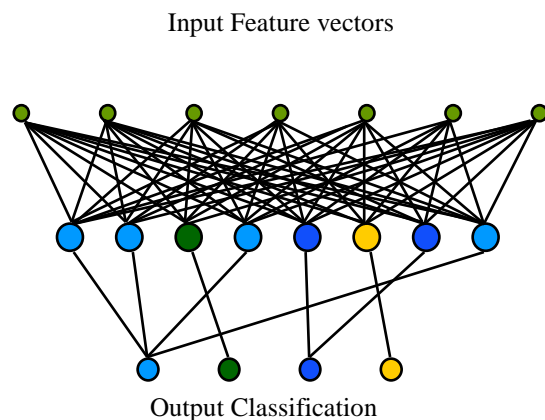


Figure 3: Multi-layer feed-forward neural network architecture.

The neural network classifies an input data to an output class, giving a confidence value between the probability from 0 – 100%. Thus a Fuzzy logic is formed between the input data and the output classes [4].

Figure 4 illustrates the neural network training process. A person with domain knowledge first picks a set of training SNT data. The expert must assign the SNT data (training inputs) into correct classes (target outputs). The feature vector is extracted from a set of SNT data, presented to the input neurons of the neural network; the neural network feed-forwards the signal and makes an attempt to classify the input to an output class; the output result is compared to the target output; the output error is

used to back-propagate through the network to tune the weights. The learning process is repeated many times until the output error of the neural network is less than a set value [5-7].

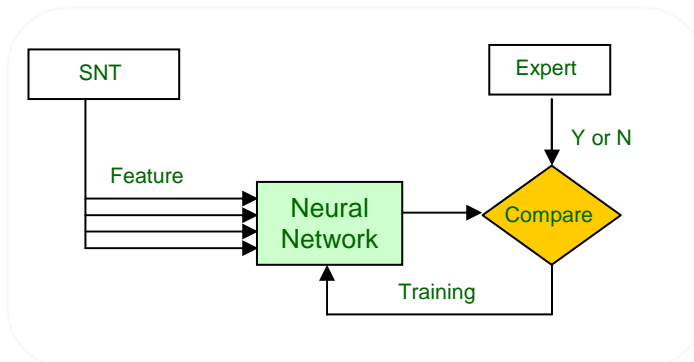


Figure 4: Illustration of neural network training process.

We used a set of SNT data from DOY 001-065 in 2007 as the training and testing data. There were a total of 1950 SNT data in the test set. Among them, there were 1329 (68.2%) valid SNT data to classify. The SNT data are classified into six categories based on observation of the patterns, as shown in Table I. Category 1 represents large SNT deviation with large peaks and slopes; Category 2 has large but smooth positive deviations; Category 3 has small deviations and small perturbations; Category 4 follows the predicted SNT consistently; Category 5 has small and smooth deviations; Category 6 has large and smooth negative deviations.

TABLE I. DEFINITION OF SNT CATEGORIES

SNT Category	Features
1	$\Delta SNT_{ave} > 10K$ or $\Delta SNT_{ave} < -10K$ or Slope $> 5K/min$ or Peak No > 5
2	$\Delta SNT_{ave} > 10K$, Slope $< 5K/min$, Peak No < 5
3	$\Delta SNT_{ave} < +/-10K$, STD $\leq 3K$, Slope $< 5K/min$, Peak No < 5
4	$\Delta SNT_{ave} \leq +/-5K$, STD $\leq 3K$, Slope $< 5K/min$, Peak No < 0
5	$\Delta SNT_{ave} \leq +/- 5K$, STD $\leq 3K$, ΔSNT_h and $\Delta SNT_l < +/-5K$, Slope $< 5K/min$, Peak No < 2
6	$\Delta SNT_{ave} < -10K$, STD $\leq 3K$, Slope $< 5K/min$, Peak No < 5

To form the training data, we randomly picked 39 samples for Category 1; 33 samples for Category 2; 61 samples for Category 3; 69 samples for Category 4; 35 samples for Category 5; and 26 samples for Category 6. The training samples are hand picked to represent varieties of feature differences in all six categories. We constructed a three-layer feed-forward neural network, each layer consists of six neurons: six input neurons for the six input

features; six output neurons for the six categories, and six hidden layer neurons are chosen to accommodate non-linear boundaries. The training data is fed into the neural net in the Matlab program. The neural net converged rather quickly; it took less than two minutes on a Windows-based computer with Intel dual-core running at 2GHz. After the training, the tool is ready for use to classify the SNT data.

IV. CLASSIFICATION OF SNT DATA

Table II shows the initial classification of the SNT data. The features were extracted based on eqs. 1-6. The six feature elements were fed into the neural network. When one or more of the six output neurons exceeded a preset threshold (nominally, 50%), the neural net would classify the input SNT as belonging to the output categories. An input could be classified in more than one category, as long as all possible likelihoods were detected. This is reflected in Table II where there is an overlap in the percentage of each category, relative to the input samples.

It is often difficult to have a clear cut set of the boundaries between categories; for example, it is hard to define a priori of the number of peaks or the peak slope value in each category. A Boolean classification approach would require such parameters be defined ahead of time. With neural net approach, it is not necessary to do so. We can pick the training samples that we believe are representative to each category, use them to train the fuzzy logic, and let the neural net feedback do the detection.

TABLE II. INITIAL CLASSIFICATION OF SNT DATA

SNT Category	No. of SNT Data	Percentage
1	170	12.9%
2	1158	87.1%
3	1030	77.5%
4	1017	76.5%
5	1004	75.5%
6	851	64.0%

In Table III, we further reduce the classes into three major classes: "Good", "Marginal" and "Bad". The neural network is constructed as six inputs, six hidden, and three output neurons. In this case, for each input data, we only pick the highest output neuron that is greater than 50% as the category. For the dates between DOY 1-65/2007, the neural network classified 67.7% of data as "good", 19.9% "Marginal", and 12.3% "Bad" data. This is a qualitative classification. Not all "Bad" SNT data result in severely impacted link performance. Further investigation is

warranted to further study the behavior of the SNT pattern related to the DSN data quality.

The neural net/fuzzy logic provides an effective tool for the SNT quality assessment. Figure 5 shows the performance of various antennas (designated as DSS) based on the SNT classification. Good SNT varies from an average of 43% (DSS-63) to 96% (DSS-14).

TABLE III. USING FUZZY LOGIC TO CLASSIFY SNT DATA INTO THREE CATEGORIES

Category	Classification	Feature Extraction	No. of SNT Data	Percentage
1	Good: SNT matches performance model	$\Delta SNT_{ave} < +/- 5K$, ΔSNT_h and $\Delta SNT_l < +/- 5K$, Slope $\leq 5K/min$, Peak No ≤ 2	853	67.7%
2	Marginal: SNT has minor deviation from performance model	$\Delta SNT_{ave} \leq +/- 10K$, ΔSNT_h and $\Delta SNT_l \leq +/- 10$, Slope $\leq 5K/min$, Peak No ≤ 5	251	19.9%
3	Bad: SNT has major deviation from performance model	$\Delta SNT_{ave} > +/- 10$, ΔSNT_h and $\Delta SNT_l > +/- 10$, Slope $> 5K/min$, Peak No > 5	155	12.3%

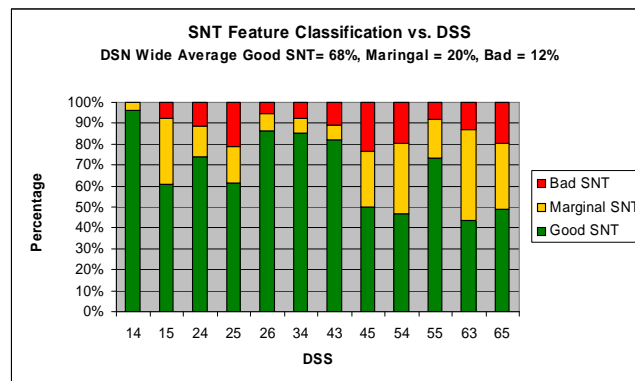


Figure 5: Classification of SNT data for various DSN antennas (DSS), DOY 1 – 65, 2007.

V. CORRELATION BETWEEN SNT AND LINK MARGIN

The Link Margin (LM) is one of the major indicators of the data communication quality. It is defined as the difference between the received symbol SNR (signal-to-noise ratio) and the decoder threshold required for

successfully decoded data. A positive link margin implies a good communications channel condition; the higher the margin, the less likely the link encounters data corruption. A negative margin, on the other hand, indicates likelihood with data demodulation and decoding; thus, would negatively affect the data return to missions. There is an inverse relationship between the SNT and link margin. An increase in noise temperature would reduce the received signal-to-noise ratio (SNR) and subsequent link margin, and vice versa. The correlation coefficient is defined as:

$$CorrCoef = \frac{\sum \Delta SNT_{ave}(i) LM(j)}{\sqrt{\sum \Delta SNT_{ave}(i)^2 \sum LM(j)^2}} \quad (8)$$

where LM is the average link margin of a given pass and where both the ΔSNT_{ave} and LM data are normalized to be within (-1, 1).

The correlation coefficient shows the relationship between the SNT and LM:

- If the ΔSNT and LM are positively correlated, then $Corr\ Coef > 0$;
- If the ΔSNT and LM are negatively correlated, then $Corr\ Coef < 0$;
- If the SNT and LM are uncorrelated, then $Corr\ Coef = 0$;

Figure 6 shows the ΔSNT -LM correlation at DSS-45 antenna for Voyager (VGR2) passes. From the graph, we can see the ΔSNT and LM data from VGR2 data are strongly negatively correlated, with $Corr\ Coef = -0.64$. It means that if the average SNT difference from the performance model increases, it will cause the link margin to drop, as expected.

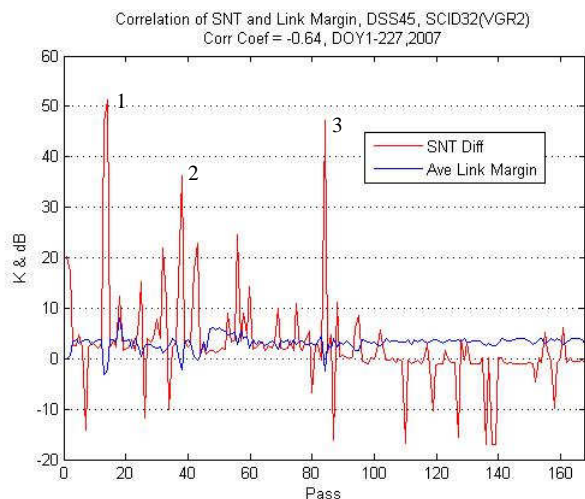


Figure 6: Correlation between SNT and Link Margin (LM) of VGR2 on DSS45 shows strong negative correlation (Corr Coef = -0.64).

We further analyze the relationship between the ΔSNT and LM in the three spikes (#1, #2, and #3) in Figure 6

In Figure 7, we can see an increased slope of the SNT between 7:47 and 9:08 GMT caused a drop in the link margin. In both Figures 8 and 9 for VGR2 passes on DOY 54 and DOY 117, we also see an increased slope of the SNT matched with a drop in link margin.

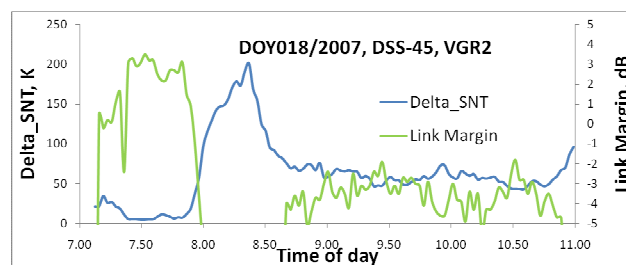


Figure 7: Negative correlation between SNT and Link Margin seen in VGR2 data on DOY18/2007 pass at DSS45.

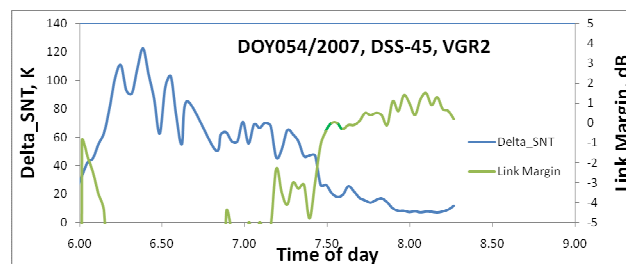


Figure 8: Negative correlation between SNT and Link Margin seen in VGR2 data on DOY 54/2007 pass at DSS45.

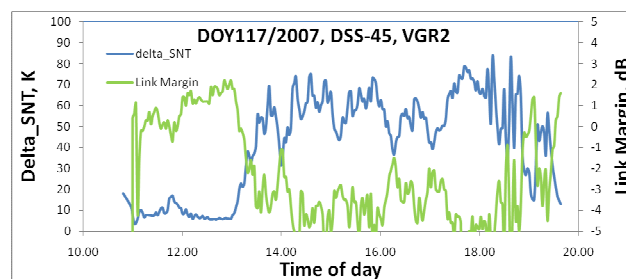


Figure 9: Negative correlation between SNT and Link Margin seen in VGR2 data on DOY 117/2007 pass at DSS45.

However, not all data have expressed a strong negative correlation between SNT and LM. We have observed that some other spacecraft data are either weakly negatively correlated ($Corr\ Coef = -0.2 - -0.3$), or uncorrelated ($Corr\ Coef = -0.2 - +0.2$). More validation effort is needed to understand these instances.

VI. CORRELATION OF SNT CLASSIFICATION WITH WEATHER

In this section, we extend the correlation to include the weather effect. Atmospheric effects in the line of sight between the ground tracking antenna and spacecraft are reflected in the observed system noise temperature measurements. Increased precipitation from rain and increased humidity would cause a higher SNT. Figure 10(a) shows the weather data during the pass. The cumulative precipitation for the day, reflecting the rain, is seen occurring at 15:00 – 18:00 GMT. The SNT starts to depart from a modeled curve and steady increases over the same period, per Figure 10(b). The received symbol signal to noise ratio, in Figure 10(c), drops as much as six (6) dB over the same period.

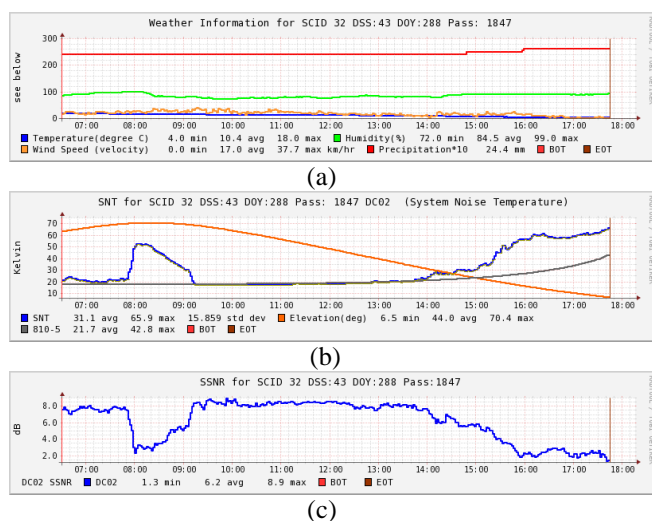


Figure 10: Correlation between (a) high SNT peaks, (b) low Link Margin, and (c) bad weather.

There is a general positive correlation among the changes in SNT, link margin and weather precipitation in this case. Note that there was similar increased SNT and decreased symbol SNR near 8:00 GMT, but surprisingly there was no indication of rain from the cumulative precipitation measurements. This is an example of possible inconsistency among the observables. Such obstacle would be hard to overcome for a detection scheme using Boolean logic. The neural network approach, given proper training data, may offer a way to overcome these difficulties.

VII. CONCLUSIONS AND FUTURE DIRECTION

We have presented the development of a neural network trained Fuzzy logic for system noise temperature classification. With the inherent advantage of neural network training using examples without setting concrete

rules, we have trained the neural network to evaluate the characteristics of measured SNT and to classify its impact to the communications link. We have observed, as expected, some correlations between “Bad” SNT category and low link margin conditions, which would affect the mission data return. In the future, adding link margin information to the training of the SNT classification should help to improve the results. Further analysis of other observed signatures of SNT deviation beyond the standard six categories discussed in this paper would further the understanding on the operating behavior and performance of DSN antennas; thus, pointing the way to possible improvement. Certainly, the potential application of this pattern recognition algorithm to other areas of DSN performance analysis should be considered.

ACKNOWLEDGMENTS

This research was carried out at the Jet Propulsion Laboratory, California Institute of Technology under a contract with the National Aeronautics and Space Administration (NASA).

REFERENCES

- [1] Pham, T. and Liao, J., “DSN Performance Dashboards”, SpaceOps 2008, Heidelberg, May 2008.
- [2] Jain, A. K., Mao, J., and Mohiuddin, K. M., “Artificial Neural Networks: A Tutorial,” Computer, vol. 29, no. 3, 1996, pp. 31-44.
- [3] Hagan, H. T., Demuth, H. B., and Beale, M.H., Neural Network Design, Martin Hagan, 2002.
- [4] Yager, R. et al. ed., Fuzzy Sets and Applications: Selected Papers by L.A. Zadeh, John Wiley, New York, 1987.
- [5] Ye, D., Edens, W., Lu, T., and Chao, T., “Neural Network target identification system for false alarm reduction,” Optical Pattern Recognition XX, Proceedings of the SPIE, Volume 7340, 2009.
- [6] Lu, T. and Mintzer, D., “Hybrid neural networks for nonlinear pattern recognition,” Optical Pattern Recognition, ed. by F. T. S. Yu and S. Jutamulia, Cambridge University Press, 1998.
- [7] Lu, T. and Lerner, J., “Spectroscopy and hybrid neural network analysis,” Proceedings of the IEEE, Volume 84, Issue 6, 1996, pp 895 – 905.

Overview of Experimental Module CANDARMA

Sinan Gökğöz, Orhan Şengül, Levent Burak Yalçiner, Mustafa Sancay Kirik, Fethi Türk, Ali Bircan
Embedded Systems Group

TUBITAK Space Technologies
Research Institute, Ankara Turkey

e-mail: sinan.gokgoz@uzay.tubitak.gov.tr, orhan.sengul@uzay.tubitak.gov.tr, burak.yalciner@uzay.tubitak.gov.tr,
sancay.kirik@uzay.tubitak.gov.tr, fethi.turk@uzay.tubitak.gov.tr, ali.bircan@uzay.tubitak.gov.tr

Abstract— The purpose of this study is to present a Real Time Operating System embedded ARM-7 microcontroller-based module, CANDARMA. CANDARMA is an experimental payload module settled in low earth orbit remote sensing satellite. The significance of CANDARMA comes from the various experimental applications performed on it. These studies include usage of an ARM-7 architecture based microcontroller, running a Real Time Operating System on the microcontroller, experiencing two different high speed analog to digital converters and various integrated circuits, which will bring in knowledge for future satellite designs. This paper describes CANDARMA's implementation key points and benchmarks in details which can be used in analog and imaging applications in satellite systems.

Keywords-Satellite; Microcontroller; Real Time Operating System; Space Heritage

I. INTRODUCTION

Turkey has made investments on space activities by setting off some satellite projects in the last decades. RASAT [1], one of the satellite projects of Turkey, is an outcome of these investments and will be an imaging satellite for civil purposes. RASAT is the second remote sensing satellite of Turkey and a TUBITAK-UZAY product and is planned to be launched in February-2011. Basic specifications of RASAT are given in Table 1 [2].

With the advance of technology, capabilities of microcontrollers have increased coarsely; they got faster and faster, became more equipped with addition of new developed peripherals. Today, an enhanced microcontroller can run up to Ghz's levels (TI- AM3703-1000 – 1 Ghz,

Intel-i7-960 - 3.20 GHz) [3][4] and be loaded with various peripherals (TI-AM1707 - EDMA3, Three Configurable 16550 type UART, Two Serial Peripheral Interfaces (SPI), Multimedia Card (MMC)/Secure Digital (SD), Card Interface with Secure Data I/O (SDIO), USB 2.0 OTG Port With Integrated PHY, Three Multichannel Audio Serial Ports, 10/100 Mb/s Ethernet MAC, Three Pulse Width Modulators, etc.) [5].

Development in microcontrollers' features lead to higher expectations from microcontrollers. Due to the fact that the internal ROM and RAM have been large enough, engineers quitted using external RAM and ROM in applications. Increase in the operating frequency results in handling more tasks, and providing the capability to run RTOS with high performance controllers.

Design engineers all around the world take the advantage of advances from the development of new architectures and increasing capabilities. Examples of new generation microcontrollers' usage can be seen in the new satellite projects. For instance, AT91SAM7A3 which is an ARM-7 architecture microcontroller has taken place in the ADCS part of AAUSAT3 [6].

AT91M55800A another ARM-7 family microcontroller was used in SwissCube satellite which was launched in 2009 [7]. Together with AT91M55800A, 16-bit TI-MSP430F1611 controller was also used in the CDMS (Control & Data Management System). While MSP430F1611 is being used for some communication work, AT91M55800A has been used for the most of the work because of its processing capability [8]. GP4020 another ARM7TDMI controller was also used in PROBA-2 Spacecraft in 2008 [9].

In imaging satellites, speed and accuracy are the most important criteria which directly affect resolution of the imaging unit. Engineers who want to design high resolution imaging satellites have to use new- generation analog to digital converter (ADC) integrated circuits (ICs), because usually newly designed ADC outclasses its formers by means of speed and accuracy.

The main handicap with using a new generation advanced IC is to find sufficient support for the product. Space Heritage is another critical issue in space applications. Using an IC that had never been experienced in space is always taking a risk. CANDARMA is designed to serve its benefit on that issue. After working successfully in space conditions, our new ICs will have space heritage

TABLE 1. TECHNICAL SPECIFICATIONS OF RASAT

Turkish EO Satellite	RASAT
Orbit	700 km circular, sun synchronous
Weight	93 kg
Spatial resolution	Panchromatic: 7.5 m Multispectral: 15 m
Expected life time	5 years
Swath width	30 km
Payloads	Optical payload: A pushbroom type imager BiLGE: Flight computer GEZGiN-2: Image process and compression module X-Band: High speed Transmitter Module CANDARMA: An Experimental ADC and Microcontroller Test Module

and they will be trusted to use for further satellite electronics applications.

This paper will describe the structure of this module. In the next section functional and architectural overview of CANDARMA will be presented and following sections, the ADCs and microcontroller of the module, qualification tests will be explained in details. Finally, paper concludes with giving ideas about future work.

II. OVERVIEW OF CANDARMA

CANDARMA is designed simple while meeting all of our goals. The block diagram of CANDARMA is schematically explained in Figure 1.

It is connected to satellite system by power and CAN bus. Module itself is supplied with unregulated 28 V and produces necessary 5V and 3.3V in the inner stages.

Functionality of CANDARMA can be divided into two main steps; CAN communication and Analog to Digital Conversion. First of all, a number for the test purpose is sent over CAN-Bus. Microcontroller picks and processes sent-data, produces an appropriate analog voltage proportional to the sent-number with the help of internal DAC module. DAC output voltage is amplified by voltage amplifier LM6646. Amplified voltage is transferred to both ADCs as an input. After conversion, most significant 8-bits of the ADCs are read by the controller at a rate of 1 Mhz and compared with the number sent over CAN. Read value is then sent back over CAN-Bus allowing us to check conversion accuracy, when needed. In this operation, necessary clocking signals for the ADCs are generated by the controller. By this functionality loop, CAN connection, basic operation and DAC channels of the controller were checked besides ADC ICs and voltage amplifier LM6646.

III. ARM-7 BASED MICROCONTROLLER

8051 core architecture was developed in 1980 by Intel and gained popularity in industrial control applications after that time. With successful experiences in space missions, 8051 architecture dominated this field for years. Up to this date in space missions 8051 architecture based microcontrollers have been widely used all over the world. TUBITAK-UZAY also used to utilize Infineon C515 microcontroller for controller work in satellite electronics. C515 is an 8-bit 8051 architecture controller which has a strong space heritage. With developments in technology and increasing needs in applications, C515 is getting out of date day by day by means of running speed and application features.

LPC2378 microcontroller, which is thought to replace C515, is a product of NXP Company. CANDARMA is connected to Satellite Can-Bus with a baud rate of 388kbit/sec with the help of LPC2378 microcontroller. This 32bit microcontroller is not radiation hardened. LPC2378 has two Can-Bus channels providing us to connect CANDARMA to primary and secondary CAN buses of the satellite at the same time.

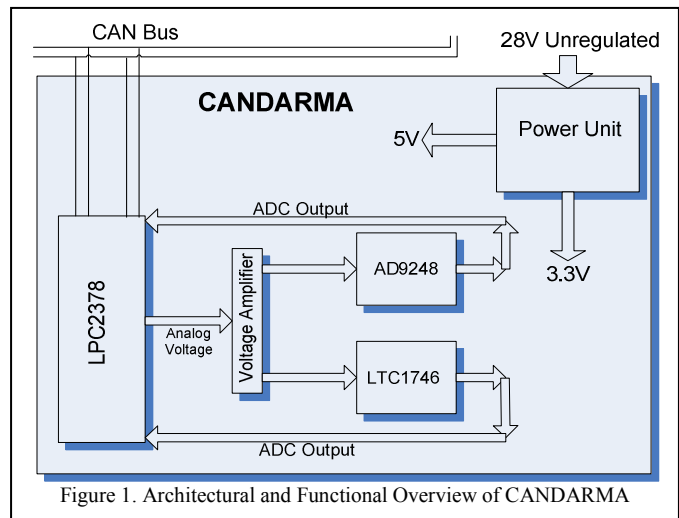


Figure 1. Architectural and Functional Overview of CANDARMA

Specifications, in which LPC2378 is better than C515 are not limited to only number of CAN Bus channels. Table 2 compares C515 and LPC2378 by means of technical specifications.

LPC2378 is faster than C515 by means of maximum oscillator frequency, but this is not the whole case. Our C515 microcontroller model has a MIPS rate of 1.66 while LPC2378 having a rate of 64 Dhrystone MIPS.

The difference between the sizes of on-chip ROMs is noticeable. Due to the limited internal ROM space of C515, an external ROM was used to store the software in our earlier applications. This solution brought in lots of burden. In order to drive the external ROM, some components as latch, inverter, capacitors and resistors were used. External components also makes memory mapping complicated, because the number of components increases, reliability of system decreases and test – manufacturing – maintenance gets harder. LPC2378 Internal ROM is exceedingly big enough for our firmware and data, which will ease our job in various ways and increase reliability.

High speed operating capability and large storage size enabled us to embed A Real Time Operating System. MicroC/OS II, is used as RTOS. All of the controller tasks, while running under MicroC/OS II, were subjected to various functionality tests, software crash never occurred.

Our satellite systems have two CAN-Buses and C515 has one CAN-Bus; therefore, a mechanical relay is included for switching between CAN-Buses. By use of dual CAN-Bus channel of LPC2378 there is no need for a mechanical switch and its peripheral components.

LPC2378 is able to boot load a new code sent by packets over CAN Bus. HY628100 is included in the design for RAM operations of RTOS and bootloader. That bootloader is tested and verified while running under MicroC/OS II.

TABLE 2. COMPARISON OF C515 & LPC2378

	C515	LPC2378
Architecture	8051	ARM7
Structure	8 bit	32 bit
Processor frequency	Up to 24 MHz	Up to 72 MHz
MIPS*	1.66 MIPS**	64 Dhrystone MIPS
Operating modes	Single 8 bit mode	16-bit Thumb mode 32-bit ARM mode
On-chip ROM	8 Kbyte	512 Kbyte
On-chip RAM	256 byte on-chip RAM	32 kB of SRAM on the ARM local bus-CPU access 16 kB SRAM for Ethernet interface*** 8 kB SRAM for USB***
ADC	8-bit ADC	10-bit ADC
I/O Pins	48 I/O pins	104 I/O pins
Peripherals	Three 16-bit timer/counters	Four 16-bit timer/counters
	Watchdog timer	Watchdog timer
	12 interrupt sources	32 vectored interrupts
	SPI controller.	SPI controller.
	1 UART Channel	4 UART Channels
	Single channel CAN controller	CAN controller with two channels
	-	USB 2.0 full-speed device with on-chip PHY and associated DMA controller
	-	Four UARTs
	-	Ethernet MAC with associated DMA controller
	-	Two SSP controllers
	-	Three I2C-bus interfaces
	-	I2S (Inter-IC Sound) interface
	-	SD/MMC memory card interface
	-	10-bit DAC.

* Million instructions per second

** For C515C-8R / -8E

*** Can also be used as general purpose SRAM.

IV. ANALOG DIGITAL CONVERSION ICs

CANDARMA also includes two types of high speed AD Converters; AD9248 and LTC1746. AD9248 is a dual input ADC and can operate up to 65 Msp/s without missing any conversion. LTC1746 is a low power ADC and can operate up to 25 Msp/s. Both ADCs can make conversions up to 14 bits of precision. Similar ADCs with the used ones in this module were subjected to radiation tests in [10]. According to the results 9-bits precision can be obtained after 20 krad(Si) total dose radiation. In CANDARMA by using the

DAC channel of microcontroller analog signals are produced and supplied as an input to the ADCs. By comparing the input analog signal and output digital signal, CANDARMA provides data about errors and deviations from expected results.

V. QUALIFICATION TESTS PERFORMED

CANDARMA was subjected to thermal and thermal-vacuum tests while functionality test results being logged continuously.

Single-cycle thermal vacuum test and 7-cycles thermal tests are performed in TUBITAK-UZAY thermal chamber. Thermal chamber and thermal-vacuum chamber are both capable of meeting ECSS-E-10-3A testing standards.

A. Thermal – Vacuum Test

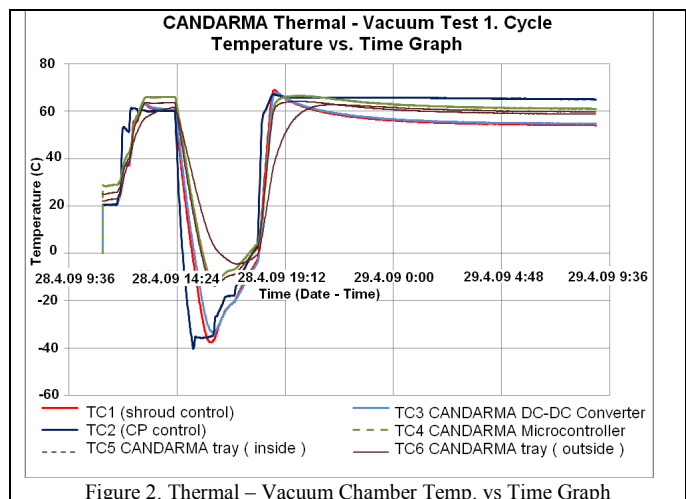
Thermal testing of CANDARMA consists of two phases: in the first phase CANDARMA is exposed to 10^{-6} mbar vacuum and temperatures of -40°C up to $+60^{\circ}\text{C}$. Thermal vacuum temperature log graph is shown in Figure 2.

Temperature values are also measured with the help of temperature sensors as can be seen from Figure 3. fixed on different parts of the module. Maximum and values logged on CANDARMA are listed in Table 3.

B. Thermal Tests

This phase consists of 7 thermal cycles. In this phase no thermal sensors are placed on CANDARMA module. Thermal chamber temperature altered between -40°C and $+60^{\circ}\text{C}$ with time, as can be seen in Figure 4.

During the test, module is also subjected to functionality test. ADC reads and CAN communication is logged during the test. The voltage to be generated by DAC of microcontroller is sent from CAN-Bus, the generated analog voltage is converted by ADCs and read back by microcontroller. The read data is sent back over CAN-Bus and logged by PC.



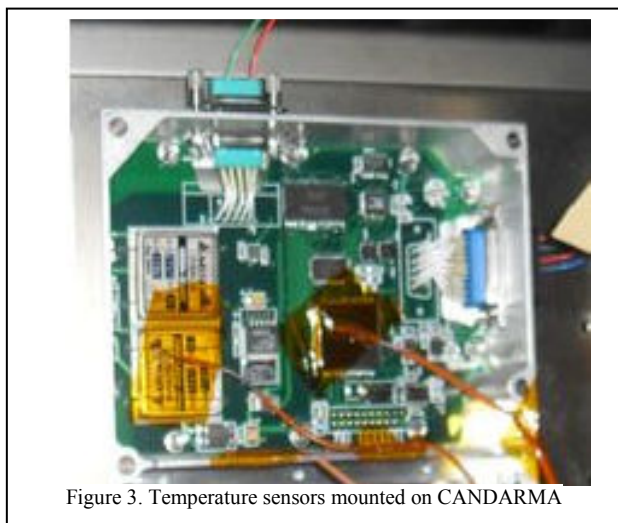


Figure 3. Temperature sensors mounted on CANDARMA

No software crash was observed during the tests. No deviation was observed for the most significant 8-bit readings. CAN-Bus check is done 10 times per second. Can-Bus connection was never lost.

VI. CONCLUSION AND FUTURE WORK

In this paper, experimental module CANDARMA was presented. Functionality of the module and functionalities of included ICs are explained.

After having a successful experience of space experience, this microcontroller will gain reliability and other design engineers will be confident for using other features like Ethernet, I²S, I²C, USB etc. Real Time Operating System will be tested with LPC2378 and will also be verified to work in space conditions with this microcontroller.

This experimental work is expected to bring in significant experience and knowledge in various fields. With accomplishment of this work LPC2378 and ADCs will gain space heritage.

TABLE 3. MINIMUM AND MAXIMUM VALUES OBTAINED DURING THERMAL – VACUUM TEST

Thermal Sensor	Position	Maximum Temperature (C)	Minimum Temperature (C)
TC1	Shroud control	68.88	-37.64
TC2	Cold plate control	67.03	-40.31
TC3	CANDARMA DC-DC converter	67.73	-33.61
TC4	CANDARMA Microcontroller	66.46	-5.71
TC5	CANDARMA tray (inside)	64.21	-1.75
TC6	CANDARMA tray (outside)	62.01	-17.61

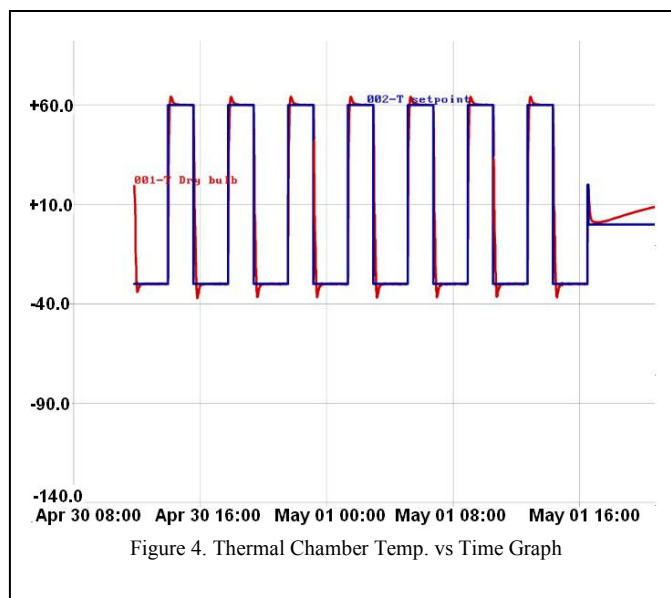


Figure 4. Thermal Chamber Temp. vs Time Graph

For future work, embedding the ARM controller in a radiation hardened FPGA for a satellite module is being planned.

ACKNOWLEDGMENT

RASAT Satellite Development Project is financed by DPT (State Planning Organization of Turkey) under grant contract no 2007K120030.

REFERENCES

- [1] G. Ytiksel, A. Okan and U. M. Leloglu, "First LEO Satellite Built in Turkey: RASAT", Recent Advances in Space Technologies, 2007. RAST'07. 3rd International Conference on, 14-16 June 2007
- [2] <<http://www.uzay.tubitak.gov.tr/tubitakUzay/en/projects/spaceApplications.asp>> 31.01.2011
- [3] <<http://focus.ti.com/docs/prod/folders/print/am3703.html>> 01.12.2010
- [4] <<http://ark.intel.com/Product.aspx?id=37151>> 01.12.2010
- [5] <<http://focus.ti.com/docs/prod/folders/print/am1707.html>> 01.12.2010
- [6] K. Fuglsang and J. K. Vinther, "Attitude determination and control system for AAUSAT3", Thesis: Aalborg University, 2010
- [7] <<http://swisscube.epfl.ch/>> 01.12.2010
- [8] D. Crettaz, "Ordinateur de bord pour mini satellite", Thesis HES: HES-SO Valais, 2007
- [9] O. Montenbruck and M. Markgraf, "Autonomous and precise navigation of the PROBA-2 Spacecraft", AIAA/AAS Astrodynamics Specialists Conference, Honolulu, Hawaii, 18-21 Aug. 2008
- [10] C. I. Lee, B. G. Rax, and A. H. Johnston, "Hardness Assurance and Testing Techniques for High Resolution (12- to 16-bit) Analog-to-Digital Converters", IEEE Transactions on Nuclear Science, vol. 42 no. 6, December 1995

Researching a Robust Communication Link for Cubesats: OPTOS, a new Approach

Víctor Miguel Aragón, Álvaro García, Ricardo Amaro, César Martínez, Fany Sarmiento
Space Programmes and Space Sciences Department
INTA (National Institute of Aerospace Technology)
Ctra. Ajalvir Km.4
28850 Torrejón de Ardoz, Madrid, Spain
victor.miguel.aragon@insa.es, agarcia@ttinorte.es, amarocr@inta.es,
martinefc@inta.es, sarmientoae@inta.es

Abstract—OPTOS is a Cubesat-based picosatellite that is been developed by INTA. The aim of this project is to provide an easy and low-cost access to space for those institutions and companies that can not afford the use of usual platforms. This is a new alternative way from the previous bigger and more expensive options to deal with small space missions. The fact that these little platforms are available in the future will promote that nowadays unfeasible projects will be able to come true, such as small microgravity experiments, observatories, material testing, etc. The advance in electronic miniaturization is expanding the possible applications that can be part of the Cubesat philosophy, which perhaps did not initially consider that complex mission could be implemented with limited resources, such as available power and volume. These payloads require reliable communication systems. From this point of view, an evolution is needed from the current technology used. OPTOS communication system tries to find a balance between limited available resources in Cubesat platform, i. e., inner dimensions and power, and having a reliable communication link. To achieve this goal OPTOS uses custom-made space-qualified equipment, deeply tested during an extensive trial campaign. To improve even more the communication link quality, OPTOS uses a non-amateur frequency band, reserved to space operations. This paper provides a general description of the OPTOS satellite and a detailed description of its communication link.

Keywords - Cubesats; communication system; transceiver; ground station; antennas.

I. INTRODUCTION

INTA is a Public Research Organization, located in Madrid, Spain, that has an extensive experience in space projects, and in all those technologies which can be applied to the aerospace field. It has the know-how and the facilities for almost every possible test related to space programs: antennas, environmental, electronics, solar, etc...

INTA has a new line of satellite pico-platforms that include state of the art technologies integrated in its subsystems, enabling high efficiency and low cost multipurpose satellite, which allows research applications at

reasonable budgets. Its technological demonstrator, OPTOS, will be launched in 2011.

OPTOS is based on a Cubesat [1] 3U structure (10cm x 10cm x 30cm, and 3 kg) with improved payload capacity, system reliability and mission life time [2]. Figure 1. shows a 1:1 model of OPTOS with deployed antennas. The management and engineering processes follow the ECSS (European Cooperation for Space Standardization) standards, in order to assure good practices that improve the long term results. The standards were tailored to the project necessities.



Figure 1. OPTOS 1:1 Model

About the mission, OPTOS will be in a LEO (Low Earth Orbit), with a lifetime of 1 year. In this time, INTA hopes to qualify the platform and experiment with the 4 payloads in space. These payloads are:

- GMR (Giant Magneto-Resistance): Earth magnetic field measurements based on COTS (Commercial Off-The-Shelf) magnetic sensors,

- ODM (OPTOS Dose Monitoring): dosimeters with commercial RadFETs, to monitor the total ionizing dose,
- FIBOS (Fiber Bragg Gratings for Optical Sensing): evaluate the feasibility of optical fiber sensors in space environment for temperature measurement, and
- APIS (Athermalized Panchromatic Imaging System): space qualification of specific glasses, the degradation under gamma rays and Earth observation.

The platform subsystems are:

- OBDH (On Board Data Handling): several units working together forming a distributed system, with different complexity degree and placed through the satellite,
- OBSW (On Board Software): control architecture of OPTOS satellite is distributed, following the hardware architecture,
- OBCOM (On Board Communication): each unit of the OBDH has an associated OBCOM module, small bidirectional terminals for optical wireless intrasatellite communication through a CAN bus,
- TCS (Thermal Control Subsystem): it is a passive subsystem, which uses paints and conductive materials on specific areas of the satellite for assuring operational temperatures,
- S&M (Structure and Mechanism): the external structure is mechanized to lodge the solar panels and one of the ADCS solar sensors, to give access to the satellite once the integration is finished and to keep free FOV for the camera and some solar sensors,
- EPS (Electrical Power Subsystem): supplies all the payloads and the platform subsystems,
- ADCS (Attitude Determination and Control Subsystem): with 2 sun sensors, 1 solar presence detector, 1 triple axis magnetometer, magnetotorques on three axes and 1 reaction wheel, and
- CS (Communication Subsystem): described in the next chapter.

Communications are essential for the success of the mission: the on-board transceiver and the ground station are both critical parts of the system. One of the main causes of unsuccessful Cubesats missions is related to the communication system, due to the use of non space-qualified electronic in the transceiver.

Section II deals with the detailed explanation of the different parts involved in the OPTOS communication subsystem. Section III describes the factors involved in the link budget and the limitations associated to each one. Section IV details both downlink and uplink link budget estimations. Finally, Section V deals with the conclusion and the future work lines derived from this project.

II. OPTOS COMMUNICATION SUBSYSTEM

CS is the most exigent subsystem in terms of budgets. On it lays the responsibility of the satellite to ground communications, the only way to know that the satellite is alive. The system has been designed with the aim of achieving at least a 3 dB margin in the final link budget result. The link budget is an estimation that considers all the gains and losses that the signal suffers along the complete path between the transmitter and the receiver, and the added noise effect that degrades the signal quality. This margin, between the estimated E_b/N_0 (bit energy over noise spectral density) at the demodulator output and the theoretical required value, allows to accomplish a certain BER (Bit Error Rate), in downlink and uplink as well. BER is a quality factor that also depends on the modulation scheme used [3].

To strengthen the communications INTA has chosen a professional on-board transceiver made by Thales Alenia Space, with an RF (Radio-Frequency) ASIC (Application Specific Integrated Circuit) designed for space [4]. The transceiver works half-duplex at 402 MHz and provides a maximum transmitted power of 25.5 dBm. A phase modulation is used, direct with Manchester data for downlink at variable rate, 5 kbps nominal, and with a BPSK (Binary Phase-Shift Keying) 16 kHz subcarrier with NRZ (Non Return to Zero) data for uplink at 4 kbps. This scheme is recommended by ESA (European Space Agency) ECSS-E-ST-50-05C standard, as well as other subsystems of OPTOS project follows the ESA recommendations. The transceiver provides housekeeping signaling that offers better control over the signal acquisition process and the transceiver health status.

Two transceiver models have been manufactured, an electrical model and a flight model. One will serve as a test model for ground working and the other will be launched. Both models are tested with the corresponding models of the rest of the communication equipment: onboard antennas, onboard computer, onboard software, ground antenna, ground equipment and ground software. Figure 2. shows the uncovered RF side of the transceiver EM, where a 4:1 splitter, Tx/Rx switch, Tx and Rx RF chains and a PLL can be appreciated. The ASIC and the current regulators are in the other side of the transceiver.

OPTOS Ground Station is located at INTA facilities. The functions of the ground station are to receive/transmit information from/to the satellite, manage the platform and the scientific payloads and distribute the data to the scientific partners. A LDRM (Low Data Rate Modem), an ELTA transceiver, has been chosen, which provides automatic signal search and lock functionality, ASB, fading, noise and Doppler effect simulation [5].

Besides, in order to improve the quality of the link, a LNA (Low Noise Amplifier) and a HPA (High Power Amplifier) are used in the downlink and uplink chain, respectively. For the data processing stage, an ELTA FS (Frame Synchronizer) has been chosen, capable of using synchronization word, Reed-Solomon encoding/decoding and uplink randomization.

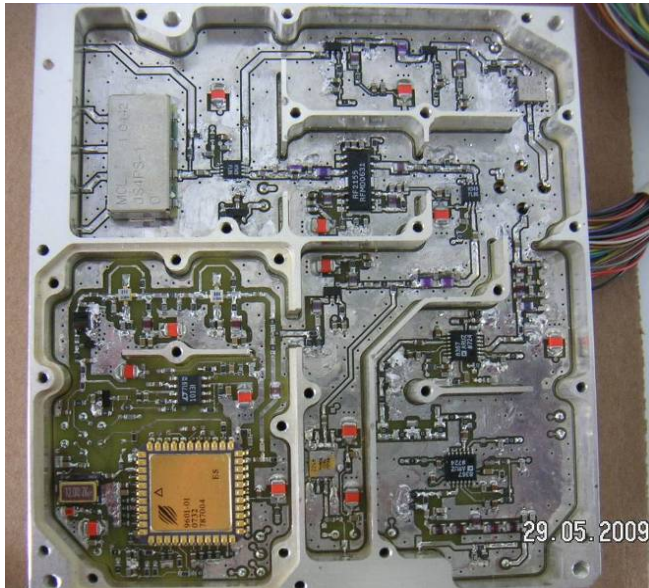


Figure 2. Uncovered on-board transceiver EM

Regarding the antennas, the on-board antenna consists of four $\lambda/4$ monopoles with circular polarization, placed in each of the four lateral sides, with a deployment system [6]. The Ground Station antenna, located at INTA facilities, is formed by an array of four Yagi antennas with circular polarization and an elevation over azimuth positioner [7]. Figure 3. shows the ground antenna lying on the elevation over azimuth positioner on top of a 3 m mast, placed on the flat roof of the Space Programmes and Space Sciences Department building.



Figure 3. Ground station antenna

INTA has developed the software to control, operate and distribute data to the scientific users. Also has made a custom Communication Protocol, with FEC (Forward Error

Correction) Reed-Solomon, and ARQ (Automatic Repeat Request) scheme.

III. FACTORS TO BE CONSIDERED IN THE LINK BUDGET

Link Budget [8] determines the feasibility of a possible bidirectional communication link between OPTOS and the ground station considered with the link margin adequate to transmit and receive the required data volume with the established bit rate attending to mission and orbital characteristics (orbital height, shape, eccentricity and contacts number, time duration and satellite-ground station relative configuration), and the communication architecture.

Due to the limited communication capacity because of the limited electrical power (therefore limited RF power) that the small effective surface of solar cells could supply, it's a challenge to attempt to communicate with such a small and light satellite.

The possibility to establish the link and the available link margin depends on:

- Orbit: range and duration of each contact satellite-ground station
- Frequency band
- RF Power available
- Bandwidth occupied and Bit Rate
- Ground Station and satellite performance: EIRP and G/T

The main objective of the link budget is to evaluate the possibility of communication fixing these parameters according to technical possibilities and the constraints imposed by the rest of subsystems and the mission.

A. Orbit

OPTOS shall describe a LEO helio-synchronous polar orbit. Different orbital heights have been considered to analyze which one gives the best conditions to carry out OPTOS and its payloads mission. Two different orbital heights have been simulated for the link budget: 670 km and 817 km. The launch has been established on 2011. The final orbit depends on the launcher, that is still to be confirmed.

The Ground Segment has been installed at INTA (40.4°N, 3.46°W). The frequency band considered is UHF (402MHz). At this frequency the ground station is an easier and cheaper solution than higher frequencies.

The contact time and the communication capacity establish the maximum data rate that OPTOS system is able to communicate in downlink and uplink.

The orbit shall be a circular one, so the orbital eccentricity is practically negligible and it will not be considered differences in range and contact time between apogee and perigee, and so, the bit rate shall be fixed for all the contacts.

Contact times have been simulated using STK software developed by AGI. OPTOS will have at least three contacts daily according to the considered elevations to each case (obviously considering contact with lower elevations the number of contacts per day increases but the communication

is more difficult due to other effects like multipath signals). The total contact time per day should be at least 28.95 minutes.

The transceiver bit rates have been set to 5 kbps for downlink and 4 kbps for uplink. There is an option to change the downlink bit rate via TC (Telecommand), but in order to simplify the subsystem testing phase, this option will not be used till the satellite mission ending. The data budget estimation, removing protocol headers and taking into account a TM (Telemetry) /TC ratio of 90/10, is: 725.37 kB/day for TM and 98.12 kB/day for TC. The total data estimation is 823.49 kB/day.

B. Frequency

The frequency band selection has been based in several factors:

- Link budget results: UHF band (402 MHz) have better results than higher frequencies
- Complexity and physical characteristics of on-board antennas and transceiver design
- ITU Frequency Coordination requirement with other countries and type of service available for the satellite related with its mission

From the antennas point of view, UHF band is more preferred than VHF because the former is compounded of shorter monopoles than the latter, and therefore more suitable for OPTOS requirements. From the design complexity point of view, transceiver and antenna are similar in both frequency bands. The double band UHF/VHF has been rejected based in the transceiver first feasibility studies. These determine that the double band requires a design that doesn't fulfil with power consumption, volume and mass requirements.

C. Power available

The low power available in the satellite is a strong handicap to fulfil OPTOS communication requirement, above all to complete the downlink with the required link margin to assure the communication.

The maximum power that the EPS could supply to the platform and payloads is estimated in 6 W. So, calculations of Link Budget must consider that the whole transceiver unit is supplied with 2.73 W to be shared between both electrical and RF components. Considering the subsystem design, 0.5 W are available at HPA output as RF Output Power.

D. Bandwidth occupied and Bit Rate

The bandwidth occupied and the bit rate are related each other by means of the spectral efficiency of the modulation used. Spectral efficiency refers to the information rate that can be transmitted over a given bandwidth, measured in (bit/s)/Hz. The spectral efficiency is 0.7 (bit/s)/Hz in the uplink (BPSK) and 0.5 (bit/s)/Hz in the downlink (Manchester).

The Bit Rate is fixed at 4 kbps in the uplink, and it is variable in the downlink, but during the mission it will be fixed at 5 kbps. At the mission conclusion, the Bit Rate can be modified to test the Link Budget margin. The rest of downlink parameters: orbit, output power, antenna gain, et al. can not be modified after the launch.

E. Ground Station and satellite performance

TABLE I. summarizes the main parameters of both the ground station and satellite communications.

Antenna gain, cable losses, amplifier maximum power and receiver noise figure have been measured at INTA RF laboratories. The GS (Ground Station) amplifier maximum power is 100 W, but, as the link budget shows, there is not need to use it at its maximum. Besides this, and in order to reduce the electromagnetic radiation in the GS surroundings, a value of 5 W is used, high enough to get the expected link budget margin.

The values of antenna noise temperature considered have been simulated through numerical integration at the worst case following ITU-R P.372-8 radio noise recommendation ($F_{\text{sky}}[\text{artificial}] = 11 \text{ dB}$ at 400 MHz). Preliminary GS antenna noise measures have been done in situ and the results indicate that the antenna noise temperature is significantly lower than the previously estimated, but until more precise measures are taken, worst case antenna temperature value has been considered to the link budget calculations.

TABLE I. COMMUNICATION PARAMETERS

Parameter	Ground Station	Satellite
Antenna Gain	18.0 dBi	-3.0 dBi
Transceiver Output Power	37.0 dBm	25.6 dBm
L_{Tx}	0.89 dB	0.30 dB
L_{Rx}	0.37 dB	0.30 dB
F_{RX}	7 dB	1.6 dB
System Noise Temperature	34.1 dBK	26.2 dBK
EIRP	24.1 dBW	-7.8 dBW
G/T	-16.5 dB/K	-29.5 dB/K

The system let to improve the ground station performance, if subsequent phases require it, adding antennas and obtaining a more complex configuration with an Antennas Array System. And so, improving the gain of the Antenna System in 2-3dB duplicating the number of antenna elements.

The antennas configuration on-board the satellite depends on the working frequency band selected and the surface available in the satellite to fix the antennas before the launch and during the mission. A four quarter-wave monopole configuration has been chosen due to OPTOS structure. The antenna has a quasi-omnidirectional radiation pattern to assure the link independently of the relative orientation of the satellite.

IV. LINK BUDGET ESTIMATIONS

The link budget estimations have been done with two different orbital heights: 670 km and 817 km. From now on, the results correspond to the worst case height, 817 km, which provides the tightest link margin.

In the next subsections, the downlink and uplink link budget estimations are presented in TABLE II. and TABLE III. respectively. The more significant parameters used are explained below:

- L_{FS} : Free space losses between satellite and ground station antennas, following ITU-R P.525-2.
- L_P : Worst case polarization losses, depending on satellite attitude.
- P_{RX} : Signal power received at the LNA input.
- P_{NOISE} : Noise power received at the LNA input.
- C/N_0 : Carrier over noise spectral density at the LNA input.
- C''/N_0 : Signal power over noise spectral density at the demodulator input.
- E_b/N_0 available: Bit energy over noise spectral density at the demodulator input, before Coding Gain.
- Required BER: Link quality factor from the OPTOS requirement specification.
- Required E_b/N_0 : Bit energy over noise spectral density necessary to achieve the required BER, depending on the modulation used.
- Coding Gain: Digital gain related to the coding scheme used, which improves the resulting BER.
- Link Margin: Difference between the available E_b/N_0 and the required E_b/N_0 , considering the increase due to Coding Gain.

Attenuation by atmospheric gases is not applicable at this low frequency in accordance with ITU-R P.676-8. For the same reason, attenuation by rain, clouds and fog has not been considered according to ITU-R P.838-3 and ITU-R P.840-4. Ionospheric scintillation exceptionally occurs in the middle latitudes, in line with ITU-R P.531-10, so it also has not been taken into account.

The minimum elevation for the link budget estimations is 10° , with a maximum distance of 2402 km.

The ground antenna includes a device that allows the polarization to be changed according to the satellite attitude. Making use of the received power marker at ground station, the system will automatically switch the circular polarization in the opposite direction when the maximum power drops off more than 3 dB. Therefore, the losses associated with this lack of polarization alignment between satellite and ground station could be 3 dB at worst case.

Both P_{RX} and P_{NOISE} permit to calculate the C/N_0 at the LNA input. In order to estimate the E_b/N_0 available at the demodulator input and compare it with the required one for the specified BER, it is necessary to calculate the carrier drop when modulating the signal and see the real signal level over noise density, C''/N_0 . To do this, the residual carrier power C'/N_0 has to be subtracted from the C/N_0 in order to

get the C''/N_0 . Then, the E_b/N_0 results from taking away the binary rate R_b and the demodulator losses (around 2 dB in both cases).

A. Downlink

In TABLE II. the more relevant downlink budget parameters are listed, together with its estimated values.

The margin is so tight because of the limited power available in the on-board transceiver and the high ground station antenna noise temperature estimated through numerical integration.

This value of 3.1 dB is calculated in worst case situation at the beginning of the pass. After that moment, as the time passes and the distance decreases, the free space losses are lower, reaching the minimum at the middle of the communication window. So, the margin increases and there is the possibility to increase the transmission bit rate to improve the throughput of the link.

TABLE II. DOWNLINK LINK BUDGET

Parameter	Estimated value
L_{FS}	152.1 dB
L_P	3 dB
P_{RX}	-145.3 dBW
P_{NOISE}	-194.5 dBW/Hz
Modulation	PM (Manchester SP-L)
Bit Rate	5 kbps (nominal)
C/N_0	49.3 dBHz
C''/N_0	48.6 dBHz
E_b/N_0 available	9.7 dB
Required BER	10^{-5}
Required E_b/N_0	9.6 dB
Coding Gain	3 dB
Link Margin	3.1 dB

B. Uplink

In TABLE III. the more relevant uplink budget parameters and its estimated values are listed.

The 18.8 dB margin is higher than in the downlink case, mainly due to the greater transmission power and the lower system noise temperature caused by the reduced noise that the antenna receives in the space. As the uplink bit rate is fixed by the transceiver, there is no possibility to improve the uplink throughput increasing the bit rate. So, the only choice is to reduce the transmitted power in the ground station, reducing in this way the electromagnetic radiation in the surroundings.

TABLE III. UPLINK LINK BUDGET

Parameter	Estimated value
-----------	-----------------

Parameter	Estimated value
L_{FS}	152.1 dB
L_P	3 dB
P_{RX}	-134.3 dBW
P_{NOISE}	-202.4 dBW/Hz
Modulation	PM/BPSK (NRZ)
Bit Rate	4 kbps (fixed)
C/N_0	68.1 dBHz
C''/N_0	67.9 dBHz
E_b/N_0 available	25.4 dB
Required BER	10^{-5}
Required E_b/N_0	9.6 dB
Coding Gain	3 dB
Link Margin	18.8 dB

V. CONCLUSION AND FUTURE WORK

This paper has presented the OPTOS CubeSat, with particular stress upon its communications subsystem. OPTOS communication subsystem uses non amateur space reserved frequency band. The subsystem is composed of custom elements purpose-made: on-board transceiver unit, ground segment equipment, and both on board and ground antennas.

The link quality depends on certain factors, which have been analyzed in order to reach a balance between limited available resources on board in such a small satellite and having a robust communication link. The critical point is the downlink received power at the ground station antenna, because of the limited transceiver output power and the antenna omnidirectional radiation pattern on board. Even with these limitations, an acceptable link budget margin has been achieved.

The values of E_b/N_0 margin obtained are always above 3 dB for worst orbital case. This positive margin, together with the ARQ protocol, result in a robust communication link.

It would be interesting to fully characterize the electromagnetic noise in the place that hosts the ground station. This possibility will be considered as an activity in next phase.

In future developments, in order to enhance the signal level at the ground station input (P_{RX} at the downlink), some communication parameters are feasible to be changed:

- P_{TX} : On-board transceiver transmission power could be improved, despite the picosatellite limitations due to the restricted available power.
- G_{RX} : The ground station gain could be improved using an antenna with better gain or an antenna system disposing them in array to enhance its behaviour.
- F_{RX} : The ground station system noise figure (or its system noise temperature) would be better using a receiver with lower noise figure, decreasing the transmission line losses and optimizing the devices set up.
- L_{TX} : Using shorter and better cables in the ground segment configuration to reduce the cable losses.

ACKNOWLEDGMENT

We would like to acknowledge the job of all OPTOS team for the good development of the project, and also to the different companies that have collaborated with INTA: Thales Alenia Space-España, TTI Norte, SENER, ELTA and Sistemas Radiantes Moyano.

REFERENCES

- [1] H. Heidt, J. Puig-suari, A. S. Moore, S. Nakasuka, and R. J. Twiggs. Cubesat: A new generation of picosatellite for education and industry low-cost space experimentation, AIAA/USU Annual Conference on Small Satellites, 2000.
- [2] F. Sarmiento, C. Arza, C. Martinez, R. Amaro, C. Campuzano, V. M. Aragón, and Á. García, "OPTOS Project: New Generation Of Innovative Satellites," Small Satellites Systems and Services - The 4S Symposium, Madeira, Portugal, 2010
- [3] G. Maral, M. Bousquet, and Z. Sun. Satellite Communications Systems: Systems, Techniques and Technology, John Wiley and Sons, 2010
- [4] E. Gonzalez, "Diseño del S/S TTC del picosatélite OPTOS," OPT/51820/TNO/001/TASE, 2008
- [5] R. Amaro, "Ground segment technical note," OPT/60000/TNO/002/INTA, 2009
- [6] M. Carbonell, "Antennas Design Technical Note," OPT/51810/TNO/002/INTA, 2008
- [7] R. Amaro, "Especificación sistema de antenas estación de tierra OPTOS," OPT/60000/SPE/003/INTA, 2008
- [8] V. M. Aragón, "Link Budget," OPT/29200/TNO/002/INTA, 2010

Manufacturing and Testing of Ka-band Communication Payload of COMS

Jin Ho Jo, Moon Hee You, Seong Pal Lee, Jae Hoon Kim

Satellite & Wireless Convergence Research Department,
Electronics and Telecommunications Research Institute (ETRI),
Daejeon City, Rep. of Korea

E-mail: jhjo@etri.re.kr, moon@etri.re.kr, spallee@etri.re.kr, jhkim@etri.re.kr

Abstract—Communication, Ocean and Meteorological Satellite (COMS) is the multi-purposed Korean geostationary satellite funded by Korean government ministry, and is to supply communication services, ocean and weather observation for 7 years. As part of Communication, Ocean and Meteorological Satellite, Ka-band communication payload is developed by Electronics and Telecommunications Research Institute. The purpose of Ka-band payload development in Communication, Ocean and Meteorological Satellite program is to acquire space proven technology of Ka-band payload and to exploit advanced multimedia communication services. The Communication, Ocean and Meteorological Satellite was launched at end of June 2010 at French Guiana. The Ka-band payload function and performance were verified by in-orbit test after launch. In this paper, we will review development and in-orbit test of Ka-band payload system in Communication, Ocean and Meteorological Satellite program.

Keywords- Communication, Ocean and Meteorological Satellite; Ka-band payload; In orbit test

I. INTRODUCTION

Communication, Ocean and Meteorological Satellite (COMS) named Chunrian is the first geostationary satellite developed by local developers funded by Korean government Ministries including Ministry of Education and Technology, Korea Communication Commission, Ministry of Land, Transport and maritime Affairs, and Korea Meteorological Agency. COMS will be used for multi-purposes such as communication services, ocean and weather observation for 7 years. Ka-band communication payload development, as a part of COMS program, is sponsored by Korea Communication Commission and developed by Electronics and Telecommunications Research Institute (ETRI) with Korean local companies [1][6].

The purpose of Ka-band Payload development is to acquire space proven technology of Ka-band equipment and system and to exploit advanced multimedia communication services. ETRI with domestic technologies successfully finished Ka-band payload equipments development and system integration and testing at ground facility [3][4][5]. After satellite launch, ETRI verified all Ka-band payload function and performance are normal state by In Orbit Test (IOT) [7].

Ka-band Payload of COMS will be applied for R&D experiment, Test-bed for new technology verification and Public services test. Domestic developed technology of Ka

communication payload will be contributed to exploit new multi-media services [1][6].

In this paper, we will review integration, manufacturing process and test validation status of Ka-band communication payload of COMS. COMS configuration will be reviewed in Section 2, followed by Ka-band payload configuration in Section 3. Manufacturing and ground test activities will be reviewed in Section 4. Finally, in orbit test results of Ka-band payload will be reviewed in Section 5. Section 6 will present the conclusion and future works.

II. THE COMS OVERVIEW

The COMS is a multipurpose hybrid geostationary satellite launched at the end of June 2010. Many of Korean research institutes and industries are participated in COMS program for first Korean hybrid satellite program success. COMS program has been led by Korea Aerospace Research Institute (KARI) with the collaboration with EADS Astrium. ETRI was involved in Ka-band payload development with cooperation with Korean industries.

The COMS is a geostationary three-axis body-stabilized platform, which can support more frequent observation of atmosphere and ocean. This feature enables the COMS system to provide large volume of source data with high quality for meteorological and ocean research organizations [1].

Three mission payloads consist of Meteorological Imager (MI), Geostationary Ocean Color Imager (GOCI) and Ka-band Communication Payload System (COPS).

The MI is a radiometer, which measures energy from Earth's surface and atmosphere, which has one visible channel with 1km spatial resolution and four infra-red channels with 4km spatial resolution. The MI can scan a scene as large as the full Earth disc every 30 minutes, or smaller area as 1000km×1000km in less than 60 seconds. Radiometric data collected with MI is useful for cloud and pollution detection, storm identification, cloud height measurement, water vapor wind vectors, surface and cloud top temperature, etc.

The GOCI is the first ocean observation instrument operating in a geostationary orbit. It has eight visible channels with a spatial resolution better than 0.5km at the center of imaging area. The GOCI imaging area is 2500km×2500km around Korean peninsula. The GOCI is a step-stare type instrument to get sufficient radiometric energy within limited imaging time.

The Ka-band payload consists of transponder subsystem, antenna subsystem, and beacon assembly for the Ka-band fixed satellite service in the required service coverage. The Transponder subsystem includes all the necessary microwave hardware in order to receive, switch, amplify and transmit microwave signals. The antenna subsystem generates the three Ka-band beams for the South Korea, North Korea and Donbei region of China. The Beacon assembly generates Ka-band beacon signal for the rain attenuation experiment and antenna tracking. Figure 1 shows the COMS configuration in space [3][4][5][6][7].

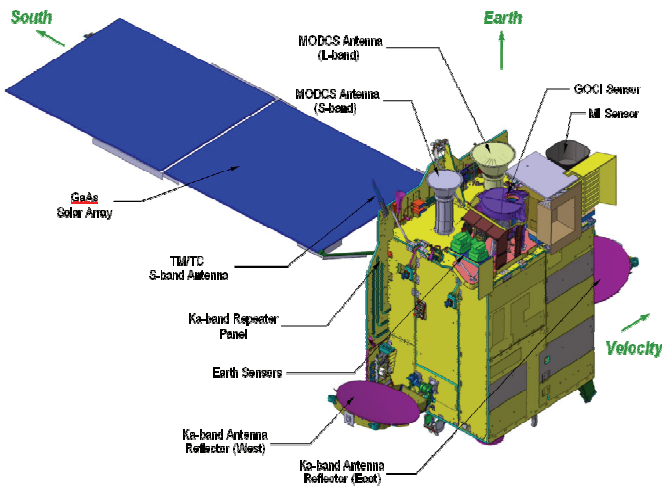


Figure 1. COMS configuration in space

III. KA-BAND PAYLOAD OVERVIEW

The Ka-band payload provides 100MHz wide four channels for fixed satellite service. Three channels are assigned for on-board switching for multi-beam connection and one channel is assigned for bent pipe connection. The uplink frequency band is 30GHz and the downlink frequency band is 20GHz. The multi-beam switching is performed at 3.4GHz band. Channel allocation and frequency plan of Ka-band payload are shown in Figure 2.

The Ka-band payload will provide communication services for natural disaster such as its prediction, prevention, recovery service in the government communication network and high-speed multimedia services such as Internet via satellite, remote-medicine, and distance learning in the public communication network. The Ka-band payload was designed to meet link availability 99.7% during the service period at BER 10^{-6} quality.

As shown in Figure 3 service coverage for the Ka-band payload system is two regions named by beam 1, 2 and 3. Beam 1 was assigned to the South Korea for national disaster service network and satellite multimedia service network, while beam 2 and 3 will be assigned to the North Korea and North-east of China respectively.

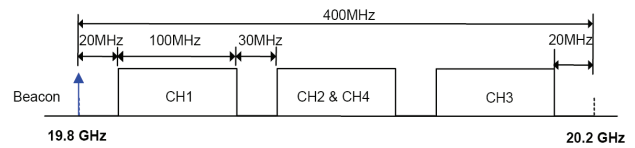


Figure 2. Ka-band payload frequency plan

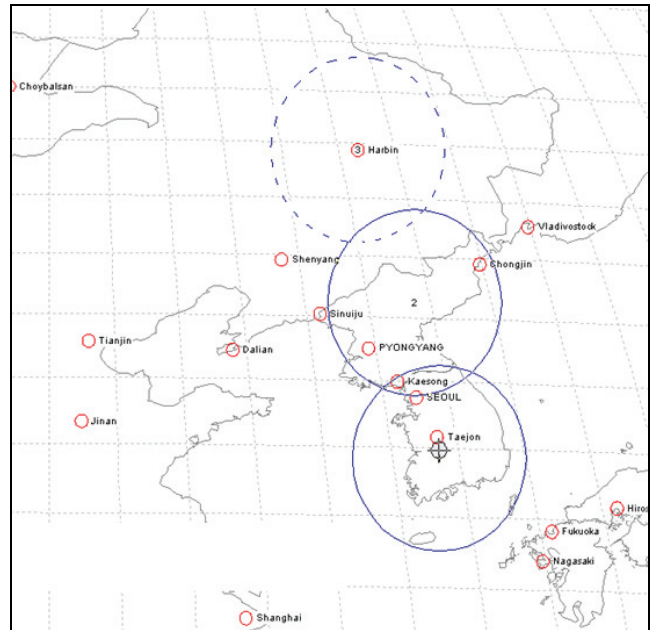


Figure 3. Ka-band payload beam coverage

The Ka-band payload consists of multi beam antenna and on-board switching transponder subsystem, which includes all the necessary microwave hardware in order to receive, switch, amplify and transmit microwave signals within the defined coverage area. The Ka-band payload system was designed to be capable of the communication service function among the individual beams [2][3][4].

The transponder subsystem supports beam switching function for high speed satellite multimedia services between each beams. To accomplish this mission 3.4GHz band Microwave Switch Matrix (MSM) was integrated in the transponder panel. The Figure 10, at end of this paper, shows the block diagram of Ka-band payload system. The antenna subsystem generates three Ka-band multi beams for the required coverage areas and simultaneously transmits and receives the microwave signal to and from the Earth station via beams, respectively. The China beam channel is reserved for standby channel for South Korea and North Korea channels. Table I shows the main specification of the Ka-band payload.

TABLE I. MAIN SPECIFICATION OF KA-BAND PAYLOAD

Parameters	Specifications
G/T	13dB/K
EIRP	58dBW
Power	< 1.1KW
Mass	< 100Kg
Frequency	TX: 19.8 ~ 20.2GHz RX: 29.6 ~ 30.0GHz
Satellite Longitude	128.2°E
Polarization	Linear

IV. MANUFACTURING AND TESTING

The Spacecraft (S/C) structure was equipped and tested with the combined propulsion system by EADS Astrium and shipped to Korea Aerospace Research Institute (KARI) in Korea. Spacecraft Assemble, Integration and Test (AIT) activities were then started with structure preparation and bus harness installation, just before unit level mechanical and electrical integration. Then, Spacecraft Functional Test (SFT) was performed [5]. The Ka-band transponder integration was performed at ETRI, in parallel, on a wall provided by EADS Astrium, and verification tests were performed at equipment level and subassembly level. Then, the wall equipped with Ka-band was delivered to KARI for spacecraft level integration and system level testing. MI and GOCI were delivered to KARI and assembled, integrated and tested at subassembly level.

The S/C system level activities were started with the transfer and the electrical coupling of the Ka-band payload onto the bus. Then, MI and GOCI were mechanically installed and electrically integrated on the bus.

The test program was continued with the “integrated system test” to baseline the satellite electrical performance prior to environmental exposures: complementary functional tests to check the integrity of both bus and payloads and to cover modified hardware and interfaces during payloads/bus mating; a conducted EMC was performed to measure the spacecraft performances.

Before mechanical qualification, the spacecraft assembly was completed with the integration of antennas and solar array wing. At this stage, all the spacecraft alignments and all the release, deployment, and trimming tests of mechanisms were performed.

The fully assembled spacecraft was submitted to a first S/C health check test then to mechanical qualification tests (sine vibration, acoustic noise). At the end of the mechanical tests, the fully assembled spacecraft was submitted to a second S/C health check test in order to verify S/C integrity and to a launch vehicle adaptor fit-check. Release/deployment tests of mechanisms, alignment checks were performed to verify the system integrity and performances after mechanical exposures. After solar array wing and the deployable antennas were removed, the spacecraft was submitted to the thermal balance and thermal vacuum exposure. Functional and performance tests are performed for selected thermal conditions.

After thermal qualification, Chemical Propulsion System (CPS) performance test was performed to verify the system integrity. The deployable reflectors were re-integrated on the spacecraft, the release / deployment / trimming tests of the mechanisms and the alignments checks was performed in the RF compact range. With the reflectors deployed and clamped in the nominal flight position, the final SFT with the same hard-line connections than the previous ones, a ground segment compatibility and authentication test, the antennas performance tests and the RF compatibility was performed to complete the spacecraft integrity and performance verification. The spacecraft integration was achieved with the final integration of solar array. After external finishes, the spacecraft physical property was measured. The spacecraft was ready for storage or shipment to the launch site. The Figure-4 shows the Ka-band payload AIT flow.

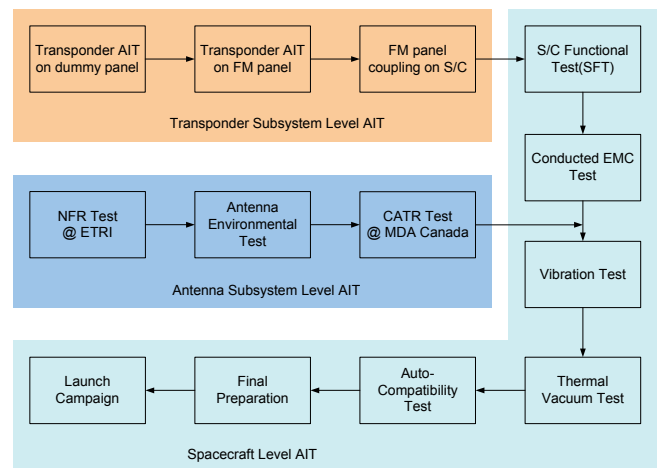


Figure 4. Ka-band payload AIT flow

V. IN ORBIT VALIDATION

After the successful launch of a satellite and verification that it has reached its geosynchronous orbit position, the spacecraft antennas have been deployed. This was followed by an intensive test program called In Orbit Test (IOT). The purpose of IOT is to determine whether the satellite and its subsystem have survived the launch, and whether subsystem performance is as expected. Hereinafter we will review IOT system configurations and review Ka-band payload IOT results.

A. IOT System

An integrated suite of microwave measurement equipment, computer hardware, and measurement software was designed, fabricated, and installed into a unified test facility for measuring the performance of Ka-band payload of COMS. IOT measurements are performed by transmitting test signals to spacecraft and comparing their power, frequency with the signals re-transmitted from the satellite. The major components of the Ka-band IOT facility are the IOT equipment, the Earth station equipment, and the large size reflector TX/RX antenna. The Earth station equipment

receives uplink signal generated by the IOT hardware, perform frequency conversion from L band to Ka-band, amplifies them, and transmits them to the antenna system. It then receives downlink signal from the spacecraft, amplifies them, perform frequency conversion from Ka-band to L band, and transmits them to the IOT equipment for measurement. Table II shows the Ka-band IOT system equipment description and Figure 5 shows the IOT system diagram respectively.

TABLE II. IOT SYSTEM EQUIPMENT

	Equipment	Description
Earth station equipment	Antenna	Reflector size: 7 meters Gain: 63.5dB in 30GHz 60.4dB in 20GHz
	Up-converter	Frequency conversion from 1.2GHz to 30GHz
	HPA	Up to 175W output
	LNA	Gain: 50dB
	Down-converter	Frequency conversion from 20GHz to 1.2GHz
IOT equipment	Signal generator	Up to 3GHz
	Spectrum analyzer	Up to 3GHz
	Power meter	Up to 33GHz
	Frequency counter	Up to 40GHz
	IOT console	PC with windows-xp

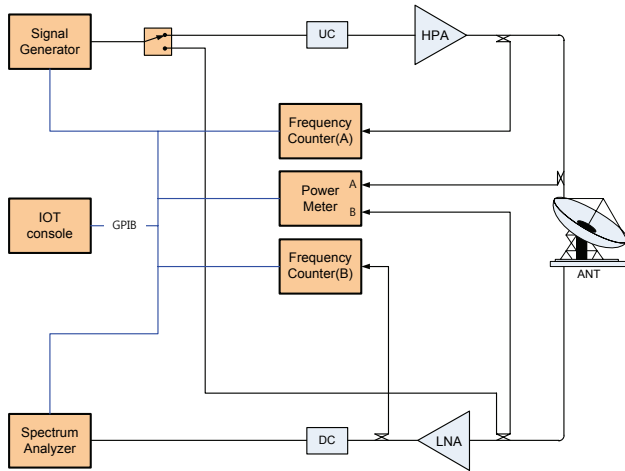


Figure 5. Ka-band IOT system diagram

B. IOT Results

Ka-band payload IOT was performed in two phases. The first phase is antenna pattern measurement and the second phase is payload RF performance measurements.

1) Antenna Pattern Measurements

The roles of the Antenna Pattern Measurements (APM) are to check that the satellite antennas were not damaged during the launch and to check that the antenna pointing alignment were not disturbed by the launch. For the APM,

the spacecraft needs to be rotated during IOT station transmit test signal to satellite and receive returned signal from the satellite. The spacecraft was rotated $\pm 1^\circ$ from the beam center in azimuth angle and elevation angle respectively with $0.1^\circ/\text{min}$. speed. The IOT station transmit CW signal to satellite and measure returned signal from the satellite to get relationship between signal strength vs. spacecraft rotation angle. During the APM, Channel Amplifier mode of Ka-band payload was selected to Fixed Gain Mode (FGM) and Automatic Level Control (ALC) respectively. The antenna Transmit (TX) pattern can be measured in ALC mode, whereas antenna Receive (RX) pattern can be derived from the measurements in ALC mode.

The antenna patterns measured during the IOT were compared with Compact Antenna Test Range (CATR) measurement results performed on ground facility. The APM of IOT and CATR are very similar and this confirms there was no antenna performance degradations by the vibration during the satellite launch. The Figure 6 and Figure 7 show APM results of IOT and compared with the CATR results performed in ground facility [4][7].

Figure 6 shows satellite antenna TX pattern of beam 1. The dotted line is APM results from IOT and solid red line is APM results from CATR measurement in ground. The two patterns similarity shows that satellite antenna performance was not degraded by the launch vibration. Figure 7 shows combined TX and RX pattern of beam 1.

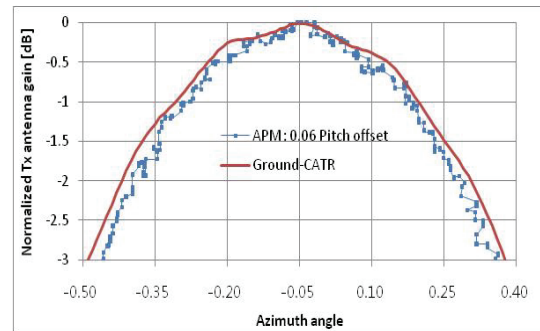


Figure 6. TX pattern of beam 1

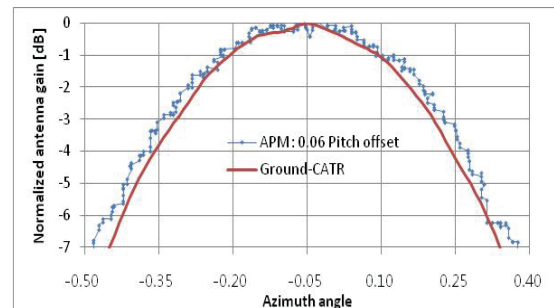


Figure 7. TX+RX pattern of beam 1

2) Payload RF Performance Tests

The purpose of payload RF performance tests are to check Ka-band transponder was not damaged during the launch. The test parameters are as followings.

- IPS/EIRP (Transfer characteristics)
- Amplitude vs. Frequency Response (AFR)
- Frequency conversion characteristics
- Payload G/T
- FGM function
- ALC function

a) IPS/EIRP Measurements

IOT station generates CW carrier and transmit to the spacecraft. The returned CW signal from the spacecraft is monitored by the Spectrum Analyzer in the IOT station and compare with the transmission signal. The uplink CW carrier signal power was increase 1dB step until monitored downlink signal power was saturated. When the downlink signal power is in saturation, input power to the spacecraft transponder is called Input Power Saturation (IPS) and transponder output power is called saturation Effective Isotropic Radiation Power (EIRP). The measured IPS/EIRP of the Ka-band payload was similar with ground test results. Figure 8 shows the transponder input and output power transfer characteristics.

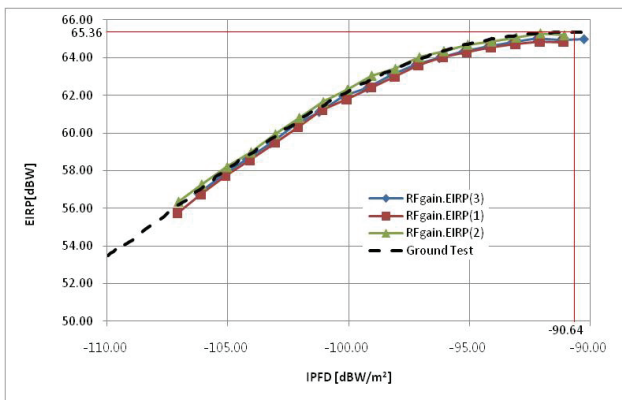


Figure 8. Transfer characteristics of channel 1

b) Amplitude vs. Frequency Response Measurements

The amplitude vs. frequency response measurement is to be performed when transponder in linear condition. The uplink signal is swept from starting frequency to stop frequency over the channel band with 2MHz steps. The downlink signal is measured by spectrum analyzer and compensate uplink path and downlink path frequency response to get satellite transponder frequency response. The measured amplitude vs. frequency response during the IOT was similar with ground test results. Figure 9 shows transponder amplitude vs. frequency response characteristic of the channel 4.

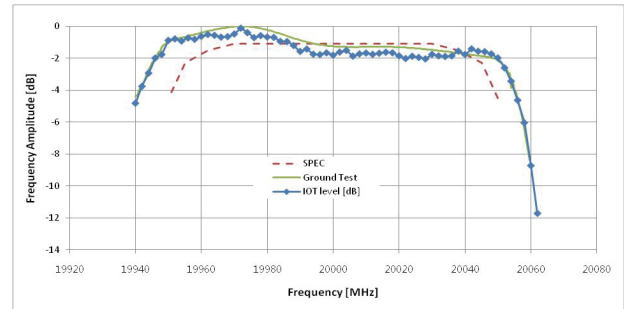


Figure 9. Amplitude vs. frequency response of channel 4

VI. CONCLUSION AND FUTURE WORKS

In this paper, we reviewed integration, manufacturing and test validation of Ka-band communication payload of COMS. The similarity between in-orbit test results and ground test results are confirms that Ka-band payload was well withstands launch environments and also performances are not degraded in space environments. At this moment, 3D-HDTV broadcasting and broadband VSAT communications are in trial service through Ka-band payload. The first made in Korea Ka-band telecommunication payload of Chunriang satellite will be used for satellite R&D experiments, test-bed for new satellite telecommunication technology verification test and public services test. The space proven technologies from the COMS program will be used for next telecommunication satellite development.

REFERENCES

- [1] S.P. Lee, "Development of Satellite Communication System for COMS", Proceedings of APSCC 2004, pp. 71-96.
- [2] J.H. Lee, J.H. Kim, S.P. Lee, and H.J. Lee, "Multi-beam Satellite Antenna Design", IEEE International Symposium on Antenna and Propagation and USNC/URSI National Radio Science Meeting, July 2004, Session 84.
- [3] J.S. Choi, Y.D. Lee, and S.P. Lee, "Development of Ka-band Multibeam Antenna", 13th Ka and Broadband Communications Conference, 2007, K000055.
- [4] J.S. Choi, Y.D. Lee, and S.P. Lee, "CATR Test for Ka-band Multi-beam Antenna", 26th International Communications Satellite Systems Conference (ICSSC), June 2008, AIAA 2008-551.
- [5] J.H. Jo, H.J. Woo, and S.P. Lee, "The Design and Implementation of Electrical Ground Support Equipment (EGSE) for COMS Ka-band Transponder Testing", 26th International Communications Satellite Systems Conference (ICSSC), June 2008, AIAA 2008-5436.
- [6] S.P. Lee, J.H. Jo, M.H. You, J.S. Choi, and K.B. Ahn, "Ka-band Communication Payload System Technology of COMS", JC-SAT2010, October 2010, pp. 19~24.
- [7] S.P. Lee, J.H. Jo, M.H. You, J.S. Choi, "Integration, Testing and In Orbit Validation of Ka-band Communication Payload of COMS", ICTC-2010, pp. 309~313.

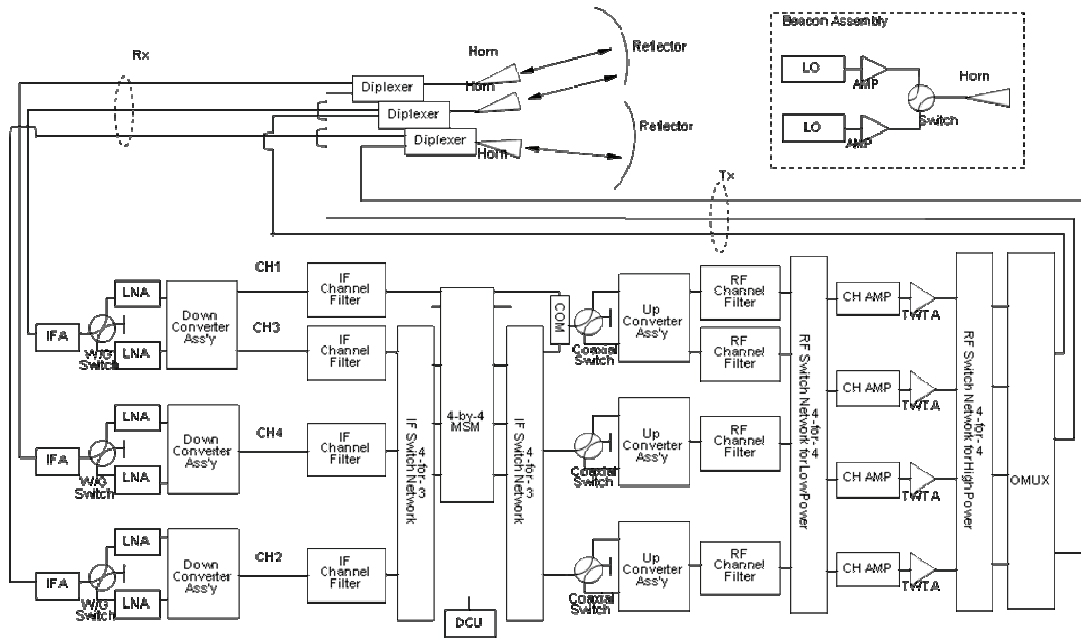


Figure 10. Block diagram of Ka-band payload system

The On Board Software of the Herschel HIFI Instrument

L. Piazzo¹, A. M. Di Giorgio², F. Nuzzolo¹, P. Cerulli-Irelli²,
L. Dubbeldam³, D. Ikhenade¹, S. J. Liu², S. Molinari² and S. Pezzuto²
(1) DIET Dept. - University of Rome "La Sapienza" - Italy
(2) IFSI Inst. - Istituto Nazionale di Astrofisica - Italy
(3) SRON - Netherlands Institute for Space Research - The Netherlands
Corresponding author: L. Piazzo - lorenzo.piazzo@uniroma1.it

Abstract—The Heterodyne Instrument for the Far-Infrared onboard the ESA Herschel satellite is a heterodyne spectrometer with unprecedented frequency range, resolution and sensibility. It is composed of two spectrometers, a Local Oscillator Unit, producing the mixing signals, a Focal Plane Unit, performing mixing and amplification, and an Instrument Control Unit, hosting a DSP where the On Board Software (OBS) runs. The OBS coordinates the other units, manages the interface with the spacecraft and monitors the instrument status. A synthetic description of the OBS organization and functioning is presented in this paper.

Keywords- space technology; satellites.

I. INTRODUCTION

The Heterodyne Instrument for the Far-Infrared (HIFI) [1] is one of the instruments onboard the ESA Herschel Space Observatory (HSO) [2], which was launched in May 2009 and is now fully operational. It is a heterodyne spectrometer where the signal from the telescope is mixed with a local reference before being fed to the spectrometers. In this way the wide frequency range from 480 to 1910 GHz can be covered with unprecedented resolution and sensibility. The instrument was developed by a team of engineers, scientists and managers from 12 European and North American countries, founded by their national space agencies.

The instrument is equipped with two spectrometers, namely the Wide Band Spectrometer (WBS) and the High Resolution Spectrometer (HRS). The WBS is an acousto-optical spectrometer covering up to 7 bands within the frequency range with a resolution of 1 MHz, each band being 4 GHz wide. In each band, the HRS, which is a correlator spectrometer, can cover up to 8 sub-bands of 235 MHz with a resolution up to 125 KHz.

A block diagram of the instrument is shown in Figure 1. In addition to the spectrometers, which are duplicated in the Vertical and Horizontal polarizations, there are the Local Oscillator Unit (LOU), the Focal Plane Unit (FPU) and the Instrument Control Unit (ICU). The LOU generates the mixing signals for the 7 bands, deriving them from a reference frequency source. In the FPU the telescope signal is mixed, amplified and fed to the spectrometers. The FPU also hosts a chopper mechanism and a calibration source. The ICU generates the control and timing signals for the

other subsystems and realizes the interface between the instrument and the spacecraft's Command and Data Management Subsystem (CDMS).

The core of the ICU is a DSP running the On Board Software (OBS). The OBS was developed in cooperation by the IFSI Institute of the INAF (Istituto Nazionale di Astrofisica) and by the DIET Department of the University of Rome. It was funded by the Italian Space Agency (ASI). The Netherlands Institute for Space Research (SRON) contributed to the specification activity. The aim of this paper is that of giving a synthetic description of the OBS organisation and functionalities, highlighting the main design issues and implementation choices.

The paper is organised as follows. After a short introduction to the ICU in Section II, the Operating System and its main services are introduced in Section III, while the OBS is described in some detail in Section IV. Finally, Section V considers the development and testing system.

II. THE ICU

The ICU was developed by Carlo Gavazzi Space S.p.A. [3] and the high level block diagram is shown in Figure 2. It is composed by two boards, a CPU board, hosting a DSP and three memory banks (RAM, EEPROM, PROM), and a Payload Interface (PL/IF) board, hosting a 1553 chip, the Low Speed interface Electronic (LSE) and the High Speed interface Electronic (HSE).

The CPU board is based on the Analog Devices 21020 DSP [4], [5]. The CPU is clocked at 20MHz, with 50ns

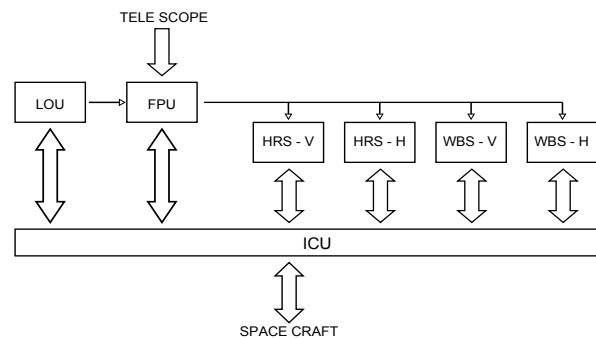


Figure 1. Block diagram of the HIFI instrument.

instruction cycle time and has a processing power of 20 MIPS with 66MFlops (peak) of instruction rate. The board includes a 2 MB data RAM (512k words of 32 bits), a 3 MB program RAM (512k words of 48 bits), a 1MB EEPROM memory (256k words of 32 bits) and a 32 KB PROM. The EEPROM is used to store the OBS whilst the PROM is used to store the Boot Software (BS), which is executed at the switch on. The BS simply loads the OBS into the program RAM, normally by copying it from the EEPROM, and starts its execution.

A. CDMS interface

The interface with the CDMS is based on a protocol structured into three layers. The highest one is the application layer, which is based on the ESA Packet Utilisation Standard (PUS) [6]. This layer defines the structure of the Telemetry (TM) and Telecommand (TC) data packets, which are used to transport the information across the interface.

The two lower layers are the physical and data link layers, which are based on the MIL-STD-1553B standard [8], [7], tailored for the specific requirements of the ESA Herschel mission. These layers regulate the exchange of the TC and TM packets. Communication takes place (at 400KHz with words of 16 bit) in regularly paced time slots and is mastered by the CDMS, which allocates the time slots (64 per second), signals the beginning of a slot by rising the 1553 interrupt (1553-INT) and possibly writes a TC in the 1553 chip memory. In response to the interrupt the OBS can upload the TC or write into the 1553 chip memory a TM packet that will be read by the CDMS at the end of the time slot.

B. Low speed interface

The LSE is the low rate (312.5KHz) interface with the subsystems and is used to transfer control and status data. The LSE has three registers, the transmit register (TXREG), the receive register (RXREG) and the Control Register (CREG), which are mapped into the DSP memory. The CREG is used to control the LSE while the other two are

used for communication with the subsystems. Specifically, when the LSE is ready, the OBS can send a Low Speed Command (LSC) to a subsystem by writing it into the TXREG. The LSE switches to the not ready status, decodes the command, dispatch it to the appropriate subsystems and, after a time that varies depending on the LSC and can be as high as 3 msec, returns to the ready status.

A special type of LSC, which can be sent to the FPU and LOU only, is the Housekeeping Request (HKR), which is a LSC requiring the destination unit to report information about its status. In response, the unit writes the requested information into the RXREG where it can be directly read by the OBS. Examples of LSC are reported in Table I.

C. High speed interface

The HSE is the high rate (2.5MHz) interface with the spectrometers and is used to gather science and status data. The HSE has four hardware FIFO, of 16K words of 24 bits, together with a control register, which is mapped into the DSP memory and is used to control the HSE. The DSP can request data to a spectrometer by sending a specific, data transfer LSC. When the LSC is received, the spectrometer forms a science data frame, constituted by spectroscopy data and housekeeping data, and writes the frame into the FIFO. The WBS frame is 8210 words long and takes approximately 900 msec to be written while the HRS frame is 4160 words and takes approximately 42 msec.

The FIFO are accessible to the OBS because the first word of each FIFO is mapped into the DSP memory and can be read. Furthermore, as soon as the word is read, all the other words are shifted downwards so that, by repeatedly reading the first word, the OBS can extract the whole frame. The OBS must be careful not to read when the FIFO is void, to avoid garbage data, and not to request a data transfer while a data transfer is already ongoing, to avoid data misalignment.

Finally, note that the HSE rises the FIFO Half Full interrupt (FHF-INT) when one of the FIFO becomes half full. This interrupt can be used by the OBS to trigger the FIFO flushing.

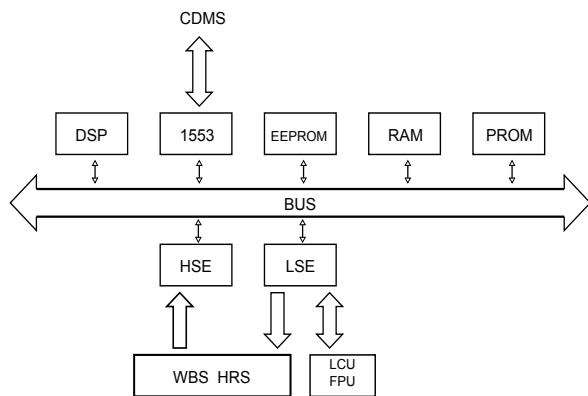


Figure 2. Block diagram of the ICU.

III. OPERATING SYSTEM AND LIBRARIES

The OBS is written in C language (except for a few lines in DSP assembler) and runs under the Eonic Virtuoso real

Hex	Destination	Action
0xFC00 0003	WBS H/V	Start integration
0xFC00 0005	WBS H/V	Stop integration
0xE400 0006	WBS H	Data transfer
0xE800 0006	WBS V	Data transfer

Table I
EXAMPLES OF LSC. COMMANDS TO START AND STOP THE WBS INTEGRATION AND TO REQUIRE THE TRANSFER OF THE INTEGRATION BUFFER.

additional type of packet that can be put in the queues is the Feedback Request (FBR), which forces the LSI module to produce feedback to some other module of the OBS and is useful to synchronise the modules.

Processing is carried out by task *ls*, which is in a wait state on the input queues. As soon as a packet is put in one of the queues the task wakes up and processes all the packets in the queues, starting from the HPQ. For a LSC the processing simply involves writing the command to the TXREG. For HKR it also includes the readout of the RXREG and the copying of the HK data in the memory address specified by the packet. A FBR typically involves putting a packet into the input queue of another module or rising an event. When the queues are void, the task goes back to a wait state.

C. High speed interface and science data processing

The high speed interface with the spectrometers is managed by the HSI module, hosting tasks *hs0*, *hs1* and an input queue for *hs1*. Science data frames are extracted from the FIFO in blocks shorter than half a FIFO. The low level reading is carried out by task *hs0*, which is in a wait state over the FHF-INT. When the interrupt is raised, *hs0* extracts a block from the FIFO, concatenates it with the previously extracted blocks and checks whether a whole science data frame has been extracted. If yes, *hs0* put a packet with the frame into the input queue of *hs1*.

Task *hs1* is in a wait state over its input queue and is waked up by the packet. This task performs initial processing of the science data. It extracts the HK information and copies it into the the HK-HDL module by direct memory access. If required, it also performs the coaddition of the frame with previously received frames. Then it checks if a fully coadded science frame has been formed. If yes, it put a packet with the frame into the input queue of module DATA-HDL.

The procedure just described is simple, prevents FIFO overflow (because the FIFO are automatically emptied when they are half full) and guarantees that no garbage data is read (because a block is less than half FIFO). However it always leaves a block in the FIFO (because a block is too short to trigger the FHF-INT) while there are times when the OBS needs to completely flush the FIFO. For this reason, the HSI module also hosts task *hs_flush*, which, upon wake up, checks the FIFO, extracts the pending blocks and passes the frames to *hs1*. That task is in a wait state over the FLUSH-EV event and can be activated by any module of the OBS by rising that event.

Finally, the DATA-HDL module completes the processing of the science data, by means of task *data_hdl*, which is in a wait state over its input queue, the Data Handler queue (DHQ). The processing varies¹ and may include computing the total power in given bands, spectrum scaling to adjust

¹The OBS maintains a global variable, *activity_id*, indicating the current activity, which is used by DATA-HDL to decide the appropriate processing.

the dynamic range, breaking the frame into a several SD-TM packets and writing the packets into the SDQ.

D. Housekeeping

HK production is carried out by task *hk_hdl* of the HK-HDL module. This task is in a wait state over the Housekeeping Timer (HKT). The countdown of the HKT is started the first time when a specific TC, switching on HK production, is received by the OBS. When the counter reaches zero, task *hs_hdl* is waked up and its first action is to start again the HKT countdown with a given, programmable initial value. In this way the task is activated on a regular basis and the activation rate is controlled by the initial value loaded in the HKT. Typical rates are from 1 to 0.25 Hz.

Task *hk_hdl* has to produce an HK-TM packet each time it is activated. Concerning the HK data from the spectrometers, these are written by the LSI module into the HK-HDL module every time that a science data frame is received. Therefore, provided that frames are regularly produced, task *hk_hdl* finds the HK in its memory and does not need to explicitly acquire them. However the task has to guarantee a regular frame production. Therefore the task's second step is to check if the spectrometers are being used by some other OBS module². If yes, the frames will be produced by the other module's transfer requests. If not, *hk_hdl* issues a data transfer request, by placing the corresponding packet into the LPQ.

The third step of the task is to send a sequence of HKR to the FPU and the LOU in order to acquire their HK. This is done by placing the corresponding packets into the LPQ. The sequence is closed by a FBR packet, requiring LS to rise the event HK-EV. Next the task goes into a wait state over the HK-EV. When LS has processed all the HKR and rises the HK-EV, the task is waked up and all the HK data are there in its memory. The task can format a HK-TM packet, put the packet in the HKQ and go back into a wait state over the HKT.

E. TC classification

There are several issues concerning TC execution. Firstly note that the TCs are received with a maximum rate of four per second, are executed in the order in which they are received and, in normal operation, they are paced so that a new TC is received only when the previous TC was completed. However the OBS needs to be robust against the case where a new command is received while an old one is still running, which can happen by mistake or because the CDMS wants to stop the running command. In such a case, normally, the old command needs to be aborted before the new one is started, even though some commands can be executed in parallel, as we see later.

Secondly, when the TC requires the use of the HSI, before starting the TC execution the OBS needs to check whether

²By checking *activity_id*.

the HSI is busy or not. In fact the HSI may be transferring data requested by the HK-HDL module or by an older TC. If the HSI is busy, the OBS has to guarantee a safe transition of the HSI to the new command, in order to avoid misalignment or garbage data.

Finally, while most commands have time requirements on the order of the msec, spectrometry commands have time requirements on the order of the usec, which are difficult to guarantee even within the Virtuoso RTOS.

In order to deal with these issues, the TCs are divided by the OBS into four classes, having different requirements. The classes are reported in the following list and will be discussed in the next subsections.

Short TC (S-TC): execution time less than 250 msec. Does not access the spectrometers. Example: OBS configuration, HK handling (switch on, switch off, rate setting).

Low Speed TC (LS-TC): execution time more than 250 msec. Does not access the spectrometers. Example: memory dumping, FPU and LCU configuration and monitoring.

High Speed TC (HS-TC): execution time more than 250 msec. Access the spectrometers with loose time requirements (msec). Example: WBS and HRS calibration and monitoring.

Real Time TC (RT-TC): execution time more than 250 msec. Access the spectrometers with strict time requirements (usec). Example: spectrometry.

F. Short TC and TC front-end

The front-end of the command execution is module CMD-SEQ, hosting task *cmd_seq*. This task is in a wait state on its input queue, the Command queue (CMDQ). As soon as TMTC put a TC packet in the queue the task wakes up and performs basic integrity checks on the TC (e.g., checksum, length). If these are passed, it decodes the command and checks its type. If the TC is a short one it is immediately executed, within the *cmd_seq* task, possibly in parallel with another, non short TC already running. This is possible because short commands are completed before the next TC is received and do not access the spectrometers.

If the TC is not a short one, task *cmd_seq* updates the data on the currently running command, possibly aborting a previously running TC, and forwards the TC either to the LS-HDL or to the HS-HDL module by copying it into a packet and putting the packet into the corresponding input queue.

G. Low speed TC

LS-TC are dispatched to and executed by the LS-HDL module, hosting task *ls_hdl*, which is in a wait state over its input queue, the Low Speed queue (LSQ). In order to simplify the command aborting and increase the code structuring, every LS-TC is broken down into a sequence of steps. Every step is triggered when a specific packet is extracted from the queue, the first step being triggered by the

LS-TC itself. Furthermore, every step ensures that a packet triggering the successive step is put in the LSQ, so that the whole command is executed.

To clarify the execution, let us discuss the processing of a simple LS-TC requiring a set of HK data from the LOU. The first step copies the TC parameters (i.e., the set of HK data to be required) into the internal memory of the LS-HDL module and put into the LSQ the packet triggering the second step. The second step put a sequence of HKR into the HPQ in order to gather the required HK data and closes the sequence with a FBR, requiring LS to put into the LSQ the packet triggering the third step. When the third step is triggered, the LS module has already processed all the HKR of the sequence. Therefore the third step can format the HK data into a HK-TM packet and put the packet into the HKQ.

H. High speed TC

HS-TC are dispatched to and executed by the HS-HDL module, hosting task *hs_hdl*. This task is in a wait state over its input queue, the High Speed queue (HSQ). Also HS-TC are broken down into smaller steps and their execution is almost identical to the execution of a LS-TC. One difference is that the first step has to check whether the HSI is busy or not. If there are no pending frames in the HSI³, it put into the HSQ the packet triggering the second step. If there are pending frames, the first step waits a programmable time⁴ and posts the HS-TC back into the HSQ in order to be triggered again. A second difference is that the successive step is typically triggered by feedback from the DATA-HDL module and not from the LS one.

To clarify the the processing let us describe (a simplified version of) the WBS calibration. The first step is triggered when CMD-SEQ put the TC in the HSQ. When the HSI is free, the first step triggers the second step by placing the corresponding packet into the HSQ. The second step issues a sequence of LSC commands to LS in order to perform a WBS integration followed by a data transfer request. The science data frame is extracted by the HSI module and passed to the DATA-HDL module, which computes the frame total power, breaks the frame into SD-TM packets, put the packets into the SDQ and eventually put a feedback packet into the HSQ triggering the third calibration step. The third step exploits the total power to set the WBS attenuators, formats an HK-TM packet with a calibration report and put the packet into the HKQ.

I. Real Time TC and the Virtual Machine

Due to the strict time requirements on the RT-TC, these TCs cannot be executed using the RTOS services, which

³The OBS maintains four counters indicating how many frames are pending within each FIFO. These counters are increased when a data transfer is requested by any module and decreased when the HSI extracts a frame.

⁴The task also issues a FLUSH-EV in order to flush the FIFO and updates *activity_id* in order to stop any data transfer request to the spectrometers.

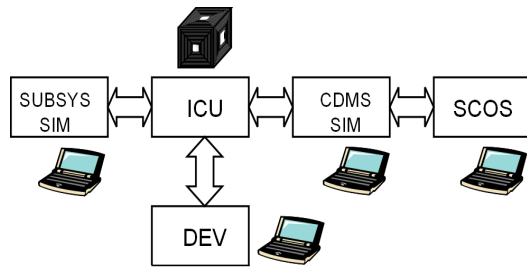


Figure 4. The development and testing system.

have a timing jitter on the order of the msec. In order to execute these commands, the OBS implements a dedicated command interpreter, termed the Virtual Machine (VM). The VM is called by the Interrupt Service Routine (ISR) of the TIME-INT interrupt, which is the DSP highest priority interrupt, raised when a hardware timer, based on the high resolution clock, reaches zero. At every call, the VM executes one or more steps of a program written in VM assembly language and restarts the timer with a proper initial value, in order to trigger its next execution round. The assembly includes basic programming instructions (e.g., assignment, *if*, *goto*). Furthermore the VM can send LSC to the spectrometers by directly accessing the TXREG. In this way the VM can execute all the spectroscopy commands. There are different VM programs for the different commands, and these are handled by the OBS, which stores the programs as binary vectors and can upload them into the VM memory for execution. Furthermore the OBS can switch on or off the VM by enabling or disabling the TIME-INT.

RT-TC are dispatched to the HS-HDL module and are handled like HS-TC with a single step. The step is similar to the first step of an HS-TC. It checks the HSI status and put the RT-TC back in the HSQ until the HSI is flushed. When the HSI is found ready, the step loads the appropriate VM program and start the VM execution by enabling the TIME-INT. From this point on the TC is executed by the VM, which typically issues a long sequence of integration and data transfer requests. The only modules of the OBS involved are the HSI, which extracts the data frames and put them into the DHQ, DATA-HDL, which breaks the frames into SD-TM packets and put the packets into the SDQ, and TMTC, which passes the TM to the CDMS.

V. DEVELOPMENT AND TESTING

The OBS development was carried out in parallel by several developers, exploiting the Concurrent Versioning System (CVS) [10]. It started in year 2000 and is now in the maintenance phase.

The development and testing system is shown in Figure 4. The core of the system is the electric model of the ICU, which is a prototype of the actual ICU, featuring all the characteristics of the final device. A second piece of

hardware is the subsystem simulator (SUBSYS-SIM), which is a board mounted on a PC, capable of emulating the signals and timing of the other HIFI units (LOU, FPU, WBS and HRS) at the electric level. These two components allow to test the interface between the ICU and the instrument. A second PC (CDMS-SIM) was equipped with an off the shelf 1553 board and a software simulator of the CDMS, allowing to emulate the interface with spacecraft. The CDMS-SIM was connected via a LAN to a third PC (SCOS) running the Satellite Control and Operation System (SCOS2000) application, which is the standard ESA mission control software [11]. In this way the whole chain, from the mission control facility to the instrument, could be emulated. An additional PC (DEV) hosted the DSP development kit, which included a JTAG probe directly connected to the DSP, allowing to place breakpoints to pause the execution and inspect the DSP memory and registry.

A test procedure involved issuing a sequence of TCs from the SCOS application and gathering the resulting TM. Since the output produced by the subsystem simulator (both the science and the HK data) can be set to given values, the resulting TM can be checked against the expected TM, thereby allowing to prove the correct functioning of the OBS. A number of test procedures, covering a wide range of functionalities, were included in a test plan and the test plan was carried out at each software update, in order to validate the OBS. Naturally additional tests were carried out at the SRON and ESA premises using the real hardware.

REFERENCES

- [1] T. de Graauw et al., "The Herschel-Heterodyne Instrument for the Far-Infrared (HIFI)", *Astronomy and Astrophysics*, Vol. 518, L6-12, July 2010.
- [2] G. Pilbratt et al., "Herschel Space Observatory", *Astronomy and Astrophysics*, Vol. 518, L1-5, July 2010.
- [3] www.cgspace.it/index.php?option=com_content&task=view&id=178 (last accessed 1/28/2011)
- [4] T. K. Pike et al. "OMI building blocks and developments for future high performance processing systems in the aerospace and automotive fields: DSP, SMCS and VIRTUOSO", *Proc. of the IEEE Conf. on Electronics, Circuits, and Systems (ICECS)*, Vol 1, pp. 610-613, 1996.
- [5] www.analog.com/en/embedded-processing-dsp/adsp-21xx/processors/index.html (last accessed 1/28/2011)
- [6] ESA Ground systems and operations - Telemetry and Telecommand Packet Utilization- ECSS-E-70-41A, January 2003.
- [7] MIL-Std-1553 B, Digital Internal Time Division Command/Response Multiplex Data Bus, Issue Notice 2, 8 September 1986
- [8] E. H. Philips, "The Electric Jet.", *Aviation Week and Space Technology*, Vol 5. No. 2, Feb. 2007.
- [9] S. Hustin, M. Potkanjak, E. Verhulst and W. Wolf, "Real-Time Operating Systems for Embedded Computing", *Proc. of the 1998 IEEE/ACM international conference on Computer-aided design*, pp. 388-392, 1998.
- [10] www.tortoise cvs.org/ (last accessed 1/28/2011)
- [11] www.egos.esa.int/portal/egos-web/products/MCS/SCOS2000/ (last accessed 1/28/2011)

Public Protection and Disaster Relief by Satellite-based Communications Network

Yong-Min Lee

Satellite & Wireless Convergence Research Dept.
Electronics and Telecommunications Research Institute
Daejeon, Republic of Korea
ymlee01@etri.re.kr

Bon-Jun Ku and Do-Seob Ahn

Satellite & Wireless Convergence Research Dept.
Electronics and Telecommunications Research Institute
Daejeon, Republic of Korea
bjkoo@etri.re.kr, ahnds@etri.re.kr

Abstract— Various communication means which are not only possible technologies of the moment but also from a peanut-size network to an extensive scale should be integrated for public protection and disaster relief (PPDR). Wireless fixed ad hoc network and mobile ad hoc networks is useful to quickly establish an instant communications system to support emergency management and the urgent missions in the incident disaster area. The competent area network is used for dedicated communication and information sharing between rescue teams and 3G/4G mobile networks could be deployed to expand local networks reaches the working terrestrial base stations. To interconnect the long distance remote disaster site and cover the wide area a satellite system is mainly used for transferring the collected data by sufficient link capacity. The example of homogeneously integrated network for PPDR is described and IP-based satellite network is proposed to provide emergency management services which facilitate the matter of high data rate and quick deployment.

Keywords- PPDR; disaster; management; satellite-based communication; interated; network

I. INTRODUCTION

Almost every day, many kinds of disaster are reported by newspapers, radio and television channels from over the world. A disaster can be defined as “A serious disruption in the functioning of the community or a society causing wide spread material, economic, social or environmental losses which exceed the ability of the affected society to cope using its own resources”[1].

A disaster is a result from the combination of hazard, vulnerability and insufficient capacity or measures to reduce the potential chances of risk. Various disasters like earthquake, landslides, volcanic eruptions, fires, flood and cyclones are natural hazards that kill thousands of people and destroy billions of dollars of habitat and property each year. The recurrent occurrences of various natural and manmade disasters like the December 2004 Tsunami, the bomb blasts in the cinema halls of Delhi and many such incidences have diverted our focus towards safety of one’s own life.

Disasters are as old as human history but the dramatic increase and the damage caused by them in the recent past have become a cause of national and international concern.

Communication means provide the critical path for relief in emergency and disaster situations. Once a disaster has occurred, however, local infra structure – including microwave, cellular and other most communications

facilities are destroyed. In the immediate aftermath of such a major emergency situation, one of the reliable solutions of communications is satellite-based communication.

Satellite technology can provide narrowband and broadband IP communications (Internet, data, video, or voice over IP) with speeds starting at 64 Kbps from handheld terminals up to 4 Mbps bi-directional from portable VSAT antennas normally. Fixed installation can bring the bandwidth up to 40 Mbps [2].

In fact, a disaster can be occurred very variously – various size, place, causes, etc. but it should be effectively controlled and managed in any emergency and disaster situations. This discussion would be complete with the quick and reliable establishment of a temporary communications network which has feasible technologies to support emergency management.

The aim of this paper is suggesting a complete wireless communications solution that can be deployed immediately, reliably, and easily before/after disaster. For this work all different systems should be hierarchical and enabling an interworking properly between different technologies as well as communication devices.

This paper is organized as follows: Section 2 introduces the recent trends of disasters and the needs of telecommunications hierarchy during a disaster situation, Section 3 explores the integrated PPDR network to mitigate the unpredictable disaster effectively and also suggests a hierarchical architecture of integrated PPDR network, and Section 4 discusses IP-based satellite network for PPDR as a generic solution for provision of multimedia services via satellite access network.

II. DISASTER TRENDS AND TELECOMMUNICATIONS HIERARCHY

A. Trends of Disasters

Over the past decade we have seen an increase in the intensity of natural disasters worldwide as shown in Fig. 1. Through the media, and for some of us, through firsthand experience, we have witnessed the awesome force of nature. In the recent past, we have had natural disasters created by the tsunami in Asia, the earthquake in Pakistan, and the hurricane Katrina in the US. These caused unprecedented devastation and great loss of life which have been etched in our minds due to the magnitude of the devastation. Disaster impact statistics show the global trend – there are now more

disasters but fewer people die in proportion, even though more population is affected and economic losses are increasing [3].

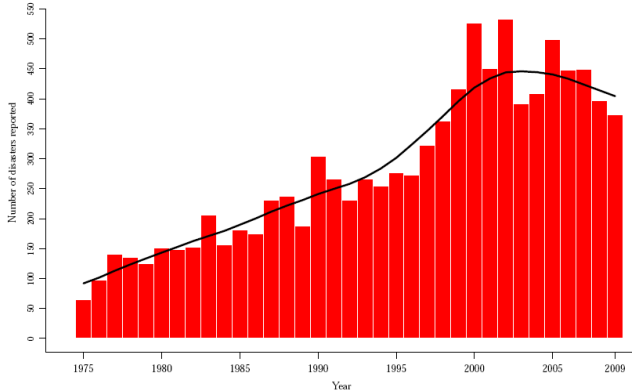


Figure 1. Number of natural disasters reported 1975-2009 (Source: EM-DAT: The OFDA/CRED International Disaster Database – www.emdat.be – Université Catholique de Louvain, Brussels – Belgium)

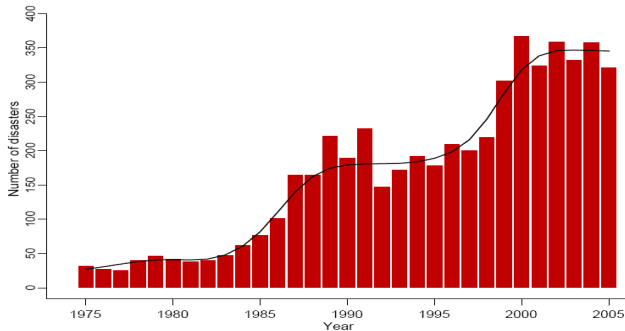


Figure 2. Technological disasters reported 1975-2005 (Source: EM-DAT: The OFDA/CRED International Disaster Database - www.em-dat.net - Université Catholique de Louvain, Brussels – Belgium)

Technological disasters often resulting from major accidents associated with industrialization and forms of technological innovation have significant socio-economic and environmental impact. Although technological hazards have been part of society for hundreds of years, the trends are showing an increasing impact in Fig. 2 [4].

Technological advancements, specifically in the energy, transport and industrial sectors, are developing innovations with associated risks that are not always understood or heeded. The adverse effects of some technological disasters, both on society and on the environment, can considerably outlast the impacts associated with natural disasters.

Comparing the last three decades, the trend shows an increase in the number of natural hazard events and of affected populations. Even though the number of disasters has more than tripled since the 1970s, the reported death toll has decreased to less than half. This is among other factors due to improved early warning systems and increased preparedness. This statistic varies enormously depending on region and figures used. One need to bear in mind those large disasters is rare events that defeat any statistical analysis in the short term. Perhaps more significant in the life of many are those daily disasters, generally underreported and not

reflected at all in global figures on losses, but accumulating to probably large tolls of both economic and health losses.

B. Telecommunications Hierarchy for Disaster Situation

In the recent trend, disaster management has emerged as an important management system to cope with any disaster events. Efficient disaster management shall able to estimate the scale of disasters and its quick responses in any incidents. Nowadays, the system of disaster management is purely a scientific phenomenon. There are three phases of disaster management which are namely Pre-Disaster Management, During-Disaster Management and finally Post-Disaster Management [5]. Pre-Disaster Management is a vital phases of this entire management system. It includes the preparation of various action plans by the relevant organizations and their objective is to minimize the risk and hazards from the specific disaster's events. The second phases of its managements are to provide responses at the time of disaster and last phases include how to tackle with the operation of relief & rehabilitation. It is really understood that the perfect Pre-Disaster Management helps with the efficient disaster management system in the strategic time.

Many types of wireless communications can help to coordinate an effort of the disaster management inside and/or outside disaster area to bridge the disaster zone to the other zone, providing telecommunications, broadcasting, logistic, and tele-medical support. Furthermore, in many scenarios, especially in disaster situations, wireless represents the only viable delivery mechanism [6].

Generally speaking, the wireless solutions in the management of emergency situations have been identified for a long time. Nowadays, however, just one wireless solution could not be capable of delivering the services to cover the complex emergency situations which are being wide area, underground area, and under constructed infra area for instance. In these areas communications networks could be either unavailable to damage and congestion or totally missing.

Very hierarchical telecommunications infrastructure is needed and it should be operated organically. Immediate availability, rapid deployment, and reliability are key factors for communication network infrastructure in emergency situations. In order to keep the telecommunications infrastructure hierarchically, it is acquired a particular significance in terms of various facets, which can be summarized as follows:

- A mobile ad-hoc network should be rapidly deployed in a disaster area.
- Broadband services (Multimedia, Internet, Telemedicine, etc.) should be deliverable to monitor the disaster situation deeply.
- Operator's terminal should be equipped with portable, compact, and easy-to-use as well as interconnected all operators.

Table I shows the comparison of mobile ad hoc network (MANET), terrestrial, and satellite system as a means of telecommunication for PPDR.

TABLE I. COMPARISON OF MANET, TERRESTRIAL, AND SATELLITE SYSTEM

	MANET	Terrestrial	GEO Satellite
Typical Cell Size	No cell	0.1-1 km	400km min.
Service Coverage	Varies	< 1 km	Up to global
Maximum Transmission rate per user	Varies from node scenario < 100 kbps	Spot service 155Mbps	Quasi-global 155 Mbps
System Deployment	Flexible, a set of mobile hosts	Several base stations before use	Flexible, but long lead time
Estimated Cost of Infrastructure	Low	Varies	High

III. INTEGRATED PPDR NETWORK

Disasters generate intense human need for communication to coordinate response activities to convey information about affected groups and individuals, and as a panic reaction to crisis. The critical disasters are the most intense generators of telecommunication traffic, and the resulting surge of demand can clog even the most well-managed networks. In addition, for economic reasons, most communications networks are engineered for peak load at levels well beneath the demands placed on them during disasters.

Generally, most of disaster might be occurred in small area which can be covered by terrestrial communications network. But sometimes the terrestrial infrastructures are damaged or missing and high risk areas damaged by disaster on the ground need to be deeply monitored in particularly. In this case satellite network can offer a stable and wide range of services. Such services may be particularly valuable where the terrestrial network is damaged severely.

So, in order to mitigate the unpredictable disaster effectively a public protection and disaster relief (PPDR) network should be integrated by various communication means which are not only possible technologies of the moment but also from a small-size network to an extensive scale in terms of coverage, data rate, and users.

A. Incident Area Network (IAN)

When a disaster occurs, a commonly accepted concept is to need a communication infrastructure that is rapidly deployable at the disaster site and able to interconnect organically among the personnel of emergency agencies such as police, fire fighter, a first-aid team, etc [7].

The quick deployment, availability, and reliability of such emergency communication network in disaster situations is of great values considering life and property of the distressed.

Wireless fixed ad hoc network and mobile ad hoc networks as shown in Fig. 3 can be quickly established as an instant communications system to support emergency management and the urgent missions in the disaster relief situation. Especially mobile ad hoc networks could be considered as a ultra-fast deployable network by automatically establishing “self-healing” network and “moving hot spot”.

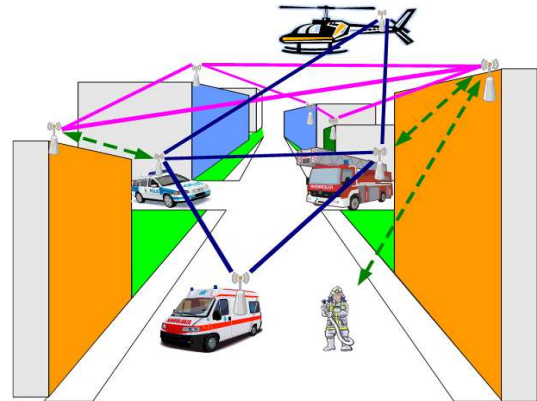


Figure 3. Wireless fixed ad hoc network and mobile ad hoc networks

This kind of ad hoc networks can be applicable to “mobile robotics” such as hazardous material removal, anti-terrorist action, rescue in hazardous locations, and remote inspection as well as “remote patient monitoring” in terms of blood pressure, cardiac activity, encephalographic data, body temperature, and positioning.

B. Competent Area Network (CAN)

Dependent on the nature of a disaster, there are usually many personnel requiring communications and because of the urgency of communications, a good Grade of Service (GoS) is required. These factors mean that a significant amount of network capacity needs to be available throughout the disaster and affected areas to support effective PPDR communications.

Generally the mobile telecommunications network will not have the capacity to provide effective PPDR communications because most of them located in a disaster area have been designed to support normal traffic loads [8]. Therefore, the dedicated communication network is needed to be secure communications to provide stable and additional capacity in competent area.

TETRA system shown in Fig. 4 is the preferred technology for constructing a competent area network because TETRA has some advantages over other technologies which are very fast call set-up and provide a number of fall-back modes such as the ability for a base station to process local call unlike most cellular technologies.

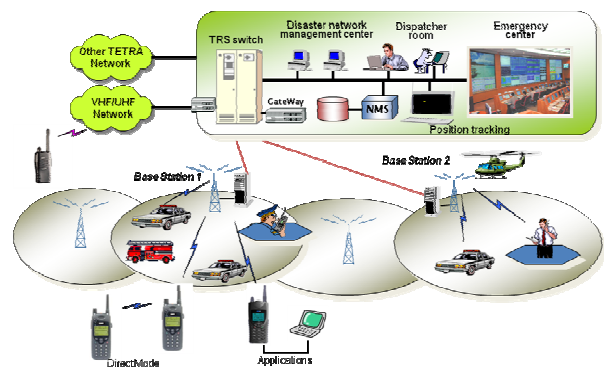


Figure 4. Competent area network by TETRA trunking system

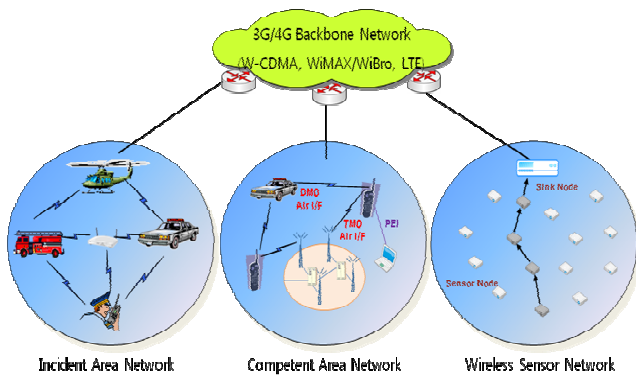


Figure 5. Extended area network by 3G/4G networks

C. Extended Area Network (EAN)

Telecommunication technologies used for emergency telecommunications are often no different than those used for routine public safety telecommunications.

3G/4G mobile systems using W-CDMA, WiMax, LTE technologies could be easily deployed to expand local networks reaches the working terrestrial base stations. These wireless technologies are likely to be combination of narrowband, wideband and broadband, and nature of application use public or private networks in order to establish the extended area network (EAN) as shown in Fig. 5.

- Public: GPRS and 3/4G
- Private: Wideband TEDS and Broadband PPDR

D. Wide Area Network (WAN)

Satellite communication is still unbeatable for broadcast and multicast services for wide area – especially cost per delivered bits independent of user position and number of users inside wide coverage area.

Furthermore satellite communications have not only high data rate capacity and long distance transmission compared other terrestrial networks but also robustness against most natural or man-made disaster that can be harmful to terrestrial infrastructure.

In addition, WAN including satellite system have own advantages which other network is not easy to provide as follows.

- Disaster prediction and detection – meteorological and earth exploration satellite services
 - Operated in the main by government and international agencies
 - Play a major role in prediction and detection of disasters (such as hurricanes, earthquakes and tsunamis, floods, fires, dangerous pollution, etc.)
- Disaster alerting – broadcasting, fixed, mobile and related satellite services
 - Alert the central/regional/local authorities responsible for warning the public – broadcasting, fixed, mobile, fixed/mobile-satellite systems

- Issue warnings to the people likely to be affected
- Broadcasting (sound and television)
- Mobile (such as TV, Radio, DMB, SMS/Cell broadcasting)
- Disaster relief – amateur, broadcasting, fixed, mobile and related satellite services
 - Earth exploration satellite – damage assessment and relief planning
 - Fixed/mobile satellite – to rapidly restore communications capabilities, coordination of relief activities

E. Example of Integrated PPDR Network Architecture

Emergency telecommunications should cover all communication services, including voice and non-voice, data, location, and so forth.

The need for emergency telecommunications includes many scenarios ranging from a minor road traffic accident, for example, to a major incident like a passenger train crash, a terrorist incident, a natural disaster (e.g. an Earthquake, Tsunami).

In order to consist of the integrated PPDR network as shown in Fig. 6 and to manage the network systematically, “Standards” for emergency communications and “Standard Operation Procedure (SOP)” are essentially needed.

While the different technologies are used, the followings are basically considered to guarantee access and successful interconnection.

- Interoperability of diverse communications systems and diverse protocols
- Interagency and cooperation between organizations
- Rapid deployment

A SOP is a set of written instructions that document a routine or repetitive activity followed by an organization to deal with the emergent situation effectively. SOPs define precisely how operations were to be conducted and also describe clearly what is expected and required of personnel during emergency response and non-emergency activities.

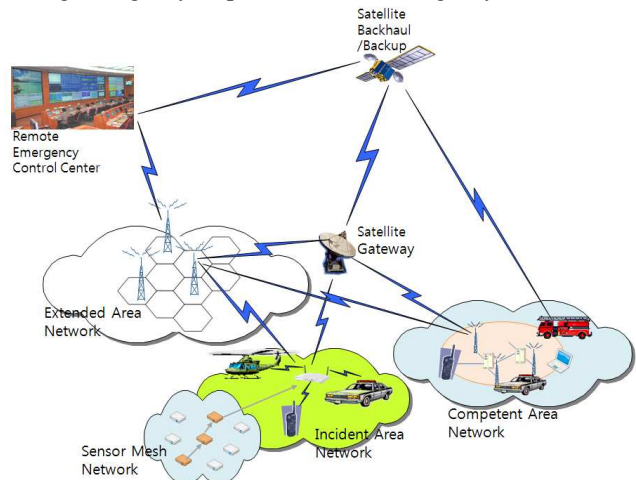


Figure 6. Conceptual architecture of integrated PPDR network

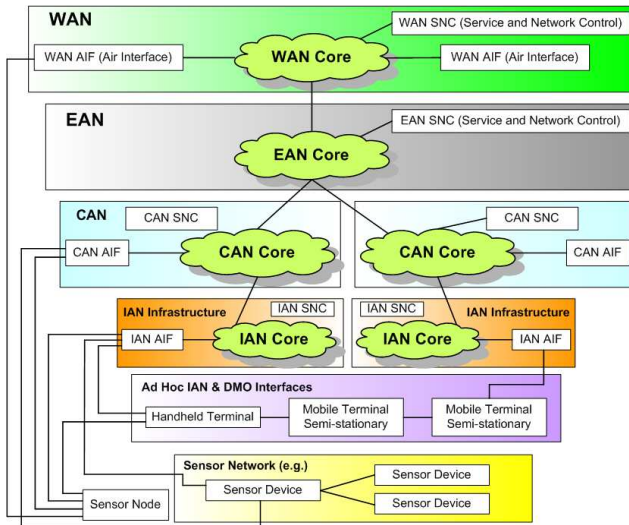


Figure 7. Hierarchical architecture of integrated PPDR network

Since a disaster occurs, different and consecutive phases can be identified for the network deployment of rescue teams in the disaster area. So the reactive mechanism should be used for the rescue and recovery of any disaster by optimal hierarchical communication network.

The proposed hybrid system architecture which is for the formation of tree structure as shown in Fig. 7 provides a strong mobility management support in order to bring seamless mobility to PPDR communication network.

IV. IP-BASED SATELLITE NETWORK FOR PPDR

The broadband multimedia satellite system is intended as a generic solution for provision of multimedia services via satellite access networks. It is required that repletion and enlarging the role of broadband mobile wireless internet through the satellite communication which has mobility, wide coverage and broadband channel as following aspects.

- Wireless internet service requests increasing the bandwidth and users also request high speed services as wire network
- Necessity of technique development for getting over the limitations of current mobile communications and Wireless LAN technologies
- Necessity of network device techniques for providing high quality of multimedia services via mobile wireless internet
- Satellite communications make possible for using whole the country and providing broadband internet multimedia services

In fact, a satellite network can offer large bandwidth and allow small aperture antenna as well as even hand held terminal like terrestrial terminal that could provide a various multimedia services for PPDR.

IP-based architecture for broadband satellite access is as shown in Fig. 8 for broadband PPDR services and it can be adapted independently to the particular GEO or LEO satellite

technology adopted in the satellite link [9]. This rapid deployable IP-based satellite network can provide the following advantages.

- Point-to-Multipoint burstable remote emergency Control Center- to-Incident Site
- Dedicated SCPC Point-to-Point Circuit
- Data Rates up to 5 Mbps [9]
- Quality of Service (QoS) support for voice & video
- IP-based flexible voice and data termination
- Real-time monitoring and reporting
- Seamless global coverage

This IP-based satellite communication capabilities-fixed and mobile is vital for effective multimedia communication, especially in video transmission and high data rate broadcasting as well as data collection, distress alerting, position location and coordinating relief operations in the field.

Recently a number of companies – including TerreStar Global – are planning to focus on the provision of PPDR services by mobile satellite services (MSS). They enable the satellite and terrestrial communications networks to provide a ubiquitous platform for communications and data transfer by integration of mobile satellite and ground component technologies.

In case of this the unique benefit to PPDR services of MSS/CGC(Complementary Ground Components) is the ability for the user to seamlessly switch between using the terrestrial component to connect a call and using the satellite to connect a call, thus providing network redundancy in times of need. These technological and regulatory factors combine to increase connectivity for emergency responders in service coverage.

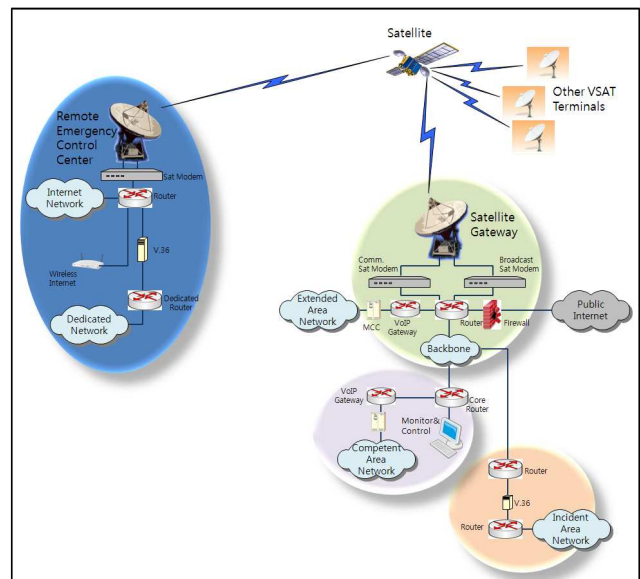


Figure 8. IP-based Satellite Network Configuration for integrated PPDR

V. CONCLUSIONS

Disasters are often combined with the destruction of the local telecommunication infrastructure, causing severe problems to the rescue operations. In these cases the only possible way to guarantee communication services is to use satellites to provide a backhaul connection to the intact network infrastructure [10]. The objective of this paper is to describe briefly the existing communication technologies for disaster management and to suggest the satellite-based PPDR (for public protection and disaster relief) communications network as an integrated system which is integrated not only possible technologies of the moment but also from an ad hoc network to an extensive scale network. It can be used for wideband applications (e.g. wireless transmission of large blocks of data and video) and/or broadband applications (e.g. high-speed data, high quality digital real time video and high volume data exchange) dependent on the use of spectrally efficient technologies and insuring interoperability like a IP-based satellite system. Such a system could be quickly set up anywhere in the disaster area where there is satellite coverage. The aim of this paper is also to identify possible candidate system when the draft standardization on PPDR communications for next generation is developed in Korea.

REFERENCES

- [1] B. Dey and R.B. Singh, *Natural Hazards & Disaster Management*, 1st Edition, 2006, pp.3-4.
- [2] <http://www.iaem.com/resources/links/documents/satellitewhitepaper060906.pdf>, 27 Nov. 2010.
- [3] <http://www.spiritualresearchfoundation.org/articles/id/spiritualresearch/spiritualscience/naturaldisasters> Climate Change and Natural Disasters, 27 Nov. 2010.
- [4] <http://www.emdat.be/natural-disasters-trends>, EM-DAT, The International Disaster Database, 28 Nov. 2010.
- [5] http://www.adrc.asia/publications/LWR/LWR_abridged/preface3.pdf Emerging trends in disaster impact, hazards and vulnerability patterns, 28 Nov. 2010.
- [6] P. Pace and G. Aloï, "Disaster Monitoring and Mitigation using Aerospace Technologies and Integrated Telecommunication Networks", *IEEE A&E System Magazine*, Apr. 2008, pp.3-9.
- [7] G. Iapichino, C. Bonnet, C. Baudoin, and I. Buret, "A Mobile Ad-hoc Satellite and Wireless Mesh Networking Approach for Public Safety Communications", 10th International Workshop on Signal Processing for Space Communications, 24 Nov. 2008, pp.1-6.
- [8] <http://www.tetramou.com/tetramou.aspx?id=2238>, 9 Jan. 2011.
- [9] D. Pompili, F.D. Priscoli, and T. Inzerilli, "Enhanced IP-based satellite architecture compatible with many satellite platforms", *IST 2004*, Nov. 2004, pp.1-5.
- [10] Y.M. Lee, B.J. Ku, and D.S. Ahn, "A Satellite Core Network System for Emergency Management and Disaster Recovery", *ICTC2010*, Jeju, 17-19 Nov. 2010, pp.1-4.

The OFDM Joint Radar-Communication System: An Overview

Yoke Leen Sit, Christian Sturm, Lars Reichardt, Thomas Zwick, Werner Wiesbeck

Institut für Hochfrequenztechnik und Elektronik

Karlsruhe Institute of Technology

Karlsruhe, Germany

{leen.sit|christian.sturm|lars.reichardt|thomas.zwick|werner.wiesbeck}@kit.edu

Abstract—This paper presents an overview of the OFDM joint radar and communication system concept which has been developed for automotive radar applications. Using an OFDM-based signal, the range and Doppler estimation algorithm are independent of the payload data and overcomes the typical drawbacks of correlation-based processing. The derivation of parameters for the operation at 24 GHz suited for automotive applications are then shown. The system concept is then verified with MATLAB simulation and measurement. A brief description of the on-going work to adapt this system to a realistic multipath-multiuser environment along with simulation results are also presented.

Keywords—Doppler processing; interference cancellation; orthogonal frequency division multiplexing; radar; ray-tracing

I. INTRODUCTION

The idea of combining a radar and a communication system on a single platform has long been proposed [1] but a relevant system concept has never been developed till now. Initially the major hurdle was that communication and radar systems utilize very different frequency ranges but as more and more radio frequency front-end architectures are replaced by processing in the digital domain nowadays, the gap between the hardware requirements for the radar and communication systems becomes narrower and the devices more similar.

A popular choice for the common radar and communication signal is the orthogonal frequency division multiplexing (OFDM) signals in combination with phase-shift keying (PSK) as OFDM offers advantages such as robustness against multipath fading and relatively simple synchronization. OFDM-like signals has been shown to be suitable for radar applications [2] and the feasibility of integrating communication functions in radar networks [3], [4] have also been explored. For the case of the radar function, it has also been pointed out in another study [5] that OFDM-coded radar signals are comparable with linear frequency modulation (LFM) signals and furthermore, experiences no range-Doppler coupling. Hence the merging of the two platforms becomes a possibility and would lead to a significant cost-efficient measure in targeted application areas such as in the intelligent transportation networks which require the ability of inter-vehicle communication as well as reliable environment sensing.

The concept of the Orthogonal Frequency Division Multiplex joint radar and communication (RadCom) [6], [7] is presented here. The system uses OFDM communication signals as radar signals leading towards its dual role in object sensing and communication between systems. Unlike conventional radar processing approaches that use correlation-based processing [8], the ranging algorithm presented utilizes only Fourier transformations. Such a method not only allows for a relatively faster processing speed but also reduces the sidelobe levels (as compared to [9]) while being independent of the transmitted data.

The OFDM RadCom concept as well as the range and Doppler processing schemes are presented in Section II. The requirements for its operation in the 24 GHz ISM band is discussed in Section III followed by the system concept verification with Matlab and measurement results in Section IV. Finally, the current on-going work to extend the RadCom for use in a multipath-multiuser scenario is presented in Section V.

II. OFDM RADCOM CONCEPT

The OFDM transmit signal consist of parallel orthogonal subcarriers, each modulated with a data. The resulting time domain signal is expressed by

$$x(t) = \sum_{\mu=0}^{M-1} \sum_{n=0}^{N-1} D(\mu N + n) \exp(j2\pi f_n t), \quad 0 \leq t \leq T \quad (1)$$

with N denoting the number of subcarriers used, M , the number of consecutive symbols evaluated, f_n , the individual subcarrier frequency, T , the OFDM symbol duration, and $\{D(n)\}$, called the 'complex modulation symbol', is the arbitrary data modulated with a discrete phase modulation technique e.g., phase-shift keying (PSK). Interference between individual subcarriers is avoided based on the condition of orthogonality given by

$$f_n = n\Delta f = \frac{n}{T}, \quad n = 0, \dots, N-1 \quad (2)$$

In the presence of a reflecting object at the distance R from the RadCom with the relative velocity of v_{rel} , which results in the Doppler frequency of f_D , the received OFDM symbol in time domain becomes

$$y(t) = \sum_{\mu=0}^{M-1} \sum_{n=0}^{N-1} D_r(\mu, n) \exp(j2\pi f_n t) \quad (3)$$

where

$$D_r(\mu, n) = D(\mu, n) \exp\left(-j2\pi f_n \frac{2R}{c_0}\right) \exp(j2\pi f_D t) \quad (4)$$

Based on (4), it can be seen that the distortions due to the channel is fully contained in the received complex modulation symbol $\{D_r(n)\}$, which is obtained at the receiver at the output of the OFDM demultiplexer prior to channel equalization and decoding. Thus comparing the transmitted signal $\{D(n)\}$ with the soft-side received signal $\{D_r(n)\}$ would yield the frequency domain channel transfer function. This is computed by simply performing an element-wise division

$$I_{div}(\mu, n) = \frac{D_r(\mu, n)}{D(\mu, n)} \quad (5)$$

In this manner, the acquisition of the range and Doppler profiles will be independent of the payload data.

A. Range Processing

For an object at the distance R from the radar, all subcarriers within the same reflected OFDM symbol will experience a linear amount of phase shift equivalent to two times the time length taken to travel the distance R . Assuming that the object is stationary, the corresponding channel transfer function is

$$I_{div}(n) = \exp\left(-j2\pi n \Delta f \frac{2R}{c_0}\right) \quad (6)$$

The channel impulse response containing the range profile of the object can then be determined by taking an inverse discrete Fourier transform (IDFT) of $\{I_{div}(n)\}$

$$\begin{aligned} h(p) &= \text{IDFT}(\{I_{div}(n)\}) \\ &= \frac{1}{N} \sum_{n=0}^{N-1} I_{div}(n) \exp\left(j2\pi \frac{n}{N} p\right), \quad p = 0, \dots, N-1 \end{aligned} \quad (7)$$

B. Doppler Processing

Unlike with communication signals, the reflected radar signal of an object moving with a relative velocity of v_{rel} will experience twice the amount of Doppler shift according to

$$f_D = \frac{2 v_{rel}}{\lambda} \quad (8)$$

where $\lambda = c_0/f_c$, with c_0 being the speed of light and f_c , the carrier frequency.

This causes a phase shift of $2\pi\mu f_D T_{sym}$ on every subcarrier of the μ -th OFDM symbol, where T_{sym} is the transmit OFDM symbol duration. It can be assumed that the Doppler affects all

subcarriers by the same amount since the system bandwidth is much smaller than the carrier frequency. Thus for an object having a non-zero relative velocity to the radar, the corresponding time-varying channel transfer function (due to the Doppler only) is

$$I_{div}(\mu) = \exp(j2\pi f_D \mu T_{sym}), \quad 0 \leq \mu \leq M-1 \quad (9)$$

By taking the discrete Fourier transform (DFT) through the time axis the Doppler term can be estimated.

$$\begin{aligned} h(q) &= \text{DFT}(\{I_{div}(\mu)\}) \\ &= \frac{1}{N} \sum_{\mu=0}^{M-1} I_{div}(\mu) \exp\left(-j2\pi \frac{\mu}{M} q\right), \quad q = 0, \dots, M-1 \end{aligned} \quad (10)$$

III. SYSTEM PARAMETERIZATION

The system parameterization presented here is oriented towards automotive applications since one of the intended application area for such a system is in the intelligent transportation systems. The operation at the frequency of 24 GHz ISM band which is suitable for both the radar and communication operations has been chosen.

A. Common constraints

There exist two major constraints pertaining the joint operation of the RadCom; the first is the subcarrier spacing and the second is the cyclic prefix (CP) length. The subcarrier spacing is limited by the Doppler frequency which has the potential to shift the alignment of the subcarriers thus destroying their orthogonality. Assuming a maximum relative velocity for typical traffic scenarios to be $v_{rel} = 200$ km/h = 55.6 m/s, according to (8) this would result in the maximum Doppler shift of $f_{D,max} = 8.9$ kHz for $f_c = 24$ GHz. Following a rule-of-thumb, it can be assumed that the subcarrier spacing of $\Delta f > 10 f_{D,max}$ will ensure that the orthogonality remains.

To avoid inter-symbol interference (ISI), each elementary OFDM symbol is prepended with a prefix containing a repetition of some of its last values (thus rendering the time domain symbol 'cyclic'). This CP duration T_{CP} is governed by the *maximum excess delay* which is the maximum time difference between the arrival of the first and last propagation path in a multipath environment. Assuming that due to the high attenuation of the scattering process the maximum detectable distance is 200 m and taking into account that the reflected signal to the radar has to travel twice the distance, we obtain a time duration of 1.33 μ s which corresponds to the maximum delay difference between the propagation path of 400 m. Hence, setting $T_{CP} > 1.33 \mu$ s would ensure that ISI is avoided.

As such, in order to obtain round numbers, the elementary symbol length of $T = 11 \mu$ s was chosen which is equivalent to $\Delta f = 90.909$ kHz. The CP length is chosen to be $T_{CP} =$

$1/8 T = 1.375 \mu\text{s}$, resulting in the total transmitted OFDM symbol duration of $T_{sym} = T + T_{CP} = 12.375 \mu\text{s}$.

B. Range resolution

The maximum unambiguous range of the radar is given by

$$r_{max} = \frac{c_0}{2\Delta f} = \frac{Tc_0}{2} \quad (11)$$

It can be seen that the unambiguity of the radar range profile is highly dependent on the elementary OFDM symbol duration. Hence for a good radar range profile, T must be chosen to be as large as possible. This also coincides with the need to obtain a sufficiently high signal-to-noise ratio. For practical applications where the transmit power is limited, the integration time of the processor must be chosen to be as long as possible to obtain a higher processing gain. Therefore T must be chosen to be as long as possible without violating the constraints due to the Doppler effect.

One of the key performance parameters of a radar is its range resolution, Δr . It is only dependent on the total bandwidth occupied by the transmit signal and the relation is given as

$$\Delta r = \frac{c_0}{2B} = \frac{c_0}{2N\Delta f} \quad (12)$$

For the intended automotive application, a range resolution of between 1 m to 2 m is sufficient. Typically a power of 2 number is chosen for the number of subcarrier N , as this allows for an efficient implementation of the necessary DFT and IDFT processing. Within the required context, $N = 1024$ is chosen. With the chosen values, $r_{max} = 1650$ m and $\Delta r = 1.61$ m. This corresponds to a total signal bandwidth of 93.1 MHz which is compliant with the regulations of the 24 GHz ISM band.

C. Doppler resolution

The unambiguous Doppler frequency is related to the symbol duration T_{sym} and can be expressed by

$$v_{max} = \frac{\lambda}{2T_{sym}} \quad (13)$$

Substituting the parameter values, $v_{max} = 505$ m/s is obtained. Since Doppler can be both positive and negative, it should rather be expressed as $v_{max} = \pm 252.5$ m/s. This then corresponds to around ± 910 km/h which is more than required for an automotive application.

The Doppler resolution is dependent on the number of evaluated symbols M , and amounts to

$$\Delta f_D = \frac{1}{MT_{sym}} \quad (14)$$

or in terms of velocity resolution, taking into account that twice the Doppler of the relative velocity occurs for a reflected wave

TABLE I
OFDM SYSTEM PARAMETERS

Symbol	Parameter	Value
f_c	Carrier frequency	24 GHz
N	Number of subcarriers	1024
Δf	Subcarrier spacing	90.909 kHz
T	Elementary OFDM symbol duration	11 μs
T_{CP}	Cyclic prefix duration	1.375 μs
T_{sym}	Transmit OFDM symbol duration	12.375 μs
B	Total signal bandwidth	93.1 MHz
Δr	Range resolution	1.61 m
r_{max}	Maximum unambiguous range	1650 m
v_{max}	Maximum unambiguous velocity	± 252.5 m/s
M	Number of evaluated symbols	256
Δv	Velocity resolution	1.97 m/s

$$\Delta v = \frac{\lambda}{2MT_{sym}} \quad (15)$$

In principle, evaluating a greater number of OFDM symbols would give a finer velocity resolution. This is however impractical as moving objects must remain within one range resolution cell during the evaluation. Hence, by evaluating over $M = 256$, with the duration of 3.17 ms, an object traveling at the maximum unambiguous velocity would have traveled only 0.8 m, which is still within the resolution cell size of 1.61 m. With this, the velocity resolution becomes $\Delta v = 1.97$ m/s or 7.1 km/h, guaranteeing an appropriate performance for practical automotive applications. All system parameters are summarized in Table I.

IV. SIMULATION & MEASUREMENT RESULTS

For the verification of the range and Doppler processing presented in Section II, a simulation of two point-scatterers has been implemented in MATLAB. The simulation model comprises a transmitter, receiver and a point-scatterer channel model utilizing the parameters in Table I. The point-scatterer channel model computes the distance, velocity, phase and attenuation for every pre-defined point scatterers and is able to support an arbitrary number of them. At the receiver, the received baseband signal is processed with the algorithm as described in (6) and (9) without prior channel equalization and decision.

Two identical point scatterers placed at $R = 20$ m from the radar with the respective relative velocities of $v_1 = 0$ m/s and $v_2 = 7$ m/s were set in the simulation. At the FFT processing, a Hamming window is applied to minimize the sidelobes. The resulting radar image is as shown in Fig. 1. The two objects are clearly separable in range and Doppler and the sidelobes only occur due to the FFT processing.

In verifying the simulation results, a measurement emulating the simulation scenario has also been done. The measurement setup is as shown in Fig. 2. A stationary corner reflector with the radar cross section (RCS) of $\sigma = 16.3$ dBm² and a car moving at 25 km/h (7 m/s) are located 20 m away from the

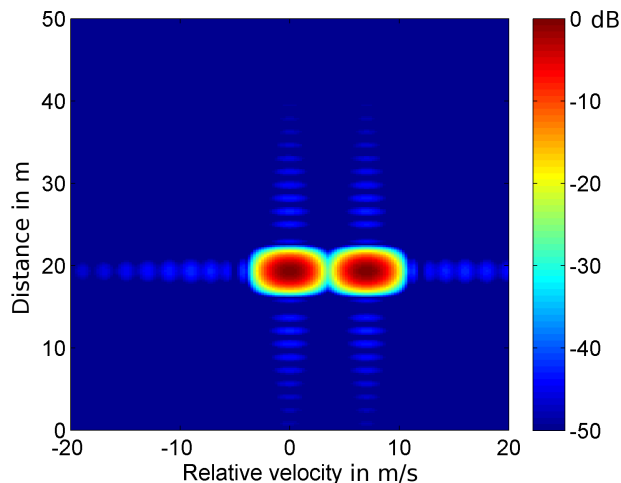


Fig. 1. Simulation of 2 point scatterers



Fig. 2. Measurement scenario

radar at the time of measurement. The resulting radar image is as shown in Fig. 3.

Thus it can be seen that the measured result corresponds highly with the simulated result. Although the reflection from the car is approximately 15 dB weaker than the reflection of the corner reflector, it is nevertheless sufficient to be distinguished in the radar image. Also seen in the figure are other reflecting objects which are the result of the metal road signs behind the car and reflections from the ground. Hence this demonstrates the capability of the processing algorithm in resolving multiple reflecting objects. The measurement setup for performance verification can be found in [10].

V. CURRENT WORK

The current work focuses on extending the OFDM RadCom to cope in a realistic road environment i.e. in multipath and multiuser scenarios. The following sections outlines the work undertaken and its outcome.

A. Multipath scenario

Within a multipath environment, a certain transmitted signal will not only arrive at the receiver over the Line-of-Sight

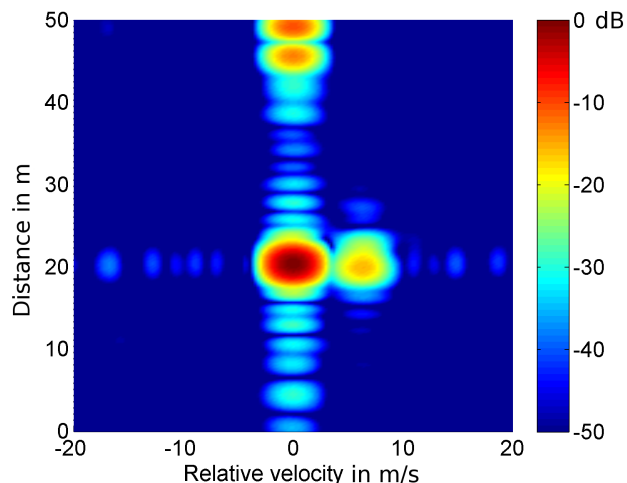


Fig. 3. Measurement result of the setup in Fig. 2

(LOS) path but also over Non-Line-of-Sight (NLOS) paths which interact in a complex manner with the objects (e.g. buildings, vehicles, persons, trees) within the propagation vicinity. These NLOS signals experience reflection, diffraction and scattering, resulting in their different attenuations, time delays, phase shifts and even polarizations. It is precisely due to the superposition of these NLOS signals that give rise to the frequency-selective, time-variant and direction-selective behavior of the mobile radio channel. As such, an accurate description of these multipath waves propagation in a given scenario is necessary to produce realistic time series of the Channel Impulse Response (CIR).

For modeling the wave propagation in a multipath scenario, a three-dimensional fully polarimetric Ray-tracing algorithm developed by [12], [13], [14] is used. This channel model is based on Geometrical-Optics (GO) and describes the asymptotic behavior of the electromagnetic fields at high frequencies with the assumption that the wavelength is very small compared to the dimensions of the modeled objects in the simulation scenario. Each propagation path is represented by a ray which may experience several different propagation phenomena.

The 3D scenario for modeling the deterministic channel model is as shown in Fig.4. This urban scenario comprises two lanes and four cars (one moving in the same direction and two moving towards the radar) with buildings and vegetation on both sides of the street. The green 'rays' depict the path traveled by the electromagnetic waves.

B. Multiuser scenario

In a multiuser scenario, the reflected OFDM signal at the receiver contains not only the effect of the channel, but also communication signals from interferers and noise. We consider here another user of the same OFDM RadCom system which is also transmitting a message-radar signal, denoted henceforth as the *interferer*. The analysis is made from the view point of the first RadCom system, denoted as the *radar*.

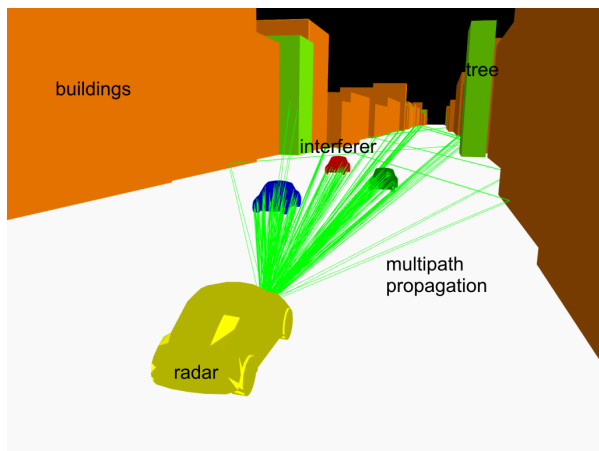


Fig. 4. Ray-tracing scenario

The Signal-to-Interferer ratio (SIR) at the radar can be estimated by taking the ratio of the receive power due to the reflecting objects in the radar's surrounding (radar equation) and the receive power due to the interferer (Friis equation), which gives:

$$SIR = \frac{R_{int}^2 \sigma}{(4\pi)^2 R_{obj}^4} \quad (16)$$

where R_{int} and R_{obj} are the distance of the interferer to the radar, and the reflecting object to the radar respectively, and σ is the RCS of the reflecting object. A reflecting object with 10 dBm^2 RCS located at 10 m, and the interferer at 50 m respectively from the radar would give an SIR of -18 dB. That is to say, the interferer signal is almost always higher than the reflected radar signal (even though the reflecting object is located nearer the radar) and hence appears as noise in the radar image, impairing the dynamic range.

From the ray-tracing results, the SIR is -48.2 dB and the strongest multipath component of the interferer is 11.7 dB weaker than its LOS. The resulting radar image for the scenario of Fig. 4 is as shown in Fig. 5 where the mean noise floor is at -20.2 dB while the dynamic range (peak-to-sidelobe level) is a mere 8.46 dB. Consequently no distinguishable object reflection is visible in the radar image.

C. Interference cancellation

As can be seen in Fig. 5, the communication signals end up as noise on the radar image. Since the radar also has access to the communication data, with a *near-precise reconstruction* of the interfering signal as received, this signal can then be subtracted from the radar signal.

In order to obtain an adequate reconstruction of the interfering signal, good time and frequency synchronization as well as channel estimation are necessary. The severity of erroneous frequency offset estimation on the reconstruction of the interferer signal is such that the difference of a mere 20 Hz residue from the real frequency offset will cause a

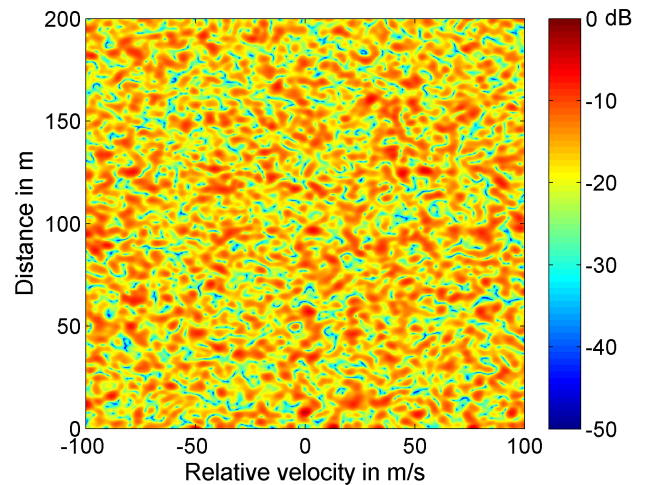


Fig. 5. Radar image of the ray-tracing scenario, before interference cancellation

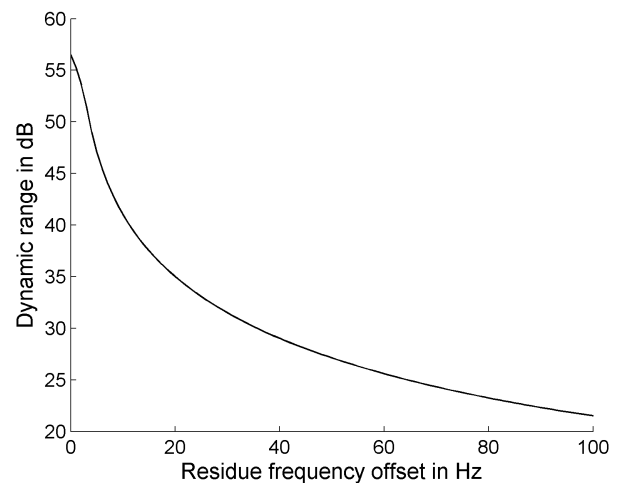


Fig. 6. Dynamic range (after interference cancellation) vs. residue frequency offset

degradation of more than 20 dB to the dynamic range, as can be seen in Fig. 6.

For the purpose of time and frequency synchronization, the Schmidl and Cox algorithm (SCA) [15] has been implemented. The OFDM frame is thus extended by the length of two symbols which does not cause any impairment to the radar's ranging capabilities. The channel estimation is done by having regularly distributed pilot symbols within the OFDM frame [11].

It has been observed however that in a multipath-multiuser environment that when the LOS or strongest signal is less than 15 dB in difference with other NLOS and reflected signals, the SCA is incapable of correctly estimating the frequency shift. This frequency shift occurs largely due to the Doppler of the reflecting objects and also the possibility of local oscillator mismatch between the transmitter and the receiver. Thus a fine frequency offset estimator has been developed [11], which

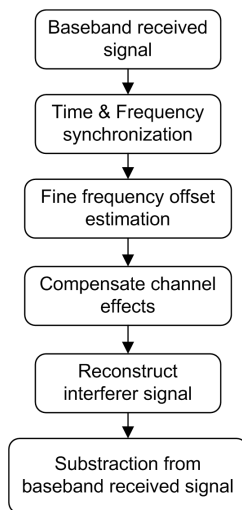


Fig. 7. Flow diagram of the interference cancellation

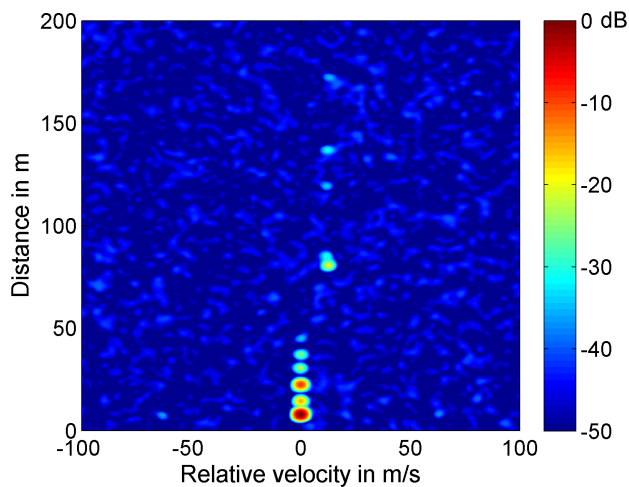


Fig. 8. Radar image after interferer's LOS component cancellation

when used with the SCA is capable of estimating the frequency offset to the accuracy of 2.5 Hz and below.

The flow of the interference cancellation scheme is as shown in Fig. 7. Interference cancellation is done based on the 'reliability' of the received signal. A signal is 'reliable' if the the SCA synchronization is able to 'identify' a signal through correlation. Shown in Fig. 8 is the resulting radar image after interference cancellation of the interferer's LOS path, where the residue frequency offset amounts to only 1.2 Hz and the mean noise floor is now at -51.8 dB along with 35.2 dB of dynamic range (peak-to-sidelobe ratio). With this, all reflecting objects in the path of the rays are visible.

VI. CONCLUSION

An OFDM system which is able to support both communication and radar applications on a single platform has been presented whereby the processing scheme is independent of the payload data, and is capable of resolving

multiple objects. The parameterization for automotive radar applications has also been derived and its implementation feasibility verified by simulations and measurements. In the subsequent step for extending the RadCom to function in a multipath-multiuser environment, the challenges of the realistic multipath scenario setup and the implication of another user in the radar's vicinity have been discussed. It has also been shown that the interfering signal severely corrupts the radar's dynamic range. Hence an interference cancellation scheme using the availability of the receive communication signal to the radar has implemented and the performance of the radar has been seen to improve by 33.3 dB after the cancellation of the strongest (LOS) path of the interferer.

REFERENCES

- [1] M. Uchida, Y. Kagawa, and A. Okuno, "A vehicle-to-vehicle communication and ranging system based on spread spectrum technique-SS communication radar," in *Vehicle Navigation and Information Systems Conference. Proceedings*, Aug. 1994, pp. 169–174.
- [2] N. Levanon, "Multifrequency complementary phase-coded radar signal," *Radar, Sonar and Navigation, IEE Proceedings -*, vol. 147, no. 6, pp. 276–284, Dec. 2000.
- [3] G. Lellouch and H. Nikookar, "On the Capability of a Radar Network to Support Communications," in *Communications and Vehicular Technology in the Benelux, 2007 14th IEEE Symposium on*, Nov. 2007, pp. 1–5.
- [4] D. Garmatyuk, J. Schuenger, Y. Morton, K. Binns, M. Durbin, and J. Kimani, "Feasibility study of a multi-carrier dual-use imaging radar and communication system," in *Radar Conference, 2007. EuRAD 2007. European*, Oct. 2007, pp. 194–197.
- [5] G. Franken, H. Nikookar, and P. van Genderen, "Doppler Tolerance of OFDM-coded Radar Signals," in *Radar Conference, 2006. EuRAD 2006. 3rd European*, Sept. 2006, pp. 108–111.
- [6] C. Sturm, T. Zwick, and W. Wiesbeck, "An OFDM System Concept for Joint Radar and Communications Operations," in *Vehicular Technology Conference, 2009. VTC Spring 2009. IEEE 69th*, Apr. 2009, pp. 1–5.
- [7] C. Sturm, M. Braun, T. Zwick, and W. Wiesbeck, "A Multiple Target Doppler Estimation Algorithm for OFDM based Intelligent Radar Systems," in *Proceedings 7th European Radar Conference, Paris, France*, Sep. 2010.
- [8] R. Tigrek, W. de Heij, and P. van Genderen, "Multi-carrier radar waveform schemes for range and Doppler processing," in *Radar Conference, 2009 IEEE*, May. 2009, pp. 1–5.
- [9] D. Garmatyuk and K. Kauffman, "Radar and data communication fusion with UWB-OFDM software-defined system," in *Ultra-Wideband, 2009. ICUWB 2009. IEEE International Conference on*, Sept. 2009, pp. 454–458.
- [10] C. Sturm, T. Zwick, W. Wiesbeck, and M. Braun, "Performance Verification of Symbol-based OFDM Radar Processing," in *Radar Conference, 2010 IEEE*, May. 2010, pp. 60–63.
- [11] Sit, Y. L. and Reichardt, L. and Sturm, C. and Zwick, T., "Extension of the OFDM Joint Radar-Communication System for a Multipath, Multiuser Scenario," in *Radar Conference, 2011 IEEE*, May. 2011.
- [12] J. Maurer, "Strahlenoptisches Kanalmodell für die Fahrzeug-Fahrzeug Kommunikation," Ph.D. dissertation, Institut für Hochfrequenztechnik und Elektrotechnik, Universität Karlsruhe (TH), May 2005.
- [13] T. Fügen, J. Maurer, T. Kayser, and W. Wiesbeck, "Capability of 3-D Ray Tracing for Defining Parameter Sets for the Specification of Future Mobile Communications Systems," *Antennas and Propagation, IEEE Transactions on*, vol. 54, no. 11, pp. 3125–3137, Nov. 2006.
- [14] L. Reichardt, T. Schipper, and T. Zwick, "'Virtual Drive' Physical Layer Simulation for Vehicle-to-Vehicle Communications," in *Proceedings of the 2010 International Symposium on Electromagnetic Theory EMTS2010, Berlin, Germany*, Aug. 2010.
- [15] T. Schmidl and D. Cox, "Robust Frequency and Timing Synchronization for OFDM," *Communications, IEEE Transactions on*, vol. 45, no. 12, pp. 1613–1621, Dec. 1997.

Study on CFDP and DTN Architectures for ESA Space Missions

Felix Flentge

Ground Systems Engineering Department
ESA / ESOC
Darmstadt, Germany
felix.flentge@esa.int

Abstract—Upcoming file-based operations concepts and more complex communication topologies for space missions require modifications and extensions to the ‘traditional’ space and ground communication architectures. This paper reports on a study initiated by the European Space Agency (ESA) to analyse the suitability of the CCSDS File Delivery Protocol (CFDP) and Delay Tolerant Networking (DTN) architectures for future ESA missions. Starting from an analysis of potential future missions, generic mission scenarios involving complex communication topologies have been studied and corresponding communication requirements have been defined. Based on these generic mission scenarios and the communication requirements two reference architectures have been designed: one using CFDP on top of already deployed protocols and one combined CFDP/DTN architecture. A simulation environment to evaluate the reference architectures has been created and various communication scenarios have been evaluated. The paper introduces both reference architectures and presents some results of the simulation activities. These results and further analysis of the reference architectures lead to the conclusion that both architectures are quite similar in terms of performance and can satisfy most requirements. However, in the short to medium-term time frame CFDP without DTN seems to provide the easier way to adoption since it is conceptually simpler and more mature while the additional features of DTN may only be required in the long-term.

Keywords - Bundle Protocol (BP); CCSDS File Delivery Protocol (CFDP); Delay Tolerant Networking (DTN); Licklider Transmission Protocol (LTP)

I. INTRODUCTION

The trends towards more file-based operation concepts for space missions and increased complexity of space and ground communication topologies (e.g., data relays in space) has lead ESOC (the European Space Operations Centre) to initiate a study analysing how CFDP and DTN could be utilised in future ESA missions. Currently, support for file transfers and data relaying is mainly implemented by ‘private’ means for each mission. In conjunction with ongoing work on file-based operations at ESOC [1], generic communication requirements to support file-based operations and complex communication topologies have been defined.

The Consultative Committee for Space Data Systems (CCSDS) has standardised a CCSDS File Delivery Protocol (CFDP) [2] and is in the process of standardising protocols for Delay Tolerant Networking (DTN) in space [3]. CFDP is a file delivery protocol allowing file transfers over multiple hops and taking the specific space environment (like line-of-sight disruptions, long delays, etc) into account. DTN is an architecture for internetworking of networks that may be separated by disruption or delays. For space, it is typically implemented by using the Bundle Protocol (BP) [4] and underlying convergence layer protocols, like the Licklider Transmission Protocol (LTP) [5] or Proximity-1 [6]. Based on the generic communication requirements and the mission scenarios two reference communication architectures involving ground and space segment have been designed: one using CFDP on top of already deployed protocols and one combined CFDP/DTN architecture. In the former architecture store-and-forward features and retransmission capabilities of CFDP are utilised to provide multi-hop file transfer and reliability. In the latter architecture these functionalities are provided by BP and LTP, and CFDP just provides file transfer. Both reference architectures have been analysed and simulated using the ESOC Ground System Test and Validation Infrastructure (GSTVi) [7].

The paper starts with introducing the mission scenarios, communication requirements and the relevant standards. The reference architectures are presented and results from the simulation activities are reported. The paper finishes with some conclusions concerning the use of CFDP and DTN for future ESA missions and points to areas for future work.

II. MISSION SCENARIOS & COMMUNICATION REQUIREMENTS

In order to define generic communication requirements ongoing and planned ESA missions have been analysed in terms of communication architectures and topologies. Astronomy, Earth observation and planetary missions involving planetary landers have been taken into account. A ‘Complex Mission Topology’ has been derived from this analysis and includes all elements of the relevant missions:

- A complex space segment containing spacecrafts potentially owned by different space agencies that may be used as data relays as well as a landed asset on a planetary surface.

- An interoperating ground segment with ground stations owned by different agencies, (interoperating) Mission Control Centres (MCC), Lander Control Centres (LCC) and User Support and Operations Control Centres (USOC).
- Bi-directional asymmetric and uni-directional potentially disrupted and delayed communication links between the various elements.

The Complex Mission Scenario has formed the basis for the definition of the CFDP and the CFDP/DTN reference architectures. Detailed communication requirements have been defined based on the analysed missions and in conjunction with a working group on file-based operations at ESOC [1]. These requirements are related to different topics:

- **Communication Environment:** The reference architecture has to take the special characteristics of space communication into account. This includes long communication delays, low signal-to-noise ratios, high bandwidth/delay products as well as predictable (orbits, planetary rotation) and unpredictable disruptions (e.g. solar environment).
- **Communication Services:** Two types of co-existing communication services should be supported:
 - **File Services:** The transport of large data structures that are self-contained and persisted at source and target destination in file systems.
 - **Message Services:** Usually smaller data structures that are atomic and immediate in nature from operations point of view.
- **Quality of Service** aspects including completeness, error-free and in-sequence delivery may have to be regarded. Priority and pre-emption of certain data should be ensured, notification of end-to-end delivery and session control have to be provided.
- **Data Management** (of data in transfer): Information related to data transfer has to be available to the operators and data management operations (deletion of data in transfer, queue re-ordering, changing priorities, etc) should be possible to give the operators full control of all data transfer.
- **Security and Safety** including authentication, integrity and confidentiality services has to be taken into account. Of particular interest are also mission safety concerns. The Mission Control Centre (MCC) should have full visibility and control over the data uploaded to a spacecraft.
- **Routing** is expected to be static and planned based on link availability. Recovery from failure is likely to take the form of using pre-configured backup routes rather than dynamic route discovery.
- **Interoperability** at protocol level and cross-support between different agencies must be possible at various points, e.g., between MCC and ground station networks, ground stations and data relays in space or data relays and landed assets.

III. STANDARDS AND PROTOCOLS

The reference architectures take available and upcoming communication standards into account to facilitate future deployments and cross-support between different agencies. The following standards are used:

- **CFDP:** CFDP is used for bi-directional file transfer between various elements in the architecture [2]. CFDP includes different classes for reliable (Class 1) and unreliable (Class 2) file transfer as well as special features for relaying file transfers through intermediate waypoints (Store-and-Forward Overlay; CFDP Class 3 for unreliable and CFDP Class 4 for reliable multi-hop transfer). CFDP also contains a set of file manipulation primitives for managing remote file stores by operations such as file or directory creation, deletion and copying.
- **DTN:** DTN (Delay or Disruption Tolerant Networking) is an architecture for internetworking between separated (e.g., by delays or disruption) networks [3]. This is implemented by the use of the Bundle Protocol (BP) for the necessary store-and-forward capabilities and Convergence Layer Protocols for providing data transport [4]. For terrestrial networks this may be provided by UDP or TCP while for space links LTP (Licklider Transmission Protocol) may be chosen [5]. LTP is based on a negative acknowledgment scheme similar to the one used by CFDP and allows marking parts of the data for reliable (red mode) and for unreliable (green mode) data transport.
- **CCSDS Data Link Layer Protocols:** For the space links the usual CCSDS Data Link Layer Protocols are used. These include Packet Telemetry (TM) and Telecommand (TC), Advanced Orbiting Systems (AOS) Space Data Link and Proximity-1 for the link between a landed asset and an orbiter [6].
- **Encapsulation Packet:** The CCSDS Encapsulation Packet provides the means to multiplex packets from different user protocols (like space packets or CFDP) into the space link [6].
- **SLE:** CCSDS Space Link Extensions services are used to extend the services offered by the Data Link Layer Protocols from the ground station to the service user at the mission control centre [6].

IV. COMMUNICATION REFERENCE ARCHITECTURES

Based on the communication requirements and the available standards and protocols two reference architectures, one applying CFDP on top of 'traditional' protocols and one applying CFDP on top of DTN protocols, have been designed. Both reference architectures include the same key elements:

- A **Lander** on a planetary surface.
- An **Orbiter** orbiting this planet and used as a data relay for the lander.
- A **Ground Station (Network) (GS)** on Earth for communication with the orbiter and the lander.

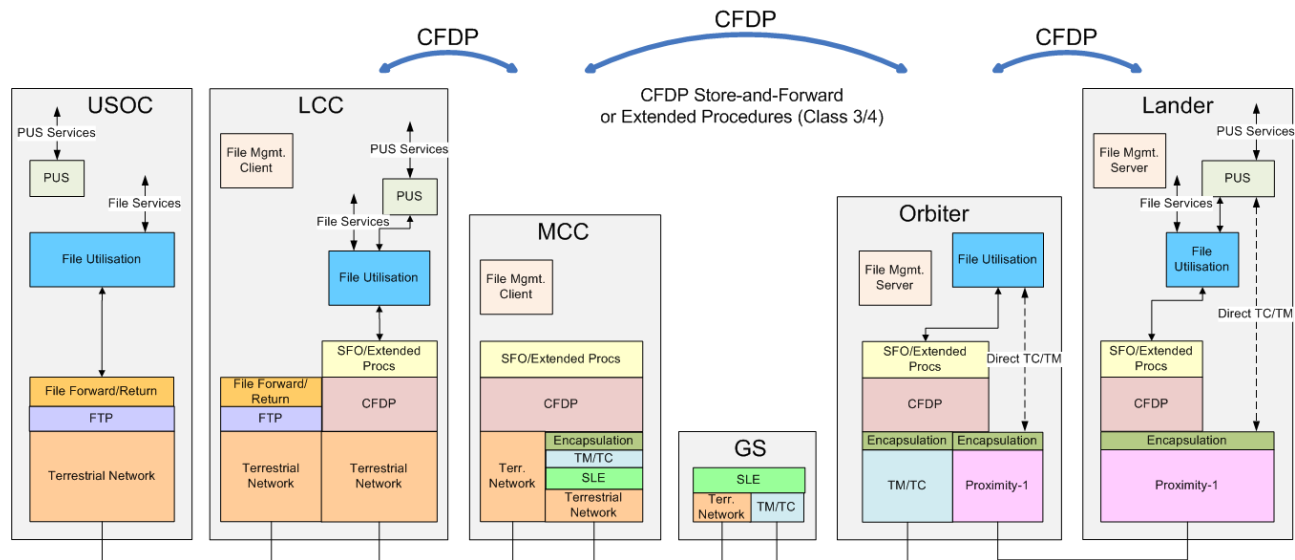


Figure 1. CFDP Reference Architecture.

- A **Mission Control Centre (MCC)** for monitoring and control of the orbiter.
- A **Lander Control Centre (LCC)** to monitor and control the lander. Data transfer using the orbiter is through the MCC.
- A **User Support and Operations Centre (USOC)** to monitor and control payloads onboard the lander. This is done by utilising the ESA Packet Utilisation Standard (PUS) [8] and a (not-yet existing) File Utilisation Standard (FUS). Data transfer is always through the LCC.

A. CFDP Reference Architecture

The CFDP Reference Architecture is shown in Figure 1. The main features of the reference architecture are:

- Use of a **conventional file transfer protocol** (like FTP) between USOC and LCC potentially enhanced by a File Forward/Return Service. A conventional file transfer protocol is chosen instead of CFDP as certain functions would have to be performed by the LCC taking mission-wide factors into account :
 - A **mission safety firewall** function at the file or packet utilisation level, which can check semantics of the file uplink/forward data against, for instance, permissions, resource allocation, etc.
 - A **pro-active fragmentation** function that, in the event of the use of multiple orbiter relays, breaks files into fragments that allow management of the transfer of each fragment in earth-orbiter and orbiter-lander contact periods.
 - A **remote file management** client, which exists to satisfy requirements for remote file fragmentation, queue reordering, status reporting and file transfer pre-emption.

- Use of **CFDP Class 1/Class 2 and Store-and-Forward Overlay (or CFDP Class 3/Class 4)** between LCC, MCC, orbiter and lander.
- Use of **SLE between MCC and Ground Station (Network)**. As the MCC – Ground Station Links can be assumed to be continuously available there seems to be no need to place CFDP inside the Ground Station as fragmentation and scheduling could be performed more easily from the MCC, in particular in the case multiple ground stations are used and files would have to be distributed to different ground stations. However, especially with the downlink of scientific data there are cases where it makes sense to terminate the CFDP traffic in the ground station. These cases have not been studied in detail, yet.
- Use of **CFDP or direct TC between orbiter and lander on top of Proximity-1**. The orbiter should provide the option to function as a CFDP intermediate waypoint (store-and-forward overlay or extended procedures) and the option to extract TC from a file and send them directly to the lander (e.g., for emergency commanding).

Please note that message services can be provided in parallel to the file transfer using the PUS standard.

B. DTN Reference Architecture

For the CFDP/DTN architecture ‘pure’ file transfer functionalities are still provided by CFDP while store-and-forward and reliability are provided by BP and LTP or Proximity-1 as underlying protocols. The CFDP/DTN Reference Architecture is shown in Figure 2. The main features are:

- Use of **CFDP Class 1 (unreliable transfer) between LCC and orbiter (direct TC) or lander**. Reliability will be provided by the underlying protocols and store-and-forward is realised by BP.

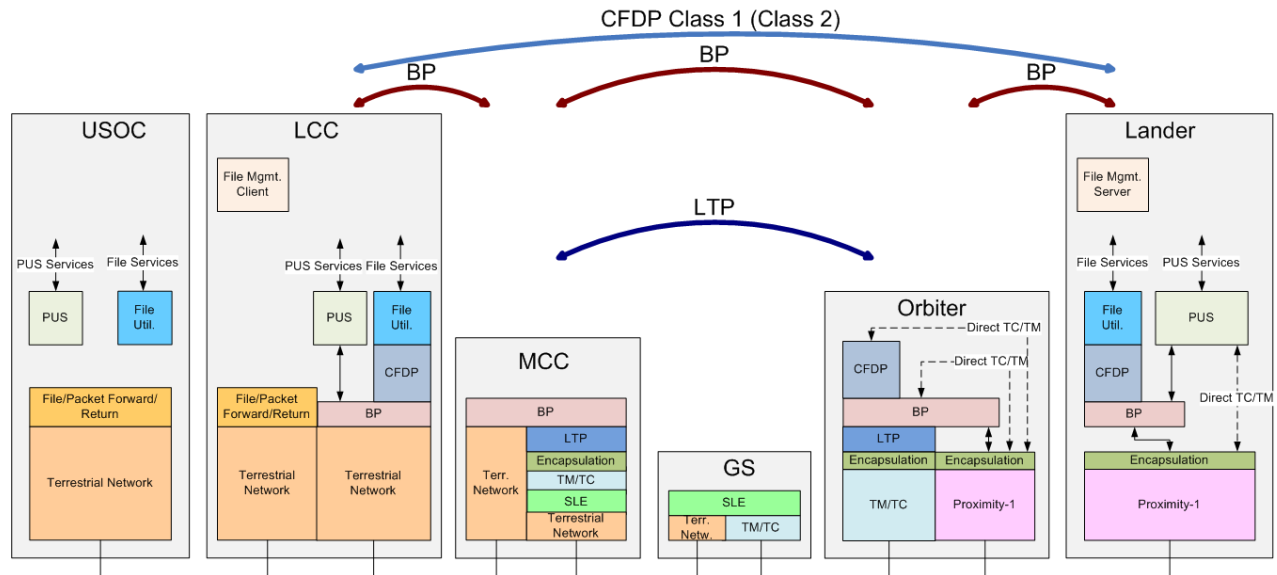


Figure 2. CFDP/DTN Reference Architecture.

As BP is a transport layer protocol additional means for end-to-end acknowledgement for a complete file transfer may be needed. This could be provided by using bundle status reports, using CFDP class 2 (without really needing retransmission) or a yet-to-be-defined CFDP Class 1a without retransmissions but with end-to-end confirmation.

- Use of **SLE between MCC and Ground Station (Network)**. As the MCC – Ground Station Links can be assumed to be continuously available there seems to be no need to apply the store-and-forward of BP in the ground station. However, under some circumstances (downlink with routing of bundles to different users, low link capacity between GS and MCC) supporting BP and providing bundle storage in the ground station is desirable.
- Use of **BP over LTP and CCSDS Encapsulation Packets between MCC and Orbiter** with LTP providing (selective) reliability and the encapsulation packet providing multiplexing of different protocols if necessary.
- Use of **BP or direct TC on top of proximity-1 between orbiter and lander**. Again, a direct TC capability should be provided by the orbiter by either extracting TC packets from bundles or from files.

In this case message services can be provided by PUS or the upcoming Asynchronous Message Service [6].

V. ARCHITECTURE SIMULATION

In order to validate the proposed reference architectures a simulator based on ESOC's GSTVi [7] and the SIMSAT simulation framework has been created. For initial tests SCOS 2000 has been connected as Mission Control System to initiate file transactions, send TC and receive TM packets. For more systematic and automated tests a traffic load generator component has been used. ESOC's CFDP Entity

implementation for the ground segment [9], the DTN2 implementation of the BP from the Delay Tolerant Network Research Group and the LTPlib from Trinity College Dublin for LTP have been used to simulate the necessary protocols. As no Proximity-1 implementation has been available, only a basic Proximity-1 emulation based on UDP has been created.

A. Mission Test Scenarios

Many simulations with different mission configurations have been performed. In this paper we concentrate on:

- **'Relay Mission with CFDP Only'** including the MCC, a single ground station, an orbiter and a lander.
- **'Relay Mission with CFDP over DTN'** including the same elements as the 'Relay Mission with CFDP Only' mission configuration but using CFDP on top of BP and LTP.

Acknowledged and unacknowledged file transfers putting files to the simulated lander and getting files from the lander (using CFDP proxy put requests) have been evaluated. Getting a file involves both - sending a request to the lander and the actual transmission of the file to Earth. Two 'error conditions' have been tested:

- **Best Case:** Continuous end-to-end link without QoS errors, i.e., no retransmissions occur.
- **Dropped packets:** The 4th TM packet and the 4th TC packet that are sent from/to ground are dropped. In acknowledged modes, this will lead to retransmissions.

Typical bandwidths have been selected: 10 kbps for the earth-orbiter link and 500 kbps for the orbiter to lander link. A large latency between Earth and orbiter (1200 sec) and a small latency between orbiter and lander (1 sec) have been used. CFDP PDU sizes have been chosen to be completely carried in a PDU of the most restrictive underlying protocol (220 byte / 1024 byte for 'CFDP only' uplink / downlink on

earth-orbiter link; 10240 byte for ‘CFDP/DTN’ for uplink and downlink on earth-orbiter link). The experiments have been performed with different file sizes (1k, 10k, 100k).

B. Simulation Results

During the simulations it has been detected that getting files from the lander using a CFDP proxy put request could not be executed for the relay missions with CFDP Store-and-Forward Overlay (SFO). The reason is that SFO currently cannot carry a proxy request to the destination waypoint. This has been reported to the CCSDS Working Group.

Furthermore, 100k file transfers with CFDP/DTN have not been possible with the UDP-emulated Proximity-1 link since files have been put in a single bundle and bundles exceeding the maximum size of UDP datagrams cannot be send over the UDP convergence layer.

1) Unacknowledged File Transfers

For unacknowledged file transfers CFDP Class 3 was compared with CFDP Class 1 SFO and CFDP Class 1/BP/LTP green mode.

a) Putting files to the spacecraft – Best Case

The time needed for sending a file from ground to the lander is only slightly above the One Way Light Time (OWLT) for all protocol configurations with very little differences. As shown in Figure 3, the protocol overhead on the orbiter to lander link is quite high for small files (around 15%) but drops significantly for larger file sizes. For large file sizes there is a considerable overhead for CFDP class 3 compared to the other protocol configurations. This can be attributed to the fact that CFDP Class 3 because of the CFDP PDU forwarding mechanism uses a smaller CFDP PDU size on this link (220 bytes) compared to the other protocol configurations. For example, in the 10k file size case 49 packets are send, compared to respectively 8 and 6 packets for Class 1 SFO and Class 1/BP/LTP green.

b) Getting files from the spacecraft – Best Case

As explained above, the CFDP SFO does currently not allow initiating a proxy get operation over hops, so just CFDP Class 3 and CFDP Class 1/BP/LTP green have been compared. Transaction durations are for both configuration about 2 x OWLT (1 OWLT to initiate the put request to downlink the file + 1 OWLT to downlink the file).For the 1k file there is about 15% protocol overhead for CFDP Class 3

and about 23% protocol overhead for CFDP Class 1/BP/LTP green on the lander to orbiter link. For 10k files, the protocol overhead is only about 2.5% for both configurations.

2) Acknowledged File Transfers

For acknowledged file transfers CFDP Class 2 SFO and CFDP Class 4 were compared with CFDP Class 1/BP/LTP red and CFDP Class 2/BP/LTP green (to see whether reliability should be provided by CFDP or LTP). Dropping of packets has only been investigated with 10k files.

a) Putting files to the spacecraft – Best Case

Transaction durations are about 3 OWLT for all protocol configurations but Class 2 SFO, which needs about 4 OWLT. Three OWLT are needed for sending the file to the lander, sending a notification that the file transfer has finished back to ground and getting an acknowledgment for this notification. Class 2 SFO needs more time because the file transaction between ground and the orbiter has to be completed (3 OWLT) before the file is sent to the lander and a SFO Report is sent back from the lander to the ground (1 OWLT). As usual, protocol overheads are quite high for 1k files (15% to 24 % with CFDP Class 2/BP/LTP green having the highest overhead) but are small for larger files (5% for CFDP Class 4 and around 2.5% for the rest).

b) Putting files to the spacecraft – Dropped Packet

The whole picture changes as soon as TC/TM packets are dropped (see Figure 4). CFDP Class 4 has the shortest duration (4 OWLT), with CFDP Class 1/BP/LTP red and CFDP Class 2 SFO taking 50% longer. CFDP Class 2/BP/LTP green takes twice as long as CFDP Class 4. The good performance for CFDP Class 4 is due to the fact that the retransmission request for the lost TM is send back to Earth immediately and is not affected by the dropped TC packet (as only the 4th packet is dropped). For CFDP Class 2 SFO and CFDP Class 1/BP/LTP red, the completion of the file transfer is affected by the dropped TM and the dropped TC and taking 2 OWLT more. CFDP Class 2/BP/LTP green detects the missing TM packet only at the lander and is affected by the dropped TC. This leads to a retransmission of the whole bundle and a very long duration (8 OWLT).

The protocol overheads for the 10k file are similar to the results without dropped packages with the exception of CFDP Class 2/BP/LTP green that has an overhead of 100% that reflects the resending of the whole bundle.

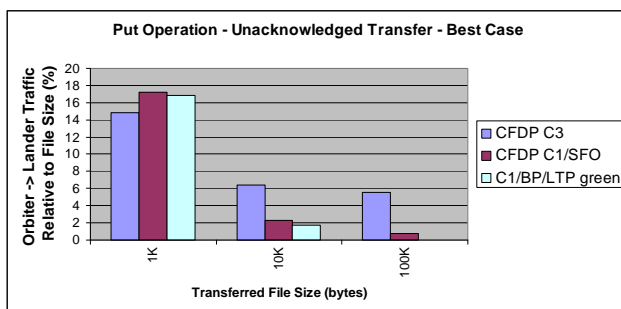


Figure 3. Comparison of protocol overhead on the orbiter to lander link by different communication architectures to an unacknowledged file transfer to a lander in best case error conditions.

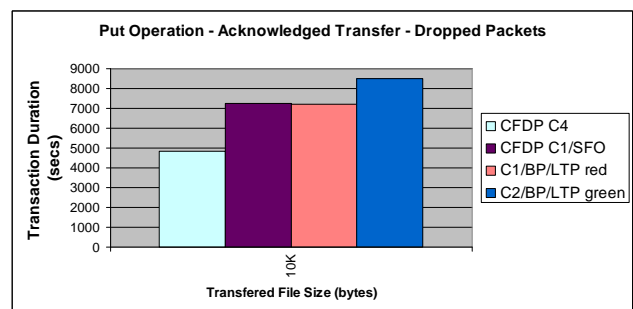


Figure 4. Comparison of transaction durations by different communication architectures to an acknowledged file transfer to a lander in dropped packets error conditions.

c) Getting files from the spacecraft – Best Case

The transaction durations for getting a file from the spacecraft (i.e., proxy put request + acknowledged downlink of the file) takes for all protocol configurations about 4 OWLT (1 OWLT to initiate the downlink + 3 OWLT for the downlink; SFO is not possible in this case). Protocol overhead is high to very high for 1k files (23% CFDP Class 1/BP/LTP red, 32% CFDP Class 2/BP/LTP green, 50% CFDP Class 4) but comparable to the overhead in other scenarios for bigger file sizes (2.3% to 3.5%) with a larger overhead for CFDP Class 4 (5.4%), which can again be attributed to the smaller PDU size as explained for CFDP Class 3 in the unacknowledged case.

d) Getting files from the spacecraft – Dropped Packet

For acknowledged transfer with dropped packets CFDP Class 4 and CFDP Class 1/ BP/LTP red need about 8 OWLT. This is because a TC and a TM packet are dropped, causes retransmissions due to negative acknowledgements and inactivity timeouts. In this scenario, CFDP Class 2/BP/LTP green could not deliver the complete file because LTP is used in unreliable mode and one TC packet containing an LTP segment is dropped. At the receiving end the bundle is reassembled but part of the data is missing, leads to an incomplete file when the bundle is passed to CFDP. As CRC has not been used for CFDP PDUs in this case, the PDU is accepted but a file checksum error is raised. Looking at protocol overhead with 10k files reveals again a larger overhead for CFDP Class 4 (8%) compared to CFDP Class 1/BP/LTP green (2%) caused by the smaller CFDP PDU on the lander to orbiter link for CFDP Class 4.

VI. CONCLUSION AND FUTURE WORK

Both, the CFDP only and the CFDP/DTN reference architectures, provide solutions to the provision of message and file services over noisy, long-delay, disrupted channels as found in typical ESA missions. The preliminary conclusion is that, once the timeouts were tuned to those appropriate for the mission scenario, there is little to choose between any of the communication architectures in terms of transaction duration and protocol overheads. For retransmission of lost packages hop-by-hop retransmission (CFDP Class 4, SFO, LTP Red Mode) is generally preferable over end-to-end retransmissions (CFDP Class 2 over BP). SFO has a slight disadvantage in terms of transaction duration as all of the file must be transferred to and stored on the relay before it can be forwarded. Furthermore, CFDP SFO has currently some conceptual problems with proxy put requests over multiple waypoints.

However, for specific missions, further simulation with more realistic link characteristics and an optimisation of the protocol configurations as well as formal analysis is needed to compare potential architectures more realistically and to understand potential trade-offs. For example, on the one hand CFDP lacks security primitives, and arguably includes too many “layers” in a single specification while DTN is architecturally cleaner and is not limited to file transfers. On the other hand, some aspects of DTN are still subject to active research (network management, routing, security

aspects for BP) and there are a number of operational uncertainties that need to be studied before one would mandate its use in future ESA missions. In particular, the network management aspects of DTN are not yet well-developed and may require significant additions to the BP before DTN can meet the current operational requirements.

Apart from these operational aspects, for the missions and scenarios analysed in the study, the bulk of the requirements can be satisfied by adoption of existing CCSDS recommendations including CFDP or by a CFDP/DTN architecture. However, some of the additional features that DTN supports are not yet required for upcoming and planned ESA missions. From the operational point of view there may be difficulties in accepting the new model of control that is implied with a DTN based architecture and further research and development into DTN may be necessary to establish that DTN can meet these operational requirements. In addition, CFDP has been already standardised by CCSDS and ESA implementations for the ground and space exist while DTN-related protocols are still in the CCSDS standardisation process. So, in the short to medium-term time frame CFDP without DTN seems to provide the easier way to adoption since it is conceptually simpler and more mature while the additional features of DTN like dynamic routing or reactive fragmentation may only be required in the long-term. DTN does appear to provide a solution in the long-term when more complex networks of interoperating assets in space and on ground (Earth and other planets) exist.

ACKNOWLEDGMENT

The CFDP/DTN Study has been performed by SciSys, UK in cooperation with Trinity College Dublin, Ireland and Keltik Ltd., UK. Without their excellent work and expertise it would not have been possible to achieve the high quality results reported in this paper.

REFERENCES

- [1] M. Pecchioli, E. Montagnon, G.P. Calzolari, F. Flentge, and A. Kowalczyk, “Towards File Based Operations”, AIAA 2010-2190, Electronic Proceedings for SpaceOps 2010.
- [2] CCSDS 727.0-B-4. CCSDS File Delivery Protocol (CFDP), Recommended Standard, Blue Book, January 2007.
- [3] V. Cerf, S. Burleigh, A. Hooke, L. Torgerson, R. Durst, K. Scott, K. Fall, and H. Weiss, “Delay-Tolerant Networking Architecture”, Network Working Group, RFC 4838, April 2007.
- [4] K. Scott and S. Burleigh, “Bundle Protocol Specification”, Network Working Group, RFC 5050, November 2007.
- [5] M. Ramadas, S. Burleigh, and S. Farrell, “Licklider Transmission Protocol – Specification”, Network Working Group, RFC 5326, September 2008.
- [6] Consultative Committee for Space Data Systems (CCSDS), <http://public.ccsds.org>, access date: 31 January 2011.
- [7] M. Goetzelmann, N. Lindmann, P. Ellsiepen, C. Laroque, M. Niezette, and A. Walsh, “Ground Systems Test and Validation Infrastructure – from Concept to Implementation”, AIAA 2006-5540, Electronic Proceedings for SpaceOps 2006.
- [8] ECSS-E-70-41A. Ground Systems and Operations – Telemetry and Telecommand Packet Utilization, January 2003.
- [9] F. Flentge and M. Jordan, “Design and Implementation of CCSDS File Delivery Protocol for ESA Ground Segment”, ESA SP-669 (CD-ROM), Proceedings of DASIA 2009.

Setting up a Student Satellite Receiving System in the United Arab Emirates

Yousef El-Haj, Mustafa Harbaji, Lutfi Albasha
 Department of Electrical Engineering,
 College of Engineering
 American University of Sharjah
 Sharjah, United Arab Emirates
 e-mail: albasha@aus.edu

Nidhal Guessoum
 Department of Physics
 College of Arts and Sciences
 American University of Sharjah
 Sharjah, United Arab Emirates
 e-mail: nguessoum@aus.edu

Abstract—The successful setting up of a research satellite system (signal receiving and data acquisition station) in the United Arab Emirates is reported. The process of drawing up the basic system architecture and determining the essential requirements of the receiving station that is the satellite dish and components and the reception unit (hardware and software) is described. The challenges encountered and the mitigations and report on the success achieve so far: system set up, signal acquisition, quick data analysis and image processing is discussed. Preliminary conclusions are presented from this first phase of the project.

Keywords- satellite receiving station; EUMETSAT; students project

I. INTRODUCTION

The aim of this project is to set up a satellite reception station by students in a multi-phase timeline. There are various educational, scientific, and technical objectives to this project – the first of its kind in the region. A few similar projects have been undertaken elsewhere [1, 2, 3].

In the first phase, the station was constructed from a blueprint as recommended by the European Organization for the Exploitation of Meteorological Satellites (EUMETSAT).

EUMETSAT’s network provides useful meteorological and environmental data; its scheme allows it to transmit weather, climate, and geographical data to large regions of the world [4]: the data is sent to a ground station (the European uplink) which acts as a router; then the received signal is sent to a geostationary satellite.

In order to receive the signal in the United Arab Emirates (UAE), the need arised to turn to the Atlantic Bird 3 geostationary satellite, which receives the data from the African Service station. Atlantic Bird 3 covers mainly the African continent; however, the UAE is just within the footprint covering Africa [5]. This has posed an interesting challenge, that had to be dealt with.

This paper presents a project of building a receiving station that can receive EUMETSAT satellite data. In the first phase, the receiving station was built from off-the-shelf components; that is, the station was assembled from components that are available in the market. Students then moved to the second phase where the receiving station

was designed and built essentially from scratch. The main task was to build the appropriate receiver for obtaining a good-quality satellite signal (a good signal-to-noise ratio). The second phase, well under way, will be considered complete once the data, thus obtained and analyzed, matches with that from Phase One. A later phase will consist of a full scientific analysis of the data [6].

The first task was to perform a simulation analysis on the link budget to determine the required technical specifications of the needed components as shown in Figure 1. This analysis considers the signal strength, the data type, the hardware, software and components gain, noise and linearity requirements.

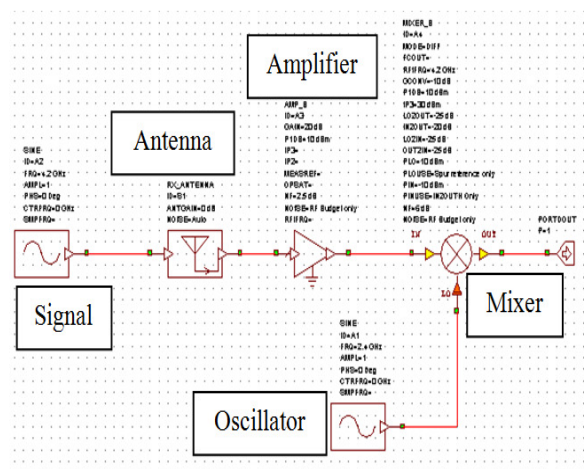


Figure 1: Block diagram of the simulation analysis using AWR tool of the Low Noise Block (LNB)

II. PROCEDURE

The next task was to assemble the receiving station using ready-made components in order to acquire, record, and test the signal from the Atlantic Bird 3 satellite. A block diagram showing the main components of the station is given in Figure 2.

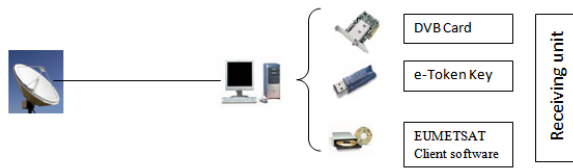


Figure 2 – Block diagram of the project

A. The satellite dish and Low Noise Block (LNB)

An essential part of any receiving station is the antenna. At United Arab Emirates, it is possible to receive both Ku-band and C-band signals, but the geographical coverage of the C-band signal is much better as recommended by EUMETSAT . Figure 3, at the end of the paper, adapted from a EUMETSAT diagram, shows the recommended satellites for each region.

An appropriate Low Noise Block converter (LNB) had to be selected for the purpose of receiving a C-band signal; however, we installed an LNB with a duality feature for the future possibility of using the Ku band (perhaps with a different satellite). Figure 4 shows the LNB used and its band frequency specifications.



Figure 4: LNB selected in the AUS Student Satellite receiving station.

As can be read on the LNB shown in Figure 4, the frequency of the input signal is in the range of 3.4 to 4.2 GHz for the C band (with the possibility of detecting signals in the Ku band range of 10.7 to 12.75 GHz). The output frequency of this LNB for the C band is 950 to 1750 MHz, with a gain of 65 dB. For the Ku band, the output frequency would be 950 to 2150 with 65 dB gain. Nevertheless, the noise level of the LNB in the C band is 17° K, and for the Ku band it is 0.5 dB.

Another major consideration in the design is the antenna’s dish size. According to EUMETSAT recommendations (Table 1 below) and taking into account the expected signal level due to the geographical location of the station (almost at the edge of the satellite’s footprint, as seen from Figure 2) the size of the dish to be used in this area should be at least 3.7 meter.

TABLE I. RECOMMENDED DISH SIZE ACCORDING TO THE COVERED REGIONS BY EUMETSAT

Band	Location	Antenna Size
Europe (Ku-band)	within the "core" geographical footprint of the spacecraft, the area bounded by the inner contour depicted in the Hot Bird™ 6	85cm or larger
Europe (Ku-band)	within the "extended" geographical coverage (remote European islands, Turkey East of Ankara and Eastern European countries)	1.8m or larger
Africa (C-band)	within the "core" geographical footprint , the area bounded by the inner contour depicted in the Atlantic™ Bird 3	2.4m or larger
Africa (C-band)	within the "extended" geographical coverage (e.g. Madagascar, La Reunion, Mauritius and parts of North America)	3.7m or larger
South America (C-band)	within the area bounded by the 39 dBW contour depicted in the NSS806 graphic	2.4m or larger
South America (C-band)	smaller antennas may be sufficient, depending upon individual location, for details for your location, please contact the EUMETSAT User Service	1.8m or larger

For this work we elected to use a 4.2 meter dish, shown in Figure 5, to receive a good signal as much as possible



Figure 5 – AUS Student Satellite Station’s receiving dish

B. Personal Computer (PC) Receiving Station

The DVB card used in our station is the Technisat™ SkyStar 2, which is one of the recommended DVB cards for receiving EUMETSAT broadcasts. The card is shown in Figure 6, as installed in a PCI slot of a computer.



Figure 6 – Technisat™ SkyStar 2 DVB PCI Card

Figure 7 shows the LNB frequency setting on the DVB card and the corresponding received signal quality and strength.

This, however, was not enough to ensure receiving the right signal and data. For that, the EUMETCast Client Software is used, both to insure the integrity of the signal, and to decode the incoming data.

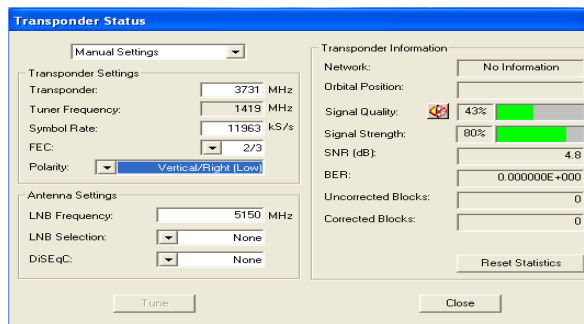


Figure 7 – Technisat™ SkyStar 2 DVB Card Transponder Status

C. The Client Software

The EUMETCast Client Software is provided by EUMETSAT to access, decode, and process the received signal through the DVB card. This software is a client/server system linking the server at the EUMETCast uplink site with the system at the user side. When the software is installed and run, it showed an “Active” status (figure 8), thus confirming that a signal was being received and the system was establishing a connection to try to decode it.

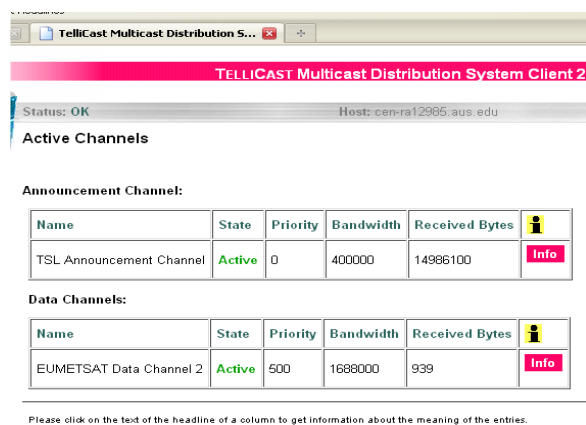


Figure 8 – EUMETSAT Client Software

The connection has indeed been fully established. The signal could then be analyzed for validity by a visualizing software (see Figure 9). In a later phase, the scientific analysis of the data can be undertaken, extracting real information from the data/images.

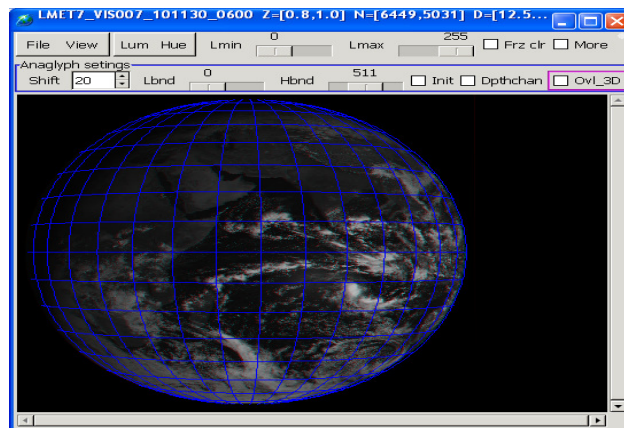


Figure 9 – Visualized picture of the downloaded data

III. DISCUSSION: WORK SO FAR AND CHALLENGES ENCOUNTERED

The main objective of this project is educational, that is for the students to acquire scientific knowledge and technical skills and apply them in a concrete task of a modern field. This is clearly being achieved with the successful setting up and completion of the main parts of the project and with the outcomes now produced (Figure 9).

Indeed, the outcomes that had been set for this project, or at least its first phases, are:

- ◆ Constructing an electronic blueprint for the station;
- ◆ Assembling the station;
- ◆ Testing the reception of the satellite signal;
- ◆ Ensuring the integrity and validity of the data;
- ◆ Producing images.

All the above objectives have been achieved and by visualizing the data, phase one has been completed successfully.

This first part of the project, though simple in concept and apparently straight-forward to implement (assembling dish, LNB, and computer hardware, and installing and executing the appropriate software), was actually far from trivial and raised some very useful issues, which were tackled as pedagogical (learning) opportunities.

Once the EUMETSAT satellite network and its data had been settled, the remained part was to determined which specific satellite was needed to target and how to ensure that a good signal was to be detected and recorded. As the UAE is located at a far point of the contour footprint of the Atlantic Bird 3 satellite’s C band coverage area, the dish size had to be at least 3.7 meters wide, though for the reasons explained above a conclusion was drawn to have a satellite about 4.2 meter. However, most markets in the UAE offer only dishes that range between 90 and 120 centimeter in diameter. However, a company which would install a 4.2 meter parabolic dish was found.

Once the dish was installed, the strength of the signal was checked. The Technisat™ SkyStar 2 DVB PCI Card software contains a pre-setting for most used satellites, like Hotbird 13E and Nilesat 101/102 7 W (see Figure 10), a setting which can determine and show the signal strength and quality.

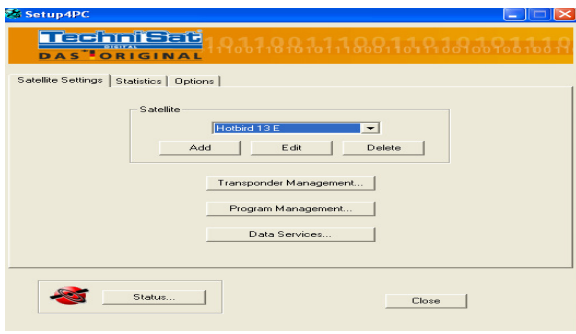


Figure 10 – Hotbird example for available Satellites

Not surprisingly, the Atlantic Bird 3 satellite is not included in this pre-setting, as it is not a satellite which consumers normally access. To overcome this issue, we updated the software of the TechniSat™ SkyStar 2 DVB PCI card manually by contacting the manufacture. After this modification, access to the signal from Atlantic Bird 3 was possible. But in order to make sure that we were indeed receiving a real signal we measured the Signal-to-Noise ratio, using the following connection:

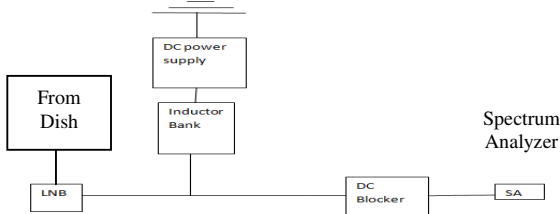


Figure 11: Testing the Signal using Spectrum Analyzer Circuit Diagram

The DC power supply is adjusted to 14 Volt to model the vertical polarization. The inductor bank acts as an open circuit in which the final circuit diagram in AC small signal analysis will be the model of the LNB and SA only. By testing the signal we found a signal-to-noise ratio of 65 dB.

IV. CONCLUSIONS

In this report we have summarized the main steps and procedures we followed in setting up a satellite receiving

station in the UAE. Phase One of our project has enabled us to acquire multi-faceted experience and expertise on such a project. It was important to start with a phase in which we take ready-made components and assemble them, as this helps the project participants begin with basics before launching into more ambitious electronic design topics.

This project has now moved to Phase 2, as the first phase has been completed and a signal has been obtained and confirmed by visual display of the data, and the learning has been substantial and important.

The project is now proceeding with the building of a receiver unit, mainly the DVB card, from scratch. We anticipate this part of the project to be both challenging and of great potential rewards, as the students will be able to show their technical knowledge, skills, and capabilities, and may produce units that might be of much better performance than the ready-made components that were used in Phase 1. All in all, the receiver should have a high sensitivity to receive the signal at high SNR that is to have a signal strength of 4.9 dB, as the UAE is located at the far edge of the satellite footprint.

ACKNOWLEDGMENT

This work was in large part supported by a grant from the Emirates Foundation (UAE). We also thank administrators and staff of the American University of Sharjah for their assistance and support.

REFERENCES

- [1] B. Maathuis and V. Retsios, "Installation, setup and use of a low cost C-band Meteosat-8 ground receiving station in Rwanda," 2006, <http://www.cgisnur.org/IMG/pdf/full-paperAARSE2006-MSG-CGIS.pdf> [March 31, 2011].
- [2] J. D. Mazimpaka, "Meteosat second generation ground receiving station at CGISNUR: reinstallation and reconfiguration technical report", 2009, http://www.cgisnur.org/IMG/pdf/Meteosat_Reinstallation.pdf [March 31, 2011].
- [3] Mercury: A Satellite Ground Station Control System – <http://gs.stanford.edu/mercury/main.php> [March 31, 2011].
- [4] EUMETSAT: <http://www.eumetsat.int/Home/Main/DataAccess/EUMETCast/SystemDescription/index.htm?l=en> [March 31, 2011].
- [5] EUMETSAT'S Africa (C-band) geographical footprint: <http://www.eumetsat.int/Home/Main/DataAccess/EUMETCast/index.htm?l=en> [March 31, 2011].
- [6] A. K. Maini and V. Agrawal, Satellite Technology: Principles and Applications, Wiley, 2007, pp. 394–410.

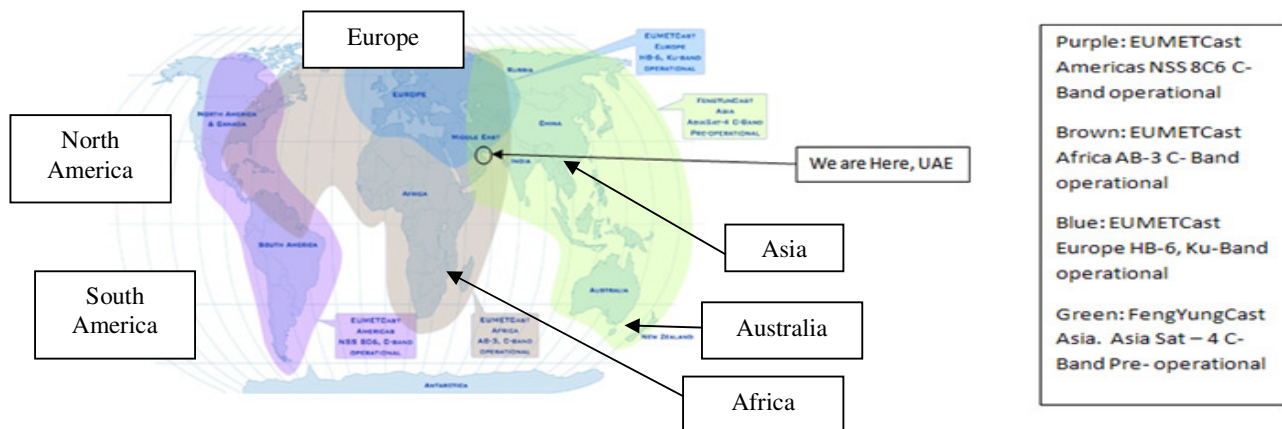


Figure 3 – The location of UAE with respect to the contour of the footprint of the Atlantic Bird, C-Band

Characterizing Network Architecture for Inter-satellite Communication and Relative Navigation in Precise Formation Flying

Rui Sun, Jian Guo, Eberhard Gill, Daan Maessen
 Chair of Space Systems Engineering, Faculty of Aerospace Engineering
 Delft University of Technology
 Kluyverweg 1, 2629 HS, Delft, the Netherlands
 r.sun@tudelft.nl

Abstract—Precise formation flying (PFF) missions require formation acquisition and maintenance through interactions among spacecraft by inter-satellite communication and relative navigation. That requires the network architecture to satisfy dedicated system constraints of time-criticality for updating navigation measurements and flexibility for implementation across various phases of mission operations. Potentially applicable architectures that combine different multiple access technologies, half-duplex/full duplex configurations, and network topologies are discussed and evaluated. Half-duplex CDMA with roles rotating among all spacecraft is shown more suitable and efficient for PFF missions. Its limitation in terms of multiple access interference is analyzed as well.

Keywords - *precise formation flying; communication; relative navigation; time-critical; various mission phases; CDMA*

I. INTRODUCTION

Precise formation flying (PFF) missions involve the acquisition and maintenance of spacecraft in a desired relative geometric configuration, especially when trying to create a large virtual spaceborne instrument, such as telescope or interferometer. Coordinating the components of such instruments on separate spacecraft can require highly accurate relative orientation and positioning.

The common way to perform such PFF missions is to use differential Global Navigation Satellite System (GNSS) by exchanging GNSS-based navigation measurements via inter-satellite links [1]. Yet this method is limited to low earth orbit (LEO). Many missions such as PROBA-3, Darwin and TPF require the spacecraft flying in high earth orbit (HEO) or Lagrange points, where GNSS signals are very weak or not available at all [2]. As a result, a dedicated formation flying radio frequency (RF) technique using locally generated inter-satellite ranging signals is necessary. It is expected to integrate with inter-satellite communication for system efficiency. Thanks to the widespread use of spread spectrum techniques, RF signals modulated with a pseudo random noise (PRN or PN) code appears to be advantageous in such integrated system, since they allow both reliable communication and accurate ranging measurements [3].

In considering the properties of communication and ranging driven PFF network, interactions among spacecraft should satisfy system constraints including time-criticality of updating measurements, and flexibility for implementation across various phases of mission operations. This paper will address these constraints, and propose potentially applicable

architectures that use fixed assignment for all possible connections by multiple access (MA) technologies. The applicable combinations among different MA, half-duplex/full duplex configurations, and network topologies are discussed and evaluated.

The paper is organized as follows. In Section II, the inter-satellite communication and relative navigation sensor is introduced in order to propose the dedicated constraints for PFF network in Section III. Candidate network architectures and their comparison are presented in Section IV. Network capability in terms of multiple access interference is analyzed in Section V. Section VI concludes the paper and discusses future directions.

II. INTER-SATELLITE COMMUNICATION AND RELATIVE NAVIGATION SENSOR

An inter-satellite sensor for PFF missions is under development that should integrate communication and relative navigation into one package. The method traces heritage to GPS-like technology and is expected to satisfy the following specific high-level requirements:

- Communication and relative navigation are integrated into one package, with mass less than 2 kg, and power consumption less than 2 W;
- Operating range less than 30 km;
- Omni-directional (4π steradian) coverage;
- Flexible to implement across various phases of mission operations in two modes: coarse-mode during the deployment, reconfiguration and collision avoidance tasks; fine-mode during the formation maintenance process;
- Navigation accuracy is 1 m for coarse-mode using code measurement (pseudorange) only, and 1 cm for fine-mode using the combination of code and carrier phase measurements;
- Resolution of related integer ambiguity problem of carrier phase measurement;
- Measurement update rate ≥ 1 Hz.

The inter-satellite sensor functional block diagram is in Fig. 1. Software-defined transceiver is used, in which way the signal generation and processing is accomplished via a programmable microprocessor e.g. FPGA or DSP. The current transceiver version implements the signal generation and processing on PC via Matlab/Simulink.

As shown in Fig. 1, the software-defined transceiver comprises the transmitter and receiver front-end part and

signal simulator and processing part. The front-end is based on hardware design that comprises signal amplifier, band pass filter, down-conversion, sampling, and quantization. The signal simulator and processing are realized only based on software through the signal generation module to generate carrier and PRN code modulated signal, and acquisition, tracking and decoding modules for data recovery, code and carrier phase extraction, and pseudorange (-rate) derivation.

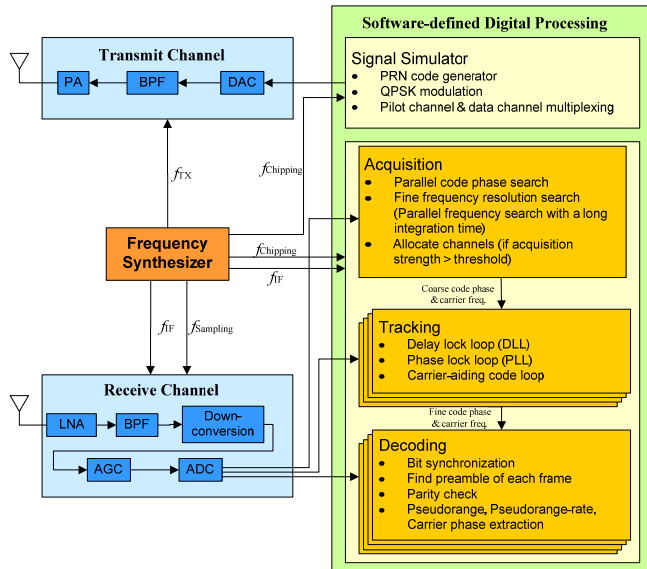


Figure 1. Inter-satellite sensor functional block diagram

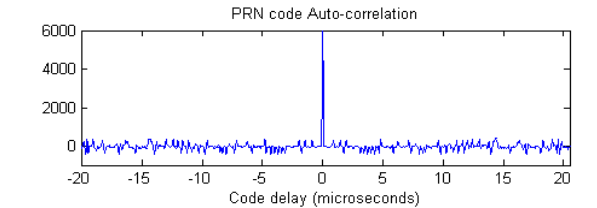
Fig. 2 depicts the signal generation and processing simulation results assuming that intermediate frequency (IF) is 9.55 MHz and a sampling rate is 38.19 MHz. In signal simulator, PRN code is generated with a chipping rate of 10.23 Mcps and length of 1023 chips. Compared to GPS C/A code, such signal can increase the theoretical lower bound of code tracking accuracy of approximately 3 times better at the same noise level and same front-end bandwidth according to the Cramér-Rao lower bound theory [4]. Doppler shift is generated following a linear function.

The process of acquisition is a global search in a two dimensional search space for approximate values of Doppler shift and code phase. This process is time and computation consuming. Therefore, parallel code/frequency one-dimensional search using Fast Fourier Transform (FFT) is implemented. After acquisition, control is handed over to delay lock loop (DLL) and phase lock loop (PLL), which yield fine estimates of code and carrier phase continuously and track the variations due to dynamics between satellites. Communication bits can be extracted from the tracking loops. Pseudorange measurements are derived afterwards.

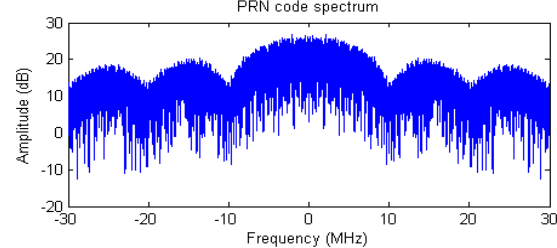
III. CONSTRAINTS ON PFF NETWORK ARCHITECTURE

A. Time-critical requirements

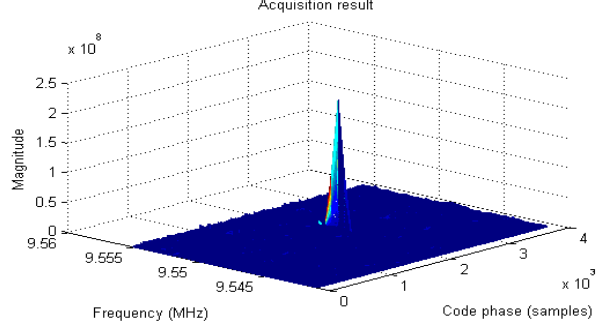
Time-critical requirements are driven by the nature of dynamic relative navigation process that contains two steps: propagation in the filter and measurement update.



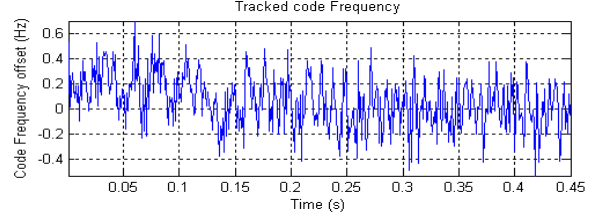
(a) Auto-correlation, chipping rate is 10.23 Mcps



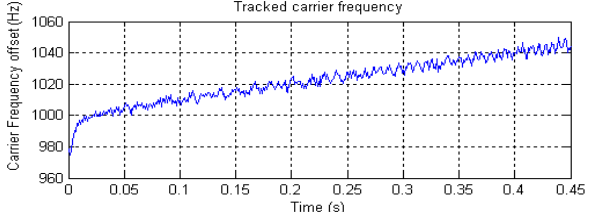
(b) Code Spectrum, chipping rate is 10.23 Mcps



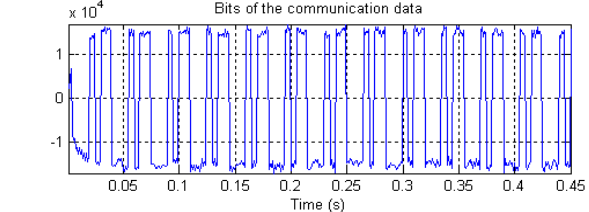
(c) Acquisition results, the peak is present at the point where the code offset is at 2100 sample (3819 samples in total for one PRN sequence) and carrier frequency is at 9.54904 MHz (that is, Doppler offset at 1038 Hz)



(d) Code frequency offset in DLL



(e) Carrier frequency offset in PLL



(f) Communication bits extraction. The values are not ± 1 because of the quantization in the front-end and integration in the tracking loops.

Figure 2. Software-defined signal generation and processing results

Relative navigation filter (e.g. extended Kalman filter) is used to account for the relative position errors resulting from all relevant non-modeled accelerations acting on the spacecraft. This process employs a numerical integration scheme in the filter that is updated at discrete intervals (t_i) as illustrated in Fig. 3. The estimated relative state vector is obtained from an interpolation of the previous cycle. Based on all the measurements between t_i and t_{i+1} , a continuous polynomial representation of the trajectory is made available, which serves as starting point for the next filter update and relative orbit prediction [5]. Obviously the propagation period $t_i - t_{i-1}$ has to be small if better approximations of relative state vectors are required. On the other hand, $t_i - t_{i-1}$ is limited by the processing time Δt_{proc} . Its typical value is 30 s for low earth orbits. While in deep space, this period can be extended to several minutes.

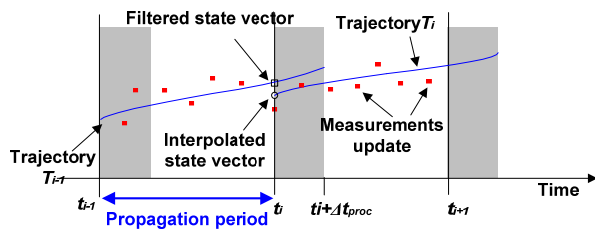


Figure 3. Timeline of relative navigation filter [5]

The measurements used in the filter are provided by the inter-satellite sensor. They can be unambiguous coarse code measurements or ambiguous precise carrier phase measurements. Fig. 4 gives their measurement update timelines. The biggest difference between these two timelines is the extra time for integer ambiguities, which should be initialized before using carrier phase to provide precise measurements. The method used by PRISMA mission is to rotate a spacecraft for solving line-of-sight (LOS) ambiguity problem firstly and then distance ambiguity afterwards, taking 5 mins and 10 mins, respectively. The resolution is combined with tabulated multipath correlation through a filtering and smoothing process [6].

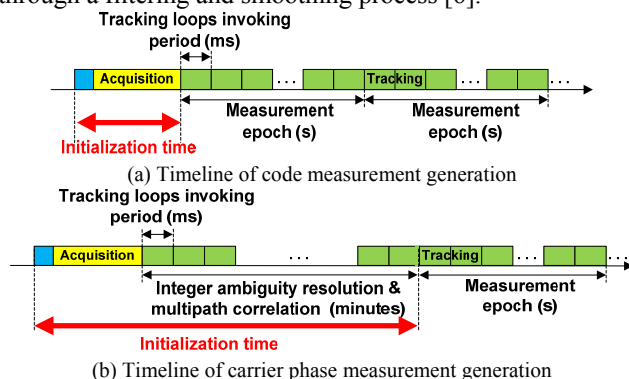


Figure 4. Timeline of code and carrier phase measurements generation

B. Flexible operations across all mission phases

Another important consideration in PFF network is to recognize that the relative navigation requirements may change during the course of the mission's operations. Inter-satellite sensor is expected to operate across various phases

of formation precision, requiring different levels of position sensing and control maneuvering as shown in Fig. 5. A connectivity index table (CIT) is proposed to be part of traffic exchanged among spacecraft to share the current network condition. The measured range can also be filled in CIT, in which way a spacecraft can know where the others are even though not all of them are directly connected.

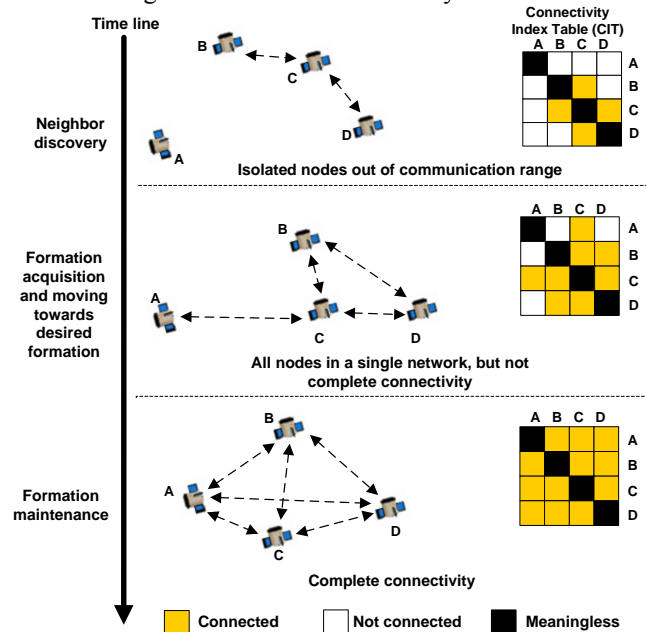


Figure 5. Evolutionary phases of a PFF mission

In the initial deployment where spacecraft may be separated by substantial distances from one to another, the resolution of position and orientation data are based perhaps on coarse-mode sensors using code measurements only for collision avoidance and enabling further movement toward the desired configuration. Some spacecraft are possibly out of communication range of others as shown in the top of Fig. 5. As the spacecraft continue to aggregate into the desired spatial arrangement, they will eventually discover other spacecraft. This condition is defined as formation acquisition and depicted in the center of Fig. 5. Finally, when all spacecraft are in a “complete connectivity” and settled into the desired pattern, formation maintenance is performed as shown in the bottom of Fig. 5. A much greater degree of positional knowledge is acquired by switching the inter-satellite sensors into the fine-mode to facilitate science operations such as multi-point observation.

IV. NETWORK ARCHITECTURE FOR PFF

As a result of time-critical demands, networking solutions prefer the network nodes in a fixed assignment for all possible connections by multiple access (MA) technologies TDMA, CDMA, FDMA or their combinations, since they enable each spacecraft providing measurements from each of the others equally and timely [3]. Before discussing network architectures, choices of half-duplex/full-duplex configurations and centralized/distributed topologies need to be considered.

Inevitably, if transmitting and receiving happen at the same time, some of the transmitted signal will leak into the receiver front ends and may easily saturate the receiver front ends or otherwise overwhelm the external signals. Half-duplex transceiver enables the transmitter and receiver taking turns to work, in which way “self-signals” are avoided. Full-duplex transceiver uses an appropriate filter to isolate the transmitter and receiver at their separated frequency bands to reject “self-signals”. If the navigation measurements are not required simultaneously and continuously, half-duplex configuration is adequate and power-saving.

Network topology is expected to operate in a flexible arrangement, so as to account for the evolutionary phases of a PFF mission as shown in Fig. 5. Neither solely centralized nor distributed topology is efficiently applicable during the neighbor discovery and formation acquisition phases, because some spacecraft are possibly out of communication range of others and could not access to the network. As the spacecraft progress towards the desired formation, it is better for the topology to evolve to a centralized graph in order to enable at least one spacecraft as reference for precise relative navigation and formation control. The role of reference can rotate from one spacecraft to another to avoid the problem of single point of failure.

Roles rotating at different time slots will give a robust and efficient connectivity. It can be implemented in a TDMA sequence with a strict timing boundary or a CDMA configuration with an adjustable period of time slot. Constraints of operating any of them come from the time-critical navigation requirements. Details will be explained in the following parts taking four spacecraft for example.

A. Half-duplex TDMA

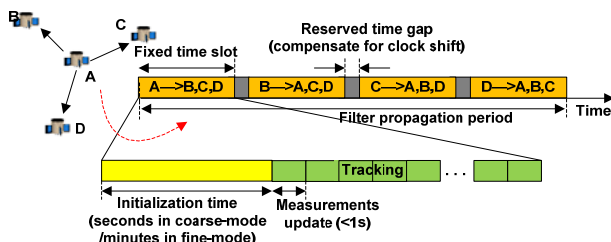


Figure 6. Half-duplex TDMA

A half-duplex TDMA architecture is illustrated in Fig. 6. It should be noted that the onboard relative navigation filters for a certain spacecraft are expected to propagate using complete measurements from all of the other spacecraft. In TDMA mode, these measurements are given in different time slots. Therefore, the time slot is limited by the filter propagation period. That is, if a complete duty cycle of one TDMA sequence is as long as propagation period $t_f - t_{i-1}$, time slot will be one-quarter ($1/\text{number of spacecraft}$) of $t_f - t_{i-1}$, or even smaller to compensate for clock drift by reserving a time gap between two time slots. During each time slot, the roles of spacecraft rotate, thus the signals should be re-acquired. Signal re-acquisition takes long time and has the possibility of exceeding the filter propagation period, especially when implementing carrier phase measurement and associated integer ambiguity re-initialization.

Under such circumstances, choosing time slot is in a dilemma, unless the time-critical constraint is loosened by increasing the propagation period or limiting the re-acquisition time. It is possible to extend the propagation period, or equivalently let the filter freely propagate without measurement updates, however, at the expense of an increase of the relative navigation error. Otherwise, it is promising to shorten initialization time through a rapid integer ambiguity resolution instead of maneuvering spacecraft in long time.

Apart from the time-critical constraint, another limitation of TDMA scheme is the need of time synchronization. Inevitably, the clock drift makes time unsynchronized on different spacecraft. An easy way to reduce its influence on TDMA is to reserve a time gap between two time slots in order to compensate for clock drift. However, it involves the risk that the drift may exceed time gap.

B. Half-duplex CDMA with roles rotating

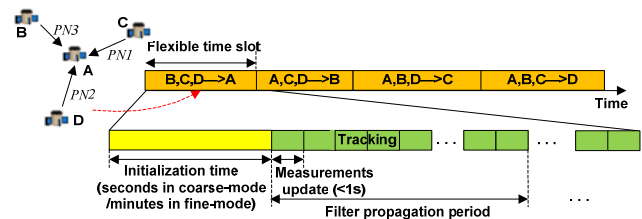


Figure 7. Half-duplex CDMA with roles rotation

Half-duplex CDMA with roles rotating architecture poses better capability than TDMA as show in Fig. 7. For a certain spacecraft, complete measurements from all of the other spacecraft are obtained in the same time slot simultaneously, which makes the duration of time slot much more flexible. It can be long enough to account for propagation period and re-acquisition time. The time slot is also adjustable during the implementation to enable code or carrier phase measurements at different mission phases. In addition, the signals transmitted from other spacecraft are not necessary to start at the same time, because the duration of a time slot can be relatively long and tolerant if one spacecraft is joining in or dropping out of the formation. It is applicable if assigning different time slots for different spacecraft, which happens when a spacecraft needs following long time measurement updates to precisely estimate the relative trajectory change e.g. in a maneuver operation, while others do not.

Some limitations of this concept also exist. The use of CDMA structures results in the well-known near-far problems when different separation distances between spacecraft cause various signal power levels at the receiver. CDMA performance will be discussed in the next section.

C. Full-duplex CDMA in centralized topology

As comparison, another candidate architecture using full-duplex CDMA in centralized topology is introduced as shown in Fig. 8. Isolation between transmitter and receiver is realized by separated frequencies and appropriate filters. The measurements can be generated simultaneously and continuously, taking the advantage of permitting ranging signals passed between spacecraft without the necessity of re-acquisition each time at different time slots. Time-critical

requirement is satisfied in an extreme solution that is continuous connectivity. Besides, this method brings its unique benefit that both clock offset and relative distance can be yielded using dual one-way ranging [7].

However, the flexibility is low because it uses centralized topology. Otherwise, full connectivity is possible by CDMA/FDMA combination, but at the expense of high complexity of sensor design with multi-frequency transmitter and multi-frequency multi-channel receiver.

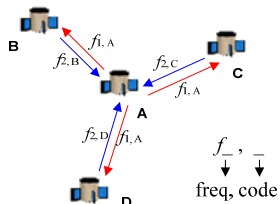


Figure 8. Full-duplex CDMA

D. Evaluation of different architectures

To evaluate different architectures, weighted criteria are given in Table I from 1 to 5 based on the degree of importance to balance mission operations and design cost. Candidate architectures are scored from 1 to 3 to show their capability to satisfy each criterion. The scores for the former three criteria are self-explanatory according to the analysis indicated above. Regarding power consumption, as a rule of thumb, a half-duplex transceiver consumes less power than a full-duplex one; the transmitter consumes more power than the receiver. Therefore, for a half-duplex TDMA architecture which arranges one spacecraft in transmit-mode while the others are in receive-mode, power consumption is the lowest. Full-duplex CDMA is the most power consuming one. With respect to system complexity criterion, TDMA based on simple timing logic access strategy is easier to implement than multi-channel PRN-based CDMA; Half-duplex configuration simplifies the system by switching transmitter and receiver to reject self-signal instead of using complex filters at separated frequencies in full-duplex configuration.

By calculating the score results for different architectures in Table I, half-duplex CDMA with roles rotating is the best-suited architecture for PFF missions.

TABLE I. COMPARISON OF DIFFERENT POTENTIALLY APPLICABLE NETWORKING ARCHITECTURES

Weighted Criteria		Candidate Network Architectures		
		Half-duplex TDMA	Half-duplex CDMA with roles rotating	Full-duplex CDMA
Tolerance of time-critical constraint	5	1	2	3
Flexibility to support various mission phases	4	2	3	1
Scalability to enable s/c joining in or dropping out of the formation	1	1	3	2
Low Power consumption	3	3	2	1
Low System complexity	2	3	2	1
$\sum \text{weight} * \text{score}$		29	36	26

V. CDMA PFF NETWORK CAPABILITY: MULTIPLE ACCESS PERFORMANCE AND NEAR-FAR PROBLEM

The multiple access capability of CDMA can be achieved by using spread spectrum orthogonal signals. However, a completely orthogonal signaling is not possible, which means cross-correlations are nonetheless present and induce noise in terms of multiple access interference (MAI).

Assume that there are two signals, which are all uncorrelated PRN codes with identical spectrum $G_s(f)$ and received at the same power level of P_s . The MAI term is introduced due to cross-correlation between undesired signal $c_m(t)$ and desired reference signal $c_k(t)$, where $c(t)$ represents PRN code. Ignoring the data modulation, Doppler frequency differences and noise for the moment, the MAI term is $c_m(t - \tau_m)c_k(t - \tau_k)$ with code delay τ_m, τ_k . Its power spectrum $G_{MAI}(f)$ is thus obtained by convolving the individual signal spectrum $G_s(f)$ [8]:

$$G_{MAI}(f) = P_s \int G_s(f)G_s(v-f)dv \quad (1)$$

Only the MAI spectrum near $f=0$ is important because the correlation filters have a very small bandwidth. $G_s(f)$ is in the form of sinc^2 , thus [8]:

$$G_{MAI}(0) = P_s \int G_s^2(v)v = P_s \int_0^\infty \left(\frac{\sin \pi f / f_c}{\pi f / f_c} \right)^4 df = \alpha P_s / f_c \quad (2)$$

where f_c is chipping rate, α is a coefficient as a function of the filtered spectrum of sinc^2 . If the spectrum includes all of its sidelobes, α is 2/3. If the spectrum is filtered to include only the mainlobe, α increases to approximately 0.815 [8].

Assuming M spacecraft in the formation, all of exactly at the same separation distances, $M-1$ interfering multiple access signals exist. Considering white noise with noise spectrum density of N_0 , the equivalent noise density and the effective energy per bit to equivalent noise density ratio are:

$$N_{0eq} = N_0 + \alpha(M-1)P_s / f_c \quad (3)$$

$$\frac{E_b}{N_{0eq}} = \frac{P_s T_d}{N_0 + \alpha(M-1)P_s / f_c} \quad (4)$$

where $T_d = 1/f_d$, f_d is data bit rate. E_b/N_{0eq} determines the bit error rate. It is on the order of 10 dB if BER=10⁻⁵ and BPSK modulation without error correction coding is employed.

Furthermore, if we take into account of the various separation distances between spacecraft during operations, the near-far problem shows up in which the effective E_b/N_{0eq} from a remote transmitter is further reduced due to the increase of MAI from a transmitter in close proximity. Because the received power is inversely proportional to the square of distance, MAI spectrum density in eq. (2) is consequently multiplied by a factor of R_f^2/R_n^2 , which means the far desired signal to near undesired interferences range-squared ratio. E_b/N_{0eq} can then be revised to:

$$\frac{E_b}{N_{0eq}} = \frac{P_s T_d}{N_0 + \alpha(M-1)(R_f^2 / R_n^2)P_s / f_c} = \frac{P_s}{N_0 f_d \beta} \quad (5)$$

The multiple access effect of $M-1$ near interferences degrades the equivalent noise density by a factor of $\beta = 1 + \alpha(M-1)(R_f^2 / R_n^2)P_s / (f_c N_0)$. Fig. 9 displays the

energy per bit to noise ratio reduction effects of MAI. Assume that Gold code chipping rate f_c is 10.23 Mcps, data bit rate f_d is 2 kbps, and coefficient α is 0.815 using front-end filter with bandwidth of 20 MHz to only filter mainlobe spectrum. Note that signal to noise ratio is at least satisfied to $P_s / N_0 = f_d * E_b / N_0 = 43$ dB when E_b/N_0 is 10 dB.

In the case of a small scale network and small distance diversity, this degradation can be negligible. However, in reality, a wide range of satellite distances exists, especially during the initial deployment phase. According to communication link budget, E_b/N_0 is a distance dependant parameter. The impact of E_b/N_0 degradation can further be related to the reduced maximum operating range or reduced maximum achievable number of spacecraft.

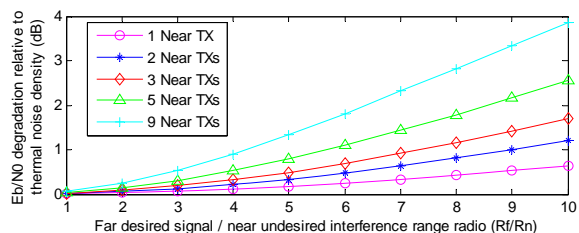


Figure 9. Energy per bit to noise ratio degradation effect resulting

The aforementioned results are based on the assumptions that code spectrum has the form of sinc^2 and Doppler frequency differences are ignored. However, the code is not continuous but 1023 chip length sequence periodically repeated every 0.1 ms, which means that the spectrum is made up of 10 kHz ($f_c/P=10.23\text{Mcps}/1023$) separated lines following sinc^2 envelop [8]. The impact of the existing line components in the spectrum makes the MAI performance much worse than indicated above.

The presence of cross-correlations is the essential reason for MAI. The normalized cross-correlations between pairs of Gold codes have three different spurious peaks taking on values as the following equations with probabilities of 0.75, 0.125 and 0.125, respectively [9]

$$R^{(k,l)}(\tau = iT_c) \in \left\{ \frac{-1}{P}, \frac{-2^{[(n+2)/2]} - 1}{P}, \frac{2^{[(n+2)/2]} - 1}{P} \right\} \quad (6)$$

where R is cross-correlation, $T_c=1/f_c$, n is number of shift register stages, and $P = 2^n - 1$ is code length. For Gold code of length 1023, spurious peaks are $-65/1023$, $-1/1023$ and $63/1023$. The strongest and average peaks are approximately -24 dB and -30 dB, respectively, relative to the main auto-correlation peaks. This limits the dynamic range of a typical receiver employing these spreading codes to 24dB at worst case if only taking one interference transmitter for example. Multiple transmitters will further decrease this level.

If Doppler frequency difference $\Delta f_{m,k}$ and phase difference $\Delta \phi_{m,k}$ are taken into account, cross-correlation term turns to $c_m(t - \tau_m) c_k(t - \tau_k) \cos(2\pi \Delta f_{m,k} t + \Delta \phi_{m,k})$, which produces a line component $\Delta f_{m,k}$ at the spectrum. Ordinarily, the correlation process spreads this line, but the mixing process at the existing code line frequencies results in the interference being minimally suppressed. That is, if Doppler difference is a multiple of line component spacing

10 kHz, MAI noise energy “leaks” through the correlation process, and exacerbates cross-correlation levels to -21.1 dB [8]. Thanks to the code chipping rate increasing to 10.23 Mcps, a 10 kHz Doppler frequency does not occur frequently, relative to 1 kHz line component spacing in C/A code.

VI. CONCLUSIONS AND FUTURE WORK

In this paper, network architecture is presented to support inter-satellite communication and relative navigation for precise formation flying missions. Half-duplex CDMA with roles rotating is selected as a suitable architecture, as it enables system working with a wide range of flexibility, such as enabling both code and carrier phase measurements, allowing to detect some spacecraft while tracking others, and being insensitive to a spacecraft joining in or dropping out of the formation. Its limitation in terms of multiple access interference is also highlighted by analyzing signal cross-correlation performance. It is shown that equivalent energy per bit to noise density ratio is reduced due to the near-far problem, and the limited length of PRN code makes the situation worse at certain Doppler frequency offsets.

The future work includes an improvement of network performance by the following implementations:

Firstly, signal structure will be updated to reduce cross-correlation levels and mitigate multiple access interference.

Secondly, adaptive power control mechanism is useful to accommodate a wide range of inter-satellite distances, as well as minimize the impact of near-far problems.

Thirdly, integer ambiguity problem should be solved rapidly, in order to reduce initialization time, and consequently reduce its impact on time-critical requirements and allow the network in a more flexible manner.

REFERENCES

- [1] R. Kroes, “Precise relative positioning of formation flying spacecraft using GPS”, PhD thesis, Delft University of Technology, The Netherlands, 2006.
- [2] T. Grelier, A. Garcia, E. Peragin, et al., “GNSS in space: Formation flying radio frequency techniques and technology”, Inside GNSS, Jan/Feb, 2009, pp. 43-51.
- [3] R. Sun, D. Maessen, J. Guo, and E. Gill, “Enabling inter-satellite and ranging for small satellites”, 9th Symposium on Small Satellites Systems and Services, Funchal, Portugal, 31 May – 4 Jun., 2010.
- [4] J. Betz, “Binary Offset Carrier Modulations for Radionavigation”, Journal of the Institute of Navigation, vol. 48, 2001, pp. 227-246.
- [5] E. Gill, O. Montenbruck, K. Arichandran, and S. Tan, “High-precision onboard orbit determination for small satellites-the GPS-based XNS on X-SAT”, 6th Symposium on Small Satellites Systems and Services, La Rochelle, France, 20-24 Sep. 2004.
- [6] V. Barrena, M. Suatoni, C. Flores, J. Thevenet, and C. Mehlen, “Formation flying RF ranging subsystem for RPISMA: navigation algorithm design and implementation”, Proc. 3rd Int. Symposium on Formation Flying, Missions and Technologies, Noordwijk, the Netherlands, 23-25 Apr. 2008.
- [7] J. Kim and B. Tapley, “Simulation of dual one-way ranging measurements”, Journal of Spacecraft and Rockets, vol. 40, 2003, pp. 419-425.
- [8] J. Spilker, “Signal structure and theoretical performance”, Global Positioning System: Theory and Applications, Vol. 1, pp. 57-105.
- [9] M. Pratap and P. Enge, Global Positioning System: Signals, Measurements and Performance, 2nd ed., pp. 365-379.

Hybrid Acquisition of CBOC Galileo Signals under Multiple Correct-window Hypothesis

Elena Simona Lohan

Department of Communications Engineering
Tampere University of Technology (TUT Foundation)
Tampere, Finland
elena-simona.lohan[at]tut[dot]fi

Alexandru Rusu Casandra and Ion Marghescu

Faculty of Electronics, Telecommunications and
Information Technology
University Politehnica of Bucharest
Bucharest, Romania
rusu.alex[at]yahoo[dot]com, marion[at]comm.pub.ro

Abstract— This paper computes the mean acquisition time for a hybrid search acquisition stage of Galileo signals, under the assumption of multiple correct windows in the search space. The assumption of multiple correct windows is a realistic assumption both in single and multipath-fading channels, due to the fact that the width of the main lobe of the correlation envelope is at least 2 chips (depending on the receiver front-end bandwidth) and the time-bin step of scanning the multiple code phases is typically below 0.5 chips. The multiple-window hypothesis acquisition is poorly addressed in the Code Division Multiple Access (CDMA) literature, and the comparison of multiple-dwell acquisition strategy is completely novel in the Global Navigation Satellite System (GNSS) literature, to the best of the authors' knowledge. One of the main results of the paper is that choosing an increased false alarm probability per dwell when going from one dwell to the next one, in conjunction with an increasing integration time, offers better results for the mean acquisition time.

Keywords—unambiguous code acquisition, Galileo, hybrid search, multiple correct-window hypothesis

I. BACKGROUND AND PROBLEM DEFINITION

In 1998, the European Union decided to pursue a satellite navigation system independent of the U.S. Global Positioning System. This European satellite system, namely Galileo, is designed specifically for civilian use worldwide. When completed, the Galileo system will provide multiple levels of service to users throughout the world. This paper studies the acquisition of Galileo E1 Open Service (OS) signals with multi-dwell hybrid search acquisition algorithm. Also the serial search will be incorporated in the simulations results, as a particular case of the hybrid search and in order to offer a benchmark for the results. The acquisition problem of any pseudorandom code (as those used in CDMA systems such as Galileo) is equivalent with the classical detection problem of testing two hypotheses H_0 versus H_1 :

$$\begin{cases} H_1 : \text{signal is present} \\ H_0 : \text{signal is absent} \end{cases}$$

The H_0 and H_1 hypotheses are in fact associated with the envelope of the correlation between the incoming signal and a locally generated reference code, with different tentative delays and Doppler frequencies. Each pair of tentative delay and Doppler frequency defines as bin (or a cell), as shown in Fig. 1. Several bins (or cells) are grouped together in a so-

called search window, as illustrated in Fig. 1. A test statistic is formed in each window, such as the maximum correlation value among all bins in a window, and that test statistic is compared with a threshold, in order to detect the presence or the absence of the signal.

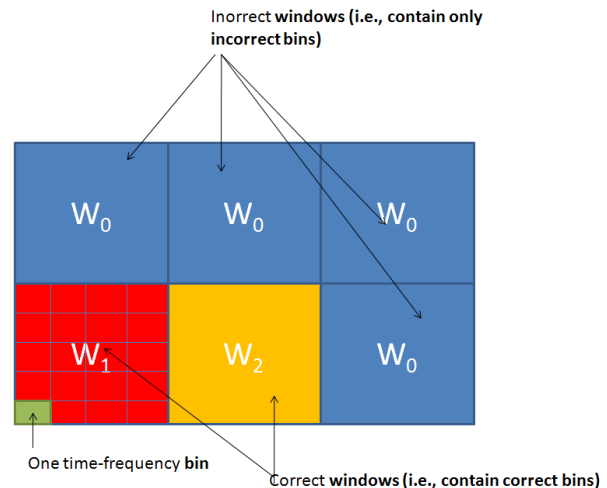


Figure 1. Illustration of hybrid search space

The classical situation, analyzed so far in the literature is the situation when the whole main correlation lobe is contained in only one window. However, due to the randomness of the channel delays, this is not always true, and it is possible to encounter a situation as shown in Fig. 2, where parts of main lobe of the correlation envelope are contained in one window, and the other parts are contained in the second window. Both windows are 'correct' windows, satisfying hypothesis H_1 , and they are denoted in what follows by W_1 , and W_2 , as illustrated in Fig. 1. This is the case we address in this paper and that has not been reported before in literature, to the best of the author's knowledge. The benefit of studying the case of two correct search windows is that the conclusions can be used for further improving the acquisition algorithms implemented in GNSS receivers. Previous studies dealing with the mean acquisition time in GNSS signals in the presence of single correct window can be found, for example, in [1,2,3,4].

The second section of this paper presents the model of the acquisition stage that has been used for computing the mean acquisition time. Section III explains how the variable

threshold algorithm works. The results obtained from the Matlab simulations are illustrated in Section IV and the conclusions are drawn in the fifth Section.

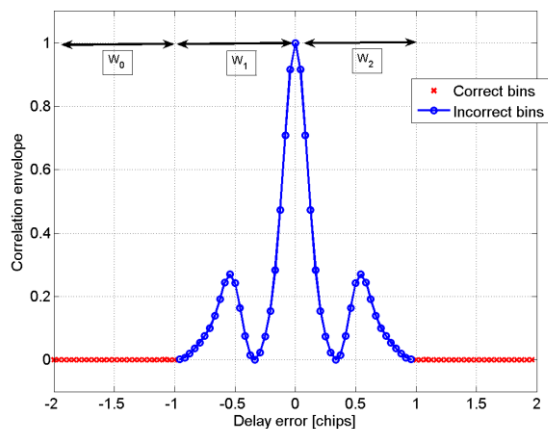


Figure 2. Example of multiple correct-window hybrid search. Galileo CBOC(-) signal, specific to E1-C, and 24.552 MHz double-sided bandwidth.

II. ACQUISITION MODEL

From the point of positioning, only the first path (or Line of Sight, LOS) is of interest. The size of the hybrid search window typically depends on the available number of correlators. For a pure software implementation, the window length can cover the whole code uncertainty (of 1023 chips for GPS and 4092 chips for Galileo). In this situation, the hybrid search is equivalent with parallel search. However, in most of the cases, the search window length is much smaller (few tens or few hundreds of chips). We may however assume that there are at most $Q=2$ windows containing signal cells (and thus the maximum channel delay spread is less than twice of search window length). In Fig. 1, the illustrated window length is of one chip.

Each window is formed by several cells. Their number depends on the step of scanning the time-bin hypotheses. For example, if this step is $(\Delta t)_{bin}$ (in chips) and the window length in chips is L_w , then there are N cells per search window, where N is given by:

$$N = \frac{L_w}{(\Delta t)_{bin}} \quad (1)$$

A cell can be either a H_1 (hypothesis one) cell, meaning that it contains signal coming from one channel path (the signal level is dependent on path position and on the modulation type, which defines the correlation function shape), or a H_0 (hypothesis 0) cell, meaning that it contains only noise. Even in single-path case, due to the 2-chip width correlation function, we may have more than one H_1 cells per window.

We denote by W_1 and W_2 the windows containing signal H_1 cells and by W_0 the windows containing only H_0 cells. As explained in the previous section, the assumption with at most two windows with H_1 cells is reasonable. We also assume that there are L_i , $i=1,2$ cells containing signal in W_i window (i.e., H_1 cells) and $N - L_i$ cells with only noise (i.e., H_0 cells) (N being the total number of cells per window).

It is straightforward to show that, after non-coherent integration, the signal in H_1 cells obeys a χ^2 non-central distribution of Cumulative Distribution Function (CDF) $F_{nc}(\gamma, \lambda_0)$, $l=1, \dots, L_i$, and the signal in H_0 cells obeys a χ^2 central distribution of CDF $F_c(\gamma)$. Above, γ is the detection threshold [5] and λ_i is the non-centrality parameter in cell L_i , related to signal power E_b and to the envelope of the BOC/BPSK auto-correlation function $R(\Delta\tau_l)$ in l -th cell or bin, which is spaced with $\Delta\tau_l$ chips from the maximum; e.g., $R(0) = 1$. Thus, λ_i is defined as:

$$\lambda_i = E_b R(\Delta\tau_l) \quad (2)$$

For multiple dwell search (K dwells), the state transition diagram between one state to another can be divided into 3 regions, as seen in Fig. 3: transition between W_1 and W_2 windows, transition between W_2 and W_0 windows, and transitions between W_0 and W_0 windows. We assume that there are ν windows in the search space: maximum 2 windows (W_1 and W_2) containing signal H_1 cells (a particular case here is the situation when only the first window contains signal cells $W_2=W_0$) and $\nu - 2$ windows containing only noise H_0 cells.

In here, we use also the assumption that the correct cell is at the edge between two windows (W_1 and W_2), and the acquisition state can be achieved from both W_1 and W_2 windows. The state flow diagram is shown in Fig. 3. τ_k is the k -th dwell time. We used the notation $H_M^{(k)}$ for a ‘‘missed detection’’ transfer function and the notation $H_W^{(k)}$ for a transition from one correct window to the second correct window. We also used the notations $H_{FA}^{(k)}$ and $H_{NFA}^{(k)}$ for the false alarm (FA) and non-false alarm (NFA) transfer functions, at k -th dwell. The penalty factor to return from a false alarm state is denoted via ζ_p .

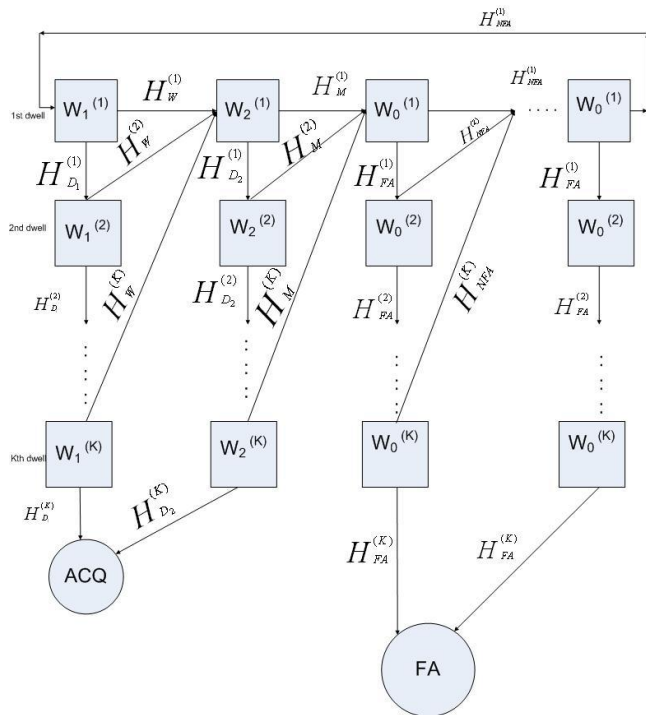


Figure 3. Flow chart for the assumed case (first path at the border between two windows).

The transfer functions shown in Fig. 3 are given by:

$$H_{D_1}^{(k)}(z) = P_{d_1}^{(k)} z^{\tau_k}, i=1,2 \quad (3)$$

$$H_W^{(k)}(z) = (1 - P_{d_1}^{(k)}) z^{\tau_k} \quad (4)$$

$$H_M^{(k)}(z) = (1 - P_{d_2}^{(k)}) z^{\tau_k} \quad (5)$$

$$H_{FA}^{(k)}(z) = P_{fa}^{(k)} z^{\tau_k} \quad (6)$$

$$H_{NFA}^{(k)}(z) = (1 - P_{fa}^{(k)}) z^{\tau_k} \quad (7)$$

and

$$H_R(z) = z^{\xi_p \tau_k} \quad (8)$$

where the detection and false alarm probabilities are:

$$P_{d_1}^{(k)} = 1 - (F_c(\gamma^{(k)}))^{N-L_1} \prod_{l=1}^{L_1} F_{nc}(\gamma^{(k)}, \bar{\lambda}_l^{(k)}) \quad (9)$$

$$P_{d_2}^{(k)} = 1 - (F_c(\gamma^{(k)}))^{N-L_2} \prod_{l=1}^{L_2} F_{nc}(\gamma^{(k)}, \bar{\lambda}_l^{(k)}) \quad (10)$$

and

$$P_{fa}^{(k)} = 1 - (F_c(\gamma^{(k)}))^N \quad (11)$$

Above, $\gamma^{(k)}$ is the detection threshold at k -th dwell, $k=1, \dots, K$, $\lambda_l^{(k)}$ is the non-centrality parameter in l -th cell of window W_l , at k -th dwell, and is defined as:

$$\lambda_l^{(k)} = E_b R^{(k)} (\Delta \tau_l) \quad (12)$$

and $\bar{\lambda}_l^{(k)}$ is the non-centrality parameter in l -th cell of window W_2 , at k -th dwell, and is defined as:

$$\bar{\lambda}_l^{(k)} = E_b \bar{R}^{(k)} (\Delta \tau_l) \quad (13)$$

The equivalent flow chart of Fig. 3 is given in Fig. 4. The equivalent transfer functions of Fig. 4 are given below:

$$H_W(z) = H_W^{(1)}(z) + \sum_{k=1}^K H_W^{(k)}(z) \prod_{i=1}^{k-1} H_{D_1}^{(i)}(z) \quad (14)$$

$$H_M(z) = H_M^{(1)}(z) + \sum_{k=1}^K H_M^{(k)}(z) \prod_{i=1}^{k-1} H_{D_2}^{(i)}(z) \quad (15)$$

$$H_T(z) = H_{NFA}^{(1)}(z) + \sum_{k=1}^K H_{NFA}^{(k)}(z) \prod_{i=1}^{k-1} H_{FA}^{(i)}(z) \quad (16)$$

$$+ H_R(z) \prod_{i=1}^K H_{FA}^{(i)}(z)$$

From [6], the equivalent transfer function of Fig. 3 is:

$$H(z) = \sum_{i=1}^{\nu-1} p_i T_i(z) + p_\nu T(z) \quad (17)$$

where

$$T_i(z) = \frac{H_T^i(z) H_{D_1}(z)}{1 - H_W(z) H_M(z) (H_T(z))^{\nu-2}} \quad (18)$$

$$T(z) = \frac{H_{D_2}(z)}{1 - H_W(z) H_M(z) (H_T(z))^{\nu-2}} \quad (19)$$

Again, if all the states are equally probable, then:

$$p_i = \frac{1}{\nu}, i=1, \dots, \nu. \quad (20)$$

If we start from the correct state (e.g., assisted acquisition), then $p_1 = 1$ and $p_i = 0$, $i=2, \dots, \nu$.

The Mean Acquisition Time (MAT) can be computed as [7]:

$$MAT = \left. \frac{dH(z)}{dz} \right|_{z=1} \quad (21)$$

and it can be straightforwardly calculated numerically (e.g., via Matlab).

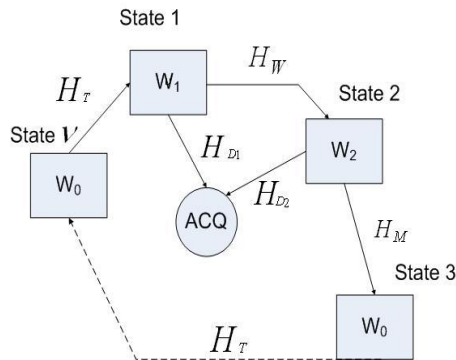


Figure 4. Equivalent flow chart for the assumed case (first path at the edge of two windows).

III. VARIABLE THRESHOLD, FIXED DWELL TIME ALGORITHM

In order to compute the detection and false alarm probabilities needed in the MAT computation, we fixed a target false alarm at the output of all dwells (which is the product of the individual false alarm in each dwell, and will be specified in the parameters table) and we also fixed the total integration time per dwell, as the product between a certain coherent integration interval N_c and a certain non-coherent integration interval N_{nc} . With the desired false alarm and the specified coherent and non-coherent integration intervals, a variable threshold per each dwell was computed, according to eq. (11). The variable threshold was then introduced in equations (9) and (10) in order to compute the corresponding detection probabilities.

As illustrated in Fig. 5, by reducing the false alarm, we increase the detection threshold, and thus we also reduce the detection probability. It is usually preferred that the first dwell has a lower false alarm probability and a lower integration time (or dwell time), while in the sub-sequent dwells we try to improve the detection probabilities, by allowing a higher integration time and, typically, a higher false alarm probability.

IV. SIMULATION RESULTS

The main simulation parameters, common for all considered scenarios, are illustrated in TABLE I. The number of states ν is computed as the total number of time-Doppler bins (i.e., $18 \times 11691 = 210438$), divided by the number of bins per window (given in TABLE I). The analyzed case was the situation of a CBOC(-) modulated signal (e.g., pilot channel E1-C in Galileo, according to [8]) with a reference CBOC modulated code and a wideband receiver front-end of 24.552 MHz, as specified in [8]. Several scenarios were analyzed, as given in TABLE II. The results are presented in the following sub-sections.

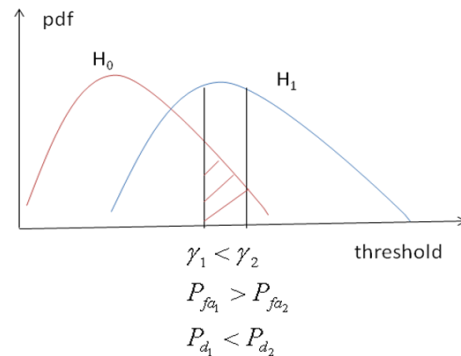


Figure 5. Illustration of the variable threshold concept.

TABLE I. PARAMETERS USED IN THE SIMULATIONS

Parameters	Value
Penalty factor ζ_P	10
Time bin step $(\Delta t)_{bin}$	0.35 chips
Receiver front-end bandwidth (double-sided)	24.552 MHz
Channel type	Static, single path
Number of bins per window in the hybrid search	4000 (moderate) and 100000 (high)
Number of bins per window in the serial search	1
Galileo signal	E1-C (CBOC(-) modulation)
Doppler frequency uncertainty	From -9 kHz to +9 kHz with a step of 1 kHz (i.e., a total of 18 Doppler bins)
Code phase uncertainty	4092 chips, with a step $(\Delta t)_{bin}$ (i.e., a total of 11691 time bins)

TABLE II. DWELL PARAMETERS

	Single dwell	Two dwells	Three dwells
<i>Scenario 1</i> (global false alarm 10^{-5} , a global integration time of 256 ms)	$P_{fa}=[10^{-5}]$ $N_c=[16]$ $N_{nc}=[16]$	$P_{fa}=[10^{-3}$ $10^{-2}]$ $N_c=[4 \ 4]$ $N_{nc}=[1 \ 16]$	$P_{fa}=[10^{-3}$ $10^{-1}]$ $N_c=[2 \ 2 \ 4]$ $N_{nc}=[1 \ 2 \ 8]$
<i>Scenario 2</i> (global false alarm 10^{-3} , a global integration time of 512 ms)	$P_{fa}=[10^{-3}]$ $N_c=[64]$ $N_{nc}=[8]$	$P_{fa}=[0.07$ $0.014]$ $N_c=[4 \ 16]$ $N_{nc}=[1 \ 8]$	$P_{fa}=[0.2$ $0.05]$ $N_c=[4 \ 4 \ 4]$ $N_{nc}=[1 \ 2 \ 4]$
<i>Scenario 3</i> (global false alarm 10^{-3} , a global integration time of 512 ms)	$P_{fa}=[10^{-3}]$ $N_c=[64]$ $N_{nc}=[8]$	$P_{fa}=[0.014$ $0.07]$ $N_c=[4 \ 16]$ $N_{nc}=[1 \ 8]$	$P_{fa}=[0.05$ 0.1 $0.2]$ $N_c=[4 \ 4 \ 4]$ $N_{nc}=[1 \ 2 \ 4]$

A. Moderate number of correlators in the hybrid search

In the first analyzed situation, we assumed that each decision window has 4000 complex correlators (or bins). The results are shown in Fig. 6 to Fig. 8, for the 3 scenarios shown in TABLE II.

It is to be noticed that *Scenario 3* differs from *Scenario 2* only in that the false alarm probabilities in multi-dwell case are increasing (instead of decreasing). From the comparison of Fig. 7 with Fig. 8, we see that *Scenario 3* (increasing false alarm probabilities) gives slightly better results (than *Scenario 2*) in the 2-dwell and 3-dwell cases. As seen in the following figures, at low Carrier to Noise Ratio (C/N_0), single-dwell approaches have very good performance (either comparable or even better than multiple-dwell approaches), in both serial and hybrid searches. At higher C/N_0 , typically above 30 dB-Hz, multi-dwell approaches do bring an improvement in MAT, but the improvement from passing from 2-dwell to 3-dwell architecture is not as significant as the improvement from single dwell to 2 dwells. Also, there is a significant improvement if several correlators can be used in parallel (hybrid approach), compared to the serial case.

B. High number of correlators in the hybrid search

In the second analyzed situation, we assumed that each decision window has 100000 complex correlators (or bins), corresponding to only 2 search windows in the whole uncertainty space. The results are shown in Fig. 9 to Fig. 11. Clearly, going from 4000 to 100000 correlators per search window improves the MAT performance (the gap versus serial search is higher for higher number of correlators).

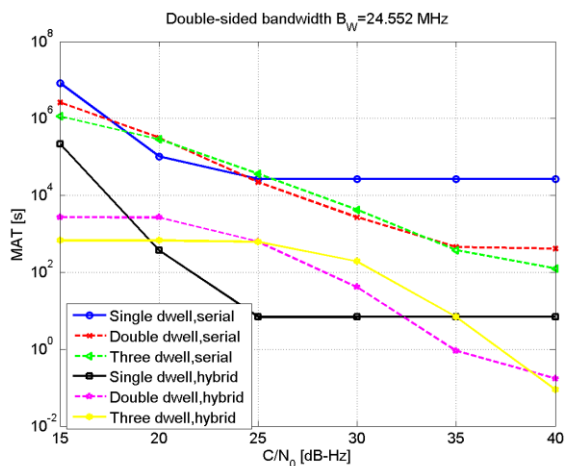


Figure 6. Performance of multi-dwell acquisition, *Scenario 1*, wideband receiver (BW=24.552 MHz), 4000 complex correlators (or number of bins per window)

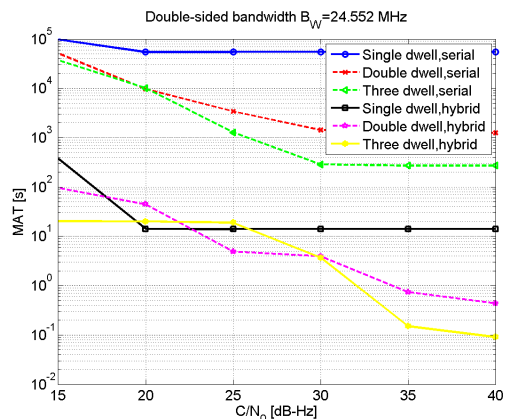


Figure 7. Performance of multi-dwell acquisition, *Scenario 2*, wideband receiver (BW=24.552 MHz), 4000 complex correlators.

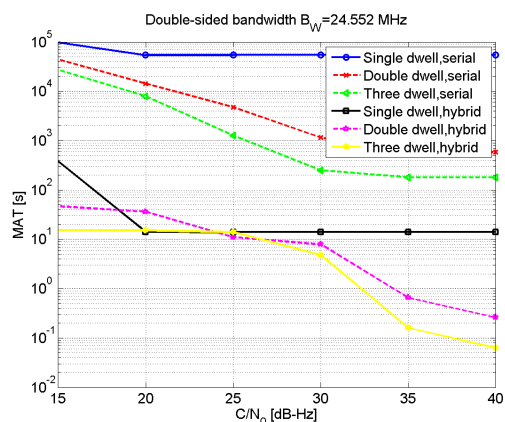


Figure 8. Performance of multi-dwell acquisition, *Scenario 3*, wideband receiver (BW=24.552 MHz), 4000 complex correlators.

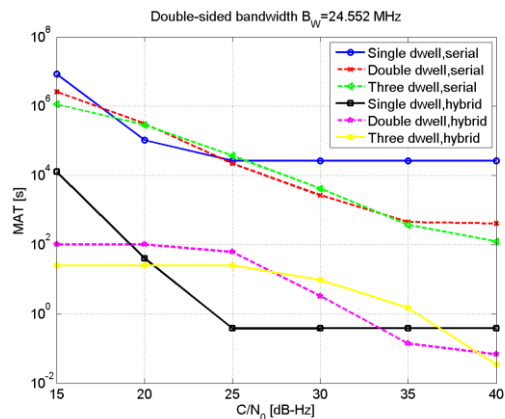


Figure 9. Performance of multi-dwell acquisition, *Scenario 1*, wideband receiver (BW=24.552 MHz), 100000 complex correlators

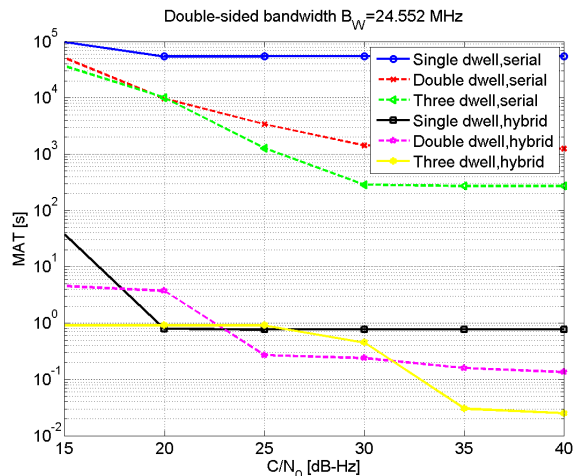


Figure 10. Performance of multi-dwell acquisition, *Scenario 2*, wideband receiver (BW=24.552 MHz), 100000 complex correlators.

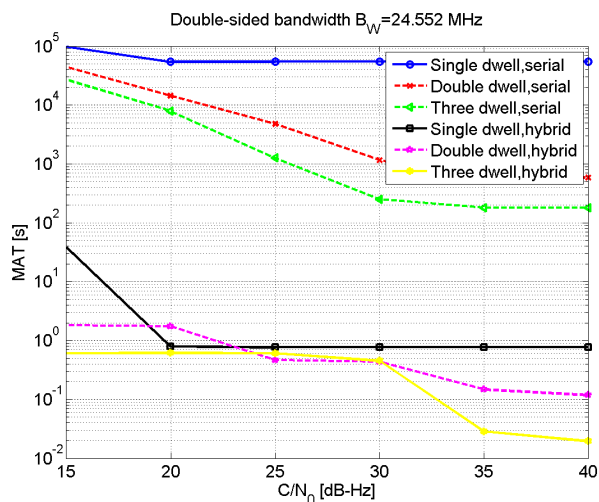


Figure 11. Performance of multi-dwell acquisition, *Scenario 3*, wideband receiver (BW=24.552 MHz), 100000 complex correlators.

V. CONCLUSION

This paper introduces a semi-analytical expression for the computation of the Mean Acquisition Time for the hybrid search of Galileo CBOC-modulated signals, under the hypothesis of multiple correct windows (due to the randomness of the delays introduced by the wireless channel and to the width of the main correlation lobe). Simulation results under static channels and multiple correlators per search window for Galileo E1-C pilot channels were also presented. Also the serial search case was maintained as a benchmark. It was seen that increasing the number of dwells can bring some benefit in the MAT, if the parameters of each dwell (e.g., integration times and false alarm probabilities per dwell) are chosen properly. It was also seen that choosing an increasing false alarm probability per dwell (i.e., smallest false alarm at the first dwell and highest as the last dwell), in conjunction with an increasing integration time

(i.e., smallest at the first stage, highest at the last stage) offers the best results. It was also shown that increasing the coherent integration time, while keeping the same overall integration time offers slightly better MAT results. The coherent integration length is of course, limited by the presence of data bit transitions and local oscillator drifts. Further studies are dedicated to the behavior in multipath fading channels (however, analytical and semi-analytical MAT expressions for these cases are hard to get and the results are likely to be obtained in an empirical manner, via Monte-Carlo simulations).

ACKNOWLEDGMENT

This work has been supported by the Academy of Finland and by Nokia Foundation grant. This work has also been supported partly by the Sectoral Operational Programme Human Resources Development 2007-2013 of the Romanian Ministry of Labour, Family and Social Protection through the Financial Agreement POSDRU/88/1.5/S/61178.

REFERENCES

- [1] E. S. Lohan, A. Burian, and M. Renfors, "Acquisition of Galileo signals in hybrid double-dwell approaches", in CDROM Proceedings of ESA NAVITEC, Dec 2004.
- [2] S. Lohan, A. Lakhzouri, and M. Renfors, "Selection of the multiple-dwell hybrid-search strategy for the acquisition of Galileo signals in fading channels", in CDROM Proc. of IEEE PIMRC, Sep 2004.
- [3] A. Lakhzouri, E. S. Lohan, and M. Renfors, "Hybrid-search single and double-dwell acquisition architectures for Galileo signal", in CDROM Proc. of IST mobile & wireless communications workshop, Jun 2004.
- [4] A. Konovaltsev, A. Hornbostel, H. Denks, and B. Bandemer, "Acquisition Trade-Offs for Galileo SW Receiver". In: European Navigation Conference ENC-GNSS 2006, ENC2006 CD. European Navigation Conference and Exhibition 2006, 2006-05-07 - 2006-05-10, Manchester, UK.
- [5] S. Turunen, "Network assistance: what will new GNSS signals bring to it," in *Inside GNSS*, Spring 2007, pp. 35–41.
- [6] B.J. Kang and I.K. Lee, "A performance comparison of code acquisition techniques in DS-CDMA system", *Wireless Personal Communications*, vol. 25, 2003, pp. 163-176.
- [7] A. Polydoros and C.L. Weber, "A unified approach to serial search spread-spectrum code acquisition – Parts I and II: A matched filter receiver", *IEEE Trans. On Comm.*, vol 32(5), May 1984, pp. 542-560.
- [8] European Commission/GSA, "Galileo Signal In Space- Interface Control Documentation" (Galileo SIS-ICD), version Feb 2010.

UWB Localization System with TDOA Algorithm Using Experimental Measurements

Abdelmadjid Maali, Abdelaziz Ouldali

Communications Systems Laboratory
Military Polytechnic School
BP 17, Bordj El Bahri, Algiers, Algeria
e-mail : maalia@esiee.fr, aaziz_ouldali@yahoo.fr

Hassane Mimoun, Geneviève Baudoin

Signal Processing and Telecommunications Laboratory
Université Paris Est, ESIEE Paris
2 Bd Blaise Pascal, F-93162 Noisy-le-Grand Cedex
e-mail : {h.mimoun, g.baudoin}@esiee.fr

Abstract—This paper investigates a 2D experimental location system based on time difference of arrival (TDOA) of ultra wideband (UWB) signals measured in line-of-sight (LOS) and non-line-of-sight (NLOS) environments. These measurements are carried out with the UWB radios PulsON 210 from Time Domain Corporation. The measured signals are collected with four antennas which are connected through cables and a power combiner to PulsON 210 receiver. After the calculation of the electric delays cables, we applied maximum energy selection with search back (MESSB) and cell averaging constant false alarm rate (CA-CFAR) algorithms to estimate the TDOA. These algorithms use the output of non-coherent energy detection (ED) receivers. The experimental results show that the performances of TDOA estimation obtained by MESSB and CA-CFAR algorithms give almost identical performances in the LOS environment, but in NLOS case, the performances of CA-CFAR algorithm are higher than those obtained by MESSB algorithm.

Keywords—Ultra wideband (UWB); time difference of arrival (TDOA); maximum energy selection with search back (MESSB); cell averaging constant false alarm rate (CA-CFAR).

I. INTRODUCTION

Impulse Radio UWB (IR-UWB) technology uses a very short pulse with a duration typically shorter than 1 nanosecond. Therefore it can achieve high resolution ranging in the order of tens of centimeters. Consequently, with its precise ranging and location estimation, it is an ideal candidate for space applications, such as tracking of Lunar/Mars rovers and astronauts [1][2].

Many methods have been applied to estimate the location of a radio source, such as received signal strength (RSS) indicators, time of arrival (TOA), time difference of arrival (TDOA) or angle of arrival (AOA). For some applications, the TDOA approach has been chosen as an ideal method for tracking since it does not require synchronization between the transmitter and receiver [1].

The methods used in [1] and [2] to estimate TDOA are classified in matched filter (MF) receivers, that operate at high sampling frequency and use complex algorithms. Energy detection (ED) receivers work at sub Nyquist sampling frequency and use low complex algorithms that make them low cost and low power consumption.

In this paper, we use the ED receivers with maximum energy selection with search back (MESSB) [3] and cell

averaging constant false alarm rate (CA-CFAR) [4] algorithms to estimate the TDOA. The algorithms are tested on measured data obtained by using a pair of UWB radio transceivers “PulsON 210” developed by the Time Domain Corporation [5].

The remainder of the paper is organized as follows. In Section II, we briefly review the state of the art of the MF and ED receivers. In Section III, the prototype system of localization is presented, and the CA-CFAR and MESSB algorithms to estimate the TDOA are described. In Section IV, mobile localization is done in ESIEE gymnasium applying TDOA algorithm. In Section V, the experimental results are analyzed. The concluding remarks and future work are given in Section VI.

II. STATE OF THE ART

TOA estimation algorithms based on MF receivers can obtain high localization precision by means of high sampling rate, which leads unfortunately to high implementation cost. On the other hand, the algorithms which use ED receivers are based on a simple architecture which can operate at very low sampling rates compared to the Nyquist rate.

In UWB receivers, the received signal is amplified by a low noise amplifier (LNA), passed through a band-pass filter (BPF) with bandwidth B as indicated in Fig. 1. In UWB ranging approaches based on the MF receivers [6], the received signal is sampled after being correlated with a reference signal as illustrated in Fig. 1 (a), and high sampling rate ($1/T_e$) is used to detect the peak correlation corresponding to TOA. In the ED receivers, the filtered signal fed to an “integrate and dump” device with an integration and sampling duration T_b as shown in Fig. 1 (b), and the TOA estimation depends on a threshold [3].

Among the algorithms based on MF receivers, a simplified version of the Maximum Generalized Likelihood (GML) algorithm has been analyzed in [6]. In [7], the authors have proposed a Low Complexity (LC) algorithm which is based on the idea of a “noisy template”. The GML algorithm provides ranging accuracies, but requires very high sampling rates which may be a major drawback in practical applications [8].

For the ED receivers, the TOA estimation problem consists of detecting the first energy cell containing the received signal energy overcomes a suitable threshold. In

[3], the MESSB algorithm based on a fixed normalized threshold has been presented. In [4], we have proposed a CA-CFAR algorithm based on an adaptive threshold comparison. Adaptive threshold techniques are used in radar detection to maintain a constant false alarm rate (CFAR) in a non stationary environment [9][10].

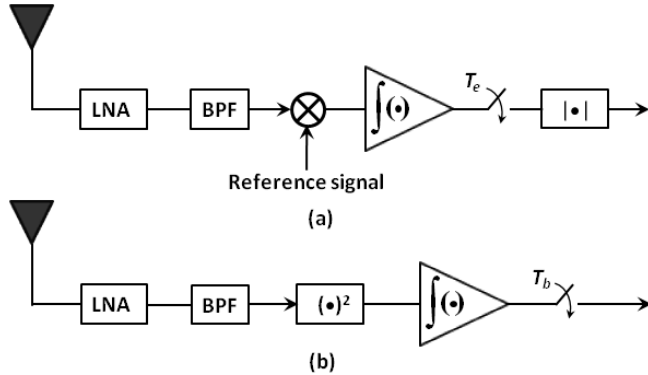


Figure 1. Types of UWB receivers. (a) MF receiver; (b) ED receiver.

More generally, in most applications, the goal is to achieve ranging accuracy of a meter with low-power and low-complexity algorithms [8]. In this order, the ED receiver combined with CA-CFAR algorithm, for ranging in UWB systems, constitute a better solution for these applications.

III. TDOA ESTIMATION

The core equipment employed in our experiment is a pair of UWB PulsON 210 transceivers. We show in Fig. 2 one UWB radio transceiver PulsON 210. Its specifications are as follows [5]:

- Pulse repetition frequency : 9.6 MHz;
- Data rates : 9.6~0.15Mbps ;
- Center frequency : 4.7 GHz ;
- Bandwidth : 3.2 GHz, [3.1-6.3] GHz ;
- Effective Isotropic Radiated Power (EIRP) : -12.8 dBm ;
- Power consumption : 6.5 W ;
- Dimensions : 16.5 cm x 10.2 cm x 5.1 cm.



Figure 2. PulsON 210 UWB.

Our prototype system is based on “One-Receiver-Four-Antennas” as indicated in Fig. 3, where four antennas are connected through a power combiner to one UWB receiver using three different cables with precisely calibrated delays. Therefore, three delayed versions of the received UWB pulse are obtained at the single receiver. In our experimentation, we used only three cables because the length of the cables does not enable us to confine the four received signals in the frame duration (104 ns). Consequently, the measurements are divided into two phases. The first phase relates to the acquisition of the signals collected by antennas 1, 2 and 3. In the second phase, the received signals measurements are carried out by antennas 1, 4 and 3. This is realized by the connection of the green cable (dashed line) to antenna 4 as shown in Fig. 3.

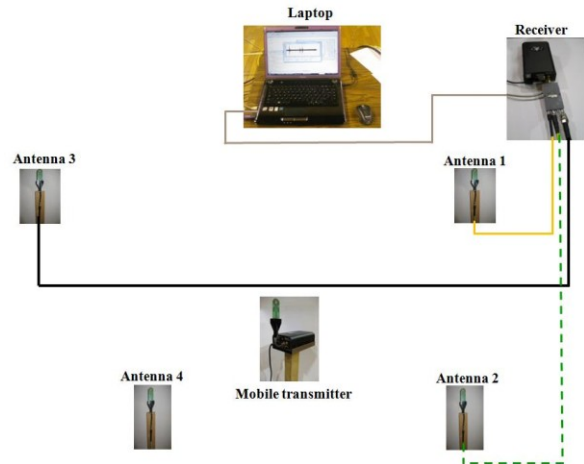


Figure 3. Prototype of localization.

The purpose of our system is the measurement of the distances between the reception antennas and the transmitter, which is equivalent to the measurement of TOA (t_{10}, t_{20}) as indicated in the example of Fig. 4. However, if the system is not synchronized, we must rather measure relative times of arrival, after we carry out the difference to eliminate the unknown initial time t_0 . It is also necessary to determine the electric delays caused by the cables (t_{cable1}, t_{cable2}).

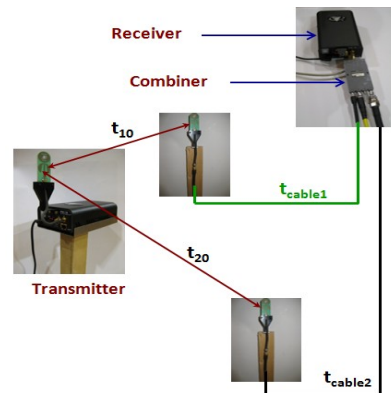


Figure 4. Diagram illustrating the electric delays of the cables.

A. TOA estimation with CA-CFAR and MESSB algorithms

As considered previously, before calculating the TDOA we calculate initially relative TOA (t_1, t_2, t_3 and t_4), where $t_i = t_{i0} + t_{cablei}, i = 1, \dots, 4$. In this section we describe the estimate of the relative TOA by CA-CFAR and MESSB algorithms. These algorithms use the output of energy detector as shown in Fig. 5 and Fig. 6. The integrator output samples can be expressed as

$$z(n) = \int_{(n-1)T_b}^{nT_b} |r(t)|^2 dt. \quad (1)$$

Where $n \in \{1, 2, \dots, N_b\}$ denotes the sample index. N_b is the number of samples contained in a given time frame. The resulting samples are employed in our modified approach based on CA-CFAR technique as illustrated in Fig. 5. Where the samples (cells) are sent serially into a tapped delay line of length $N + 1$, excluding guard cells (the guard cells duration is chosen larger or equal to the channel mean delay [11]). The $N + 1$ samples correspond to the reference cells $z(i)$ ($i = n + 1, \dots, N + n$) and the test cell $z(n)$.

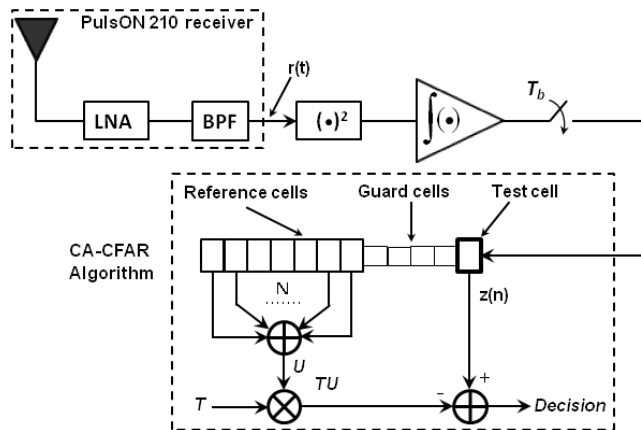


Figure 5. Block diagram of ED receiver employing CA-CFAR approach.

The cell averaging (CA) detector gives an alarm when the value of the test cell, $z(n)$, exceeds TU , where T is a scaling factor and $U = \sum_{i=n+1}^{N+n} z(i)$ is the CA of the reference cells. The arrival time of the first sample crossing the respective threshold value is estimated as TOA [4], i.e.,

$$\hat{t}_{CA-CFAR} = \left[\min_n \{n | z(n) > TU\} - 0.5 \right] T_b. \quad (2)$$

For the MESSB algorithm, the energy samples prior to the maximum should be searched as shown in Fig. 6. The TOA estimate with thresholding and backward search is then given [3]

$$\hat{t}_{MESSB} = \left[\min_n \{n | \bar{z}(n) > \lambda\} - 0.5 + (n_{max} - w_{sb} - 1) \right] T_b, \quad (3)$$

where $\bar{z}(n) = [z(n_{max} - w_{sb}), z(n_{max} - w_{sb} + 1) \dots z(n_{max})]$, the threshold λ is a function of the minimum and maximum values of $z(n)$

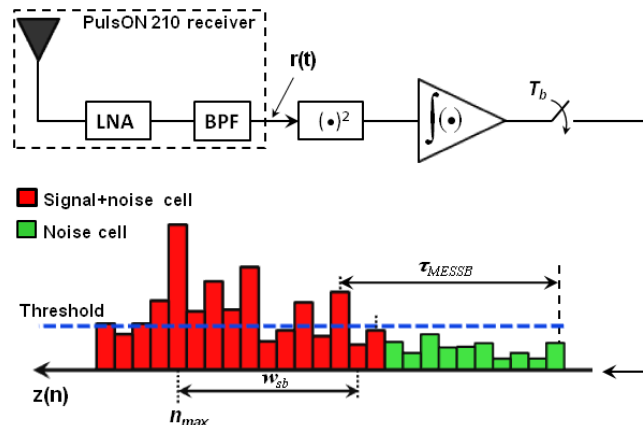


Figure 6. Block diagram of ED receiver employing MESSB algorithm.

$$\lambda = \min\{z(n)\} + \xi_{norm} [\max\{z(n)\} - \min\{z(n)\}]. \quad (4)$$

The optimal value of the normalized threshold ξ_{norm} is experimentally chosen, w_{sb} denotes search-back window in number of samples and $n_{max} = \operatorname{argmax}_{1 \leq n \leq N_b} \{z(n)\}$.

IV. MOBILE TRANSMITTER LOCALIZATION

We study in this section the TDOA localization algorithm. But let us start first by the description of the localization experiment set-up. Firstly, we have a PulsON 210 transmitter fixed on a wooden support for mobility. Secondly, four antennas with known positions are mounted on a wooden support. The four static receiving antennas and the PulsON 210 transmitter were approximately 1.5 m high. These antennas are connected through a power combiner (PS4-7) to PulsON 210 receiver using three different cables with precisely calibrated delays. The PulsON 210 receiver is connected to the Laptop through standard Ethernet cable to communicate the received signals for the user as indicated in Fig. 7.

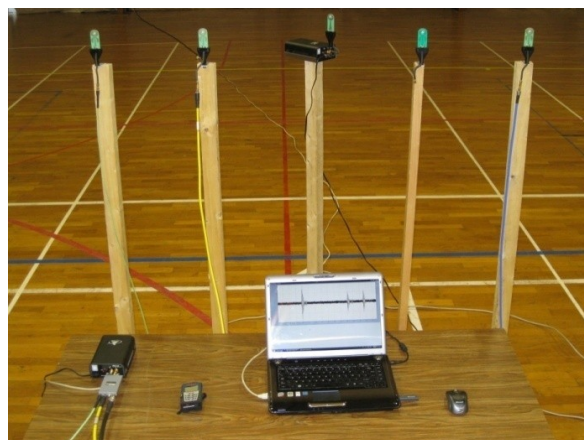


Figure 7. UWB TDOA localization experiment set-up.

For the environment of localization, we place the four antennas at places quite selected in the space of the ESIEE gymnasium. This choice is dictated by the used cables length

and the reference antenna position as shown in Fig. 8. The cables lengths which are connected to the antennas 1, 2 (4) and 3 are 2 m, 10 m and 13.5 m, respectively.

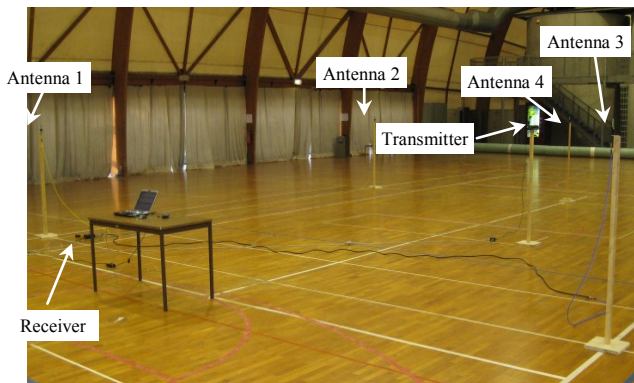


Figure 8. Environment and prototype of localization.

A. Localization algorithm

We describe in this section the used algorithm for the mobile transmitter localization where we are interested in the 2-D localization. Let (x, y) be the mobile station (transmitter) position, (x_i, y_i) be the position of i^{th} receiving antenna and $d_{i1} = c\hat{t}_{i1}$ an estimate of the distances difference between $d_i = ct_i$ ($i = 2, 3, \dots, M$) and $d_1 = ct_1$. We note M the number of antennas, $c = 3 \times 10^8$ m/s the propagation velocity of the signals and \hat{t}_{i1} an estimate of the TDOA. If we fix antenna 1 at the position $(0, 0)$, then we can estimate the position of the mobile by the following matrix form [2] :

$$\theta = G^{-1}h, \quad (5)$$

where

$$h = \begin{bmatrix} c^2 t_{21}^2 - D_2 \\ c^2 t_{31}^2 - D_3 \\ \vdots \\ c^2 t_{M-1,1}^2 - D_{M-1} \end{bmatrix}, \quad (6)$$

$$G = -2 \begin{bmatrix} x_2 & y_2 & ct_{21} \\ x_3 & y_3 & ct_{31} \\ \vdots & \vdots & \vdots \\ x_{M-1} & y_{M-1} & ct_{M-1,1} \end{bmatrix}, \quad (7)$$

and

$$\theta = \begin{bmatrix} x \\ y \\ r \end{bmatrix}. \quad (8)$$

Where $D_i = x_i^2 + y_i^2$, $r = \sqrt{x^2 + y^2}$ and $M = 4$ in our case.

To evaluate the performances of CA-CFAR and MESSB algorithms to estimate the TDOA as well as the algorithm of localization, we proceed as follows: The transmitter trajectory contains 26 positions, and for each position of the trajectory we carry out 10 measurements of the received signal, what gives thirty values of TDOA per position and in total we obtain 780 values of TDOA.

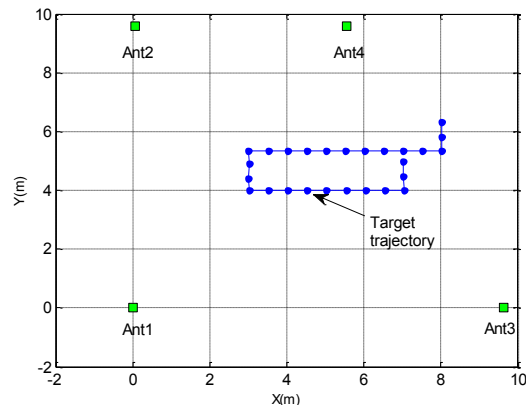


Figure 9. Environment of localization.

The coordinates of the antennas Ant1, Ant2, Ant3 and Ant4 are measured in meters and are respectively as follows: $(x_1 = 0, y_1 = 0)$, $(x_2 = 0.051, y_2 = 9.588)$, $(x_3 = 9.638, y_3 = 0)$ et $(x_4 = 5.557, y_4 = 9.594)$. We show in Fig. 9 the environment of localization.

V. EXPERIMENTAL RESULTS

To analyze the performances of the CA-CFAR and MESSB algorithms in the estimate of the TDOA and in localization, we use the Mean Absolute Error (MAE) $MAE = E(abs(t_{i1} - \hat{t}_{i1}))$ and Root Mean Square Error (RMSE) $RMSE = \sqrt{E\{(x - \hat{x})^2 + (y - \hat{y})^2\}}$ respectively.

For the calculation of the energy blocks $z(n)$, we choose the three following values of the parameter T_b : $T_b = 0.5$ ns, $T_b = 1$ ns and $T_b = 2$ ns. The experiment is made in LOS and NLOS cases. The remainder of the parameters is given as follows:

- $N = 50$ (Number of reference cells) for $T_b = 0.5$ ns and $T_b = 1$ ns ;
- $N = 26$ for $T_b = 2$ ns ;
- $N_g = 6$ ns (Guard cells duration) ;
- $w_{sb} = 8$ ns (search-back window for MESSB).

A. LOS case

In LOS case, there are no obstacles between the receiving antennas and the transmitter antenna. The UWB signals received through three receiving antennas from the mobile transmitter antenna are shown in Fig. 10.

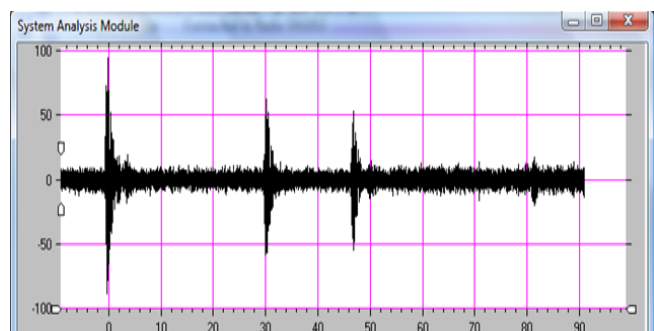


Figure 10. UWB signals received through three receiving antennas.

MAE versus scaling factor T and the normalized threshold ξ_{norm} for the algorithms CA-CFAR and MESSB respectively, are given in Fig. 11. We observe that the performances obtained for the two algorithms are almost identical. For the two algorithms, the curves decrease quickly for the weak thresholds, then the curves converge towards constants. Furthermore, this figure clearly shows that the obtained results are close to the MAE theoretical limit $(c \frac{T_b}{4})$.

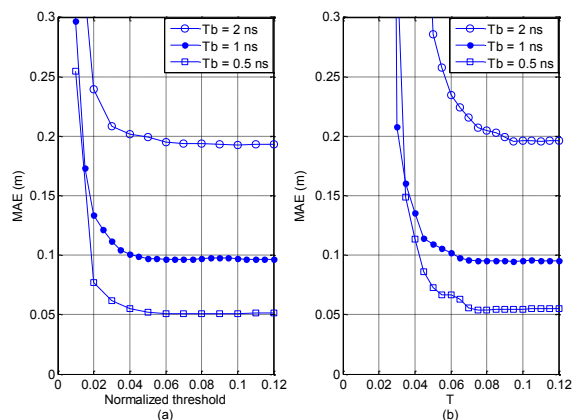


Figure 11. MAE versus thresholds detection. (a) : MESSB algorithm; (b) : CA-CFAR algorithm.

Now we give in table I the performances of the two algorithms for the optimal thresholds and for two orientations 1 and 2 of the antennas. We study the effect of the antennas orientations, because when two antennas at the same elevation are rotated so the flat sides of the antennas face one another, radiation performance will be approximately 6 dB higher than when the antennas are edge-on [5]. We show that there exists a weak difference in performances between the antennas orientations 1 and 2, this is due to the fact that these algorithms are not sensitive to the 6 dB average losses caused by the orientations of the antennas. This table illustrates that CA-CFAR algorithm gives better results except for $T_b = 0.5 \text{ ns}$, because the number of reference cells is insufficient ($N = 50$). The results in table I also show, that the RMSE increases exponentially with the increase of the T_b .

TABLE I. Performances comparison between MESSB and CA-CFAR algorithms.

		MAE (cm)		RMSE (cm)	
		MESSB	CA-CFAR	MESSB	CA-CFAR
$T_b = 0.5 \text{ ns}$	Direction 1	5.08	5.45	12.75	13.25
	Direction 2	5.09	5.6	12.79	13.85
$T_b = 1 \text{ ns}$	Direction 1	9.63	9.51	29.12	27.93
	Direction 2	9.77	9.41	29.22	27.26
$T_b = 2 \text{ ns}$	Direction 1	19.60	19.50	95.45	87
	Direction 2	19.34	19.30	90.64	89.92

B. NLOS case

In the preceding case, the receiving antennas and the mobile transmitter have a LOS condition, where the SNR is higher than 20 dB. Now, a metallic obstacle is placed between the mobile transmitter and antenna 2 in order to create an NLOS channel as indicated in Fig. 12. An example of a signal in such environment is given in Fig. 13.



Figure 12. Metallic obstacle between the mobile transmitter and the receiving antenna 2.

We show in Fig. 13 and Fig. 14 that the received impulse by antenna 2 in NLOS case is attenuated and delayed compared to that received in LOS case. We also show that it is followed by a more powerful reflected impulse by the floor that can cause an additional positive error to the estimate of the relative TOA.

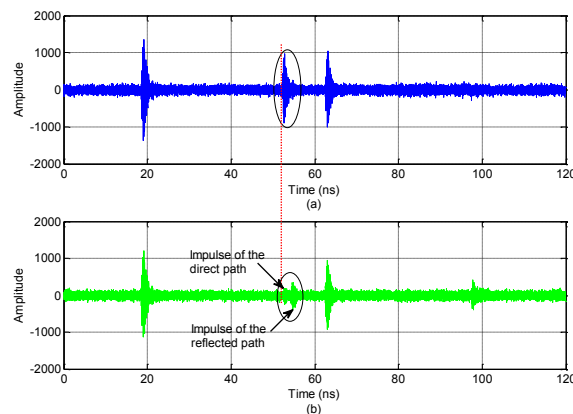


Figure 13. Comparison between LOS/NLOS received signals. (a): LOS received signal, (b): NLOS received signal.

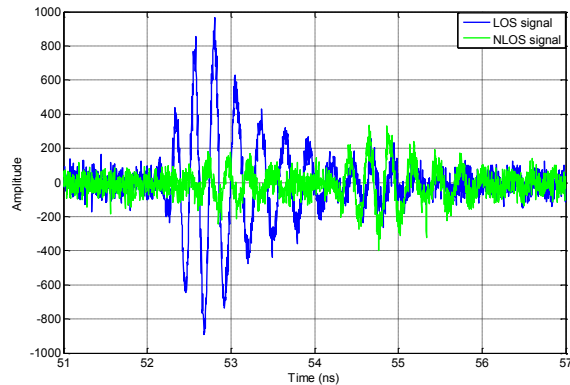


Figure 14. Zoom of the selected zones in Fig. 13.

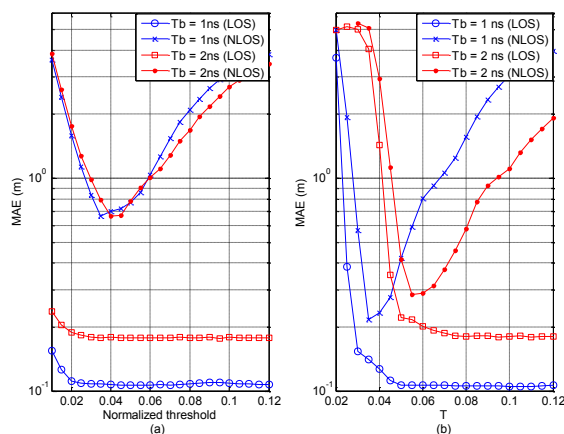


Figure 15. MAE versus thresholds detection in LOS/NLOS situations. (a) : MESSB algorithm, (b) : CA-CFAR algorithm.

We only consider in this section the MAE and we study the following cases: $T_b = 1 \text{ ns}$ and $T_b = 2 \text{ ns}$ with the same algorithms of TDOA estimation and the same parameters. The obtained results are given in Fig. 15. This figure clearly shows that the CA-CFAR algorithm gives better performances than the MESSB algorithm in NLOS situations. This is due to the fact that the CA-CFAR uses an adaptive threshold which detects the attenuated signals, and the MESSB detects the impulse of the reflected path instead of the impulse of the direct path which is much attenuated. Also, Fig. 15 shows that in NLOS situation, the MESSB algorithm gives the same performances for $T_b = 1 \text{ ns}$ and $T_b = 2 \text{ ns}$. This is due to the fact that the duration of the reflected impulse is lower than the duration of the LOS impulse as indicated in Fig. 14. But for CA-CFAR algorithm, the obtained performances are different for $T_b = 1 \text{ ns}$ and $T_b = 2 \text{ ns}$ because the algorithm detects the weak signals.

VI. CONCLUSION AND FUTURE WORK

In the present paper, the performances of UWB experimental location system in LOS/NLOS environments have been investigated. For ranging, low complexity CA-CFAR and MESSB algorithms for relative TOA estimation are used. These algorithms are based on the use of the output of non-coherent energy detection receivers. For location estimation, TDOA algorithm is used. The system of location is based on the use of UWB radios PulsON 210 from Time Domain Corporation. Experimental results have shown that the MESSB and CA-CFAR algorithms give almost identical performances in the LOS environment. But in NLOS environment, CA-CFAR algorithm gives better results. As future work, the comparison between the two approaches can be carried out on signals measured in a dense multipath environment.

REFERENCES

- [1] J. Ni, D. Arndt, P. Ngo, C. Phan, K. Dekome, and J. Dusl, "Ultra-Wideband Time-Difference-Of-Arrival High Resolution 3D Proximity Tracking System," in *Proc. IEEE Position Location and Navigation Symposium (PLANS)*, Indian Wells, CA, USA, pp. 37 - 43, May 2010.
- [2] J. Ni and R. Barton, "Design and Performance Analysis of a UWB Tracking System for Space Applications," in *Proc. IEEE/ACES Int. Conf. on Wireless Communications and Applied Computational Electromagnetics*, pp. 31- 34, April 2005.
- [3] I. Guvenc and Z. Sahinoglu, "Threshold based TOA estimation for impulse radio UWB systems," in *Proc. IEEE Int. Conf. UWB (ICU)*, Zurich, Switzerland, pp. 420-425, Sep. 2005.
- [4] A. Maali, A. Mesloub, M. Djeddou, G. Baudoin, H. Mimoun, and A. Ouldali, "Adaptive CA-CFAR threshold for non coherent IR-UWB energy detector receivers," *IEEE Communications Letters*, Vol. 13, No. 12, pp. 1-3, December 2009.
- [5] System Analysis Module User's Manual PulsON 210 UWB Reference Design, Time Domain Corporation, P210-320-0102B, Aug 2005.
- [6] J. Y. Lee and R. A. Scholtz, "Ranging in a dense multipath environment using a UWB radio link," *IEEE J Select Areas Commun*, Vol. 20, pp. 1677-1683, 2002.
- [7] S. Gezici, Z. Tian, G. B. Biannakis, and H. Kobayashi, "Localization via Ultra-Wideband Radios, A look at positioning aspects of future sensor networks," *IEEE Signal Processing Magazine*, pp. 70-84, July 2005.
- [8] Z. Shahinoglu, S. Gezici, and Ismail Guvenc, "Ultra-wideband Positioning Systems : Theoretical Limits, Ranging Algorithms, and Protocols," Cambridge University Press, 2008.
- [9] A. Farrouki and M. Barkat, "Automatic censoring CFAR detector based on ordered data variability for nonhomogeneous environments," *IEE Proceedings, Radar, Sonar Navigation*, Vol. 152, No. 1, pp. 43-51, February, 2005.
- [10] C.-M. Cho and M. Barkat, "Moving ordered statistics CFAR detection for nonhomogeneous backgrounds," *IEE PROCEEDINGS-F*, Vol. 140, No. 5, pp. 284 -290, October 1993
- [11] B. R. Mahafza, "Radar Systems Analysis and Design Using MATLAB," Chapman & Hall/CRC, 2000.